



**HELLENIC REPUBLIC**

**UNIVERSITY OF IOANNINA**

**SCHOOL OF ENGINEERING**

**DEPARTMENT OF MATERIALS SCIENCE AND ENGINEERING**

# **Blood Flow Modelling in Arteries with Deformable Walls**

**Panagiotis K. Siogkas**

PhD Thesis

**IOANNINA 2018**









**ΕΛΛΗΝΙΚΗ ΔΗΜΟΚΡΑΤΙΑ  
ΠΑΝΕΠΙΣΤΗΜΙΟ ΙΩΑΝΝΙΝΩΝ  
ΠΟΛΥΤΕΧΝΙΚΗ ΣΧΟΛΗ  
ΤΜΗΜΑ ΜΗΧΑΝΙΚΩΝ ΕΠΙΣΤΗΜΗΣ ΥΛΙΚΩΝ**

**Μοντελοποίηση ροής αίματος σε αρτηρίες με κινούμενα  
τοιχώματα**

**Παναγιώτης Κ. Σιόγκας**

**ΔΙΔΑΚΤΟΡΙΚΗ ΔΙΑΤΡΙΒΗ**

**ΙΩΑΝΝΙΝΑ 2018**





**HELLENIC REPUBLIC**

**UNIVERSITY OF IOANNINA**

**SCHOOL OF ENGINEERING**

**DEPARTMENT OF MATERIALS SCIENCE AND ENGINEERING**

# **Blood Flow Modelling in Arteries with Deformable Walls**

**Panagiotis K. Siogkas**

PhD Thesis

**IOANNINA 2018**





*«Η έγκριση της διδακτορικής διατριβής από το Τμήμα Μηχανικών Επιστήμης Υλικών της Πολυτεχνικής Σχολής του Πανεπιστημίου Ιωαννίνων δεν υποδηλώνει αποδοχή των γνωμών του συγγραφέα Ν. 5343/32, άρθρο 202, παράγραφος 2».*



**Date of application of Mr. Siogkas:** 1<sup>st</sup> July 2009

**Date of appointment of PhD Advisory Committee:** 8<sup>th</sup> July 2009

**Members of the 3 member Advisory Committee:**

Thesis Advisor

Prof. Dimitrios I. Fotiadis, Dept. of Materials Science and Engineering, Polytechnic School, University of Ioannina.

Members

Prof. Lampros Michalis, Medical School, University of Ioannina.

Prof. Demosthenes Polyzos, Dept. of Mechanical Engineering and Aeronautics, Polytechnic School, University of Patras.

**Date of Thesis subject definition:** 8<sup>th</sup> July 2009

Title: Blood Flow Modelling in Arteries with Deformable Walls

**Date of appointment of the 7 member Examination Committee:** 5/12/2016

**Members of the 7 member Advisory Examination Committee:**

- 
1. **Prof. Dimitrios I. Fotiadis**, Dept. of Materials Science and Engineering, Polytechnic School, University of Ioannina, **Thesis Advisor**.
  2. **Prof. Lampros K. Michalis**, Medical School, University of Ioannina, **member of the 3 member Advisory Committee**.
  3. **Prof. Demosthenes Polyzos**, Dept. of Mechanical Engineering and Aeronautics, Polytechnic School, University of Patras, **member of the 3 member Advisory Committee**.
  4. **Prof. Dimitrios Koutsouris**, Dept. of Electrical and Computer Engineering, National Technical University of Athens.
  5. **Prof. Simeon Agathopoulos**, Dept. of Materials Science and Engineering, Polytechnic School, University of Ioannina.
  6. **Assoc. Prof. Christos Katsouras**, Medical School, University of Ioannina.
  7. **Assist. Prof. Leonidas Gergidis**, Dept. of Materials Science and Engineering, Polytechnic School, University of Ioannina.
- 

The PhD thesis is approved, with «**Excellent**» on 21-3-2018

The Chairman of the Department  
Prof. Alkiviadis Paipetis

The secretary of the Department  
Maria Kontou



**Ημερομηνία αίτησης της/του κ. Παναγιώτη Σιόγκα: 1-7-2009**

**Ημερομηνία ορισμού Τριμελούς Συμβουλευτικής Επιτροπής: 8-7-2009**

**Μέλη Τριμελούς Συμβουλευτικής Επιτροπής:**

Επιβλέπων

Δημήτριος Ι. Φωτιάδης - Καθηγητής Μηχανικών Επιστήμης Υλικών, Παν/μιο Ιωαννίνων

Μέλη

Λάμπρος Μιχάλης - Καθηγητής Ιατρικής, Παν/μιο Ιωαννίνων

Δημοσθένης Πολύζος – Καθηγητής Μηχανολόγων και Αεροναυπηγών Μηχανικών, Παν/μιο Πατρών

**Ημερομηνία ορισμού θέματος: 8-7-2009**

**Θέμα:** Μοντελοποίηση της ροής αίματος σε αρτηρίες με κινούμενα τοιχώματα

**ΔΙΟΡΙΣΜΟΣ ΕΠΤΑΜΕΛΟΥΣ ΕΞΕΤΑΣΤΙΚΗΣ ΕΠΙΤΡΟΠΗΣ : 5/12/2016**

- 
- 1.Καθ. **Δημήτριος Φωτιάδης**, Τμήμα Μηχανικών Επιστήμης Υλικών, Σχολή Θετικών Επιστημών, Παν/μιο Ιωαννίνων
  - 2.Καθ. Καρδιολογίας **Λάμπρος Μιχάλης**, Τμήμα Ιατρικής, Σχολή Επιστημών Υγείας, Παν/μιο Ιωαννίνων
  - 3.Καθ. **Δημοσθένης Πολύζος**, Τμήμα Μηχανολόγων και Αεροναυπηγών Μηχανικών της Πολυτεχνικής Σχολής, Παν/μιο Πατρών
  - 4.Καθ. **Δημήτριο Κουτσούρη**, Τμήμα Ηλεκτρολόγων Μηχανικών και Μηχανικών Υπολογιστών, Εθνικό Μετσόβιο Πολυτεχνείο
  - 5.Καθ. **Συμεών Αγαθόπουλος**, Τμήμα Μηχανικών Επιστήμης Υλικών, Σχολή Θετικών Επιστημών, Παν/μιο Ιωαννίνων
  - 6.Αναπλ. Καθ. Καρδιολογίας **Χρήστος Κατσούρας**, Τμήμα Ιατρικής, Σχολή Επιστημών Υγείας, Παν/μιο Ιωαννίνων
  - 7.Επικ. Καθ. **Λεωνίδας Γεργίδης**, Τμήμα Μηχανικών Επιστήμης Υλικών, Σχολή Θετικών Επιστημών, Παν/μιο Ιωαννίνων
- 

Έγκριση Διδακτορικής Διατριβής με βαθμό «**Άριστα**» στις 21-3-2018

**Ο Πρόεδρος του Τμήματος**

**Αλκιβιάδης Παϊπέτης**

**Καθηγητής**

**Η Γραμματέας του Τμήματος**

**Μαρία Κόντου**



## **Dedication**

*To my parents and my wife*





## Acknowledgements

First of all, I would like to thank my family, who all these years support my dreams and my effort. My parents deserve special thanks for their unlimited support and encouraging. I would also like to thank my wife for supporting me and for motivating me to complete my thesis.

I would like to cordially thank my supervisor Prof. Dimitrios I. Fotiadis, Dept. of Materials Science and Engineering, University of Ioannina for his support and great assistance in order to complete this thesis. I would like to emphasize my sincere appreciation for the financial support I had all these years and the contribution of Prof. Fotiadis. I would also like to thank the members of my advisory committee, Prof. Lampros Michalis, Medical School, University of Ioannina and Prof. Demosthenes Polyzos, Dept. of Mechanical Engineering & Aeronautics, University of Patras, for the inspiration, guidance and continuous support.

I would also like to sincerely thank Dr. Themis Exarchos, Dr. George Rigas and Mr. Kostas Stefanou for their collaboration and support all these years. I would like to warmly thank all my colleagues and friends from the Unit of Medical Technology and Intelligent Information Systems for the excellent cooperation, friendship and support in demanding working conditions.

Furthermore, I would also like to thank Dr. Constantinos Anagnostopoulos, Dr. Michail Papafaklis and Dr. Lampros Lakkas for the excellent collaboration that we had through these years.

This research was part funded by: the European Commission [Project ARTREAT: Multi-level patient-specific artery and atherogenesis model for outcome prediction, decision support treatment, and virtual hand-on training, FP7-224297, Project CHRONIUS: An Open, Ubiquitous and Adaptive Chronic Disease Management Platform for COPD and Renal Insufficiency, FP7-ICT-2007-1- 216461, Project HEARTEN, grant agreement No 643694, Project SMARTool, Grant Agreement number 689068, as well as, through the Operational Program “THESSALY- MAINLAND GREECE AND EPIRUS-2007-2013” of the National Strategic Reference Framework (NSRF 2007-2013).



## Table of Contents

<b>Chapter 1: Introduction .....</b>	<b>1</b>
1.1    Physiology of the Cardiovascular system .....	1
1.1.1    Heart and the coronary network.....	2
1.1.2    Functions of the Heart.....	4
1.1.3    Coronary Network .....	5
1.1.4    Blood Vessels.....	6
1.2    Atherosclerosis.....	8
1.2.1    Introduction.....	8
1.2.2    Blood flow effect on atherosclerosis.....	11
1.2.3    Treatment and management of atherosclerosis .....	12
1.3    Coronary Imaging Modalities .....	13
1.3.1    Introduction.....	13
1.3.2    Non-Invasive Coronary Imaging Modalities .....	13
1.3.3    Invasive Coronary Imaging Modalities .....	15
1.3.4    Coronary artery functional assessment techniques .....	19
<b>Chapter 2: Literature Overview.....</b>	<b>23</b>
2.1.    Introduction.....	23
2.2.    Blood Flow Modeling .....	24
2.3.    CCTA derived computational FFR assessment .....	26
2.4.    Invasive Coronary Imaging derived functional assessment.....	28
2.5.    Other virtual indices of coronary functional assessment .....	32
2.6.    Contribution of this Thesis.....	33
<b>Chapter 3: Blood Flow Simulations in arteries with rigid or deformable walls .....</b>	<b>37</b>
3.1.    Introduction.....	37
3.2.    Blood Flow Modeling .....	38
3.3.    Blood flow simulations on arteries with rigid or deformable walls.....	44
3.3.1    Rigid walls assumption .....	44
3.3.2    Fluid Structure Interaction simulations.....	45

3.3.3	Dataset.....	47
3.3.4	Results.....	48
3.3.5	Discussion .....	49
3.4.	Patient-Specific Simulation of Coronary Artery Pressure Measurements.....	50
3.4.1	Patient Data.....	51
3.4.2	3-dimensional Reconstruction .....	52
3.4.3	Blood Flow Simulations .....	53
3.4.4	Boundary Conditions .....	54
3.4.5	Results.....	57
3.4.6	Validation results .....	57
3.4.7	Rigid Wall versus FSI Simulations.....	57
3.4.8	Transient versus Steady Flow Simulations .....	58
3.4.9	Discussion .....	60
3.4.10	Clinical Implications and Challenges. ....	63
3.4.11	Conclusions.....	64
<b>Chapter 4: Computational assessment of coronary stenoses using non-invasive or invasive techniques.....</b>		<b>65</b>
4.1.	Introduction.....	65
4.2.	Computational assessment of coronary stenosis using non-invasive techniques ....	66
4.2.1	CT-based hemodynamic assessment of coronary lesions derived from fast computational analysis: a comparison against fractional flow reserve.....	66
4.2.2	Characterization of functionally significant coronary artery disease by a novel coronary computed tomography angiography-based index: a comparison with PET perfusion .....	81
4.2.2.1	Study Population.....	81
4.2.2.2	CCTA Imaging.....	82
4.2.2.3	PET imaging and data analysis .....	83
4.2.2.4	Statistical analysis.....	83
4.2.2.5	Results.....	84
4.2.2.6	Impact of stenosis severity on quantitative PET indices .....	85
4.2.2.7	Impact of stenosis severity on vFAI .....	86
4.2.2.8	Relationship between vFAI and quantitative PET indices .....	87

4.2.2.9	Diagnostic accuracy of vFAI for detecting reduced hyperemic response or MFR.....	88
4.2.2.10	Performance of vFAI and quantitative PET indices for detecting inducible perfusion defects.....	89
4.2.2.11	Discussion.....	90
4.3.	Computational assessment of coronary stenosis using invasive techniques.....	94
4.3.1	Virtual Functional Assessment of Coronary Stenoses Using Intravascular Ultrasound Imaging .....	94
4.3.2	Computational Assessment of the Fractional Flow Reserve using IVUS and ICA.....	100
4.3.3	smartFFR: a novel, fast index for the functional assessment of coronary stenoses.....	104
<b>Chapter 5: Integrated Systems for 3D Coronary Reconstruction, Functional Assessment and Multiscale modelling .....</b>		<b>109</b>
5.1.	Introduction.....	109
5.2.	Multiscale - Patient-Specific Artery and Atherogenesis Models.....	110
5.2.1	3D image reconstruction .....	111
5.2.2	Blood flow and Biological Process Modelling .....	111
5.2.3	Plaque Characterization .....	114
5.2.4	Results.....	114
5.2.5	Discussion.....	117
5.3.	Art Care: A Multi-Modality Coronary 3D Reconstruction and Hemodynamic Status Assessment Software .....	118
<b>Chapter 6: Conclusions and Future Work .....</b>		<b>133</b>
6.1	Computational Assessment of the Severity of Coronary Stenoses.....	133
6.2	Future Work.....	135
<b>Author's Publications .....</b>		<b>153</b>



## List of Figures

Figure 1: Anatomy of the heart [1] .....	2
Figure 2: Circulatory System Diagram {Mohr, 2006 #1253}. ....	4
Figure 3: The coronary arteries [4]. ....	6
Figure 4: Structure of the arterial wall [8]. ....	7
Figure 5: Pathogenesis of atherosclerosis. Endothelial dysfunction [14]. (b) Adhesion of blood leucocytes (T lymphocytes, white; monocytes, orange) and thrombocytes . Immigration of adhered monocytes into subendothelial areas (diapedesis). Immigration of smooth muscle cells [15] from the media (light blue) into subendothelial tissues (adaptive intimal thickening) and foam cell formation (formation of an atheroma). The immigration of smooth muscle cells is accompanied by a switch to a synthetic phenotype (purple). Hence, subendothelial deposition of extracellular matrix material (purple) is increased. Thickening of the lesion by enhanced foam cell formation (white spots within the cells), immigration of smooth muscle cells and further deposition of extracellular matrix proteins (purple). (f) Formation of a fibrous cap (purple) and a necrotic lipid core [15]. The latter appears because of the death of foamy macrophages. Due to the synthesis of proteases by macrophages, the fibrous cap covering the lipid core is thinned. Plaque rupture or erosion of the endothelium occurs. (i) The contact of blood with the subendothelial tissue activates the clotting cascade and a thrombus is formed [10]......	9
Figure 6: Blood flow and the consequent stresses that are created within the artery [23]. ....	12
Figure 7: CCTA image from a 320-slice scanner of a right mammary artery bypass graft (free transplant with end-to-side anastomosis on left mammary artery) with anastomosis on obtuse marginal branch [9]......	14
Figure 8: Typical Invasive Coronary Angiography projection of a RCA (red arrow indicates a stenosis).....	16
Figure 9: Typical IVUS image (left) and its respective VH-IVUS (right). ....	17
Figure 10: Typical OCT images of a healthy lumen (left) and of a stented region (right). ....	18

Figure 11: Fractional Flow Reserve illustration [52].....20

Figure 12: (a) X-ray angiography showing diffused stenoses at the left anterior descending artery. (b) Three-dimensional angiographic reconstruction and the generated meshes. (c) Simulated pressure distribution at hyperemia. The computed FFR-QCA was 0.59 and the wire-based FFR was 0.60 at the distal position indicated by the arrow. (d) Simulated hyperemic flow colored by the velocity [85]. magnitude. (e) Virtual ‘reversed’ FFR pullback along the centerline of the left anterior descending artery. FFR-QCA: computed quantitative coronary artery (QCA) fractional flow reserve. Reproduced from Tu et al [84]. .....29

Figure 13: (a) Representative example of a left anterior descending artery (LAD) with a moderate lesion (arrow: maximal stenosis) in angiography (3D-QCA %diameter stenosis: 35%) that had (b) a low fractional flow reserve (FFR = 0.64) measured at a distal location (dotted arrow) using the pressure wire. (c) 3D-QCA coronary lumen reconstruction with the pressure distribution in a color- coded map for two different flow rates (Q), which resulted in a pressure gradient ( $\Delta P$ ) of 13.7 and 60.9 mmHg. The computed artery-specific  $\Delta P$ -Q relationship is provided. The arrows denote the location of maximal stenosis. (d) Relationship between the ratio of distal to aortic pressure ( $P_d/P_a$ ) and flow for the studied artery, and calculation of the artery-specific virtual functional assessment index (vFAI: 0.62) shows the good agreement with wire-FFR [87].....31

Figure 14: a) Right coronary artery with a moderate lesion in angiography and a high fractional flow reserve (FFR = 0.90) measured using the pressure wire. (b) 3D-QCA coronary lumen reconstruction with the pressure distribution (resting conditions) in a color-coded-map which resulted in a virtual resting  $P_d/P_a$  of 0.97. (c) Left anterior descending artery with a moderate lesion in angiography and a low FFR (0.70) measured using the pressure wire. (d) 3D-QCA coronary lumen reconstruction with the pressure distribution (resting conditions) in a color-coded- map which resulted in a virtual resting  $P_d/P_a$  of 0.85. The arrows denote the location of maximal stenosis in each case. 3D-QCA: 3-dimensional quantitative coronary angiography [88]. .....33

Figure 15: The top row images depict the inlet and outlet boundary conditions for the first arterial model, whereas the bottom row images depict the boundary conditions for the second one, respectively. ....47



Figure 16: Calculated WSS distribution for the FSI (top left) and rigid wall (top right) simulations. Areas of low WSS (0-1 Pa) for the FSI (bottom left) and rigid wall (bottom right) simulations (Arterial Model 1).....	48
Figure 17: Calculated WSS distribution for the FSI (top left) and rigid wall (top right) simulations. Areas of low WSS (0-1 Pa) for the FSI (bottom left) and rigid wall (bottom right) simulations (Arterial Model 2).....	49
Figure 18: The two views depict the exact locations of the start (a) and end (b) of the pullback procedure as well as the exact positions of the pressure and flow measurements acquisition. ....	52
Figure 19: Three-dimensional reconstruction of the lumen of a right coronary artery for patient #2 (a) and patient #1 (b).....	53
Figure 20: Measured pressure profile for patient #6 for a full cardiac cycle.....	54
Figure 21: Mean velocity values calculated for patient #1 in order to determine the optimal velocity profile for validation. ....	55
Figure 22: Left image: (a) depicts the pressure waveforms for the examined cardiac cycles (measured and calculated results) and (b) exhibits the linear regression analysis for patient #1. Right image: (a) depicts the pressure waveforms for the examined cardiac cycles (measured and computed results) and (b) exhibits the linear regression analysis for patient #6. ....	58
Figure 23: (a) pressure waveforms for the examined cardiac cycles (measured and computed results) and (b) linear regression analysis for patients #2 (upper left image), #3 (upper right image), #4-RCA (lower left image) and #4-LAD (lower right image), respectively. ....	59
Figure 24: Left image: (a) depicts the pressure waveforms for the examined cardiac cycles (measured and computed results) and (b) exhibits the linear regression analysis for patient #5, right coronary artery. Right image: (a) depicts the pressure waveforms for the examined cardiac cycles (measured and computed results) and (b) exhibits the linear regression analysis for patient #5, left anterior descending coronary artery. ....	60
Figure 25: Bland-Altman plot for all 8 cases.....	62
Figure 26: Enrolment and diagnostic procedures. ....	68

Figure 27: A) Reconstruction process flow chart. B) Reconstruction process. The arrow indicates the point of the RCA that was annotated by the user. C) 3D reconstructed artery, which is derived from the previously annotated point. D) Pressure distribution for flow rates of 1 ml/s and 3 ml/s. E) Invasively measured FFR was 0.92, the same as the respective vFAI. ....	72
Figure 28: Regression plot comparing the two methods. ....	75
Figure 29: Bland-Altman plot comparing the two methods ....	76
Figure 30: ROC curves comparing vFAI vs. CTCA diagnostic performance to recognize hemodynamically significant coronary lesions ( $FFR \leq 0.80$ ). The area under the curve for the vFAI is 0.90 ( $P < 0.0001$ ), whereas for CTCA is 0.51 ( $P = 0.93$ ). ....	77
Figure 31: Enrolment and data acquisition scheme. ....	82
Figure 32: Impact of stenosis severity on vFAI and MFR, respectively. ....	86
Figure 33: Impact of stenosis severity on several PET indices. ....	87
Figure 34: Diagnostic accuracy of vFAI for detecting reduced hyperemic response or MFR. ....	89
Figure 35: Performance of vFAI and quantitative PET indices for detecting inducible perfusion defects ....	90
Figure 36: Annotation and segmentation process of the IVUS frames. ....	96
Figure 37: IVUS 3D reconstruction method.....	97
Figure 38: Point cloud to 3D volume transformation process. ....	97
Figure 39: <b>A.</b> Angiographic image of a Left Anterior Descending artery with a functionally significant lesion assessed by fractional flow reserve (0.71). The two straight lines indicate the proximal and distal ends of the segment interrogated by intravascular ultrasound (IVUS). The arrow indicates the location of the minimum lumen area. <b>B.</b> IVUS image corresponding to the minimum lumen area ( $1.82 \text{ mm}^2$ ) of the lesion. <b>C.</b> Three-dimensional coronary lumen reconstruction after linearly stacking the lumen borders of the IVUS images. A color map denotes the pressure distribution for the simulated rest and hyperemic flow rates which are used for the computation of the virtual functional assessment index (vFAI). The arrow denotes	

the location of the minimum lumen area shown in the IVUS image. <b>D.</b> Relationship between the ratio of distal to aortic pressure ( $P_d/P_a$ ) and flow for the studied artery, and calculation of the virtual functional assessment index as the ratio of the area under the curve to the total area. <b>E.</b> There was a close correlation between the IVUS-based vFAI and fractional flow reserve (FFR; $r_s=0.88$ ). <b>F.</b> The Bland-Altman plot showed a mean difference of 0.020 (solid line) between vFAI and FFR; the dashed lines represent the values at $\text{mean} \pm 1.96\text{SD}$ . Of note, 20 plotted values are shown in graphs E and F due to overlapping of cases with identical FFR and vFAI values (i.e. there were two cases with $\text{FFR}=0.96$ and $\text{vFAI}=0.98$ , and another two cases with $\text{FFR}=0.93$ and $\text{vFAI}=0.94$ ). ....	99
Figure 40: Flow Rate Measurement Process. ....	101
Figure 41: Pressure and flow waveforms during the cardiac cycle; the wave-free period in diastole is denoted [53]. ....	102
Figure 42: Simulated FFR distribution throughout a LAD segment and comparison to the measured FFR value. ....	103
Figure 43: Linear Regression plot and Bland Altman plots for all 7 cases. ....	103
Figure 44: Boundary conditions for the smartFFR calculation. ....	105
Figure 45: Regression plot between smartFFR and the invasively measured FFR. ....	106
Figure 46: Bland-Altman plot for the two methods. ....	107
Figure 47: ROC analysis for the smartFFR index. ....	107
Figure 48: Matching IVUS and histological cross-sectional geometry. Shear stress distribution is shown along the internal arterial wall. ....	115
Figure 49: Computer reconstruction of a cross-section of LAD at 15mm after bifurcation (left panel), with computed concentration of macrophages [mg/ml] (middle panel); histological analysis (right panel) after 2 months of the high fat diet. ....	116
Figure 50: System Architecture Diagram. ....	120
Figure 51: A) IVUS load and R-peak frame selection screen, B) OCT load and R-peak frame selection screen, C) Angiography DICOM file load and R-peak frame selection screen, D)	

IVUS lumen border detection screen, E) Side branch detection screen and, F) OCT luminal border detection screen. ....121

Figure 52: A) 3D-QCA luminal border detection and 2D centerline extraction screen, B) 3D centerline extraction screen, C) 3D model rotation using side branches and final back projection to the respective angiography, D) vFAI calculation screen, E) Final 3D model with the corresponding IVUS frame and the calculated results and, F) Fly-through camera option for the final 3D model. ....124

Figure 53: Correlation diagrams and Bland-Altman plots for: A) the calculated volumes, B) minimum lumen diameters, C) segment length, and D) calculated vFAI. Bland-Altman plots for: E) the calculated volumes, F) minimum lumen diameters, G) segment length, and H) calculated vFAI.....127

Figure 54: A) Bland-Altman plot for the comparison of manual IVUS lumen detection versus software IVUS lumen detection, B) Bland-Altman plot for the comparison of manual OCT lumen detection versus software OCT lumen detection, C) Correlation plot for the comparison of manual IVUS lumen detection versus software IVUS lumen detection and, D) Correlation plot for the comparison of manual OCT lumen detection versus software OCT lumen detection .....130

## List of Tables

Table 1: Blood vessel classification and structural characteristics.....	8
Table 2: The risk factors of Atherosclerosis [18]. .....	11
Table 3: Performance of computational models for virtual functional assessment against fractional flow reserve (cut-off $\leq 0.80$ ) [92]. .....	34
Table 4: Patient demographic and Clinical Characteristics .....	53
Table 5: Results of the mesh sensitivity analysis in the lumen (rigid wall assumption). .....	56
Table 6: Results of the sensitivity analysis in the deformable wall assumption (lumen face size was 0.09–0.12 mm). .....	57
Table 7: Comparison between the wire-based measured pressure values ( $P_{out}$ ) and the computed values from the four types of simulations ( $P_{out(comp)}$ ).....	62
Table 8: Results of the parametric study concerning the velocity profiles (steady-state simulations).....	63
Table 9: Baseline Characteristics of the study population (N=44) .....	73
Table 10: Characteristics of the coronary vessels at invasive evaluation (N=51) .....	74
Table 11: Per-vessel Diagnostic performance for vFAI and CTCA.....	76
Table 12: Baseline demographic, clinical and lesion characteristics.....	84
Table 13: Agreement between vFAI and MFR for $^{15}\text{O}$ -water PET measurements (vessels $>30\%$ , n=73) .....	87
Table 14: Agreement between vFAI and MFR for $^{15}\text{O}$ -water PET measurements .....	88
Table 15: Agreement between vFAI and MFR for $^{13}\text{N}$ -ammonia PET measurements .....	88
Table 16: Per-vessel Diagnostic performance for smartFFR.....	106
Table 17: Values for the animal experiments. ....	117

Table 18: Validation results of the comparison between CAAS QCA 3D® and Art Care regarding calculated volumes, vFAI, segment length and minimum lumen diameter .....	126
Table 19: Validation results of the comparison between manual lumen detection and software lumen detection for processing IVUS and OCT images.....	129
Table 20: Comparison of similar software suites to the proposed software suite. ....	131

## List of abbreviations

3D	3-dimensional
3D-QCA	3-dimensional quantitative coronary analysis
ACS	acute coronary syndrome
ADVISE	Adenosine Vasodilator Independent Stenosis Evaluation
AV	Atrioventricular Valve
BL	Baseline
CAD	Coronary Artery Disease
CCA	Common Carotid Artery
CI	confidence interval
CT	computed tomography
CTCA	computed tomography coronary angiography
CVD	CardioVascular Disease
DeFACTO	Determination of Fractional Flow Reserve by Anatomic Computed Tomographic Angiography
DISCOVER-FLOW	Diagnosis of Ischemia-Causing Stenoses Obtained Via Noninvasive Fractional Flow Reserve
ESS	Endothelial shear stress
EVINCI	Evaluation of Integrated Cardiac Imaging for the Detection and Characterization of Ischemic Heart Disease
FFR	Fractional Flow Reserve

FLAIR	Functional Lesion Assessment of Intermediate Stenosis to Guide Revascularization
FSI	Fluid Structure Interaction
FU	Follow-up
GMM	Gaussian Mixture Model
GMRES	Generalized Minimal Residual
HDL	High density lipoprotein
ICA	Invasive Coronary Angiography
iFR	Instantaneous wave-free ratio
IHC	Immunohistochemistry
IVPA	IntraVascular PhotoAcoustic
IVUS	intravascular ultrasound
LCx	left circumflex coronary artery
LDL	Low density lipoprotein
MRI	magnetic resonance imaging
MSCT	Multi-slice computed tomography
NO	Nitric oxide
NPV	Negative Predictive Value
NURBS	non-uniform rational B-spline
OCT	optical coherence tomography
PDA	Posterior Descending Aorta



PLATFORM	Prospective Longitudinal Trial of FFRct: Outcome and Resource Impacts
PPV	Positive Predictive Value
RCA	right coronary artery
RF-IVUS	RadioFrequency Intravascular UltraSound
ROI	Region of Interest
SA	Sinoatrial Artery
SMC	Smooth Muscle Cells
TNF- $\alpha$	Tumor necrosis factor alpha
TOF	Time-of-Flight
vFAI	Virtual Functional Assessment Index
VH	Virtual histology
VIRTU-1	VIRTUal Fractional Flow Reserve from Coronary Angiography
WSS	Wall Shear Stress

## List of symbols

$\dot{\gamma}$	strain rate
$c$	solute concentration
$D$	Diffusivity
$\rho$	density
$\mu$	viscosity
$v_x, v_y, v_z$	velocity components
$p$	pressure
$g$	gravitational accelerator
$t$	time
$\tau$	stress tensor
$N$	interpolation functions
$\{\mathbf{v}_x\}, \{\mathbf{v}_y\}$ and $\{\mathbf{v}_z\}$	nodal velocities in $x, y, z$ direction, respectively
$Q$	mass flow rate
$D_l$	Lumen diffusivity
$P$	Endothelial permeability
$D_w$	Wall diffusivity
$\sigma_d$	Solvent reflection coefficient
$\lambda$	Time constant
$k_w$	Darcian permeability

$K_{lag}$	Solute lag coefficient
$c_0$	Initial LDL concentration
$r_w$	LDL degradation rate
$a$	Yasuda exponent
$n$	Power law index
$p_w$	Pressure in the arterial wall
$\mu_p$	Plasma viscosity
$J_v$	transmural velocity
$J_s$	solute flux
$L_p$	hydraulic conductivity
$\Delta p$	pressure difference
$\Delta \pi$	oncotic pressure difference
$ \tau_w $	absolute value of ESS
$K_m$	Michaelis constant
$PO_2$	partial pressure of oxygen
$c_{OxLDL}$	oxidized LDL
$D_{OxLDL}$	diffusion coefficient
$M$	macrophages number
$D_M$	diffusion coefficients for macrophages
$D_S$	diffusion coefficients for cytokines

$c_M$	macrophages concentration
$c_s$	cytokines concentration
$\bar{I}_1$	First deviatoric strain invariant
$\bar{I}_2$	Second deviatoric strain invariant
$J$	Determinant of the elastic deformation gradient tensor
$\mathbf{f}_s^B$	Body forces per unit volume
$\ddot{\mathbf{d}}_s$	Local acceleration of the solid
$k_I$	growing plaque coefficient
$f_s$	Coefficient of pressure loss due to flow separation
$f_v$	Coefficient of pressure loss due to viscous friction

## **Abstract**

This thesis deals with blood flow modelling in arteries with rigid or deformable walls. Its primary scope is to investigate the influence of the arterial wall on blood flow modelling and in particular, on important hemodynamic parameters such as intravascular pressures and wall shear stress. In this direction, finite element simulations are performed on patient-specific 3-dimensional coronary arterial models using real patient-specific boundary conditions in order to validate the efficacy of both methods (i.e. rigid or deformable walls). The subsequent scope of the thesis is to establish new computational methods for the functional assessment of coronary stenoses utilizing non-invasive or invasive coronary imaging modalities, with emphasis given on non-invasive techniques. The final aim of this thesis is to create integrated software suites of 3D reconstruction and functional assessment of coronary arteries that will aid the clinician in every day clinical practice.

In the first chapter, the medical background of the cardiovascular system is given. A detailed description of the physiology of the cardiovascular system, beginning from the heart and the coronary network and concluding with the blood vessels of the circulatory system is presented. A detailed description of the process of atherosclerosis is also presented in the first chapter and, in particular, the pathogenesis, as well as, the main risk factors that lead to plaque progression. Moreover, the most well-known coronary imaging modalities are presented in detail, including Invasive Coronary Angiography (ICA), IntraVascular UltraSound (IVUS), Optical Coherence Tomography (OCT), Coronary Computed Tomography Angiography (CCTA) and Magnetic Resonance Coronary Angiography (MRCA). Finally, an overview of the most well-known coronary artery functional assessment techniques is presented with emphasis given on the fractional flow reserve (FFR).

In the second chapter, the state of the art in the field of blood flow modelling in coronary arteries is presented. The second chapter includes the current status of literature in blood flow modelling (i.e. with rigid or deformable walls), CCTA derived computational FFR assessment, invasive coronary imaging derived functional assessment, as well as, several other virtual indices of coronary functional assessment. It also includes the contribution of the thesis along with the novelties that it introduces.

In the third chapter, two thorough analyses of blood flow simulations on several patient specific arterial models using both rigid and deformable arterial walls, and steady-state or transient simulations are presented. The first part of the chapter focuses on a comparison

between rigid and deformable walls simulations, whilst the second one presents a validation study on patient-specific simulations of coronary artery pressure measurements. Furthermore, the general mathematical background of the equations used to model blood flow, as well as the theoretical background of the finite element method are presented in detail. The aim of this chapter is to validate the accuracy of the entire blood flow modelling process regarding the calculation of important hemodynamic parameters such as intravascular pressures.

The fourth chapter presents a series of techniques regarding the computational functional assessment of coronary stenoses. The chapter is practically divided into two main parts. The first part presents techniques that utilize non-invasive coronary imaging modalities (i.e. Coronary Computed Tomography Angiography) and compares them directly to other established indices such as FFR or stress Myocardial Blood Flow (MBF) derived from Positron Emission Tomography (PET). These techniques utilize either the virtual functional assessment index (vFAI), an already validated technique, or smartFFR, a novel index for the functional assessment of coronary arteries. The second part presents techniques that utilize invasive coronary imaging modalities such as IVUS or ICA. A novel reconstruction method is also presented in this chapter that utilizes only IVUS images and creates 3D models of the artery of interest in a straight manner. These straight 3D models are also used for the computational functional assessment of coronary stenoses, thus incorporating the anatomic and physiologic info deriving from IVUS.

The fifth chapter of the thesis presents two integrated systems for 3D coronary reconstruction, functional assessment and multiscale modelling that were developed. The first software suite called ARTool, integrates technologies of 3D image reconstruction from various image modalities, blood flow and biological models of mass transfer, plaque characterization and plaque growth. The second software platform called Art Care, is an innovative suite of software modules that performs 3D reconstruction of coronary arterial segments utilizing different coronary imaging modalities such as IntraVascular UltraSound (IVUS) and invasive coronary angiography images (ICA), Optical Coherence Tomography (OCT) and ICA images, or plain ICA images and can safely and accurately assess the hemodynamic status of the artery of interest.

Finally, in the sixth chapter, the conclusions of this thesis are highlighted, based on the results and limitations as they result from the previous chapters. Directions and trends for future research in the field are also discussed.

The main contributions of this thesis can be summarized as: (i) the validation of the accuracy of blood flow simulations regarding important hemodynamic factors such as intravascular pressures, (ii) the thorough comparison between blood flow simulations in coronary arteries using rigid or deformable arterial walls, (iii) the application and establishment of indices (i.e. vFAI and smartFFR) for the functional assessment of coronary stenoses using either non-invasive (i.e. CCTA) or invasive coronary imaging modalities (i.e. IVUS or IVUS-ICA fusion), (iv) their comparison to already established techniques such as FFR and stress MBF and (v) the development of integrated systems for 3D coronary reconstruction, functional assessment and multiscale modelling.





## Περίληψη

Η παρούσα διατριβή ασχολείται με τη μοντελοποίηση της ροής αίματος σε αρτηρίες με παλλόμενα τοιχώματα. Βασικός της στόχος είναι η μελέτη της επίδρασης του αρτηριακού τοιχώματος στη μοντελοποίηση της ροής αίματος και πιο συγκεκριμένα, σε σημαντικές αιμοδυναμικές παραμέτρους όπως είναι οι ενδοαγγειακές πιέσεις και οι διατμητικές τάσεις που δημιουργούνται στο τοίχωμα. Σε αυτή την κατεύθυνση λοιπόν, έχουν πραγματοποιηθεί προσομοιώσεις με τη χρήση της μεθόδου των πεπερασμένων στοιχείων σε τρισδιάστατα μοντέλα στεφανιαίων αρτηριών με τη χρήση πραγματικών συνοριακών συνθηκών για την επαλήθευση της αποτελεσματικότητας των δύο μεθόδων (χρήση άκαμπτου τοιχώματος ή παραμορφώσιμου τοιχώματος). Επόμενος στόχος της διατριβής είναι η εγκαθίδρυση νέων υπολογιστικών μεθόδων για την εκτίμηση λειτουργικότητας στεφανιαίων βλαβών με τη χρήση μη επεμβατικών ή επεμβατικών μεθόδων στεφανιαίας απεικόνισης, με μεγαλύτερη έμφαση να δίνεται στις μη επεμβατικές τεχνικές. Τελικός σκοπός της διατριβής είναι η δημιουργία λογισμικού για την τρισδιάστατη ανακατασκευή αγγείων και την εκτίμηση της λειτουργικότητας στεφανιαίων αρτηριών, το οποίο θα μπορεί να βοηθά τον καρδιολόγο στην καθημερινή του εργασία.

Στο πρώτο κεφάλαιο παρουσιάζεται το ιατρικό υπόβαθρο του καρδιαγγειακού συστήματος και πιο συγκεκριμένα, με λεπτομερή περιγραφή της φυσιολογίας του καρδιαγγειακού συστήματος ξεκινώντας από την καρδιά και το στεφανιαίο δίκτυο και καταλήγοντας με τα αγγεία αίματος στο κυκλοφορικό σύστημα. Δίνεται ακόμη μια λεπτομερής περιγραφή της διαδικασίας της αθηροσκλήρωσης και πιο συγκεκριμένα, η τρόπος εμφάνισης καθώς και οι παράγοντες κινδύνου που οδηγούν στην εξέλιξη της νόσου. Επιπλέον, παρουσιάζονται οι γνωστότερες απεικονιστικές τεχνικές στεφανιαίων αγγείων όπως είναι ο ενδοαγγειακός υπέρηχος (IVUS), η επεμβατική στεφανιογραφία (ICA), η οπτική τομογραφία συνοχής (OCT), η αξονική στεφανιογραφία (CCTA) και η μαγνητική στεφανιογραφία (MRCA). Τέλος, δίνεται και μια επισκόπηση των γνωστότερων τεχνικών εκτίμησης της λειτουργικότητας των στεφανιαίων αγγείων, με μεγαλύτερη έμφαση να δίνεται στην τμηματική εφεδρεία ροής (FFR).

Στο δεύτερο κεφάλαιο, παρουσιάζεται η τεχνολογική στάθμη στον τομέα της μοντελοποίησης της ροής αίματος σε στεφανιαία αγγεία. Το δεύτερο κεφάλαιο περιλαμβάνει την τρέχουσα βιβλιογραφία στη μοντελοποίηση της ροής αίματος (με άκαμπτα ή με παραμορφώσιμα τοιχώματα), στην υπολογιστική εκτίμηση της τμηματικής εφεδρείας ροής σε

τρισδιάστατα μοντέλα προερχόμενα από αξονική στεφανιογραφία, στην υπολογιστική εκτίμηση της λειτουργικότητας των αγγείων με τη χρήση επεμβατικών τεχνικών, καθώς επίσης και σε διάφορους άλλους παρόμοιους εικονικούς δείκτες. Τέλος, συζητείται ακόμη ο στόχος και η συμβολή της παρούσας διατριβής.

Στο τρίτο κεφάλαιο παρουσιάζονται δύο εκτενείς αναλύσεις προσομοιώσεων ροής αίματος σε αρκετά τρισδιάστατα μοντέλα στεφανιαίων αρτηριών με τη χρήση άκαμπτου ή παραμορφώσιμου τοιχώματος. Το πρώτο σκέλος του κεφαλαίου επικεντρώνεται στη σύγκριση μεταξύ των προσομοιώσεων με χρήση άκαμπτου ή παραμορφώσιμου τοιχώματος, ενώ το δεύτερο σκέλος παρουσιάζει μια μελέτη επαλήθευσης στον υπολογισμό των ενδοστεφανιαίων πιέσεων μέσω της χρήσης των πεπερασμένων στοιχείων. Επιπρόσθετα, παρουσιάζονται εκτενώς το μαθηματικό υπόβαθρο των εξισώσεων για τη μοντελοποίηση της ροής αίματος, καθώς επίσης και το θεωρητικό υπόβαθρο της μεθόδου των πεπερασμένων στοιχείων. Σκοπός του κεφαλαίου είναι η επαλήθευση της ακρίβειας ολόκληρης της διαδικασίας μοντελοποίησης της ροής αίματος σε ό,τι έχει να κάνει με τον υπολογισμό σημαντικών αιμοδυναμικών παραμέτρων όπως είναι οι ενδοαγγειακές πιέσεις.

Το τέταρτο κεφάλαιο παρουσιάζει μια σειρά τεχνικών με ό,τι έχει να κάνει με την υπολογιστική εκτίμηση της σοβαρότητας στεφανιαίων βλαβών. Το κεφάλαιο πρακτικά χωρίζεται σε δυο μεγάλες υποενότητες. Το πρώτο κομμάτι παρουσιάζει τις τεχνικές που κάνουν χρήση μη επεμβατικών απεικονιστικών μεθόδων (αξονική στεφανιογραφία) και τις συγκρίνει με άλλους εγκαθιδρυμένους δείκτες όπως η τμηματική εφεδρεία ροής ή η ροή αίματος του μυοκαρδίου. Οι μέθοδοι που παρουσιάζονται κάνουν χρήση είτε του δείκτη vFAI, είτε του νέου δείκτη smartFFR που παρουσιάζεται για πρώτη φορά. Το δεύτερο σκέλος του κεφαλαίου παρουσιάζει μεθόδους που κάνουν χρήση επεμβατικών απεικονιστικών τεχνικών όπως το IVUS και η επεμβατική στεφανιογραφία. Παρουσιάζεται επίσης και μια νέα τεχνική τρισδιάστατης ανακατασκευής που κάνει χρήση εικόνων IVUS και δημιουργεί τρισδιάστατα αρτηριακά μοντέλα σε ευθεία. Τα μοντέλα αυτά χρησιμοποιούνται στη συνέχεια για την εκτίμηση της λειτουργικότητάς τους, ενσωματώνοντας όμως και όλη την ανατομική και φυσιολογική πληροφορία που προέρχεται από το IVUS.

Το πέμπτο κεφάλαιο της διατριβής παρουσιάζει δύο πλήρη λογισμικά για την τρισδιάστατη ανακατασκευή αγγείων, την εκτίμηση της λειτουργικότητάς τους και την πολυεπίπεδη μοντελοποίηση. Το πρώτο σύστημα που ονομάζεται ARTool, ενσωματώνει τεχνολογίες τρισδιάστατης ανακατασκευής από διάφορες απεικονιστικές τεχνικές,

μοντελοποίηση ροής αίματος καθώς και βιολογικά μοντέλα μεταφοράς μάζας, χαρακτηρισμού αθηρωματικής πλάκας και εξέλιξης της νόσου. Το δεύτερο λογισμικό (ArtCare) πραγματοποιεί τρισδιάστατη ανακατασκευή αγγείων με χρήση διάφορων απεικονιστικών τεχνικών και μπορεί να εκτιμήσει την αιμοδυναμική κατάσταση της εξεταζόμενης αρτηρίας με ακρίβεια.

Τέλος, στο έκτο κεφάλαιο επισημαίνονται τα συμπεράσματα αυτής της διδακτορικής διατριβής με βάση τα αποτελέσματα και τους αναγκαίους περιορισμούς της ερευνητικής εργασίας όπως προκύπτουν από τα προηγούμενα κεφάλαια. Επίσης, συζητούνται κατευθύνσεις και τάσεις για μελλοντική έρευνα στο συγκεκριμένο πεδίο.

Η συμβολή της παρούσας διδακτορικής διατριβής συνοψίζεται στους παρακάτω παράγοντες: (i) επαλήθευση της ακρίβειας της μοντελοποίησης ροής αίματος σε ό,τι σχετίζεται με τον υπολογισμό σημαντικών αιμοδυναμικών παραμέτρων, (ii) η εκτενής σύγκριση προσομοιώσεων ροής αίματος με τη χρήση άκαμπτων ή παραμορφώσιμων τοιχωμάτων, (iii) η εφαρμογή και η εγκαθίδρυση δεικτών για την εκτίμηση της λειτουργικότητας στεφανιαίων αρτηριών, (iv) η σύγκρισή τους με ήδη αποδεκτές τεχνικές όπως η FFR και το MBF και (v) η δημιουργία συστημάτων για την τρισδιάστατη ανακατασκευή αγγείων και την εκτίμηση της λειτουργικότητας στεφανιαίων αγγείων.



## Chapter 1: Introduction

---

1.1 Physiology of the Cardiovascular System

1.2 Atherosclerosis

1.3 Coronary Imaging Modalities

---

### 1.1 Physiology of the Cardiovascular system

The circulatory system is a body-wide network of blood, blood vessels, and lymph. It can be divided into two categories: the cardiovascular system and the lymphatic system. The circulatory system transports nutrients via amino acids, lymph, electrolytes, hormones and oxygenated to the entire human body.

The cardiovascular system consists of a driving pump, the heart, and, of a closed vascular system through which blood circulates. Oxygenated blood is transported to the tissues and organs of the human body and the respective de-oxygenated blood is transported to the respective respiratory organs. The cardiovascular system is divided into the pulmonary circulation, which moves blood through the lungs and creates a connection with the gas transfer function of the respiratory system, and the systemic circulation, which provides blood to the rest of the tissues in the human body. The pulmonary network is often combined with the coronary system, thus constituting the cardiopulmonary system. Both circulations have an arterial system, capillaries and a venous system. The arteries and arterioles act as a blood distribution system to the tissues, the capillaries favour the exchange of substances and the veins act as a collection and storage system, which returns blood to the heart.

### 1.1.1 Heart and the coronary network

Heart is a muscular organ of four cavities with a size equal to the human fist (an average size of the heart of an adult is about 14 cm long and 9 cm wide) and is located at the mediastinum, thus between the lungs and the thoracic cavity [1]. The shape of the heart reflects a typical cone and the tip of the heart points downward. The heart is surrounded by a set of three pericardial membranes: the outer pericardium, the middle myocardium and the visceral inner myocardium. The pericardium is the outer layer, which is a loosefitting sac composed of connective tissue and some deep adipose tissue and it has the ability to protect the heart by reducing friction. The pericardium extends over the diaphragm and over the bases of the large vessels that enter and leave the heart. The myocardium consists of cardiac muscle tissue and is supplied mostly by blood capillaries, lymph capillaries and nerve fibers. Its function is to pump blood out of the chamber of the heart. Finally, the endocardium is comprised of the epithelium and connective tissue with several elastic and collagenous fibers. It also contains blood vessels and cardiac muscle fibers.

The internal part of the heart is divided into four chambers, two on the left and two on the right. The chambers of the upper part are called atria and function as the receivers of the blood that returns to the heart. The lower chambers of the heart are called ventricles and they receive blood from the atria, pumping it out into the arteries. The ventricle and atria of the left side are separated from the respective ones from the right side by the septum. The septum prevents blood from the one side to mix with blood from the other side of the heart. The atrioventricular valve (AV valve) ensures one-way blood flow from the atria to the ventricles. It consists of the tricuspid valve on the right and the mitral valve on the left .

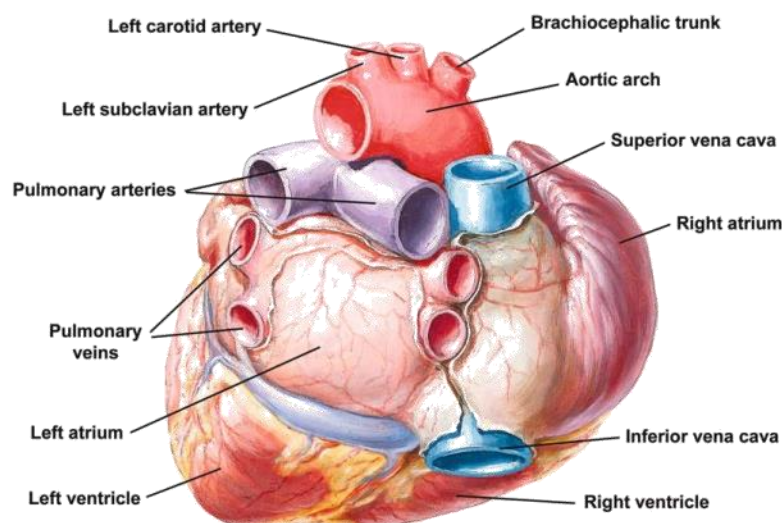


Figure 1: Anatomy of the heart [1].

The right atrium receives blood from the superior vena cava and the inferior vena cava, two large veins, as well as, a smaller vein called the coronary sinus, which drains blood into the right atrium from the myocardium. The tricuspid valve is located between the right atrium and the ventricle (Figure 1). It allows blood to move from the right atrium to the right ventricle whilst preventing backflow. The muscular wall of the right ventricle is evidently thinner than the left ventricle since it only pumps blood to the lungs with a relatively low resistance to blood flow. The left ventricle has a thicker wall because it must distribute blood to all body parts with a significantly higher resistance to blood flow. When the right ventricle contracts, its blood pressure increases, thus closing the tricuspid valve. This way, the blood of the right ventricle can only exit through the pulmonary trunk which is divided into the right and left pulmonary arteries that supply the lungs. Four pulmonary veins supply the left atrium with blood. The mitral valve allows blood to pass from the left atrium to the left ventricle, preventing blood to follow the inverse route (i.e. from the left ventricle to the left atrium). The mitral valve then closes passively, thus directing blood through a large artery, the aorta. At the bottom of the aorta we have the aortic valve which opens to allow blood to exit the left ventricle during contraction. When the ventricle relaxes, the aortic valve closes, thus preventing blood from returning to the ventricle.

Low-oxygen blood is received from the right ventricle through the coronary sinus and the vena cava. While the right atrium contracts, blood flows through the tricuspid valve to the right ventricle (Figure 2). When the right ventricle contracts, the tricuspid valve closes. Blood then flows from the pulmonary valve to the pulmonary arteries and pulmonary trunk. Then, it enters the capillaries, where gas exchange is performed. This oxygenated blood returns to the heart via the pulmonary veins directly to the left atrium.

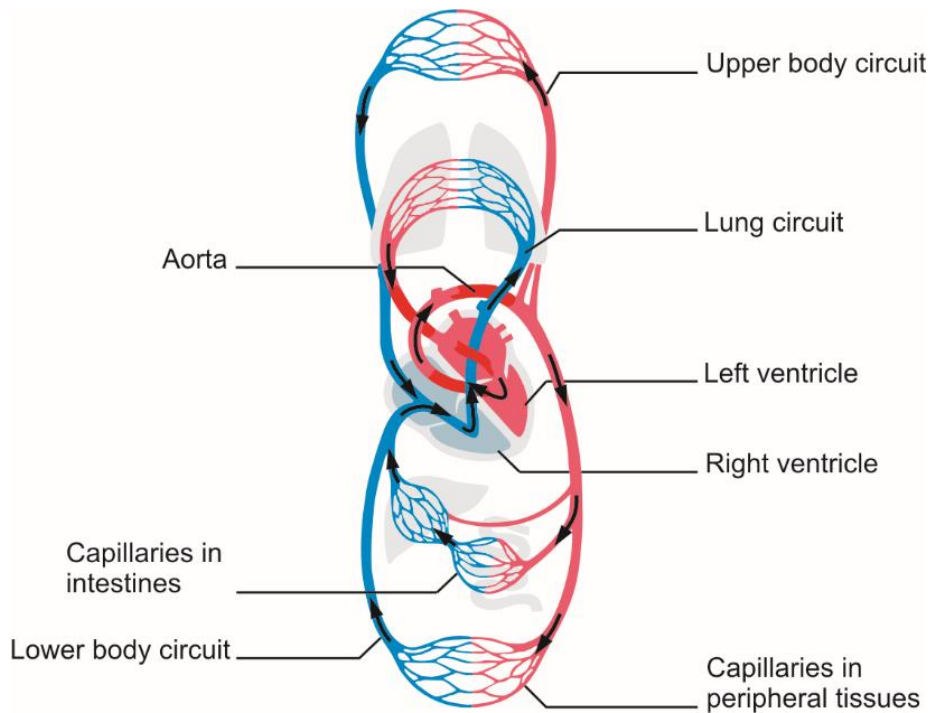


Figure 2: Circulatory System Diagram [2].

The left atrium then contracts, transporting blood through the mitral valve to the left ventricle. When the left ventricle contracts, the mitral valve closes passively. Blood then moves through the aortic valve to the aorta and its side branches. The first two branches are the so-called left and right coronary arteries. The two aforementioned arteries supply blood to the heart tissues. Body tissues require the continuous beating of the heart due to the need of freshly oxygenated blood in order to survive. The coronary artery side branches supply numerous capillaries throughout the myocardium. These arteries have smaller branches with connections called anastomoses between arteries, thus providing alternate blood flow pathways, the so-called collateral circulation. These additional pathways can supply oxygen and nutrients to the myocardium when a coronary artery is fully occluded. Side branches of the cardiac veins drain blood from the myocardial capillaries which, in turn, are then joined into the coronary sinus which then empties into the right atrium.

### 1.1.2 Functions of the Heart

The heart follows a series of coordinated actions. The atria contract (atrial systole) as the ventricles relax (ventricular diastole). In a similar manner, when the ventricles contract (ventricular systole) the atria relax (atrial diastole). These two phases are followed by a period



of relaxation of both systems. The combination of the aforementioned actions composes a heartbeat or a cardiac cycle.

During one heart cycle, pressure rises and falls in the heart chambers and valves open and close, respectively. In the first stages of diastole, blood pressure in the ventricles is low, thus causing the AV valves to open and the ventricles to fill with blood. Almost 70% the blood that returns enters the ventricles before they contract. While the atria contract, the remaining 30% enters the ventricles. When the ventricles contract, the pressure inside the ventricles increases. When the ventricular pressure is higher than the atrial, the AV valves close and papillary muscles contract. During ventricular contraction, the atrial pressure is low and blood flows into the atria during ventricular contraction so that the atria are prepared for the next cardiac cycle. When the ventricular pressure exceeds pulmonary trunk and aorta pressure, the aortic and pulmonary valves open. Blood is then transported from the ventricles to these arteries and subsequently ventricular pressure drops. When the ventricular pressure is lower than the atrial pressure, the AV valves open and the ventricles begin to refill with blood.

A heartbeat has a characteristic double thumping sound. This is caused by the vibrations of the heart tissues that are related to the closing of the valves. The first sound happens during ventricular contraction when the AV valves close. The second occurs when the ventricles relax and the pulmonary and aortic valves close.

### **1.1.3 Coronary Network**

The cardiac muscle is supplied by blood from two main arteries, the left and the right coronary artery (Figure 3). Both of them originate from the base of the ascending aorta. The left main coronary artery [3] starts from the left coronary sinus of Valsalva and is quickly divided into the left anterior descending coronary artery [4] and the left circumflex coronary artery (LCx). The LAD runs through the anterior epicardial ventricular septum and includes several side branches. It is divided into proximal, mid and distal segments. The first septal perforator separates the proximal from the mid segments of the LAD. The diagonal branches vary in number and diameter and are labelled from proximal to distal (i.e. D1, D2 etc.). the LCx courses in the left atrial-ventricular sulcus and bifurcates into obtuse marginal branches (OM). These branches are also labelled from proximal to distal (i.e. OM1, OM2 etc.).

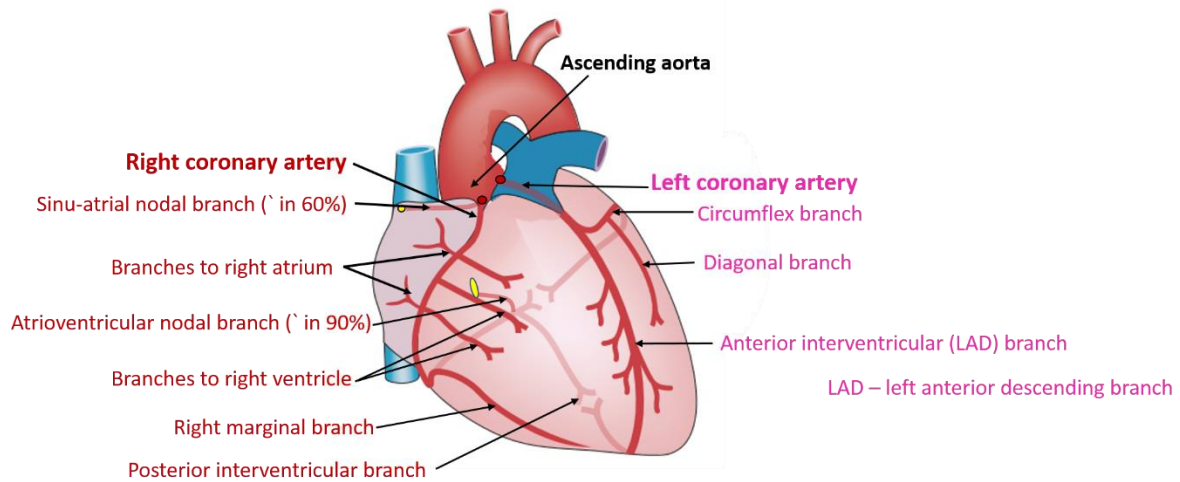


Figure 3: The coronary arteries [5].

The right coronary artery [6] starts from the right coronary sinus and is also divided into proximal, mid and distal segments. The proximal segment starts from the ostium and ends at the start of the first acute marginal artery. The sinoatrial artery (SA) is in general the second visible artery and starts from the proximal RCA and has a posterior course. The RCA bifurcates to a number of acute marginal branches (AM) which also vary in size and diameter and are labelled from proximal to distal (i.e. AM1, AM2 etc.).

Dominance is a term that refers to whether the posterior descending aorta (PDA) starts from the LCx, the RCA or both. 80% of humans are right dominant according to the literature [7]. When we have a right dominance, the distal RCA bifurcates into the PDA and a postlateral branch. In a left dominance, the PDA starts from the distal LCx. In the case of co-dominance, we have left and right PDA's starting from the RCA and the LCx.

The coronary network is the densest network of capillaries throughout the entire body. Indeed, for every muscle fiber of the myocardium there is one capillary, which roughly means 2500 capillaries/mm<sup>3</sup> of myocardium. Furthermore, the amount of oxygen supplied through blood that courses through the coronary vasculature is over two times more than what is supplied by any other tissue in the human body. During rest, the blood that courses through the coronary arteries is about 250 cm<sup>3</sup>/min and reaches a mere 1 lt/min under stress.

#### 1.1.4 Blood Vessels

Blood vessels have the ability to transport blood to every tissue and organ in the human body. Their size decreases as their distance from the heart increases (arteries and arterioles), ending in the capillaries and then it increases as they move towards the heart (venules and veins). The aorta is the largest artery and the venae cavae are the largest veins in the human body. Blood

vessels are divided into five major categories: arteries, arterioles, capillaries, venules and veins. Arteries are elastic vessels, able to transport blood away from the heart under high pressure. As they move away from the heart, they subdivide into thinner vessels, the arterioles. The wall of an artery consists of three main layers. The inner layer (tunica interna) is made of a layer called the endothelium [8, 9].

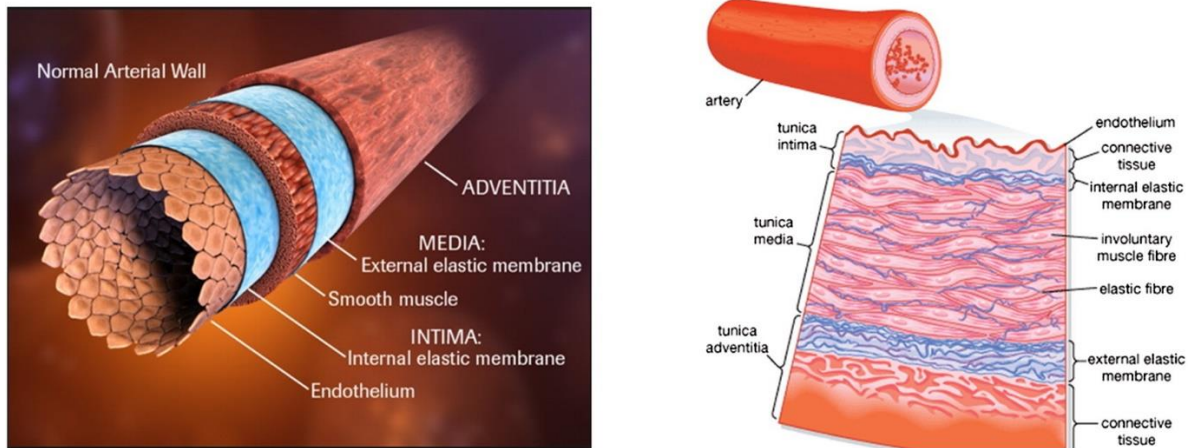







Figure 4: Structure of the arterial wall [9].

The endothelium lies on a connective tissue membrane of many elastic, collagenous fibers and prevents blood from clotting. It also aids in regulating blood flow. It has the ability to relax the smooth muscle cells of the vessel by releasing nitric oxide. The middle layer of the arterial wall is called tunica media and occupies the largest part of the wall. The tunica media includes smooth muscle fibers and a thick layer of elastic connective tissue. The outer layer is called tunica externa (tunica adventitia) and is a thin layer made from connective tissue with irregular fibers (Figure 4). The large arterioles also have three layers in their walls and tend to get thinner as we approach the capillaries. They have an endothelial lining, smooth muscle fibers and a small amount of surrounding connective tissue. The smallest blood vessels in terms of diameter are the capillaries which connect the arterioles to the venules. The walls of the capillaries are comprised of the endothelium and create a semipermeable layer through which substances from blood are exchanged with substances from tissue fluids that surround the cells of the human body. Veins, unlike arteries, don't have a predefined shape but it highly depends on the quantity of blood they contain. The vein network has almost two times the capacity of the respective arterial one due to the fact that veins are significantly wider than arteries. Vein walls consist of three layers (internal, middle, external). However, veins have a thinner middle layer than arteries. Table 1 depicts a classification of blood vessels according to their structure and dimensions.

Table 1: Blood vessel classification and structural characteristics.

	Mean Diameter	Mean wall thickness	
<b>Artery</b>	4 mm	1 mm	
<b>Arteriole</b>	30 $\mu\text{m}$	6 $\mu\text{m}$	
<b>Capillary</b>	8 $\mu\text{m}$	0.5 $\mu\text{m}$	
<b>Venule</b>	20 $\mu\text{m}$	1 $\mu\text{m}$	
<b>Vein</b>	5 mm	0.5 mm	

## 1.2 Atherosclerosis

### 1.2.1 Introduction

Atherosclerosis is a complex inflammatory disease caused mainly by excessive concentrations of low-density lipoprotein (LDL) cholesterol [10, 11]. Atherosclerosis originates from lipid retention and oxidation which, in turn, lead to chronic inflammation having as a result vessel stenosis or thrombosis [12-14]. Atherosclerotic plaques tend to occlude major arteries that supply the heart, brain and legs with blood. The aforementioned lesions originate in the intima of the artery and tend to expand towards the entire arterial wall. Some of the most common risk factors that favour the creation of such lesions are smoking, obesity, hypercholesterolemia, diabetes mellitus, hypertension and genetic predisposition. The main sites at which atherosclerosis has been studied in humans are coronary arteries, carotid arteries and the aorta.

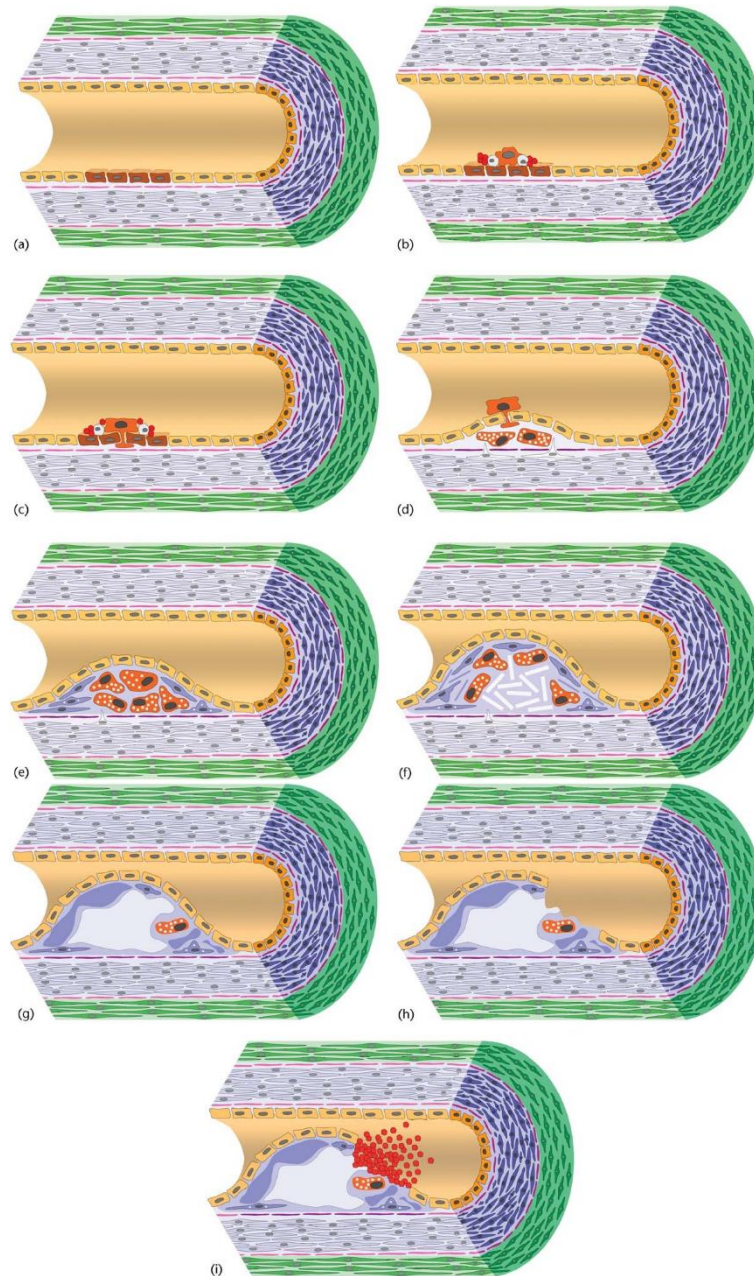


Figure 5: Pathogenesis of atherosclerosis. Endothelial dysfunction [15]. (b) Adhesion of blood leucocytes (T lymphocytes, white; monocytes, orange) and thrombocytes. Immigration of adhered monocytes into subendothelial areas (diapedesis). Immigration of smooth muscle cells [16] from the media (light blue) into subendothelial tissues (adaptive intimal thickening) and foam cell formation (formation of an atheroma). The immigration of smooth muscle cells is accompanied by a switch to a synthetic phenotype (purple). Hence, subendothelial deposition of extracellular matrix material (purple) is increased. Thickening of the lesion by enhanced foam cell formation (white spots within the cells), immigration of smooth muscle cells and further deposition of extracellular matrix proteins (purple). (f) Formation of a fibrous cap (purple) and a necrotic lipid core [16]. The latter appears because of the death of foamy macrophages. Due to the synthesis of proteases by macrophages, the fibrous cap covering the lipid core is thinned. Plaque rupture or erosion of the endothelium occurs. (i) The contact of blood with the subendothelial tissue activates the clotting cascade and a thrombus is formed [11].

The creation and progression of atherosclerosis differs from person to person. The whole process begins when cholesterol-rich lipids accumulate at the arterial wall and the

consequent inflammatory response from the arterial wall. The course of the process of plaque progression has been thoroughly studied through histopathology in human and in animal studies and follows the same rationale for the coronary arteries, the carotid arteries and the aorta (Figure 5). Atherogenesis usually begins with an initial qualitative change in the monolayer of the endothelial surface. The endothelial cells pose an initial resistance to the attachment of white blood cells and subsequently express adhesion molecules which, in turn, captivate leukocytes on their surfaces when they are affected by irritative stimuli [12]. The two major factors that favour the cholesterol-having low-density lipoprotein (LDL) to enter the arterial wall are the changes in endothelial permeability and the composition of the extracellular matrix under the endothelium. In the case where monocytes enter and reside in the arterial wall, they differentiate into macrophages. The mononuclear phagocytes are then transformed to foam cells inside the developing atheroma. The formation of atheroma includes the gathering of smooth muscle cells (SMCs) from the middle layer to the tunica intima and subsequently proliferate in response to platelet-derived growth factor [17]. Extracellular matrix molecules are then produced in the intima by SMCs and create a fibrous cap which surrounds the plaque. This cap spreads over a complex of macrophage-derived foam cells, some of which die and release several lipids that gather extracellularly. This process is called efferocytosis and can form a lipid-rich pool, the so-called necrotic core of the atheromatic plaque. Plaque lesions often cause narrowings of the arterial lumen and can obstruct blood flow, leading to tissue ischemia. In some cases, the fibrous cap of a plaque ruptures creating thrombi and enables blood coagulation elements to come into contact with the thrombogenic plaque.

As described before, there are several risk factors that favour and speed up the atherogenesis process such as hypertension, smoking, angiotensin II, diabetes and cholesterol (Table 2). Hypertension increases the arterial wall tension and can often lead to the formation of aneurysms. Angiotensin II modifies the endothelial function by aiding in the adhesion of leukocytes. Diabetes and smoking also have the ability to influence the biology of the vessel. Cholesterol also plays a key role in atherogenesis and has been thoroughly studied [18]. Lipids also have a key role in the development and progression of atheromatic plaque lesions. A direct connection between atherogenesis and lipids has yet not been identified. High LDL levels are directly associated with cardiovascular disease and with the accumulation of individual vulnerability to atherosclerosis. The cardiovascular risk can be increased by monogenic disorders and reduced LDL levels are directly connected with reduced likelihood of cardiovascular events [15].



Table 2: The risk factors of Atherosclerosis [19].

Category	Number	Risk Factor
<b>Major</b>	1	Unhealthy blood cholesterol and lipoprotein levels
	2	High blood pressure
	3	Smoking
	4	Insulin resistance
	5	Diabetes
	6	Overweight or Obesity
	7	Lack of physical activity
	8	Unhealthy diet
	9	Older age
	10	Family history of early heart disease
	11	Inflammation
<b>Emerging Risk Factors</b>	12	High levels of C-reactive protein (CRP)
	13	Triglycerides
	14	Sleep apnea
	15	Stress
	16	Alcohol

### 1.2.2 Blood flow effect on atherosclerosis

Apart from the aforementioned risk factors regarding atherosclerosis, another key element that has been proven to be linked directly to atherogenesis is blood flow itself. Blood flow applies a load on the endothelium which can be divided into two main components: one tangential which is caused by the blood viscosity and has the same direction as blood flow and one vertical which is created by the blood pressure and tends to stretch the arterial wall. The tangential load is called shear stress and the vertical one is called tensile stress. Several studies have demonstrated that endothelial shear stress (ESS) is directly linked to the development of atheroma within the arterial wall (Figure 6). In particular, areas of low shear stress are prone to develop atherosclerotic plaques. Furthermore, the endothelial function is affected by ESS which alters the local gene expression, as well as, the permeability to molecules. When the endothelium is stretched mechanically or subjected to fluid shear stress, several responses are generated, the nature of which differs in terms of the time required to trigger. Low ESS

provokes a continuous endothelial activation of proteins that upregulate the expression of genes encoding cholesterol synthase, fatty acid synthase and LDL receptor [20, 21]. This way, the endothelial permeability to LDL molecules is directly affected and the LDL accumulation within the arterial wall is increased. In addition, low values of ESS favour the creation of reactive oxygen species (ROS) into the endothelium, thus causing LDL oxidation [22, 23].

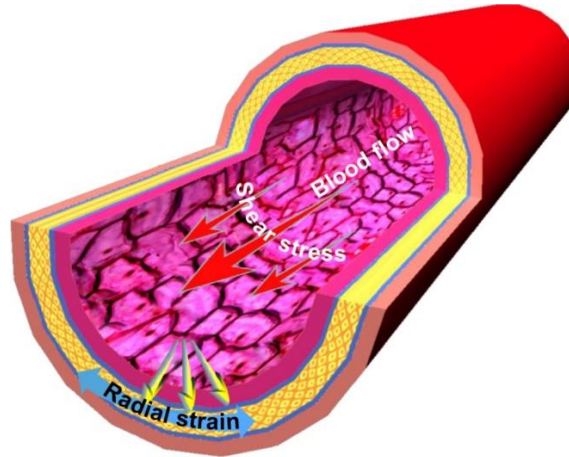


Figure 6: Blood flow and the consequent stresses that are created within the artery [24].

### 1.2.3 Treatment and management of atherosclerosis

Atherosclerosis is a disease that can affect any artery of the human body and usually appears in coronary arteries, carotid arteries, brain arteries and several peripheral arteries in the arms and legs. Their presence leads to the development of several diseases based and classified on the type of artery, which is affected. The most severe results of atherosclerosis include stroke and heart attack. In western societies, cardiovascular disease is the most common cause of death following a steadily increasing trend [25]. Cardiovascular disease appears when atherosclerotic plaque builds up in the arterial wall. The direct result of this accumulation is the narrowing of the arterial lumen, which reduces blood flow in the affected artery. The development and progression of plaque provokes the clotting of blood, which obstructs and occludes the arterial lumen, thus blocking blood flow towards the heart muscle. When the blood flow to the heart is reduced, angina symptoms tend to appear leading initially to plaque rupture and consequently to heart attack.

The symptoms are similar when dealing with carotid arteries. Plaque accumulates in the arterial wall, reducing or even blocking blood flow to the brain and consequently causing stroke. Finally, regarding peripheral arteries, atherosclerosis often leads to reduced blood flow in the affected artery causing pain, numbness and other painful symptoms [26, 27].



Due to the disturbing increase of mortality due to cardiovascular disease, atherosclerosis has been a key subject of research during the past few decades. Several atherosclerosis treatment and management methods, invasive or non-invasive, have been proposed and adopted in everyday clinical practice. Lipid-reducing medicine can lower the amount of accumulated cholesterol in the arterial wall and, in turn, stop the progression of the disease. Low-dosage aspirin treatment can also prevent blood clots [28]. Medicines specialized in coronary artery disease lower the average blood pressure, thus reducing the heart's requirements for oxygen. However, not all cases can be treated non-invasively. In cases where severe stenoses are present, only invasive interventions can provide an efficient result. Such invasive methods are coronary angioplasty, bypass, etc.

### **1.3 Coronary Imaging Modalities**

#### **1.3.1 Introduction**

The increasing trend of the mortality rate caused by CardioVascular Diseases (CVD) has constituted the fast and reliable hemodynamic assessment of the coronary vasculature a non-trivial matter in everyday clinical practice. Several imaging techniques have been developed and are currently available, in order to provide an insight of the coronary hemodynamic status. Invasive Coronary Angiography (ICA)[29], IntraVascular UltraSound (IVUS), Optical Coherence Tomography (OCT), Coronary Computed Tomography Angiography (CCTA) and Magnetic Resonance Coronary Angiography (MRCA) are some of the most well-known coronary imaging modalities.

#### **1.3.2 Non-Invasive Coronary Imaging Modalities**

The development of non-invasive techniques that can reliably assess the hemodynamic significance of coronary lesions has become of utmost importance in today's clinical practice. The most common and efficient non-invasive cardiac imaging modality that has gained substantial ground regarding its use in everyday clinical practice is Coronary Computed Tomography Angiography (CCTA). CCTA was initially introduced to clinical practice with 4-slice scanners of low image quality. Following the advances of technology, CCTA has evolved producing even 320-slice scanners of high image quality (Figure 7). The evident improvement of image quality has increased the diagnostic accuracy of the method for the detection of atherosclerotic plaques [30]. Nevertheless, the image quality of CCTA still remains inferior to other invasive imaging modalities. However, several studies have pointed out the increasingly

high diagnostic accuracy of the method in detecting atherosclerotic plaques. One of the main advantages of CCTA is the fact that besides identifying any present stenoses, it can also safely provide us with information on the morphology and composition of the atherosclerotic plaques that are detected. The types of plaque that can be detected and identified by CCTA are: calcified, non-calcified and mixed. Calcified plaques are the easiest to be detected because of their high-density values. Non-calcified plaques are more difficult to be identified due to their narrow-ranged differences in attenuation. Despite the fact that CCTA is considered as one of the most efficient non-invasive techniques in atherosclerotic plaque identification, it still suffers from two major drawbacks, the exposure in radiation and the still inferior image resolution to invasive techniques [31, 32].



Figure 7: CCTA image from a 320-slice scanner of a right mammary artery bypass graft (free transplant with end-to-side anastomosis on left mammary artery) with anastomosis on obtuse marginal branch [10].

Another efficient non-invasive technique for the assessment of atherosclerotic plaques and inflammation is the fusion of positron emission tomography and CCTA (PET-CCTA). This technique uses a device which combines a positron emission tomography scanner (PET) and a regular CCTA scanner. The simultaneously acquired images from the two scanners are fused together in one superimposed final image. The final images have the advantages of the classic CCTA, thus the accurate representation of the coronary vasculature and the advantages of PET imaging, which shows the spatial distribution of metabolic and biochemical activity in the body [33].

Magnetic Resonance Coronary Angiography [34] is another non-imaging coronary modality which has the ability to provide a detailed insight on the vessel anatomy. Coronary MRA can accurately visualize the origin and the path of anomalous coronary vessels, as well

as the presence and location of coronary aneurysms. In fact, coronary MRA can visualize the proximal segments of the main coronary arteries in almost 100% of the cases. Optimal results are obtained when dealing with the left anterior descending [4] and the right coronary artery [6], whilst when dealing with the left circumflex artery the results are inferior providing a lower image quality, mainly due to the fact that the LCx runs in the direct vicinity of the myocardium and at a greater distance from the coil elements. Current literature has reported an average visible length of 80 mm for the RCA, 50 mm for the LAD and around 40 mm for the LCx. Excellent agreement was found regarding the diameters of the proximal parts of the aforementioned vessels measured by MRA and by invasive angiography. However, the overall resolution of MRA remains significantly lower than invasive coronary angiography, thus limiting the ability to visualize small side branches and affecting the overall accuracy in stenosis detection. This fact can easily explain the low specificity in detecting CAD by using MRA [35].

### **1.3.3 Invasive Coronary Imaging Modalities**

Invasive coronary angiography is the most commonly used coronary imaging modality (Figure 8). It is considered as a minimally invasive procedure which is used both for diagnostic as well as interventional purposes [29]. The whole procedure involves an X-ray source and camera equipment on opposite sides of the patient's chest having the ability to move freely, under motorized control, around the patient's chest so that images can be taken quickly from multiple angles. A catheter is inserted into the vein and artery of the leg, arm or neck of the patient and is passed through the circulatory system until it reaches the heart. A radiocontrast agent is also injected into the patient and, therefore, mixed with the blood flowing within the arterial system. After the administration of the contrast agent, the full silhouette of the arterial tree is depicted for the arterial lumen. Occlusion, stenosis, thrombosis or even aneurysmal enlargement can be easily recognized by the acquired images. Moreover, if a present stenosis is considered to be hemodynamically significant, through ICA, the clinician has also the ability to insert a balloon with a stent wrapped around it, passing it through the narrowed area and inflate it in order to expand the stent and, therefore, treat the stenosis. One drawback of ICA is the inability of the modality to visualize the arterial wall since it can only give an insight of the arterial lumen. One other disadvantage is the exposure to radiation, even though the amount of radiation is relatively low.

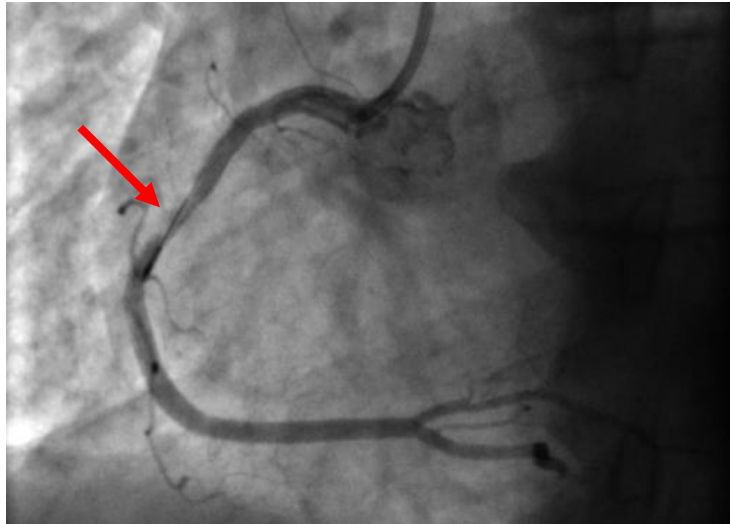


Figure 8: Typical Invasive Coronary Angiography projection of a RCA (red arrow indicates a stenosis).

IntraVascular UltraSound (IVUS) is one of the most well-known intravascular imaging modalities [36]. A catheter with a miniaturized transducer on its tip is inserted to the patient, emitting ultrasound signals perpendicular to its axis at a frequency ranging from 20-70 MHz. The emitted signals create reflections, which are received by the transducer and are consequently analysed in order to produce cross sectional images of the vessels. A clinician can analyse and identify the luminal, stent and media-adventitia borders from the produced images quantify the plaque burden and analyse the composition of the atherosclerotic plaque with moderate accuracy (Figure 9). In order to overcome this problem and increase the accuracy, several methods that utilize the IVUS backscatter signal and perform radiofrequency analysis have been introduced (RF-IVUS). The aforementioned methods take into account the amplitude and the frequency of the reflected signals, thus quantifying the composition of the atherosclerotic plaque in a semi-automated way. These methods, withal being superior to grayscale IVUS for plaque characterization, they present limitations when dealing with stented segments or areas behind calcium deposits [37]. IVUS also suffers from various additional drawbacks the majority of which are mainly due to its poor spatial resolution. Numerous artifacts are created in an IVUS sequence such as the non-uniform rotational distortion, the guidewire artifact, the ring down effect and the signal drop-out behind calcium, an artefact that prevents the visualization of deep vessel structures. The moderate resolution does not allow the visualization of the microstructure of plaques that is directly connected to an increased vulnerability such as microcalcifications, the presence of neo-vessel and macrophages. IVUS also lacks the ability to provide information on the 3D vessel geometry as well as the exact location of the atherosclerotic plaque.

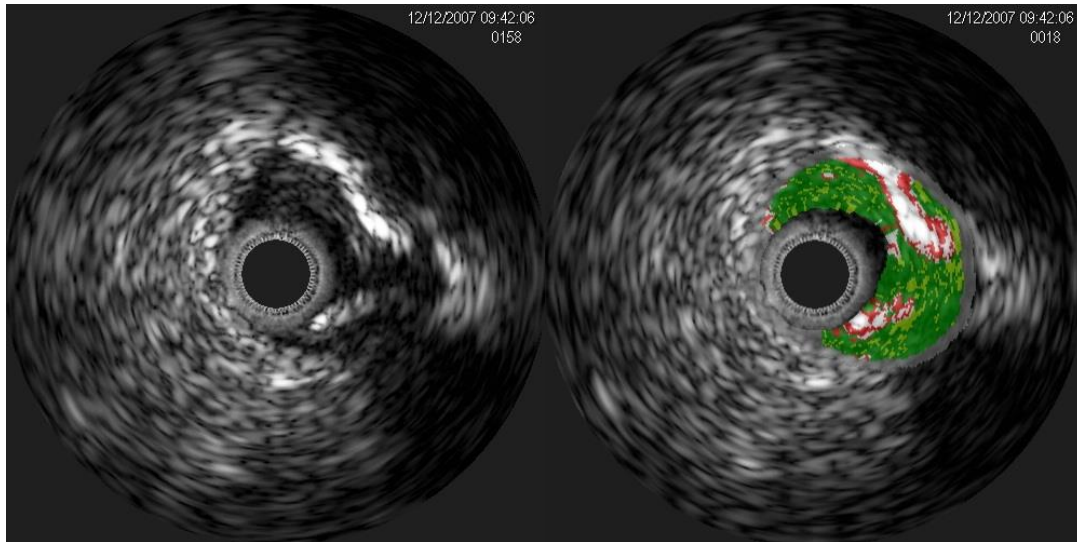


Figure 9: Typical IVUS image (left) and its respective VH-IVUS (right).

Another invasive modality that has gained ground during the past decade is the Optical Coherence Tomography (OCT) which uses near infrared light instead of acoustic waves. Its function is based on measuring the time delay and the magnitude of the backscattered light in order to produce the final images (Figure 10). It has a significantly higher axial resolution than IVUS, allowing for the detailed imaging of the arterial lumen, detection of plaque erosion and rupture, as well as, the visualization of several plaque micro features correlated to plaque vulnerability. Even in stented regions, OCT presents superior sensitivity in detecting strut coverage, malapposition, neointimal hyperplasia, vessel wall trauma and thrombus [38, 39].

However, OCT also suffers from some drawbacks such as its low signal penetration (2-3 mm) which prevents it from visualizing the outer wall, its inability to provide information on the vessel geometry and plaque distribution into the arterial wall and finally, its inability to penetrate lipid-rich cores.

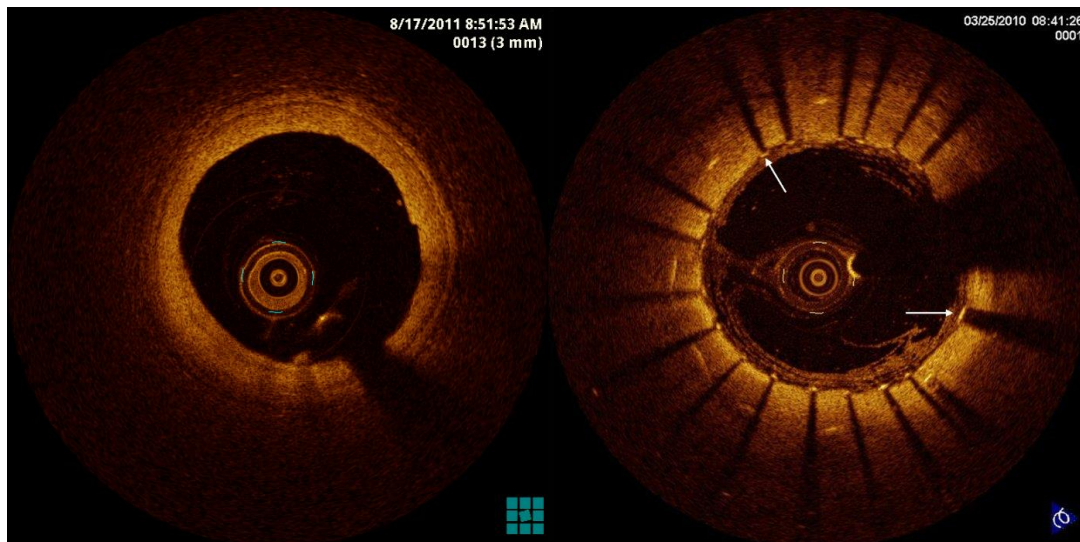


Figure 10: Typical OCT images of a healthy lumen (left) and of a stented region (right).

Another coronary imaging modality is the Near Infrared Spectroscopy (NIRS), a technique, which relies on the principle that different organic molecules absorb and scatter NIRS light to different degrees and at various wavelengths. The spectral analysis of the reflected NIRS light allows assessment of the composition of plaque and the identification of the lipid component [40]. When compared to RF-IVUS, NIRS is restricted to the identification of superficial, wide lipid cores but proves to be more reliable for the detection of lipid-rich plaques located behind calcific deposits. The main limitation of NIRS is its inability to visualize the lumen and outer vessel wall, quantify the atheroma burden and give information about the 3D vessel geometry and plaque distribution.

Besides the aforementioned invasive coronary imaging modalities which are used in everyday clinical practice, several other techniques have also been proposed, such as intravascular magnetic resonance spectroscopy which allows the detection of the lipid component, Raman spectroscopy a method able to discriminate the esterified from the non-esterified cholesterol rich plaques, intravascular photoacoustic (IVPA) imaging which can detect the presence of neo-vessel macrophages and the composition of the atheroma, intravascular magnetic imaging that has only been used in experimental models and appears as the only imaging technique that can visualize both calcific and lipid rich plaques and intravascular near infrared fluorescence imaging (NIRF) that provides high-resolution readouts of human coronary artery [41].

### 1.3.4 Coronary artery functional assessment techniques

Due to the fact that atherosclerotic lesions tend to develop focally in a progressive manner in patients with systemic risk factors, these lesions have the potential to cause acute coronary syndromes or stable angina. An invasive strategy, which might include percutaneous coronary intervention (PCI), has been proven to improve the outcome in the majority of patients that present acute coronary syndromes and in particular, those at higher risk. However, compared to standalone medical therapy in patients with stable angina, invasive strategies do not always present superior outcome [42]. The presence of atherosclerotic lesions in the coronary vasculature, although indicative of the overall atherosclerotic burden of a patient, cannot determine with certainty whether these lesions can ultimately cause ischemia of the perfused myocardial bed only by a visual inspection of the coronary anatomy [43, 44]. In the case of intermediate stenoses, testing the hemodynamic significance of obstructive CAD is of utmost importance for the clinician in order to decide the type of treatment in a population with non-acute symptoms.

The first widely accepted method for the assessment of the functional significance of stenosis was noninvasive stress imaging. However, in patients with diffuse or multilevel disease, it might not be able to determine which stenoses are functionally significant [45]. Two decades ago, fractional flow reserve (FFR) was established as an accurate and useful index for the functional assessment of the significance of coronary stenoses [46]. FFR is defined as the ratio of the pressure distal and proximal to an atherosclerotic lesion ( $P_{\text{distal}}/P_{\text{proximal}}$ ) under hyperemia which is caused by the intravenous administration of adenosine. FFR is a lesion-specific index which generally depicts the percentage of hyperemic flow despite the presence of a stenosis (Figure 11). The FFR measurement requires a dedicated pressure-flow wire, as well as, a vasodilator (i.e. adenosine) administration to induce hyperemia. The FFR cut-off value of 0.8 ( $\text{FFR} \leq 0.8$ ) can be safely used to identify ischemia-causing stenoses and critically improve clinical decision-making, PCI guidance and ultimately patient outcomes in comparison to coronary angiography alone [47, 48]. Moreover, in a large patient population with stable CAD, the FFR-guided PCI diminished the need for revascularizations which were triggered by a myocardial infarction [49].

Even though FFR has been established as a very robust and useful index, it has quite limited application in everyday clinical practice. It is used in  $\leq 20\%$  of elective PCIs in intermediate lesions in the United States and the European Union [50]. The low percentage can



be mainly attributed to the resulting increase of the total catheterization time, the invasive nature of the technique and the high total equipment and medical cost (the mean total cost of the pressure wire and the adenosine dosage exceeds 1000 USD), despite the fact that in cases of multi-vessel disease, FFR-guided PCI has been proven to be cost effective [51]. Another drawback of FFR is that it requires the intravenous administration of adenosine which is not feasible for all patients (i.e. patients with asthma, atrioventricular block, severe hypotension), and it also involves the placement of the pressure wire in the distal vessel, a non-trivial procedure for the clinician, especially in tortuous arteries with a complex anatomy or in small side branches [52].

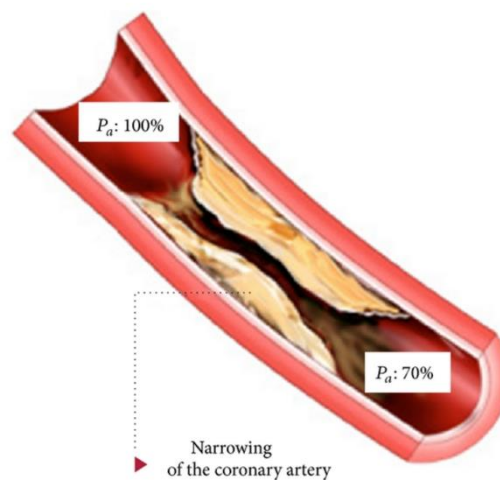


Figure 11: Fractional Flow Reserve illustration [53].

Thus, several alternative methods of functional assessment of coronary stenosis without the use of vasodilators have been proposed using either the instantaneous wave-free ratio (iFR) which is calculated during diastole [54, 55], or the resting  $P_d/P_a$  [55], avoiding the increased total cost, the central or large vein access, as well as, any possible side-effects produced by the administration of adenosine [56, 57]. However, the use of the dedicated pressure wire would still be indispensable. Due to these facts, several image-based lumen measurements have been proposed as surrogate predictors of FFR. Lumen narrowing due to atherosclerotic plaques is mainly responsible for the translesional pressure gradient, which is measured by FFR under the induction of hyperemia. Therefore, lumen measurements from a variety of imaging modalities have been used to discriminate between pathologic and normal values of FFR. Using a variety of statistical regression techniques, it has been shown that lumen area and lesion length are the strongest anatomic determinants of an abnormal FFR value in several patient populations. 50% diameter stenosis has been established as a cut-off criterion using non-



invasive coronary angiography for discriminating functionally significant stenoses as assessed by FFR. Visual angiographic assessment is heavily dependent on the user, therefore the use of dedicated software for systematic quantification results in the enhancement of the diagnostic accuracy of the angiographic modalities. However, both coronary imaging modalities have their drawbacks. Non-invasive angiography suffers mainly from its poor spatial resolution, whereas, traditional invasive coronary angiography provides only a 2-D view of the arterial lumen. Even though 3D-QCA is already available, providing a more complete aspect of the lumen anatomy, the actual quantification of coronary stenoses is a non-trivial matter because of the vagueness that surrounds the definition of the reference vessel diameter, which is also affected by atherosclerosis. Given the fact that CCTA is a non-invasive technique with high negative predictive value (NPV), it might be suitable for an initial screening of patients with suspected CAD and could clarify the diagnosis, enable the targeting of interventions and reduce the need for further stress testing [58].

Lumen measurements deriving from intravascular imaging techniques present the advantages of higher spatial resolution and direct assessment of any present atherosclerosis in the reference areas, thus increasing precision. Many studies have focused on establishing optimal cut-offs for assessing the functional significance of intermediate stenoses, presenting though high variability. The values of interest (i.e. minimum lumen diameter/area measure) are highly dependent on the reference vessel size [59], the vessel type (LAD vs. RCA) and the location within a vessel (proximal vs. distal). Several studies have shown that IVUS offers measures that present moderate correlation to FFR ( $r < 0.5$ ), low diagnostic accuracy ( $\approx 70\%$ ) and poor specificity, thus excluding IVUS as a surrogate for FFR [60]. OCT has superior diagnostic ability than IVUS in vessels of small diameter ( $< 3\text{mm}$ ) [61] but its overall diagnostic accuracy still remains rather modest [62]. Methods that combine the accurate lumen volumetric profiling provided by OCT along with approximate analytical models that account for volume-integrated pressure drops, hyperemic microvascular resistances and branch flow might further improve the assessment and provide measurements that correlate even better with FFR [63].

Having a relatively low false negative predictive value ( $< 10\%$  for IVUS) [59], intravascular coronary imaging modalities can play an important role in the decision scheme regarding the necessity for PCI by excluding non-significant stenoses and at the same time, providing a thorough stenosis assessment (i.e. high-risk plaque characteristics, plaque burden, plaque composition) and aid in the optimization of PCI regarding stent placement and deployment having a complementary role along with FFR. However, the most important

drawback of such modalities is their invasive nature due to the size of their catheters ( $\approx 3$  French) constituting them ineffective in terms of time or cost solely for diagnostic purposes.

## Chapter 2: Literature Overview

---

- 2.1. Introduction
  - 2.2. Blood flow modelling
  - 2.3. CCTA derived computational FFR assessment
  - 2.4. Invasive Coronary Imaging derived functional assessment
  - 2.5. Other virtual indices of coronary functional assessment
  - 2.6. Contribution of this Thesis
- 

### 2.1.Introduction

During the past decades, several mathematical models have been implemented and employed to quantify biomechanical conditions regarding every stage and function of the circulatory system, including blood flow within the heart chambers or deeper within the arterial tree. These mathematical models include lumped parameter, one dimensional wave propagation (1D), as well as three-dimensional numerical methods, and can safely and accurately describe cardiovascular mechanics. The first attempts to calculate velocity and pressure fields were made on idealized tubular models representing the vascular anatomy and physiology. The ongoing advances in medical 3D imaging allowed the quantification of cardiovascular mechanics in patient-specific anatomic and physiologic models. The first steps in image-based modeling for simulating blood flow were attempted in the late 1990s. Since then, many efforts have been made and are reported in the current literature, regarding the investigation and analysis of the pathogenesis of occlusive and aneurysmal disease in the carotid artery, the coronary vasculature, the aorta and the cerebral circulation. Moreover, the aforementioned patient-

specific techniques have been applied in structural analysis for aneurysm rupture prediction. In general, the combination of Computational Fluid Dynamics (CFD) with 3D medical imaging techniques enhances diagnostic assessment, device design and clinical trials. Physiological responses to interventions can now be predicted and previously unmeasurable hemodynamic parameters can be safely computed.

## **2.2.Blood Flow Modeling**

Modeling blood flow dynamics has traditionally been a field of research of wide interest. Numerous studies have been reported that try to shed light to the aforementioned matter. In rheological terms, blood behaves as a Newtonian fluid with constant viscosity in vessels of medium to large diameter, such as the main coronary arteries or the aorta. Several animal and other experimental studies have used patented apparatus to calculate and define the blood flow velocity and pressure relationship [64, 65]. Ku *et al.*[66], managed to correlate the site of the atherosclerotic plaque with the endothelial shear stress using a phantom to replicate the human carotid artery. Blood velocity was measured with laser Doppler velocimetry whilst the thickness of the intima was directly measured from carotid arteries taken from cadavers. Flow was assumed to be pulsatile. The authors concluded that low and oscillatory shear stress are correlated with the location of the atherosclerotic plaque. A similar study was presented by Zarins *et al.*[67], regarding blood flow pattern in carotid artery phantoms and concluded that the ultimate thickening of the arterial wall, as well as, the formation of the atherosclerotic plaque is related to regions with low ESS.

The most common computational method used to simulate arterial blood flow is the finite element method. In order to perform computational blood flow simulations, *in vivo* or *in vitro* flow measurements derived from Doppler ultrasound or magnetic resonance imaging are required to be applied as boundary conditions. The main assumptions of the first computational studies included that blood behaves as a Newtonian fluid and that the flow is laminar and incompressible. Simplified cylindrical pipes with non-deformable walls were used to represent the actual arterial geometry. In order to model blood flow, the three-dimensional transient Navier-Stokes equations need to be solved. Taylor *et al.*, presented a study on blood flow modelling using a stabilized form of the Galerkin finite element method [68]. The Conjugate Gradient method and the Generalized Minimal Residual methods were used to calculate the velocity and the pressure. The proposed method was used to simulate the flow in idealized models of an abdominal aorta and of an end-to-side graft-artery anastomosis. Santamarina *et al.*

[69], on the other hand, used the finite volume method to solve the Navier-Stokes equations in an attempt to study the flow in a curved cylindrical model that represented a coronary artery. In the finite volume method, the flow domain is discretised into finite volumes instead of finite elements. The equations are first integrated and linearized over a finite volume and are then combined to produce the algebraic equations for the entire flow field. The authors used and examined several radii of curvature and validated their results using an experimental flow setup.

Banerjee *et al.* [70, 71], examined the hemodynamic significance of coronary stenosis using both experimental and computational simulations. Three coronary arterial models were used to calculate *in vitro* the pressure drop distal to the stenosis. Computational models were also used to calculate the pressure drop at the same location and the results were then compared to the experimental one. The produced system of equations was solved using the Galerkin method. The problem was unsteady, therefore, a solution was reached for each time step with a successive substitution type of a fully coupled iterative solver. The authors concluded that the calculation of the pressure drop could potentially be used in everyday clinical practice to assess the hemodynamic significance of a coronary stenosis. Politis *et al.* [72, 73], investigated the wall shear stress distribution in idealized composite arterial coronary grafts. In their simulations, flow was assumed to be transient and the final numerical solution was reached using the finite element method. In order to investigate and analyse the effect of blood flow on the arterial stenosis, several degrees of stenosis, as well as, different configurations of the used grafts were used. Vasava *et al.* [74], presented a study on modelling pulsatile blood flow on an idealized model of a human aorta. The pulsatile blood flow was simulated using incompressible Navier-Stokes equations. The idealized model of the aorta along with the respective inlet pressure profile which was used as a boundary condition were modified to simulate the actual aorta under hypotension and hypertension conditions. The aortic wall was assumed to be rigid, thus simplifying further the overall model.

During the last two decades, advances in medical imaging have allowed for the development of realistic patient-specific 3D models of the coronary vasculature. The 3D models are created using data that derive from coronary imaging modalities such as invasive coronary angiography (ICA), coronary computed tomography angiography (CCTA), magnetic resonance angiography (MRA), intravascular ultrasound (IVUS) and optical coherence tomography (OCT). The fact that these 3D models are patient-specific, offers a unique opportunity to explore and understand the mechanisms that trigger the formation of atherosclerotic plaque. The first study which tried to correlate the local hemodynamics to the plaque formation was proposed by

Steinman *et al* [75]. They presented a computational simulation of blood flow in a realistic 3D model of a carotid artery, which was reconstructed using MRI. The arterial thickness was correlated to the local Wall Shear Stress (WSS) distribution.

However, in an effort to realistically simulate the complexity of the human vasculature, the interaction between the blood and the arterial wall was introduced by applying fluid structure interaction (FSI) models [76-78]. According to these models, blood flow creates loads on the surface of the arterial walls forcing them to deform. The elastic nature of the arterial wall tends to restore the wall to its original state, thereby causing the deformation of the blood domain. Both the blood and the arterial wall domains are discretized and the equations for each domain are solved and used as initial conditions to the other domain. Due to the large number of equations that need to be solved, FSI simulations are very demanding in computational resources and very time-consuming compared to the rigid wall approach but are considered to provide more accurate results for the flow field.

### **2.3.CCTA derived computational FFR assessment**

Due to the non-invasive nature of CCTA, the application of CFD on CCTA-derived 3D arterial models has received wide clinical interest regarding the non-invasive FFR assessment. According to this approach, hemodynamic factors such as flow and pressure are not known *a priori*, so lumped parameter models regarding the cardiac output, the resistance of the coronary microcirculation and the pressure of the systemic circulation are coupled with the flow domain of the aortic root and the epicardial arteries, where the governing equations of flow dynamics are solved and can consequently provide FFR calculations in 1-4 hours. Three major studies (DISCOVER-FLOW, DeFACTO and HeartFlow NXT) directly compared their computational FFR results to the measured FFR values, producing promising results and constituting the method as a valuable tool in the clinical setting [79-81].

The first study (DISCOVER-FLOW study, 103 patients, 159 arteries) exhibited a good correlation regarding  $FFR_{CTA}$  with FFR ( $r=0.68$ ) with the respective diagnostic accuracy, sensitivity, specificity, positive predictive value and negative predictive value for predicting hemodynamically significant stenoses ( $FFR \leq 0.8$ ) being 84, 88, 82, 74 and 92%, respectively [81]. Furthermore, when compared to cases of  $\geq 50\%$  stenosis detected solely by CCTA,  $FFR_{CTA}$  showed superior discrimination (AUC: 0.90 vs. 0.75,  $p=0.001$ ). In the follow-up study of DISCOVER-FLOW (DeFACTO study, 252 patients, 407 arteries), stable CAD patients underwent CCTA,  $FFR_{CTA}$  and invasive coronary angiography with FFR measurement [79].

The per patient diagnostic accuracy, sensitivity, specificity, positive predictive value and negative predictive value for predicting an  $\text{FFR} \leq 0.8$  were 73, 90, 54, 67, and 84%, respectively. Good correlation was also found between the two methods ( $r=0.68$ ). The most recent study (HeartFlow NXT, 254 patients, 484 arteries) further validated  $\text{FFR}_{\text{CTA}}$ , by making use of updated proprietary software which included image quality assessment, better image segmentation, refined mathematical models and further increased automation [80]. Diagnostic accuracy, sensitivity, specificity, positive predictive value and negative predictive value for predicting an  $\text{FFR} \leq 0.8$  were 81, 86, 79, 65, and 93%, respectively on a per-patient basis and 86, 84, 86, 61, and 95%, respectively, on a per-vessel basis. Finally, good correlation was found between  $\text{FFR}_{\text{CTA}}$  and  $\text{FFR}$  ( $r=0.82$ ). The PLATFORM [82] study (584 subjects) focused on the clinical outcomes of  $\text{FFR}$  by CCTA-guided diagnostic strategies compared to the common care in CAD-suspected patients, providing insight on the clinical utilization of  $\text{FFR}_{\text{CTA}}$ .

$\text{FFR}_{\text{CTA}}$  has gathered a very large validation dataset up to date and could potentially alter the routine clinical practice by providing a non-invasive approach regarding the functional assessment of coronary stenoses. Bearing this in mind,  $\text{FFR}_{\text{CTA}}$  might be used to screen patients with suspected CAD in order to reach a decision regarding a possible catheterization. A recent overall systematic review of 5 studies [83], depicted that the diagnostic accuracy of  $\text{FFR}_{\text{CTA}}$  varied significantly in the entire spectrum of the disease. Regarding vessels of  $\text{FFR}_{\text{CTA}} > 0.90$ , the vast majority (97.9%) met the guideline  $\text{FFR}$  criterion for deferral ( $\text{FFR} > 0.80$ ), whereas for vessels with  $\text{FFR}_{\text{CTA}} < 0.60$ , 86.4% met the  $\text{FFR}$  criterion ( $\text{FFR} \leq 0.8$ ) for Percutaneous Coronary Intervention (PCI). Regarding the values in between the aforementioned thresholds, there was less certainty on if the invasive  $\text{FFR}$  would actually meet the PCI criterion.

However, CCTA suffers from a main drawback in the assessment of lumen stenosis severity due to its limited spatial resolution, which ultimately affects the diagnostic accuracy of  $\text{FFR}_{\text{CTA}}$ . Moreover, the large variation in study outcomes is also another point of concern. Critical statistical measures such as sensitivity and specificity vary across different studies and this could be attributed to the different sample sizes and patient characteristics. Furthermore, a recent meta-analysis assessed the combination of CCTA with  $\text{FFR}_{\text{CTA}}$  in diagnosing patients with obstructive CAD and as a conclusion it introduced a useful and efficient way (i.e. “both positive” strategy) to reduce the percentage of patients with a false positive diagnosis. Finally, heavy calcifications, arrhythmia and tachycardia are factors that affect both CCTA and  $\text{FFR}_{\text{CTA}}$ .

## **2.4. Invasive Coronary Imaging derived functional assessment**

The non-invasive based diagnosis that has proven to be feasible by using CCTA-derived 3D models cannot by itself replace the up-to-date gold standard for coronary lumenography (ICA) which exhibits a significantly higher spatial and temporal resolution than CCTA [84]. The accurate 3D reconstruction of the coronary anatomy is feasible either by using ICA images alone or by fusing them with intravascular modalities.

Tu *et al.* [85], created a model which combined 3D QCA with a steady-state CFD flow analysis. Two angiographic projections with an angle difference  $>25^\circ$ , acquired by either monoplane or biplane systems, were used to reconstruct in 3D the anatomical model. Instead of using standard pulsatile flow and generic boundary conditions, the patient-specific mean flow along with the respective pressure were used as boundary conditions. The mean volumetric flow rate was calculated using the Thrombolysis In Myocardial Infarction (TIMI) frame count (Figure 12). Thus, the overall calculation time was significantly shortened, averaging less than 10 minutes per case. However, this method presented the disadvantage that the administration of a vasodilator for the induction of hyperemia was required during ICA. 77 vessels were used in the study deriving from 68 patients. Good correlation was found between  $FFR_{QCA}$  and  $FFR$  ( $r=0.81$ ,  $p<0.001$ ), with a mean difference of  $0.00 \pm 0.06$  ( $p = 0.541$ ).



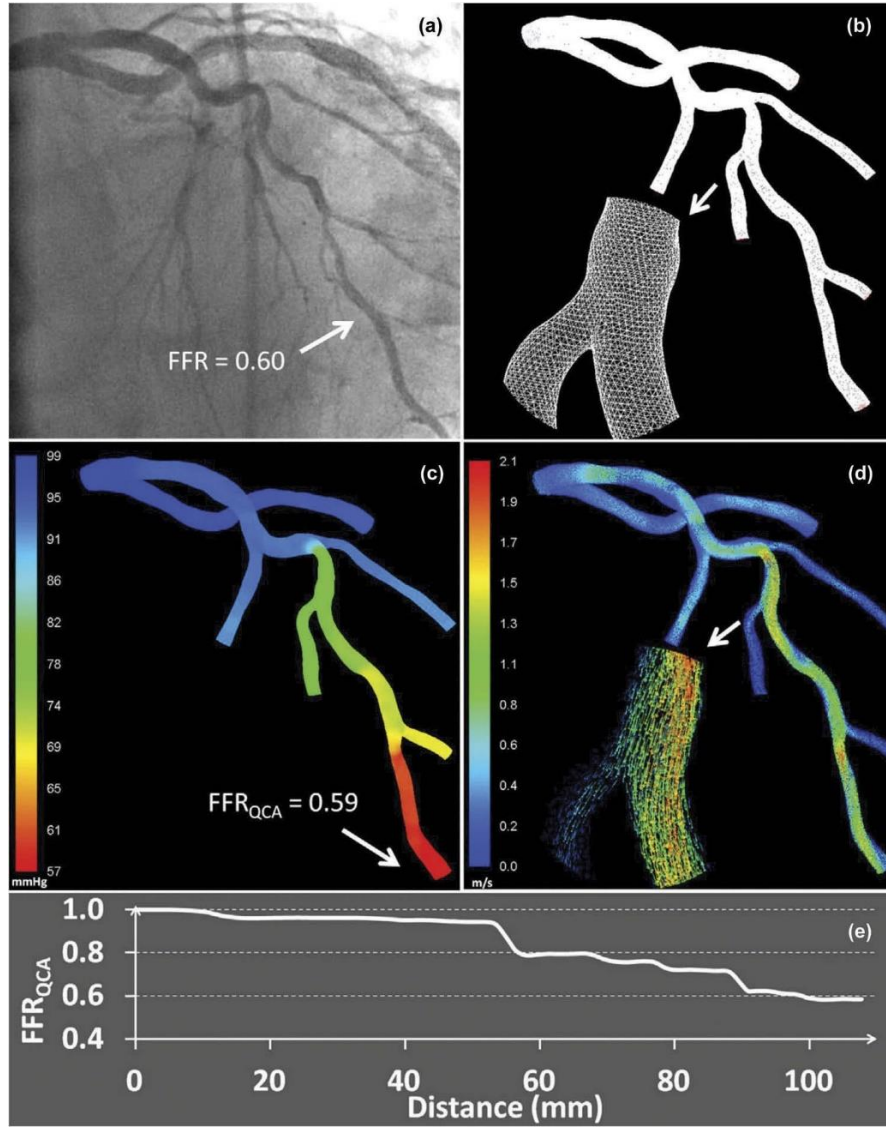


Figure 12: (a) X-ray angiography showing diffused stenoses at the left anterior descending artery. (b) Three-dimensional angiographic reconstruction and the generated meshes. (c) Simulated pressure distribution at hyperemia. The computed FFR-QCA was 0.59 and the wire-based FFR was 0.60 at the distal position indicated by the arrow. (d) Simulated hyperemic flow colored by the velocity [86]. (e) Virtual 'reversed' FFR pullback along the centerline of the left anterior descending artery. FFR-QCA: computed quantitative coronary artery (QCA) fractional flow reserve. Reproduced from Tu et al [85].

VIRTU-1 was the first study to investigate the potential of angiographic data for FFR assessment in which, 19 patients with 35 anatomical and physiological datasets were included [87]. The measured FFR values were compared to the virtual-FFR values that derived from 3D coronary reconstruction from conventional angiography, coupled with CFD as well as, a lumped model for generic downstream boundary conditions of microvascular resistance. Good correlation between the two methods ( $r=0.84$ ) and a high diagnostic accuracy (97%) for detecting pathological cases ( $FFR \leq 0.8$ ) were achieved. The VIRTU-1 study set the foundations

for less-invasive approaches in FFR assessment, presenting though contradicting results regarding the so-called “grey zone” of FFR (i.e.  $0.75 < \text{FFR} < 0.80$ ) as well as, large computational time (24h).

The evaluation of virtual functional assessment index (vFAI) has been recently suggested as a valid alternative to FFR measurements in patients submitted to ICA, allowing to determine the hemodynamic relevance of a given coronary lesion with a few minutes long computation time [88]. The algorithm uses three-dimensional (3D) coronary anatomical data and steady-flow CFD analysis to compute the ratio of distal to proximal pressure over the lesion for flows in the range from 0-4 ml/s, normalized by the ratio over this range for a normal artery, offering a measure of CAD hemodynamic significance that is numerically equal to the average of the computed pressure ratio over this flow range. vFAI was superior to 3D QCA in predicting physiological lesion significance (AUC: 78% [95% CI: 70–84%];  $p < 0.0001$  compared to vFAI). High accuracy, sensitivity, and specificity, 88, 90, and 86%, respectively, in predicting  $\text{FFR} \leq 0.80$  was reported and there was a close correlation ( $r = 0.78$ ,  $p < 0.0001$ ) and agreement of vFAI compared to wire-FFR (mean difference:  $-0.0039 \pm 0.085$ ,  $p = 0.59$ ) (Figure 13).

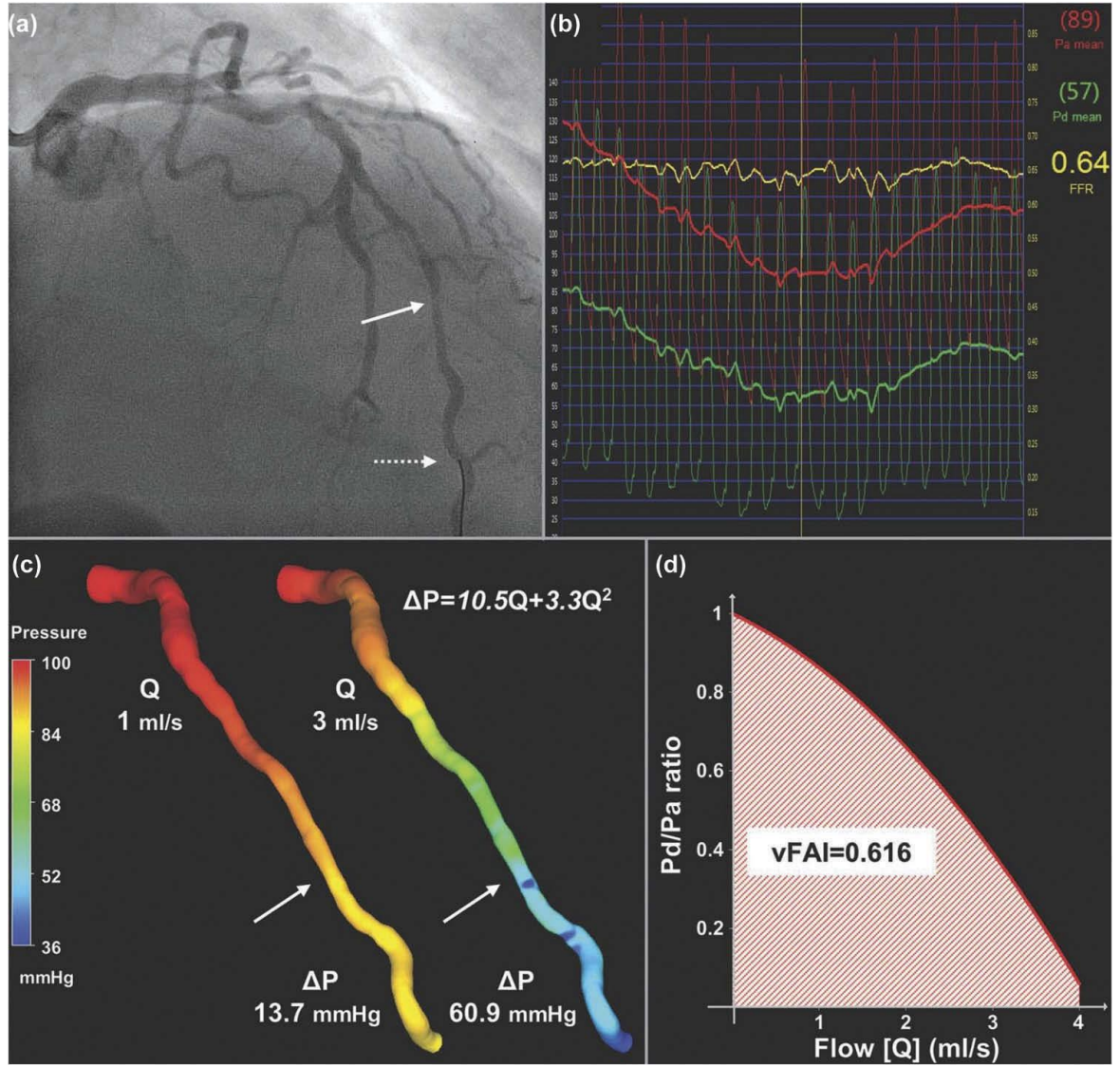


Figure 13: (a) Representative example of a left anterior descending artery (LAD) with a moderate lesion (arrow: maximal stenosis) in angiography (3D-QCA %diameter stenosis: 35%) that had (b) a low fractional flow reserve (FFR = 0.64) measured at a distal location (dotted arrow) using the pressure wire. (c) 3D-QCA coronary lumen reconstruction with the pressure distribution in a color-coded map for two different flow rates (Q), which resulted in a pressure gradient ( $\Delta P$ ) of 13.7 and 60.9 mmHg. The computed artery-specific  $\Delta P$ -Q relationship is provided. The arrows denote the location of maximal stenosis. (d) Relationship between the ratio of distal to aortic pressure (Pd/Pa) and flow for the studied artery, and calculation of the artery-specific virtual functional assessment index (vFAI: 0.62) shows the good agreement with wire-FFR [88].

Finally, some limited in size studies using either intravascular imaging or invasive angiography have been reported in the literature, which explored the potential for the virtual hemodynamic assessment of coronary stenoses, exhibiting good correlation and strong agreement, thus indicating the validity and efficacy of the proposed methods.

## 2.5. Other virtual indices of coronary functional assessment

Another simpler index for the functional assessment of coronary arteries is the distal coronary pressure to the aortic pressure ratio ( $P_d/P_a$ ) under rest, which, however, also requires the use of a dedicated pressure wire. The virtual indices that derive either from CCTA or ICA require complex CFD models, thus increasing the computational cost. The resting  $P_d/P_a$  ratio has the obvious advantage that it does not require the induction of hyperemia. Papafaklis *et al.* assessed the diagnostic performance of the virtual resting  $P_d/P_a$  ratio using ICA images and a simplified CFD model [89]. The average processing time was surprisingly low (i.e. 4 minutes/case) and the diagnostic accuracy, sensitivity, and specificity for the optimal virtual resting  $P_d/P_a$  cut-off ( $\leq 0.94$ ) were 84.9, 90.4, and 81.6%, respectively. The technique demonstrated superior diagnostic performance than 3D QCA % area stenosis (AUC: 77.5% [95% CI: 69.8–85.3%]) and a good correlation ( $r=0.69$ ) (Figure 14).

The instantaneous wave-free ratio (iFR) was established to allow the functional assessment of stenoses without the induction of hyperemia [54]. In the ADVISE II study, iFR correctly classified 82.5% of the stenoses as hemodynamically significant, using a pre-specified cut-off value of 0.89. The aforementioned study along with the DEFINE-FLAIR [90] and the iFR-SWEDEHEART [91] studies concluded that, with the use of a single cut-off value ( $\leq 0.89$ ), iFR was not inferior to a FFR-guided revascularization approach, taking into account the rate of major adverse cardiac events for a 12-month timestamp.

Ma *et al.* [92], conducted a study investigating whether iFR could be combined with CCTA (iFR<sub>CT</sub>) in order to be used as a novel non-invasive method for the diagnosis of ischemia-causing stenoses. 3D models of coronary arteries were reconstructed using CCTA images at end-diastole. Patient-specific boundary conditions were calculated taking into account the myocardial mass and the mean arterial pressure of the patient. iFR<sub>CT</sub> was calculated as the mean distal pressure divided by the mean aortic pressure during the diastolic wave-free period during rest. The total computational time for each case was 4 hours. iFR<sub>CT</sub> exhibited good correlation with FFR ( $r=0.75$ ) and the diagnostic accuracy, sensitivity, specificity, positive predictive value, and negative predictive value of iFR<sub>CT</sub> were 78.72, 70.59, 83.33, 70.59, and 83.33%, respectively (Table 3).

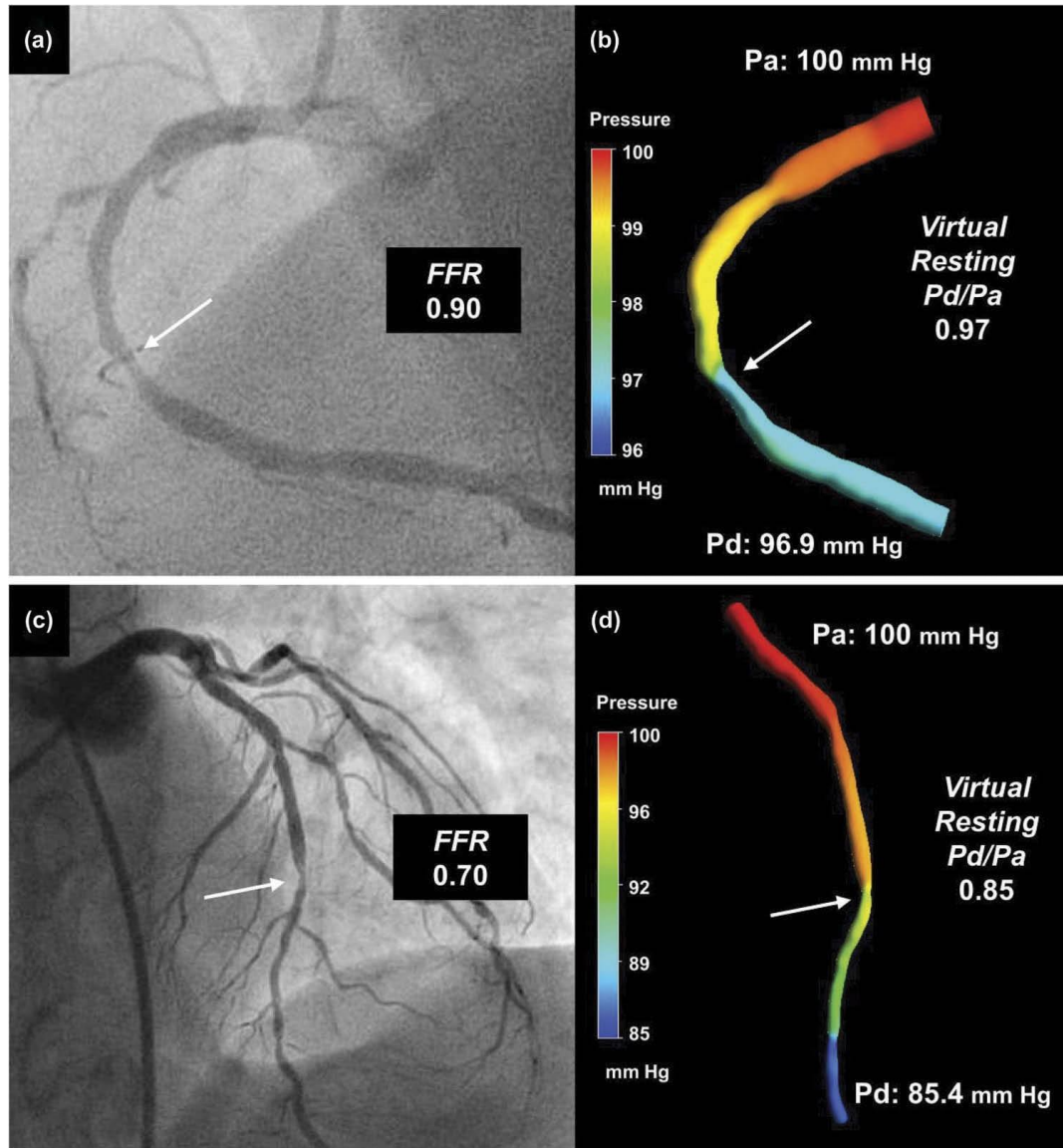


Figure 14: a) Right coronary artery with a moderate lesion in angiography and a high fractional flow reserve ( $FFR = 0.90$ ) measured using the pressure wire. (b) 3D-QCA coronary lumen reconstruction with the pressure distribution (resting conditions) in a color-coded-map which resulted in a virtual resting  $P_d/P_a$  of 0.97. (c) Left anterior descending artery with a moderate lesion in angiography and a low FFR (0.70) measured using the pressure wire. (d) 3D-QCA coronary lumen reconstruction with the pressure distribution (resting conditions) in a color-coded- map which resulted in a virtual resting  $P_d/P_a$  of 0.85. The arrows denote the location of maximal stenosis in each case. 3D-QCA: 3-dimensional quantitative coronary angiography [89].

## 2.6. Contribution of this Thesis

Numerous studies that focus mainly on introducing and establishing new, novel indices regarding the hemodynamic assessment of coronary lesions are present in the literature. Moreover, these indices have started to focus on non-invasive techniques due to the apparent advantages that are offered by such imaging techniques to the patient, as well as, to their total clinical cost. Several studies have also been reported in the literature, which take into account



the interaction between blood flow and the arterial wall in order to compute important hemodynamic factors such as endothelial shear stresses or intravascular pressures.

Table 3: Performance of computational models for virtual functional assessment against fractional flow reserve (cut-off  $\leq 0.80$ ) [93].

Study	Imaging modality	Sample size (patients, vessels)	Pearson correlation coefficient	Agreement (Bias $\pm$ SD: virtual index–FFR)	Overall diagnostic accuracy	AUC
<b>DISCOVER-FLOW [81]</b>	CCTA	103, 159	0.68	0.02 $\pm$ 0.116	84% (per vessel)	0.90
<b>DeFACTO [79]</b>	CCTA	252, 407	0.63	0.06	73% (per vessel)	0.81
<b>HeartFlow NXT [80]</b>	CCTA	251, 484	0.82	0.02 $\pm$ 0.074	86% (per vessel)	0.93
<b>Kim et al. [94]</b>	CCTA	44	0.60	0.006	77%	---
<b>Renker et al. [95]</b>	CCTA	53	0.66	---	---	0.92
<b>Coenen et al. [96]</b>	CCTA	106, 189	0.59	-0.04 $\pm$ 0.13	74.6%	0.83
<b>Kruk et al. [97]</b>	CCTA	90, 96	0.67*	-0.01 $\pm$ 0.095	74% (per vessel)	0.83
<b>Ko et al. [98]</b>	CCTA	42, 78	0.57	-0.065 $\pm$ 0.137	83.9% (per vessel)	0.88
<b>VIRTU-1 [87]</b>	Invasive angiography	19, 35	0.84	0.02 $\pm$ 0.080	97% (per vessel)	0.97
<b>Tu et al. [85]</b>	Invasive angiography	68, 77	0.81	0.00 $\pm$ 0.06	88.3%	0.93
<b>FAVOR Pilot Study (QFR) [86]</b>	Invasive angiography	73, 84	fQFR: 0.69	0.003 $\pm$ 0.068	80%	0.88
			cQFR: 0.77	0.001 $\pm$ 0.059	86%	0.92
			aQFR: 0.72	-0.001 $\pm$ 0.065	87%	0.91
<b>Papafaklis et al. (vFAI) [88]</b>	Invasive angiography	120, 139	0.78	0.004 $\pm$ 0.085	87.8%	0.92
<b>Trobs et al. [99]</b>	Invasive angiography	73, 100	0.85	-0.008 $\pm$ 0.063	90%	0.93
<b>Papafaklis et al. (virtual resting Pd/Pa) [89]</b>	Invasive angiography	120, 139	0.69	---	84.9%	0.91

This section presents the contribution of this thesis and how the proposed methodologies and results are presented and structured in the following chapters. This thesis, mainly focuses on establishing and validating hemodynamic assessment indices employing either invasive or non-invasive coronary imaging modalities. Furthermore, it examines the effect of the interaction between the arterial wall and the blood flow in order to draw interesting conclusions on whether the FSI simulations are superior in terms of computing the aforementioned hemodynamic factors when compared to the respective rigid wall simulations. Finally, two in-

house developed software suites that perform either a hemodynamic assessment of coronary arteries or incorporate atherosclerotic plaque progression models on 3D arterial models that derive from IVUS, MRI or CCTA are presented.

*Chapter 3* - Initially a study on coronary artery pressure measurements using blood flow simulation in realistic 3D reconstructed coronary arteries is presented. Its primary findings were the following: (I) computed distal coronary pressure values correlate very well with the measured ones using the pressure wire and (II) the assumption of rigid walls and steady-state flow results in negligible differences compared to the more demanding FSI and pulsatile simulations, respectively. In this work, realistic patient-specific 3D arterial models deriving from IVUS and ICA were used. Furthermore, *in vivo* data from pressure/flow measurements deriving from the use of a dedicated pressure-flow wire for validation purposes were also used. Excellent agreement was found for both methods, thus indicating the efficacy of the far less demanding rigid wall-steady state method and highlighting the value of numerical simulations applied in 3D arterial models for assessing important hemodynamic factors such as coronary arterial pressure or ESS.

*Chapter 4* - Regarding the establishment and validation of hemodynamic assessment indices, a study on the computational hemodynamic assessment of coronary lesions on 3D models deriving from compute tomography angiography is presented. Its aims were to examine the feasibility of assessing vFAI from 3D models that were reconstructed from our in-house developed CCTA 3D reconstruction software and to assess the efficacy of the proposed method by comparing the calculated vFAI values to the invasively measured FFR in intermediate coronary stenoses (i.e. 30%-70%). A study population of 44 patients (51 vessels) was used. The results were very promising, since they matched the results of the accepted gold-standard represented by invasive FFR. The computed cut-off value of 0.84 was associated with a modest sensitivity (76.9%), high specificity (88.2%) and high Negative Predictive Value (92.1%) for identifying pathologic cases of an FFR lower than the 0.80 threshold. The evident advantages of the proposed method were the non-invasive nature of the entire procedure, as well as, the very low computational time needed for the assessment.

In the context of combining coronary imaging modalities with virtual hemodynamic assessment indices, a novel method that combines the most efficient methods of anatomic and functional assessment of coronary lesions is presented. The 3D reconstruction of coronary arterial segments in a straight manner using only IVUS images is performed, thus neglecting

the actual curvature of the arterial segments. Finally, blood flow simulations using CFD, in order to calculate the virtual Functional Assessment Index (vFAI) are subsequently performed. This way, the anatomic information provided by the IVUS sequence and the functional assessment of the vessel of interest provided by the vFAI that is subsequently calculated, are combined. A dataset of 22 patients that underwent IVUS examination and FFR measurement was used in the aforementioned study. The 3D models were reconstructed using only IVUS images. The luminal borders were annotated for each R-peak frame and were then stacked linearly, creating the final models. Excellent correlation ( $r=0.92$ ), as well as, high sensitivity and specificity values were found between vFAI and FFR.

*Chapter 5* - Two software suites regarding the 3D reconstruction of coronary arteries, the hemodynamic assessment of coronary lesions and the application of plaque progression models are presented in this chapter. Regarding the first software suite, a platform for the development of multiscale patient specific atherogenesis models, called ARTool is presented. The methodology integrated three levels involved in the atherogenesis procedure, that is the anatomical model of the arterial tree, the blood flow model and the molecular/cell model of the arterial wall/blood composition and the biological mechanism involved in the generation and growth of atherosclerotic plaque.

The second software suite which was proposed as a useful tool for the hemodynamic assessment of coronary lesions was ArtCare. A software platform was developed, that provides the clinician with the ability to reconstruct in 3D the desired vessel using three different imaging modality options: fusion of IVUS and biplane angiography, fusion of OCT and biplane angiography or just biplane angiography (3D-QCA). The proposed system offers numerous 3D visualization options and has the ability to use any given IVUS, OCT or angiography formats. The key point, however, is that using a dedicated finite element module, it can calculate the virtual functional assessment index (vFAI) for the reconstructed model, thus offering both anatomic characteristics, as well as functional assessment of the diseased vessel. The system features have been extensively validated, presenting very promising results regarding the automatic lumen border detection from IVUS images and from OCT images, as well as the 3D reconstruction from the 3D-QCA module. Moreover, the calculated vFAI deriving from the 3D reconstructed models using the proposed method presented high correlation when compared to the respective calculated vFAI values deriving from the 3D models reconstructed using the CAAS QCA 3D® (PIE Medical) commercial package.



## Chapter 3: Blood Flow Simulations in arteries with rigid or deformable walls

---

- 3.1. Introduction
  - 3.2. Blood flow modelling
  - 3.3. Blood flow simulations on arteries with rigid or deformable walls
  - 3.4. Patient-Specific Simulation of Coronary Artery Pressure Measurements
- 

### 3.1. Introduction

The study and the in depth understanding of the mechanisms of atherosclerosis are of utmost importance nowadays, since cardiovascular diseases are the major cause of death in developed countries. Atherosclerosis is a cardiovascular disease, which causes the thickening and hardening of the arterial wall, resulting to reduced, or completely obstructed blood flow. Computational Fluid Dynamics (CFD) combined with 3D arterial models generated from medical images such as Intravascular Ultrasound (IVUS) with angiographies, Magnetic Resonance Imaging (MRI) and Computed Tomography images (CT) have set the ground for accurate blood flow simulations, providing some insight to the complex mechanisms of the generation and development of atheroma. In the current thesis, the 3D models that were used for the subsequent blood flow simulations derived from the most commonly used coronary imaging modalities such as invasive coronary angiography, intravascular ultrasound, computed tomography coronary angiography or the fusion of IVUS and ICA. The quality of the final 3D models strongly affects the overall accuracy of the subsequent blood flow simulations. Hemodynamic factors such as endothelial shear stress or intravascular pressures play a significant role in the development and progression of atherosclerosis, as well as, in the

hemodynamic status of the entire coronary vasculature. For the aforementioned reasons, in this chapter, we present two thorough analyses of blood flow simulations on several patient specific arterial models using both rigid and deformable arterial walls, and steady-state or transient simulations. The first part of chapter 3 focuses mainly on the comparison between rigid and deformable walls simulations whilst the second one presents a thorough validation study on patient-specific simulations of coronary artery pressure measurements. Moreover, we present in detail the general mathematical background of the equations used to model blood flow, as well as the theoretical background of the finite element method.

### 3.2. Blood Flow Modeling

Blood flow is generally modelled using the Navier-Stokes equations, as well as, the continuity equation. In this chapter, the governing equations regarding Newtonian fluids are described. The fluid density is  $\rho$  and velocity components are  $v_x, v_y, v_z$ . The equation of balance of mass within a control volume leads to the continuity equation:

$$\frac{\partial \rho}{\partial t} + \nabla \cdot (\rho \mathbf{v}) = 0, \quad (1)$$

In cases of incompressible fluids, the fluid density is constant ( $\rho = \text{constant}$ ), so Equation 1 becomes:

$$\nabla \cdot (\rho \mathbf{v}) = 0, \quad (2)$$

The 3D Navier-Stokes equations in terms of velocity gradients for a Newtonian fluid with constant density  $\rho$  and viscosity  $\mu$  are:

$$\rho \left( \frac{\partial v_x}{\partial t} + v_x \frac{\partial v_x}{\partial x} + v_y \frac{\partial v_x}{\partial y} + v_z \frac{\partial v_x}{\partial z} \right) = -\frac{\partial p}{\partial x} + \mu \left( \frac{\partial^2 v_x}{\partial x^2} + \frac{\partial^2 v_x}{\partial y^2} + \frac{\partial^2 v_x}{\partial z^2} \right) + \rho g_x, \quad (3)$$

$$\rho \left( \frac{\partial v_y}{\partial t} + v_x \frac{\partial v_y}{\partial x} + v_y \frac{\partial v_y}{\partial y} + v_z \frac{\partial v_y}{\partial z} \right) = -\frac{\partial p}{\partial y} + \mu \left( \frac{\partial^2 v_y}{\partial x^2} + \frac{\partial^2 v_y}{\partial y^2} + \frac{\partial^2 v_y}{\partial z^2} \right) + \rho g_y, \quad (4)$$

$$\rho \left( \frac{\partial v_z}{\partial t} + v_x \frac{\partial v_z}{\partial x} + v_y \frac{\partial v_z}{\partial y} + v_z \frac{\partial v_z}{\partial z} \right) = -\frac{\partial p}{\partial z} + \mu \left( \frac{\partial^2 v_z}{\partial x^2} + \frac{\partial^2 v_z}{\partial y^2} + \frac{\partial^2 v_z}{\partial z^2} \right) + \rho g_z, \quad (5)$$

where  $v_x, v_y, v_z$  are three velocity components,  $p$  is the pressure,  $g$  is the gravitational accelerator and  $t$  is the time.

The Navier-Stokes equations in terms of stress tensor  $\tau$  are:

$$\rho \left( \frac{\partial v_x}{\partial t} + v_x \frac{\partial v_x}{\partial x} + v_y \frac{\partial v_x}{\partial y} + v_z \frac{\partial v_x}{\partial z} \right) = -\frac{\partial p}{\partial x} - \mu \left( \frac{\partial \tau_{xx}}{\partial x} + \frac{\partial \tau_{xy}}{\partial y} + \frac{\partial \tau_{zx}}{\partial z} \right) + \rho g_x, \quad (6)$$

$$\rho \left( \frac{\partial v_y}{\partial t} + v_x \frac{\partial v_y}{\partial x} + v_y \frac{\partial v_y}{\partial y} + v_z \frac{\partial v_y}{\partial z} \right) = -\frac{\partial p}{\partial y} - \mu \left( \frac{\partial \tau_{xy}}{\partial x} + \frac{\partial \tau_{yy}}{\partial y} + \frac{\partial \tau_{zy}}{\partial z} \right) + \rho g_y, \quad (7)$$

$$\rho \left( \frac{\partial v_z}{\partial t} + v_x \frac{\partial v_z}{\partial x} + v_y \frac{\partial v_z}{\partial y} + v_z \frac{\partial v_z}{\partial z} \right) = -\frac{\partial p}{\partial z} - \mu \left( \frac{\partial \tau_{xz}}{\partial x} + \frac{\partial \tau_{yz}}{\partial y} + \frac{\partial \tau_{zz}}{\partial z} \right) + \rho g_z, \quad (8)$$

In the case of a Newtonian fluid the stress tensor  $\tau$  components are:

$$\tau_{xx} = -\mu \left[ 2 \frac{\partial v_x}{\partial x} - \frac{2}{3} (\nabla \cdot v) \right], \quad (9)$$

$$\tau_{yy} = -\mu \left[ 2 \frac{\partial v_y}{\partial y} - \frac{2}{3} (\nabla \cdot v) \right], \quad (10)$$

$$\tau_{zz} = -\mu \left[ 2 \frac{\partial v_z}{\partial z} - \frac{2}{3} (\nabla \cdot v) \right], \quad (11)$$

$$\tau_{xy} = \tau_{yx} = -\mu \left[ \frac{\partial v_x}{\partial y} + \frac{\partial v_y}{\partial x} \right], \quad (12)$$

$$\tau_{yz} = \tau_{zy} = -\mu \left[ \frac{\partial v_y}{\partial z} + \frac{\partial v_z}{\partial y} \right], \quad (13)$$

$$\tau_{zx} = \tau_{xz} = -\mu \left[ \frac{\partial v_z}{\partial x} + \frac{\partial v_x}{\partial z} \right], \quad (14)$$

where  $(\nabla \cdot v) = \frac{\partial v_x}{\partial x} + \frac{\partial v_y}{\partial y} + \frac{\partial v_z}{\partial z}$

The solution of the Navier-Stokes equations is achieved by using the finite element method. The Galerkin method is employed to transform the non-linear differential equations

into a system of linear algebraic equations. The basic idea of this method is to multiply the differential equations by a function of coordinates and impose the condition that the equations are satisfied over a selected domain in a weighted sense.

We consider steady state conditions, and thus the terms  $\frac{\partial v_y}{\partial t}$ ,  $\frac{\partial v_x}{\partial t}$  and  $\frac{\partial v_z}{\partial t}$  are eliminated from main equations. By ignoring the  $g$  forces eqs. 6-8 become:

$$\rho \left( v_x \frac{\partial v_x}{\partial x} + v_y \frac{\partial v_x}{\partial y} + v_z \frac{\partial v_x}{\partial z} \right) = -\frac{\partial p}{\partial x} + \mu \left( \frac{\partial^2 v_x}{\partial x^2} + \frac{\partial^2 v_x}{\partial y^2} + \frac{\partial^2 v_x}{\partial z^2} \right), \quad (15)$$

$$\rho \left( v_x \frac{\partial v_y}{\partial x} + v_y \frac{\partial v_y}{\partial y} + v_z \frac{\partial v_y}{\partial z} \right) = -\frac{\partial p}{\partial y} + \mu \left( \frac{\partial^2 v_y}{\partial x^2} + \frac{\partial^2 v_y}{\partial y^2} + \frac{\partial^2 v_y}{\partial z^2} \right), \quad (16)$$

$$\rho \left( v_x \frac{\partial v_z}{\partial x} + v_y \frac{\partial v_z}{\partial y} + v_z \frac{\partial v_z}{\partial z} \right) = -\frac{\partial p}{\partial z} + \mu \left( \frac{\partial^2 v_z}{\partial x^2} + \frac{\partial^2 v_z}{\partial y^2} + \frac{\partial^2 v_z}{\partial z^2} \right), \quad (17)$$

The 3D model of the artery is discretized into finite elements. We assume that the 3-dimensional fluid flow exists in a rigid and non-deformable domain. The velocity  $v$  is interpolated using the following functions:

$$\bar{v}_x = [\mathbf{N}] \{ \mathbf{v}_x \}, \quad (18)$$

$$\bar{v}_y = [\mathbf{N}] \{ \mathbf{v}_y \}, \quad (19)$$

$$\bar{v}_z = [\mathbf{N}] \{ \mathbf{v}_z \}, \quad (20)$$

where  $N$  are the interpolation functions and  $\{ \mathbf{v}_x \}$ ,  $\{ \mathbf{v}_y \}$  and  $\{ \mathbf{v}_z \}$  represent the approximate nodal velocities in  $x$ ,  $y$ ,  $z$  direction, respectively. The pressure is interpolated in similar way:

$$\bar{p} = [\mathbf{N}] \{ \mathbf{p} \}, \quad (21)$$

where  $\mathbf{p}$  is the nodal pressure.

The Galerkin method is applied by multiplying Equations 18-20 by the interpolation functions:

$$\rho \left( \bar{v}_x \frac{\partial}{\partial x} [\mathbf{N}] \{ \mathbf{v}_x \} + \bar{v}_y \frac{\partial}{\partial y} [\mathbf{N}] \{ \mathbf{v}_x \} + \bar{v}_z \frac{\partial}{\partial z} [\mathbf{N}] \{ \mathbf{v}_x \} \right) = - \frac{\partial}{\partial x} [\mathbf{N}] \{ \mathbf{p} \} + \mu \left( \frac{\partial^2}{\partial x^2} [\mathbf{N}] \{ \mathbf{v}_x \} + \frac{\partial^2}{\partial y^2} [\mathbf{N}] \{ \mathbf{v}_x \} + \frac{\partial^2}{\partial z^2} [\mathbf{N}] \{ \mathbf{v}_x \} \right), \quad (22)$$

$$\rho \left( \bar{v}_x \frac{\partial}{\partial x} [\mathbf{N}] \{ \mathbf{v}_y \} + \bar{v}_y \frac{\partial}{\partial y} [\mathbf{N}] \{ \mathbf{v}_y \} + \bar{v}_z \frac{\partial}{\partial z} [\mathbf{N}] \{ \mathbf{v}_y \} \right) = - \frac{\partial}{\partial y} [\mathbf{N}] \{ \mathbf{p} \} + \mu \left( \frac{\partial^2}{\partial x^2} [\mathbf{N}] \{ \mathbf{v}_y \} + \frac{\partial^2}{\partial y^2} [\mathbf{N}] \{ \mathbf{v}_y \} + \frac{\partial^2}{\partial z^2} [\mathbf{N}] \{ \mathbf{v}_y \} \right), \quad (23)$$

$$\rho \left( \bar{v}_x \frac{\partial}{\partial x} [\mathbf{N}] \{ \mathbf{v}_z \} + \bar{v}_y \frac{\partial}{\partial y} [\mathbf{N}] \{ \mathbf{v}_z \} + \bar{v}_z \frac{\partial}{\partial z} [\mathbf{N}] \{ \mathbf{v}_z \} \right) = - \frac{\partial}{\partial z} [\mathbf{N}] \{ \mathbf{p} \} + \mu \left( \frac{\partial^2}{\partial x^2} [\mathbf{N}] \{ \mathbf{v}_z \} + \frac{\partial^2}{\partial y^2} [\mathbf{N}] \{ \mathbf{v}_z \} + \frac{\partial^2}{\partial z^2} [\mathbf{N}] \{ \mathbf{v}_z \} \right), \quad (24)$$

In matrix form Equations 22-24 are:

$$\mathbf{M}\mathbf{v} + \mathbf{K}_{vv}\mathbf{v} + \mathbf{K}_{vp}\mathbf{p} = \mathbf{F}_v, \quad (25)$$

which is the Navier-Stokes equations for a finite element. Also, the Gauss theorem is used for the integration. Here  $\mathbf{v}$  is the nodal vector of blood velocity. Also:

$$[M_{KJ}]_{ii} = \int_V \rho N_K N_J dV. \quad (26)$$

The capitals represent the nodal number and the small the system coordinates  $x, y, z$ .  $V$  is the volume of the element.

$$[(\mathbf{K}_{vv})_{KJ}]_{ii} = [\hat{K}_{KJ}]_{ii} + [K_{\mu KJ}]_{ii}, \quad (27)$$

with

$$[K_{\mu KJ}]_{ii} = \int_V \mu N_{K,j} N_{J,j} dV. \quad (28)$$

Also, the nodal force vector is equal to:

$$(\mathbf{F}_v)_{Ki} = \int_V N_K f_i^v dV + \int_S N_K (-p \delta_{ij} + \mu v_{i,j}) n_j dS. \quad (29)$$

The weak form of the continuity equation arises multiplying by the interpolation function  $\hat{N}_K$  as:

$$\left( \int_V \hat{N}_K N_{J,j} dV \right) v_j^J = 0, \text{ or } \mathbf{K}_{vp}^T \mathbf{v} = 0, \quad (30)$$

$$\text{where } \left[ (\mathbf{K}_{vp})_{KJ} \right]_{ii} = - \int_V N_{K,i} \hat{N}_j dV \quad (31)$$

Equations 25 and 31 represent the system of Finite Element equations. The system is non-linear so the solution requires an iterative scheme. For a time step  $n$  the following iterative form is used:

$$\begin{bmatrix} \frac{1}{\Delta t} \mathbf{M} + {}^{n+1}\tilde{\mathbf{K}}_{nn}^{(i-1)} & \mathbf{K}_{vp} \\ \mathbf{K}_{vp}^T & \mathbf{0} \end{bmatrix} \begin{Bmatrix} \Delta \mathbf{v}^{(i)} \\ \Delta \mathbf{P}^{(i)} \end{Bmatrix} = \begin{Bmatrix} {}^{n+1}\mathbf{F}_{ext}^{(i-1)} \\ \mathbf{0} \end{Bmatrix} - \begin{bmatrix} \frac{1}{\Delta t} \mathbf{M} + {}^{n+1}\mathbf{K}_{nn}^{(i-1)} & \mathbf{K}_{vp} \\ \mathbf{K}_{vp}^T & \mathbf{0} \end{bmatrix} \begin{Bmatrix} {}^{n+1}\mathbf{v}^{(i-1)} \\ {}^{n+1}\mathbf{P}^{(i-1)} \end{Bmatrix} + \begin{Bmatrix} \frac{1}{\Delta t} \mathbf{M}^n \mathbf{v} \\ \mathbf{0} \end{Bmatrix}, \quad (32)$$

with

$$\left[ {}^{n+1}(\tilde{\mathbf{K}}_{nn}^{(i-1)})_{KJ} \right]_{ik} = \left[ {}^{n+1}K_{KJ}^{(i-1)} \right]_{ii} + \left[ {}^{n+1}K_{KJ}^{(i-1)} \right]_{ik} \quad (33)$$

$$\left[ {}^{n+1}K_{KJ}^{(i-1)} \right]_{ik} = \rho \int_V N_K^{n+1} v_{i,k}^{(i-1)} N_J dV \quad (34)$$

The iterations stop when the norm of the incremental vector of the left-hand side, or the norm of the right-hand side is smaller than a selected error tolerance.

The aforementioned formulation is applied in cases of rigid walls. When dealing with deformable walls, it is crucial to determine the stress-strain rate in the arterial wall, as well as, the effects of the deformation of the arterial wall on the characteristics of blood flow. The blood vessel tissue has complex mechanical characteristics, which are almost impossible to define with accuracy. Various material models can be used to model the arterial tissue, from linear elastic to non-linear viscoelastic. In this section, a summary of the governing finite element equations that are used to model the arterial wall deformation, is presented. Emphasis is given on the implementation of non-linear models.

The finite element equation of balance of linear momentum derives from the fundamental differential equations of balance of forces that act on an elementary material volume. In a dynamic analysis, the inertial forces are included in this equation. Subsequently,

by applying the principle of virtual work, the differential equations of motion of a finite element are obtained and defined as:

$$\mathbf{M}\ddot{\mathbf{U}} + \mathbf{B}^w\dot{\mathbf{U}} + \mathbf{K}\mathbf{U} = \mathbf{F}^{ext} \quad (35)$$

where  $\mathbf{M}$  is the mass matrix,  $\mathbf{B}^w$  is the damping matrix in cases where the material has a viscous resistance,  $\mathbf{K}$  is the stiffness matrix and  $\mathbf{F}^{ext}$  is the external nodal force that includes the body and the surface forces that act on the element. Equation 35 is then transformed to the following dynamic differential equation of motion:

$$\mathbf{M}_{sys}\ddot{\mathbf{U}}_{sys} + \mathbf{B}_{sys}^w\dot{\mathbf{U}}_{sys} + \mathbf{K}_{sys}\mathbf{U}_{sys} = \mathbf{F}_{sys}^{ext} \quad (36)$$

where  $\mathbf{M}_{sys}$ ,  $\mathbf{B}_{sys}^w$ ,  $\mathbf{K}_{sys}$  are the mass, damping and stiffness matrices of the system and  $\mathbf{F}_{sys}^{ext}$  is the system external force vector, which includes the external surface and body forces, respectively. Equation 36 can be further integrated with a selected time step size  $\Delta t$  and the nodal displacements  $^{n+1}\mathbf{U}$  at the end of the time step are finally obtained:

$$\hat{\mathbf{K}}_{tissue}^{n+1}\mathbf{U} = {}^{n+1}\hat{\mathbf{F}} \quad (37)$$

where  $\hat{\mathbf{K}}_{tissue}$  is the tissue stiffness matrix. This equation is obtained by assuming that the problem is linear, with small displacements, a constant viscous resistance and a linear elastic material regarding the arterial wall.

In cases where the arterial wall displacements due to blood flow are large, the problem becomes geometrically non-linear. Moreover, the tissue of blood vessels has non-linear constitutive laws, which lead to a non-linear Finite Element formulation regarding the tissue material. In such cases, we have the following incremental-iterative equation:

$${}^{n+1}\hat{\mathbf{K}}_{tissue}^{(i-1)}\Delta\mathbf{U}^{(i)} = {}^{n+1}\hat{\mathbf{F}}^{(i-1)} - {}^{n+1}\mathbf{F}^{int(i-1)} \quad (38)$$

where  $\Delta\mathbf{U}^{(i)}$  are the nodal displacement increments for iteration 'i', and the system matrix  ${}^{n+1}\hat{\mathbf{K}}_{tissue}^{(i-1)}$ , the vector of internal forces  ${}^{n+1}\mathbf{F}^{int(i-1)}$  and the force vector  ${}^{n+1}\hat{\mathbf{F}}^{(i-1)}$  correspond to the previous iteration. The geometrically linear part of the stiffness matrix  $({}^{n+1}\mathbf{K}_L)_{tissue}^{(i-1)}$  and the nodal force vector  ${}^{n+1}\mathbf{F}^{int(i-1)}$  are defined as:

$$({}^{n+1}\mathbf{K}_L)_{tissue}^{(i-1)} = \int_V \mathbf{B}_L^T {}^{n+1}\mathbf{C}_{tissue}^{(i-1)} \mathbf{B}_L dV, \quad ({}^{n+1}\mathbf{F}^{int})^{(i-1)} = \int_V \mathbf{B}_L^T {}^{n+1}\boldsymbol{\sigma}^{(i-1)} dV \quad (39)$$

where  ${}^{n+1}\mathbf{C}_{tissue}^{(i-1)}$  is the consistent tangent constitutive matrix of the tissue and the stresses at the end of time step  ${}^{n+1}\boldsymbol{\sigma}^{(i-1)}$ . The aforementioned matrix depends on the material model that is used for the arterial tissue.

The overall strategy that is used for the FSI simulations is based on the loose coupling approach and consists of the following steps:

- a) Determination of the blood flow for the current geometry. The wall velocities at the common interface of the wall and the blood domain are used as a boundary condition for the fluid domain.
- b) Calculation of the loads that are caused by the blood and act on the arterial wall.
- c) Definition of the deformation of the arterial wall that is caused by the blood flow.
- d) If a convergence of both domains is reached, the next step is implemented, otherwise we return to step (a).
- e) The fluid domain geometry and velocities at the common interface are updated for the next time step.

### 3.3. Blood flow simulations on arteries with rigid or deformable walls

It is a common fact that blood flow simulations that are carried out under the rigid wall assumption are generally faster and require far less computational resources than the ones carried out using fluid structure interaction techniques. However, the resulting values of important hemodynamic factors such as pressures or endothelial shear stress are questionable when compared to the FSI derived ones, since FSI simulations are considered to be more analytical and closer to the actual biological problem. In this section, a comparison study between the two types of simulations on two patient-specific coronary arteries is presented. Results on WSS distributions as well as areas of low WSS are obtained in order to demonstrate the advantages and disadvantages of the two methods.

#### 3.3.1 Rigid walls assumption

We assume that the flow is laminar and incompressible and the blood is modelled as a Newtonian fluid. Blood flow is modelled using the Navier-Stokes and the continuity equations:

$$\rho \frac{\partial \mathbf{v}}{\partial t} + \rho(\mathbf{v} \bullet \nabla) \mathbf{v} - \nabla \bullet \boldsymbol{\tau} = \mathbf{f}^v \quad (40)$$



$$\nabla \bullet (\rho \mathbf{v}) = 0 \quad (41)$$

where  $\mathbf{v}$  is the blood velocity vector,  $\boldsymbol{\tau}$  is the stress tensor and  $\mathbf{f}^B$  are the total body forces. The stress tensor is defined as:

$$\boldsymbol{\tau} = -p\delta_{ij} + 2\mu\epsilon_{ij}, \quad (42)$$

where  $\delta_{ij}$  is the Kronecker delta,  $\mu$  is the blood dynamic viscosity,  $p$  is the blood pressure and  $\epsilon_{ij}$  is the strain tensor which is defined as:

$$\epsilon_{ij} = \frac{1}{2}(\nabla \mathbf{v} + \nabla \mathbf{v}^T), \quad (43)$$

A full cardiac cycle of 0.8 sec and 0.75 sec is simulated for the two arterial models, respectively. A period of 0.05 sec is chosen for each simulation comprising a set of 17 timesteps for the first artery and 16 timesteps for the second artery. Regarding the fluid domain in both types of simulations, the same set of boundary conditions is applied. At the inlet, a flow velocity profile is applied for the first arterial model whereas a volumetric flow rate profile is applied for the second one as a boundary condition. At the outlet, a blood pressure profile is applied for both arteries. Finally, no-slip wall boundary condition is applied for both arteries.

### 3.3.2 Fluid Structure Interaction simulations

In FSI simulations, the blood domain is deformable. Therefore, the equation of momentum conservation is used:

$$\rho \frac{\partial \mathbf{v}}{\partial t} + \rho((\mathbf{v} - \mathbf{w}) \bullet \nabla) \mathbf{v} - \nabla \bullet \boldsymbol{\tau} = \mathbf{f}^B, \quad (44)$$

where  $\rho$  is the blood density,  $\mathbf{v}$  is the blood velocity vector,  $\mathbf{w}$  is the moving mesh velocity vector,  $\boldsymbol{\tau}$  is the stress tensor and  $\mathbf{f}^B$  are the total body forces. The stress tensor is described above.

In our simulations, blood was treated as Newtonian fluid with a density  $\rho=1060 \text{ kg/m}^3$  and dynamic viscosity  $\mu=0.0035 \text{ Pa s}$ .

Regarding the arterial wall domain, the following momentum conservation equation is used:

$$\nabla \boldsymbol{\tau}_s + \mathbf{f}_s^B = \rho_s \ddot{\mathbf{d}}_s, \quad (45)$$

where  $\boldsymbol{\tau}_s$  is the arterial wall stress tensor,  $\mathbf{f}_s^B$  are the body forces per unit volume,  $\rho_s$  is the arterial wall density and  $\ddot{\mathbf{d}}_s$  is the local acceleration of the solid.

The fluid and the solid domain are coupled together through displacement compatibility and traction equilibrium as it is shown in the following equations:

$$\boldsymbol{\tau}_s \bullet \hat{\mathbf{n}}_s = \boldsymbol{\tau}_f \bullet \hat{\mathbf{n}}_f \quad (x, y, z) \in \Gamma_{FSI}^S \cap \Gamma_{FSI}^F, \quad (46)$$

$$\mathbf{d}_s = \mathbf{d}_f \quad (x, y, z) \in \Gamma_{FSI}^S \cap \Gamma_{FSI}^F. \quad (47)$$

where  $\Gamma_{FSI}^S$  is a group of points on the arterial wall and  $\Gamma_{FSI}^F$  is a group of points on the lumen. Eq. (46) shows that the solid and the fluid stresses acting on the common surface of the two domains are in equilibrium, whereas Eq. (47) shows that the common surfaces of the two domains have the same displacements.

Due to the lack of universal values for the parameters of the material properties of the arterial wall, we have used a nine- parameter Mooney-Rivlin model to describe the material properties of the wall. Despite the fact that the coronary arterial wall is considered to have an anisotropic and heterogeneous structure due to the complex composition (e.g., collagen fibers), we applied an isotropic and homogenous material model because of the absence of *in vivo* data regarding the fiber direction and the heterogeneity that describes the anisotropic behavior of the arterial tissue. The parameters of the Mooney-Rivlin model were set as previously described in FSI analyses in the human right coronary artery. The following equation is used to calculate the strain energy function [15]:

$$\begin{aligned} W = & c_{10}(\bar{I}_1 - 3) + c_{01}(\bar{I}_2 - 3) + c_{20}(\bar{I}_1 - 3)^2 + c_{11}(\bar{I}_1 - 3)(\bar{I}_2 - 3) \\ & + c_{02}(\bar{I}_2 - 3)^2 + c_{30}(\bar{I}_1 - 3)^3 + c_{21}(\bar{I}_1 - 3)^2(\bar{I}_2 - 3), \\ & + c_{12}(\bar{I}_1 - 3)(\bar{I}_2 - 3) + c_{03}(\bar{I}_2 - 3)^3 + \frac{1}{d}(J - 1)^2. \end{aligned} \quad (48)$$

where  $\bar{I}_1$  is the first deviatoric strain invariant,  $\bar{I}_2$  is the second deviatoric invariant and  $J$  is the determinant of the elastic deformation gradient tensor. The other parameters are set as  $c_{10}=0.07$  MPa,  $c_{20}=3.2$  MPa,  $c_{21}=0.0716$  MPa whereas the rest are set equal to zero, as calculated in an FSI analysis of a human RCA by Koshiba *et al* [16].  $d$  is the compressibility parameter which is calculated as:

$$d = \frac{2}{K}, \quad (49)$$

where K is the bulk modulus which is set equal to  $1 \times 10^{-5}$ .

Again, the applied boundary conditions for the fluid domain are the same as in the rigid walls simulations whereas, for the wall domain, the distal ends of both arteries are assumed as fixed supports to restrict motion at these points (Figure 15).

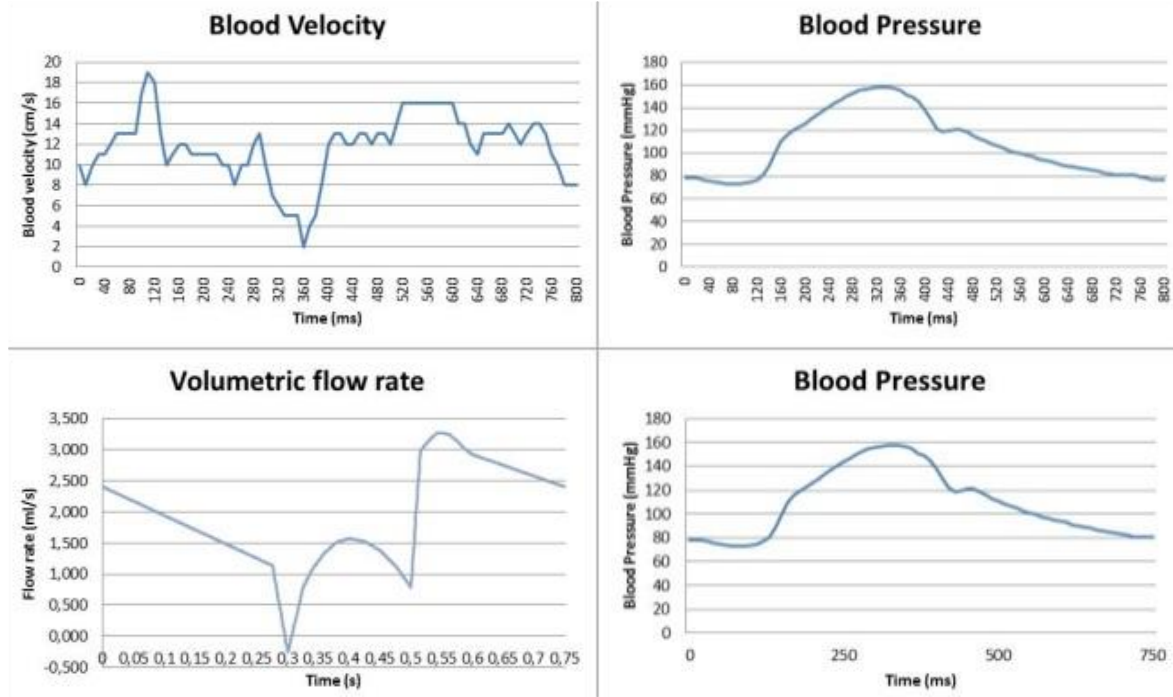


Figure 15: The top row images depict the inlet and outlet boundary conditions for the first arterial model, whereas the bottom row images depict the boundary conditions for the second one, respectively.

### 3.3.3 Dataset

Two patient-specific coronary arteries reconstructed from IVUS and biplane angiography images are used. Two 3D models are generated from each artery, one representing the lumen and one representing the arterial wall. The generated models are then discretized. In order to define the mesh size, we performed a sensitivity analysis to identify which mesh size values achieve accurate results in the best possible simulation time. The two lumen models are discretized into 200000 hexahedral elements, whereas the two wall models are discretized into 275000 tetrahedral elements.

### 3.3.4 Results

We performed transient simulations on both arteries producing results on average WSS as well as areas of low WSS. We finally performed a regression analysis to see how the results of the two methods correlate. The two methods presented strong correlation, thus indicating the efficacy of the simpler method. The areas of low WSS were similar, presenting a Pearson correlation coefficient of 0.99. Regarding the average WSS throughout the vessel, strong correlation was also found ( $r=0.9$ ).

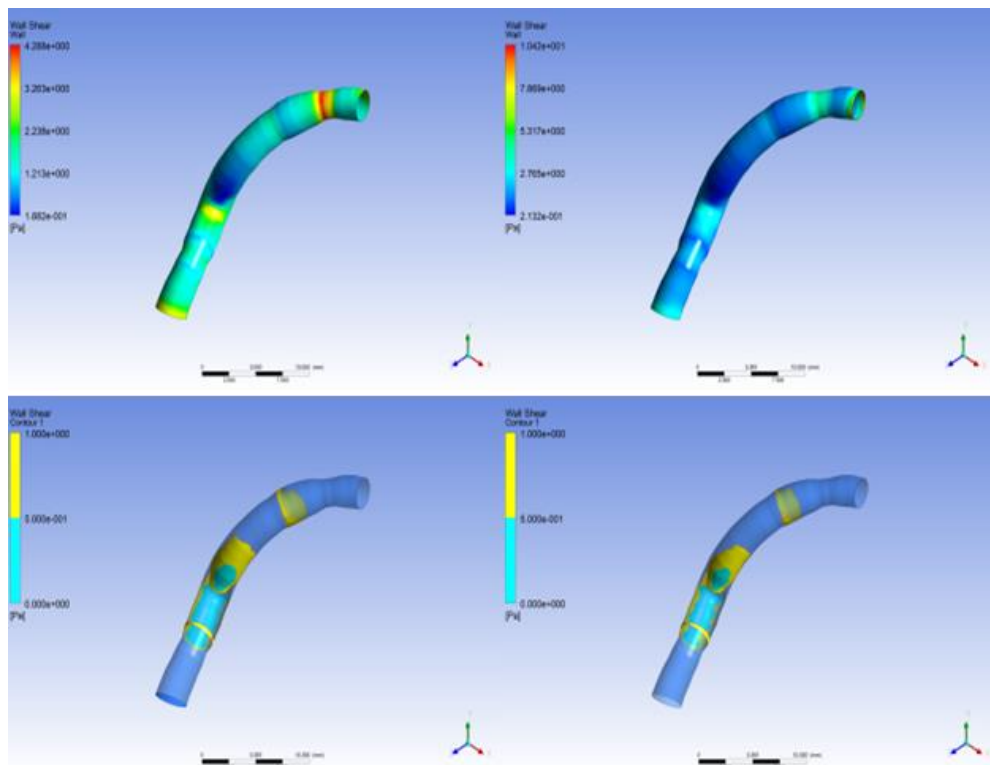


Figure 16: Calculated WSS distribution for the FSI (top left) and rigid wall (top right) simulations. Areas of low WSS (0-1 Pa) for the FSI (bottom left) and rigid wall (bottom right) simulations (Arterial Model 1).

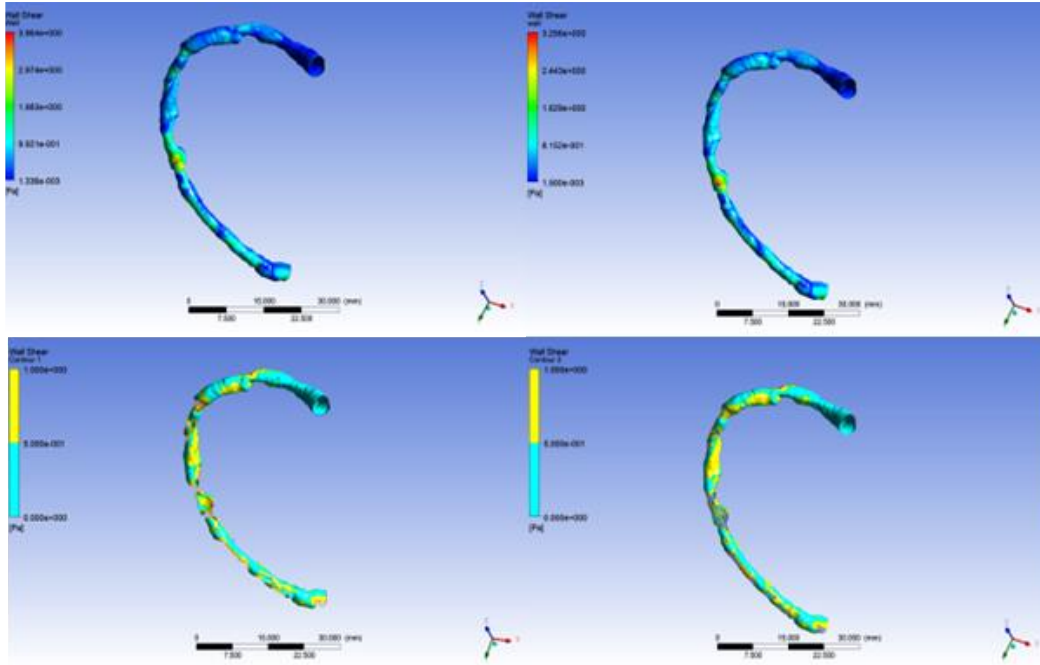


Figure 17: Calculated WSS distribution for the FSI (top left) and rigid wall (top right) simulations. Areas of low WSS (0-1 Pa) for the FSI (bottom left) and rigid wall (bottom right) simulations (Arterial Model 2).

### 3.3.5 Discussion

We model blood flow in arteries with rigid and deformable walls in order to examine if the produced results are comparable. We assume a hyperelastic arterial wall model, which accurately simulates the arterial wall. The comparison of the two methods reveals a surprisingly good agreement between the results on the average WSS. However, we must note that this comparison is made on arterial segments of a certain length following the boundary conditions, which have been produced by experimental work and are described above. In particular, Figure 16 and Figure 17 depict the WSS distribution on both arterial models during the systolic phase of the cardiac cycle. From the obtained results, we observe that WSS distribution is very similar for both types of simulation. Furthermore, the areas of low WSS, which have a high clinical value due to their complication to atherosclerotic plaque development, are both qualitatively and quantitatively similar. Comparing the average WSS for every timestep, we calculated a correlation coefficient of 0.9 for both cases, respectively. Moreover, the correlation coefficient is increased for the case of the region of low WSS, as it is 0.998 and 0.999 for the two case studies.

It should be noted that, in contrast to the similar simulation results, the computational time between the simulation with rigid walls and the one with deformable walls is evidently different. In particular, while the time required for the simulation with rigid walls is approximately 30-40 minutes, the computational time for the FSI simulation is almost 5 hours for the same mesh for the blood fluid domain and an adequate mesh size for the wall domain. All simulations were carried out on an HP Workstation with a Xeon E5405 quad-core CPU and 8 GB of RAM.

However, FSI analyses have the advantage that they are considered to be more accurate and realistic since they incorporate the interaction between the blood and the wall domain. Moreover, as future work, the material characteristics of the atherosclerotic plaque will be incorporated into the arterial wall domain, making thus FSI simulations even more accurate and realistic.

Concluding, the calculated WSS distributions are evidently similar. Keeping in mind the required computational time, FSI simulations can be used when the displacement of the arterial wall is required for important clinical decisions. In cases where speed is crucial for the clinician, blood flow with rigid wall can produce accurate results regarding the WSS distribution. However, further investigation of arterial wall mechanics and their relation to atherosclerosis must be performed.

### **3.4. Patient-Specific Simulation of Coronary Artery Pressure Measurements**

Pressure measurements using finite element computations without the need of a wire could be valuable in clinical practice. Critical hemodynamic indices such as FFR are of utmost importance in the clinical field. Several studies which attempt to calculate with high accuracy such hemodynamic parameters have been reported in the literature. In this section, we present a validation study for coronary artery pressure measurements using patient-specific 3D coronary artery reconstructions and investigate (a) the accuracy of the computed pressure results using the invasive pressure measurements as the gold standard and (b) the differences in computed pressure measurements between different critical boundary conditions (steady versus pulsatile flow and rigid wall versus FSI).

### 3.4.1 Patient Data

Six subjects underwent intravascular ultrasound (IVUS) and angiography examinations for angina symptoms at CNR (Institute of Clinical Physiology, Milan, Italy). The clinical and demographic patient characteristics are presented in Table 4. A coronary guide wire (0.014-inch diameter) with miniaturized tip transducers for pressure and flow measurements (Combo wire, Volcano Corp.) was used. The pressure-flow wire was inserted in the coronary artery until a stable recording of the flow velocity was obtained at a distal coronary location. The aforementioned parameters were measured at the baseline and during maximal coronary vasodilation (hyperemic conditions) which was achieved with the intravenous administration of adenosine (140 mcg/kg/min). The parameters measured under hyperemic conditions were used as boundary conditions for the simulations and are described in detail below. The final measurements included pressure values throughout three cardiac cycles at the proximal (guiding catheter at the ostium of the artery) and distal locations of each arterial segment, combined with flow velocity values at the distal location both at baseline and during maximal hyperemia. A 3- French catheter with a 64-crystal electronic ultrasound probe was used for IVUS examination (Eagle-Eye, Volcano Corp.). The catheter was placed in the distal part of the examined vessel and then a motorized pullback (speed 1mm/sec) was performed. Following contrast injection, two isocentric angiographic views were obtained to depict the position of the catheter inside the vessel before the start of the pullback. The IVUS probe was positioned distally at the same location where the distal coronary pressure-flow measurements were performed so that these measurements could be applied as boundary conditions for the blood flow simulations in 3D reconstructed arterial models as it is described below. Figure 18 shows the angiographic images with the exact locations of the acquired measurements for the right coronary artery of patient 4.

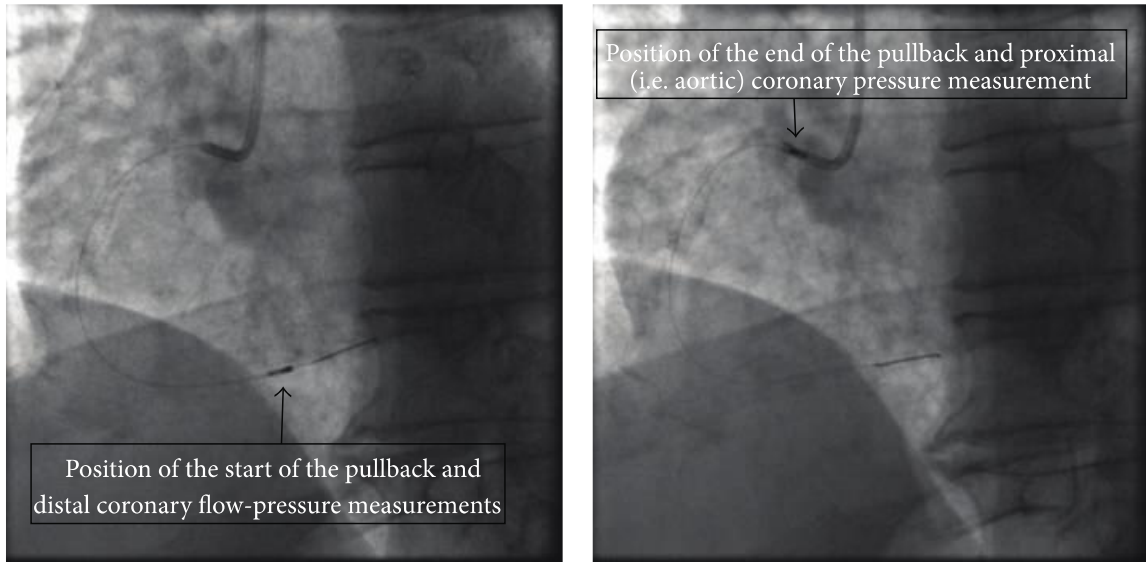


Figure 18: The two views depict the exact locations of the start (a) and end (b) of the pullback procedure as well as the exact positions of the pressure and flow measurements acquisition.

### 3.4.2 3-dimensional Reconstruction

The 3D reconstruction of the 8 arterial segments was performed using a methodology which is based on the fusion of IVUS and biplane angiographic data [100]. The end-diastolic frames were selected for segmenting the lumen and the external elastic media (i.e., vessel wall) borders. Then, the corresponding angiographic end-diastolic images were used to reconstruct the 3D IVUS catheter path. The segmented frames were then placed onto the generated 3D catheter path and were appropriately oriented. Finally, two point clouds representing the lumen and vessel wall were derived for each artery and were processed to non-uniform rational B-spline (NURBS) 3D surfaces. Figure 19 depicts two 3D reconstructed models of two RCA segments. Our dataset includes 4 RCA and 4 LAD segments with mild or moderate lumen stenoses.



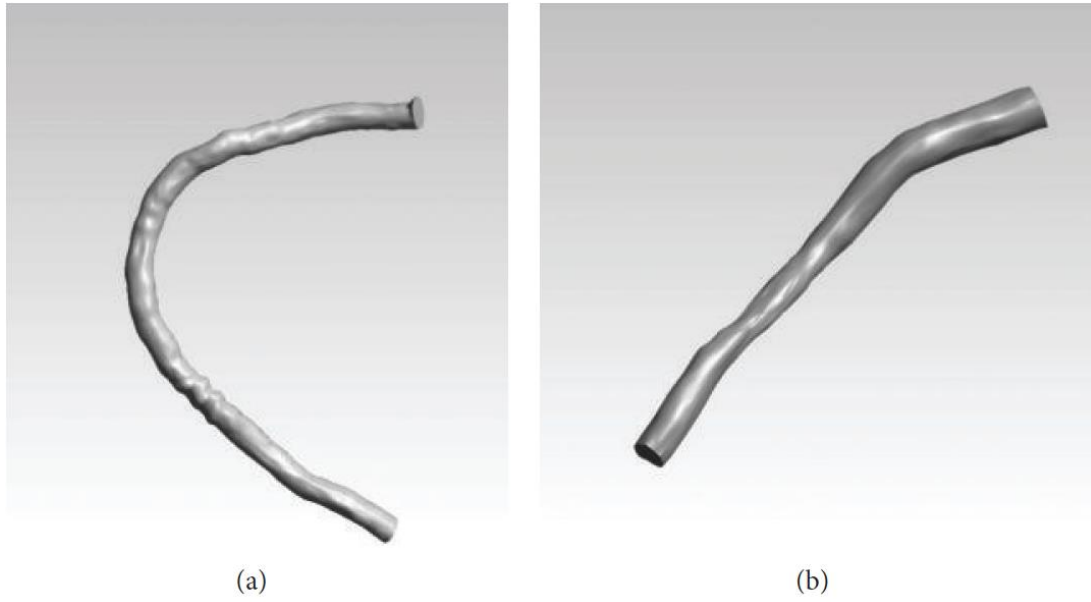


Figure 19: Three-dimensional reconstruction of the lumen of a right coronary artery for patient #2 (a) and patient #1 (b).

Table 4: Patient demographic and Clinical Characteristics

Patient	Age	Sex	Familiarity	Hypertension	Hypercholesterolemia	Diabetes	Angina
01	73	M	N	Y	Y	Y	N
02	55	M	N	Y	Y	N	Y
03	56	M	Y	Y	Y	Y	N
04	56	M	N	Y	Y	Y	N
05	70	M	Y	Y	Y	N	N
06	75	M	N	Y	Y	N	N

### 3.4.3 Blood Flow Simulations

Transient as well as steady flow simulations were carried out on all 8 arterial segments with either rigid or deformable wall assumptions. In total, four different approaches were used: FSI-transient, FSI-steady flow, rigid walls-transient and rigid walls-steady flow. The most demanding in terms of computational resources is the one using FSI models with transient flow as it is time dependent, whereas the lowest computational requirements are for the one with the rigid walls assumption and the steady flow. The boundary conditions are presented below. Blood was treated as a Newtonian fluid having a density of  $1060 \text{ kg/m}^3$  and a dynamic viscosity  $0.0035 \text{ Pa} \cdot \text{s}$ . The blood flow was considered laminar with the Reynolds number ranging between 126 and 883.

### 3.4.4 Boundary Conditions

#### i. Inlet

Regarding the inlet, a measured pressure profile in the catheterization laboratory was applied as a boundary condition. In particular, for the transient simulations, a full cardiac cycle (either the second or the third measured in order for the measurements to be stable and accurate) was divided into time steps of 0.05 seconds (Figure 20 exhibits the applied inlet pressure profile for patient 6), while for the steady flow simulations, the mean pressure value of the same cardiac cycle that was used in the transient ones was applied as the inlet boundary condition.

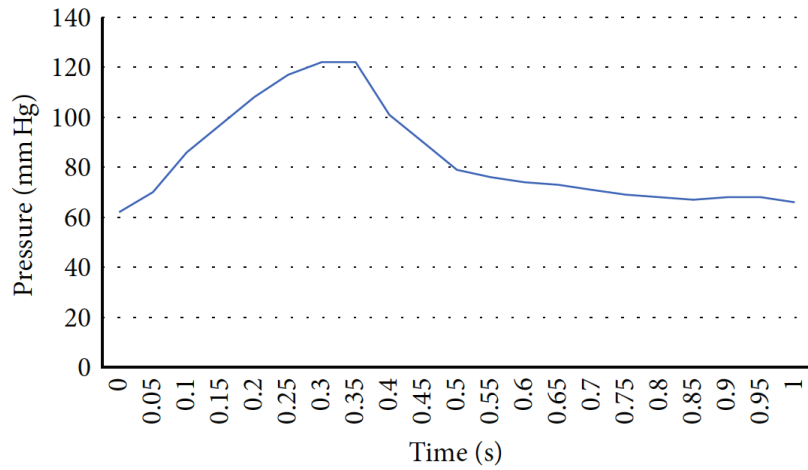


Figure 20: Measured pressure profile for patient #6 for a full cardiac cycle.

#### ii. Outlet

Velocity profiles were available at the distal end of the reconstructed artery (measured invasively using the combo pressure-flow wire) and were prescribed as outlet boundary conditions. To capture the true nature of the velocity profile of the outlet, we used the developed flow (this has a paraboloid profile) derived from the 3D geometry and we defined the “magnitude” of the developed flow according to the flow measurements. To achieve that, we applied the mass flow rate profile for each case, which was calculated as:

$$\dot{m} = \rho \mathbf{v} A \quad (50)$$

where  $\rho$  is the blood’s density,  $\mathbf{v}$  is the velocity of blood, and  $A$  is the cross-sectional area of the outlet. However, due to the nature of the Doppler wire measurements, we executed a parametric

study regarding the accuracy of the measured velocity values. The measured velocity values from the wire cannot be considered to be the highest of the cross-section due to the fact that either the wire is not aligned in the centre of the vessel or due to the fact that the wire itself interrupts the flow. The velocity value that is inserted in the mass flow rate equation is the mean velocity value of the profile. We tried three different velocity profiles to examine which fits our problem best. In the first case scenario, the measured values from the Doppler wire as the mean profile value were used; in the second scenario a ratio of 0.76 ( $v_{\text{mean}} = 0.76 * v_{\text{measured}}$ ) as it was previously suggested [101]; and in the third scenario a ratio of 0.5 which is common in the generalized Poiseuille flow. Figure 21 depicts the velocity profiles of the three cases for an RCA segment of patient 1. The closest results to the measured values were achieved by using the measured velocity values as the mean value of the profile. The results of the parametric study are presented in detail below.

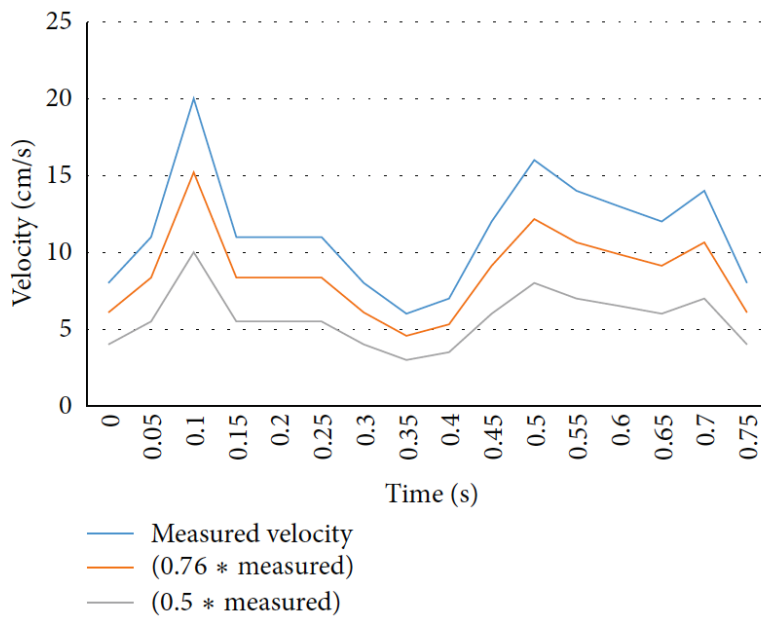


Figure 21: Mean velocity values calculated for patient #1 in order to determine the optimal velocity profile for validation.

### iii. Lumen-Wall Interface

At the lumen wall, a no-slip boundary condition was applied, meaning that the blood had zero velocity relative to the solid-fluid interface.

#### iv. Arterial Wall

The distal ends of the arterial wall (inlet and outlet) were assumed to be fixed on all directions so that motion was restricted at these sites.

#### v. Mesh

The lumen was discretized into hexahedral elements, with an element face size ranging from 0.09 to 0.12mm, with an increased mesh density throughout the boundary layer of the flow close to the arterial wall. The arterial wall was discretized into tetrahedral elements with an element face size 0.09 mm and 15 layers of brick elements with a thickness of 0.03 mm at the interface with the lumen. The brick element layers were first generated from the interface of the wall and the lumen towards the outer perimeter of the wall and then the remaining volume was discretized into tetrahedral elements.

The mesh size both for the lumen and the wall was selected after performing a mesh (face size) sensitivity analysis. The sensitivity analysis was performed in a representative case both for the rigid (Table 5) and deformable (Table 6) wall assumption using steady-state flow. The mesh sensitivity analysis for the deformable wall simulation (Table 6) was performed using a face size of 0.09–0.12 mm for the lumen (as derived from the initial sensitivity analysis for the rigid wall assumption in Table 5). The analysis was based on the correlation between the mesh size and the produced results regarding the average wall shear stress of the same cross-section on 4 different mesh sizes. The mesh size with <5% difference in wall shear stress values was used in the final simulations; of note, computed pressure values at the outlet, on which we focus in the current study, were also minimally influenced by the mesh size (<0.05% difference, Table 5 and Table 6).

Table 5: Results of the mesh sensitivity analysis in the lumen (rigid wall assumption).

Face size	Lumen mesh size (elements)	Outlet pressure (mm Hg)	Difference in pressure (%)	Cross-sectional WSS (Pa)	Difference in WSS (%)
0.13–0.15 mm	87 K	105.516	0.053	6.31	21.22
0.12–0.15 mm	176 K	105.512	0.049	7.14	10.86
<b>0.09–0.12 mm</b>	<b>400 K</b>	<b>105.483</b>	<b>0.022</b>	<b>7.78</b>	<b>2.87</b>
0.07–0.09 mm	657 K	105.460	—	8.01	—

WSS: wall shear stress.

The selected mesh size for the final simulations is indicated in bold font (<5% difference in WSS).

Table 6: Results of the sensitivity analysis in the deformable wall assumption (lumen face size was 0.09–0.12 mm).

Element size	Wall mesh size (elements)	Outlet pressure (mm Hg)	Difference in pressure (%)	Cross-sectional WSS (Pa)	Difference in WSS (%)
0.13 mm	292 K	105.494	0.048	6.38	21.62
0.10 mm	540 K	105.487	0.042	7.19	11.67
<b>0.09 mm</b>	<b>582 K</b>	<b>105.458</b>	<b>0.014</b>	<b>7.85</b>	<b>3.56</b>
0.07 mm	1.232 M	105.443	—	8.14	—

WSS: wall shear stress.

The selected mesh size for the final simulations is indicated in bold font (<5% difference in WSS).

### 3.4.5 Results

A series of blood flow simulations using different assumptions and approaches was carried out, a linear regression analysis on all 8 vessels was performed, and the respective aggregate Bland-Altman plot was obtained in order to examine the correlation of the computed results to the measured ones.

### 3.4.6 Validation results

We performed transient FSI simulations for one cardiac cycle. The produced results show excellent correlation between the measured and the calculated values with the worst case scenario having a coefficient of determination  $r^2 = 0.8902$  and the best case scenario having an  $r^2 = 0.9961$ . The Bland-Altman plots also depict a high similarity between the measured and the computed values with almost all values being within the  $1.96 \times \text{SD}$  cut-offs. Figures 23-25 depict the pressure waveforms of the measured and the rigid wall computed as well as the FSI computed values and the linear regression analysis plots for all cases. Moreover, Figure 25 represents an aggregate Bland-Altman plot for all 8 cases with a mean difference close to zero.

### 3.4.7 Rigid Wall versus FSI Simulations

The calculated mean difference between the rigid wall and the FSI simulations for all cases reached the statistically negligible value of 0.26%. The rigid wall simulations produced slightly higher-pressure values than the FSI simulations on most of the examined cases. Moreover, compared to the values measured in the catheterization laboratory, and the FSI simulations produced slightly more accurate results than the rigid wall ones. In Table 7, a comparison between the measured and the computed mean outlet pressure values for all cases is presented.

### 3.4.8 Transient versus Steady Flow Simulations

The computed pressure of the steady flow simulation was compared to the average pressure of the same cardiac cycle as it was computed from the transient simulation. Our results demonstrated a very close match between the steady flow and the transient results for both rigid and FSI simulations. In detail, the two simulation types exhibited a mean difference of 0.44% (Table 7). The results that were closest to the measured wire-based values were the ones obtained using the transient simulations as expected. Table 8 demonstrates the results of the parametric study related to the flow velocity values used in the mass flow rate equation for the outlet boundary condition. It seems that the optimal results were obtained when the measured flow velocity values from the combo wire were used as the maximum and not the mean values of the velocity profile.

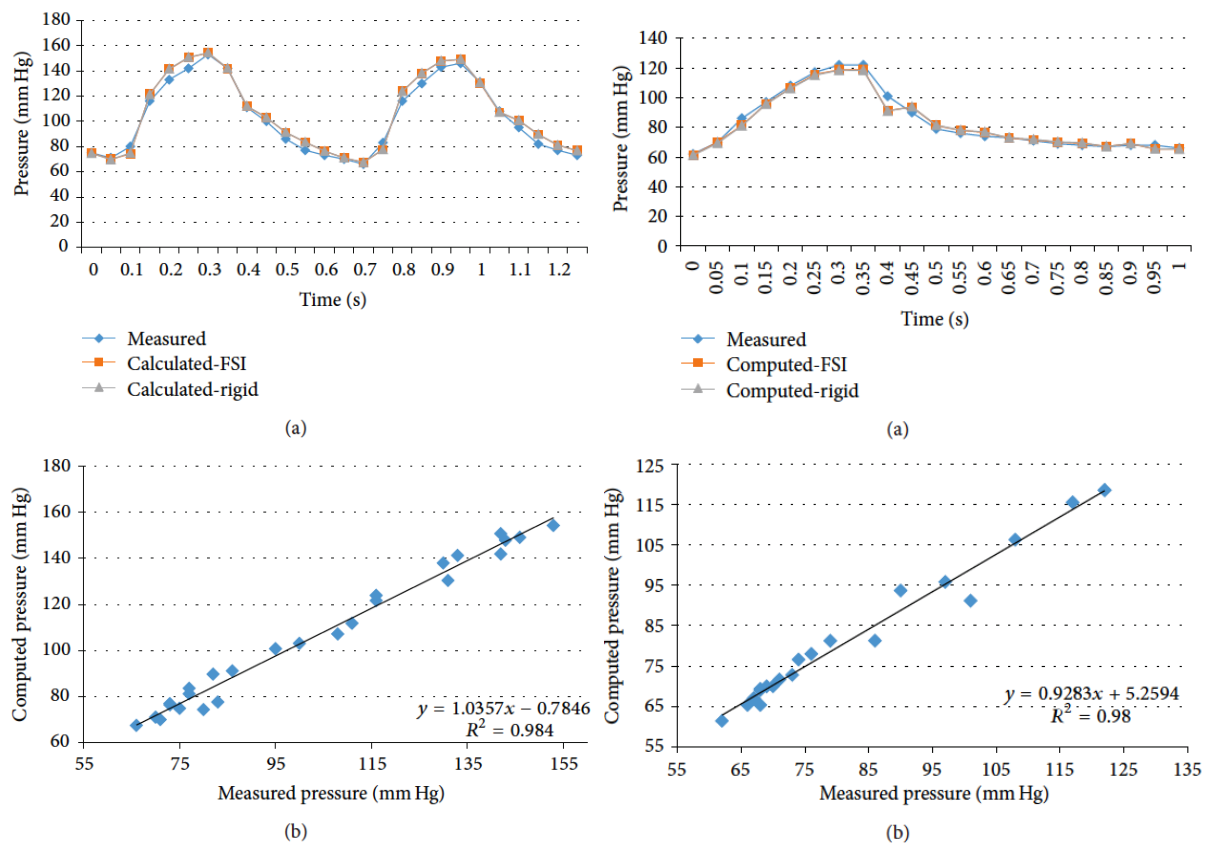


Figure 22: Left image: (a) depicts the pressure waveforms for the examined cardiac cycles (measured and calculated results) and (b) exhibits the linear regression analysis for patient #1. Right image: (a) depicts the pressure waveforms for the examined cardiac cycles (measured and computed results) and (b) exhibits the linear regression analysis for patient #6.

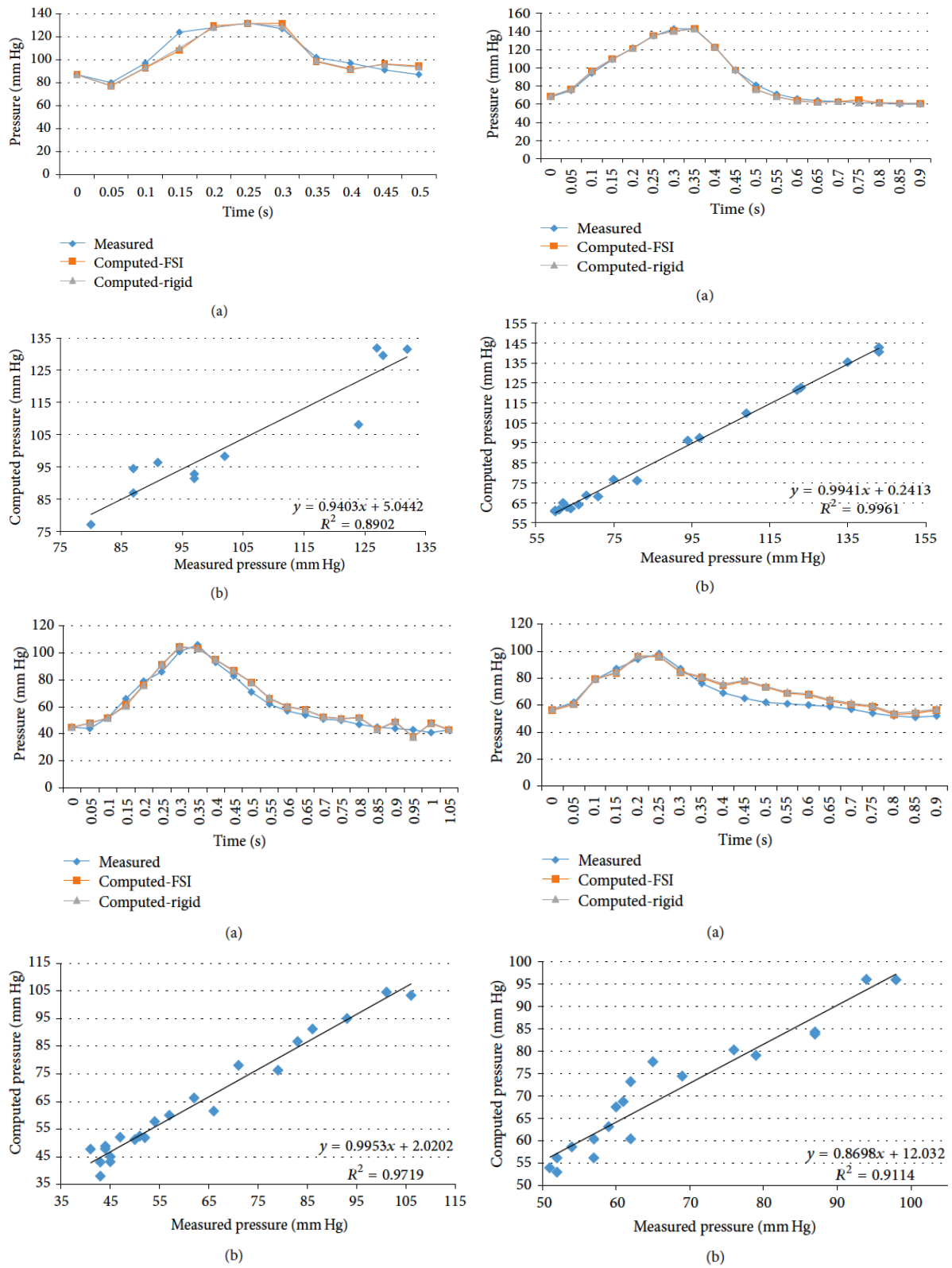


Figure 23: (a) pressure waveforms for the examined cardiac cycles (measured and computed results) and (b) linear regression analysis for patients #2 (upper left image), #3 (upper right image), #4-RCA (lower left image) and #4-LAD (lower right image), respectively.

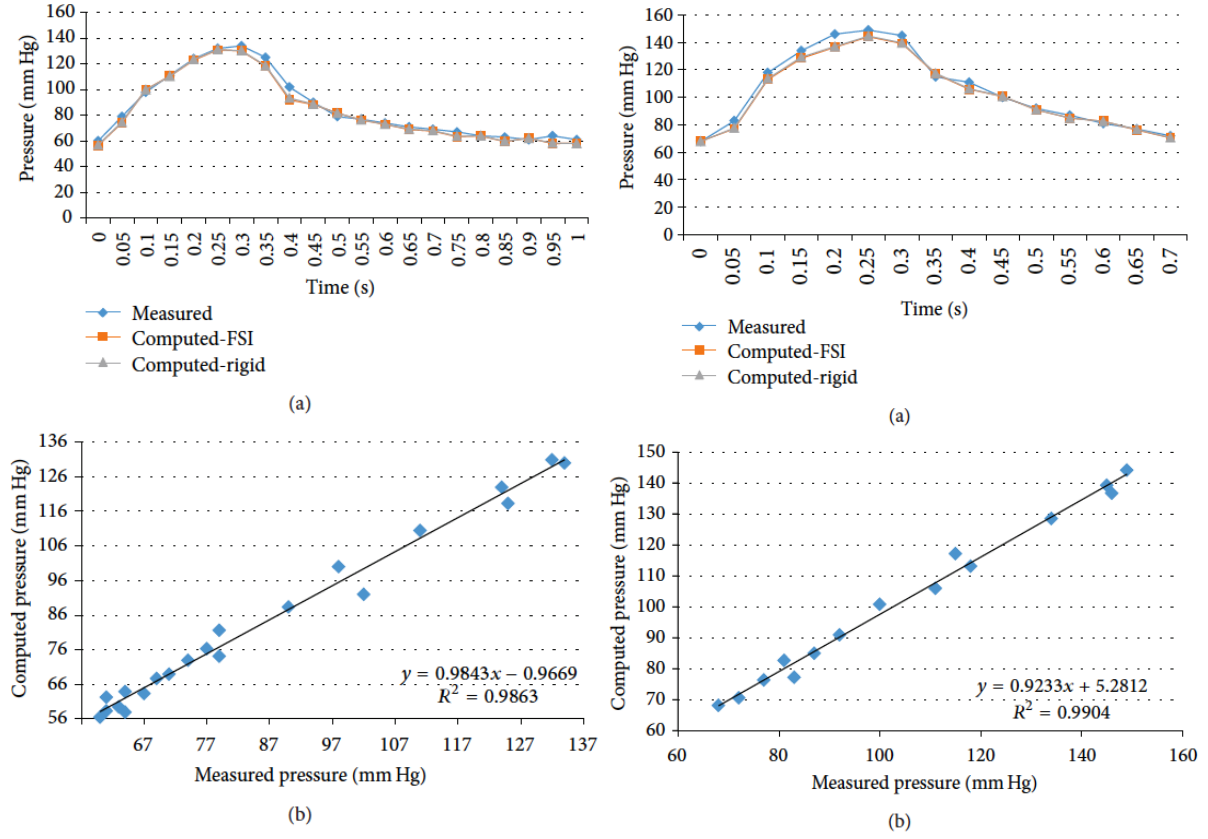


Figure 24: Left image: (a) depicts the pressure waveforms for the examined cardiac cycles (measured and computed results) and (b) exhibits the linear regression analysis for patient #5, right coronary artery. Right image: (a) depicts the pressure waveforms for the examined cardiac cycles (measured and computed results) and (b) exhibits the linear regression analysis for patient #5, left anterior descending coronary artery.

### 3.4.9 Discussion

We presented a study on coronary artery pressure measurements using blood flow simulation in realistic 3D reconstructed coronary arteries. Our primary findings are the following: (I) computed distal coronary pressure values correlate very well with the measured ones using the pressure wire and (II) the assumption of rigid walls and steady flow results in negligible differences compared to the more demanding FSI and pulsatile simulations, respectively.

Several validation studies have been previously carried out to test the accuracy and validity of numerical methods. Phantom, simplified 3D models or patient-specific arterial models have been previously employed in order to perform blood flow simulations. Left coronary artery bifurcations and carotid bifurcations, as well as mesenteric arterial segments were included. The computed velocity profiles were then compared to the measured ones resulting in a fairly good agreement between the measured and the computed values [69, 102-



105]. A recent study examined the correlation of flow and pressure patterns between the computed and the measured values for two deformable flow phantoms mimicking a normal and an obstructed aorta, respectively [6]. Good qualitative agreement was found between the measured and the computed values for flow, exhibiting a better correlation for the pressure results. The majority of those studies focus on the carotid vasculature due to the technical difficulty that arises when dealing with the coronary vasculature. Coronary arteries require invasive imaging methods in order to acquire information related to the size and complex anatomy of the obstruction. Therefore, there is a lack of data on the accuracy of the results regarding numerical simulations in human coronary arteries.

In our study, we focus on coronary arteries and use realistic patient-specific reconstructed coronary arteries derived from angiographic and IVUS data. Furthermore, we use *in vivo* data from invasive flow/pressure measurements in the catheterization laboratory for our validation purposes. The results exhibited a very high correlation of the computed pressure values compared to the measured ones. The pressure waveforms between the measured and the computed values distally in coronary arteries were very close to each other, and the mean computed pressure values for each case showed very small relative error values. Moreover, there was a very good agreement between the measured and the computed values. In addition, our findings demonstrate that the less demanding simulations using steady flow and rigid walls instead of pulsatile flow and FSI result in very small relative error. Therefore, our results support the use of the simpler and less time-consuming simulations for coronary artery pressure computation.

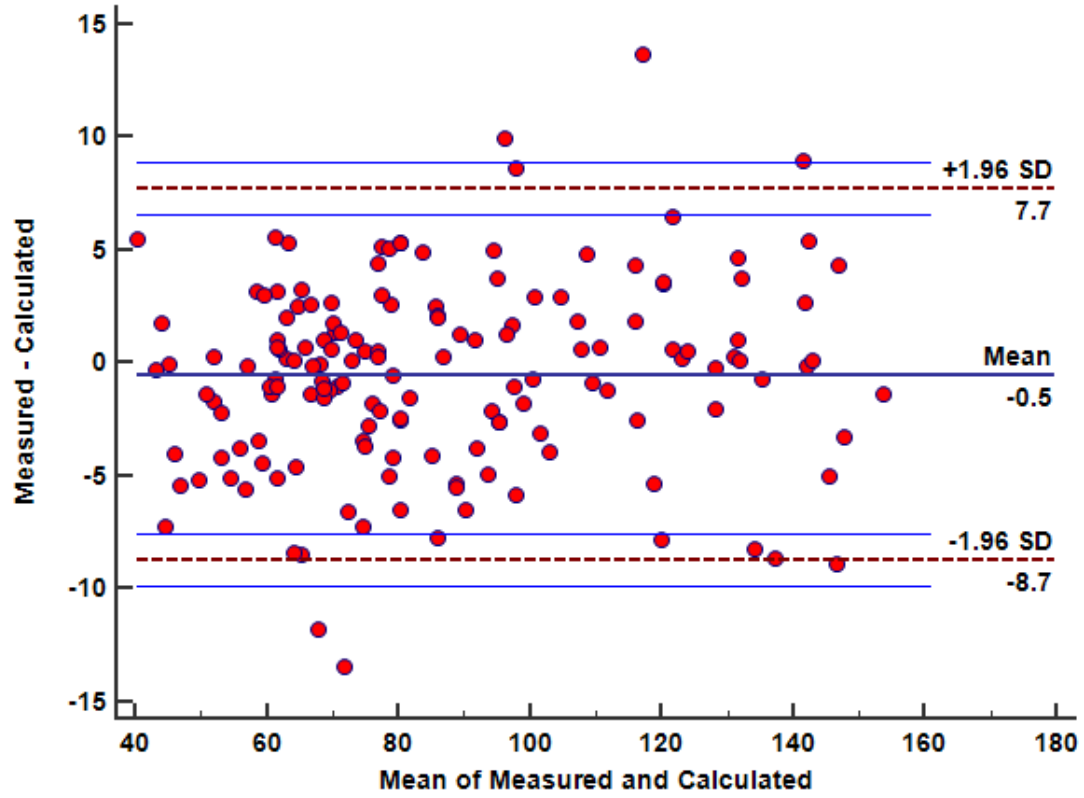


Figure 25: Bland-Altman plot for all 8 cases.

Table 7: Comparison between the wire-based measured pressure values ( $P_{out}$ ) and the computed values from the four types of simulations ( $P_{out(comp)}$ ).

Patient #	$P_{out}$ (mm Hg)	FSI-transient $P_{out(comp)}$ (mm Hg)	Rigid-transient $P_{out(comp)}$ (mm Hg)	FSI-steady state $P_{out(comp)}$ (mm Hg)	Rigid-steady state $P_{out(comp)}$ (mm Hg)
1-RCA	103.04	105.93	106.06	105.46	105.48
2-RCA	104.73	103.52	103.38	103.82	103.71
3-LAD	89.32	89.03	89	89.17	89.15
4-RCA	61.95	63.68	63.83	64.01	64.22
4-LAD	67.47	70.72	71.45	70.94	71.59
5-RCA	105.2	102.42	102.68	102.51	102.58
5-LAD	85.95	83.64	83.85	83.59	83.72
6-LAD	83.52	82.8	82.77	82.98	83.03

Table 8: Results of the parametric study concerning the velocity profiles (steady-state simulations).

Patient #	$P_{\text{out(comp)}} \text{ (mm Hg)}$	$P_{\text{out}(v_{\text{max}})} \text{ (mm Hg)}$	$P_{\text{out}(0.76 * v_{\text{max}})} \text{ (mm Hg)}$	$P_{\text{out}(0.5 * v_{\text{max}})} \text{ (mm Hg)}$
1-RCA	103.04	105.48	106.16	106.75
2-RCA	104.73	103.71	106.56	107.6
3-LAD	89.32	89.15	90.48	91.19
4-RCA	61.95	64.22	65.02	65.66
4-LAD	67.47	71.59	73.21	74.68
5-RCA	105.2	102.58	103.18	103.53
5-LAD	85.95	83.72	84.07	84.55
6-LAD	83.52	83.03	85.23	86.96

### 3.4.10 Clinical Implications and Challenges.

Hemodynamic factors such as arterial pressure both proximal and distal to coronary stenoses are of great clinical importance. FFR, calculated as the ratio of distal to proximal coronary pressure under maximal vasodilation, has been shown to discriminate functionally significant stenoses and help in patient management leading to favourable clinical outcomes [106]. Our results support the use of numerical simulations for assessing distal coronary pressure in humans. This approach implemented in 3D realistic human coronary arteries could open the pathway to FFR assessment based on imaging data only without the need of a pressure wire. However, several challenges lie in the pathway of virtual FFR assessment including the “*a priori*” selection of the appropriate boundary condition for hyperemic flow, the incorporation of the resistance of the distal myocardial bed into the simulation, and the effect of flow division in the branched coronary tree. Although our results demonstrated that finite element simulation in realistic 3D coronary models may yield accurate distal pressure measurements if aortic pressure and coronary flow are known, further clinical studies are needed to test the accuracy of virtual pressure measurements when patient-specific hemodynamic conditions at the inlet are not known.

### Limitations

The reconstructed segments in the current study neglect the presence of bifurcations, which influence flow distribution. Moreover, the hemodynamic significance (i.e., pressure drop) of the coronary stenoses in the arteries studied was not large, and thus we did not have the opportunity to test the accuracy of the computed pressure values in cases with large pressure gradients.

### **3.4.11 Conclusions**

Our aforementioned studies highlight the value of numerical simulations applied in 3D models for assessing hemodynamic factors such as coronary artery pressure. The accuracy of the computed results supports the use of this approach for virtual pressure calculation, which may have major clinical implications for assessing the hemodynamic significance of coronary stenoses without using a pressure wire in the catheterization laboratory.

## **Chapter 4: Computational assessment of coronary stenoses using non-invasive or invasive techniques**

---

4.1. Introduction

4.2. Computational assessment of coronary stenosis using non-invasive techniques

4.3. Computational assessment of coronary stenosis using invasive techniques

---

### **4.1. Introduction**

Ischemic heart disease [16] has conventionally been associated with the presence of anatomically obstructive coronary lesions. However, disagreement exists between the anatomic relevance of coronary artery disease (CAD) as defined by the degree of coronary artery luminal narrowing and its hemodynamic impact on downstream coronary pressure and flow. The link between coronary stenosis severity, as assessed at invasive coronary angiography (ICA) or computed tomography coronary angiography (CTCA) and downstream inducible myocardial ischemia may be even more elusive. Indeed, a number of studies have shown that IHD can occur in the presence or absence of obstructive CAD and that coronary atherosclerosis is just one element in a complex multifactorial pathophysiological process that includes inflammation, microvascular coronary dysfunction, endothelial dysfunction, thrombosis, and angiogenesis [107, 108]. Accordingly, current clinical guidelines make assessment of ischemic burden by functional non-invasive testing a mandatory step (class I) in the evaluation of patients with intermediate (15-85%) probability of disease, acknowledging at the same time the usefulness

of a combined coronary anatomic-functional assessment for guiding management decisions (class IIa).

Due to the fact that fractional flow reserve (FFR) has evolved as the invasive reference standard for functional assessment of coronary stenoses and guidelines recommend its routine application in patients undergoing ICA in the absence of previously non-invasively documented significant inducible ischemia [109], the development of computational coronary assessment techniques is of utmost importance. In patients with stable CAD, FFR does not substitute the assessment of inducible myocardial ischemia, but it has proven to be superior to classical coronary anatomic parameters (i.e. stenosis severity) in guiding patients' management, reliably discriminating the coronary lesions which have hemodynamic significance and could be revascularized from those that can be safely managed conservatively, with improved patients' clinical outcome and overall resource utilization. In this chapter, we present and analyse in detail our proposed computational coronary assessment techniques using either invasive (fusion of IVUS and ICA) or non-invasive (CCTA) coronary imaging modalities.

## **4.2. Computational assessment of coronary stenosis using non-invasive techniques**

This section presents in detail our proposed method for the computational assessment of the severity of coronary stenoses using non-invasive imaging modalities and in particular, using CCTA-based 3D models. The validation of the proposed method is two-fold. In the first section, our method is directly compared to the invasively measured FFR values, whereas, in the second section, our method is directly compared to PET perfusion values.

### **4.2.1 CT-based hemodynamic assessment of coronary lesions derived from fast computational analysis: a comparison against fractional flow reserve**

The evaluation of virtual functional assessment index (vFAI) [88] has been recently suggested as a valid alternative to FFR measurements in patients submitted to ICA, allowing to determine the hemodynamic relevance of a given coronary lesion with a few minutes long computation time. The algorithm uses three-dimensional (3D) coronary anatomical data and steady-flow CFD analysis to compute the ratio of distal to proximal pressure over the lesion for flows in the range 0 to 4 ml/s, normalized by the ratio over this range for a normal artery, offering a measure of CAD hemodynamic significance that is numerically equal to the average of the computed pressure ratio over this flow range.

However, while vFAI measures have been successfully derived from 3D-ICA datasets, positively mimicking invasive FFR results, the possibility to compute this coronary functional parameter from CTCA-based coronary anatomical models has not yet been investigated. The first aim of the current study is to test the feasibility of assessing vFAI by using our automated in-house developed CTCA 3D reconstruction software for generating 3D arterial models, and performing the required blood flow simulations on the aforementioned models [110]. The second aim is to evaluate the efficacy of our method by comparing the derived vFAI values to the invasively measured FFR in coronary stenoses ranging between 30%-70%.

#### **4.2.1.1 Study population**

In the context of the EVINCI (EVALuation of INtegrated Cardiac Imaging for the Detection and Characterization of Ischaemic Heart Disease) study, 475 symptomatic patients with intermediate pre-test probability (20–90%) of CAD underwent between March 2009 and June 2012, a study of coronary anatomy by CTCA and at least one functional imaging test, with the recommendation to perform ICA with FFR in intermediate lesions [111, 112]. The characteristics of the study population and details on imaging procedures and protocols have been already described elsewhere. As per EVINCI study protocol, 307 patients with  $\geq 1$  abnormal noninvasive test underwent ICA, and in 45 of them (showing only intermediate coronary stenoses with 30-70% luminal reduction at ICA) invasive FFR was measured. Dedicated core-labs were responsible for harmonization of imaging protocols, quality assessment of imaging tests and independent imaging analysis.

In order to evaluate the accuracy of vFAI as compared to invasive FFR in predicting the presence of hemodynamically significant CAD in a population of patients of high clinical relevance, a subgroup of 35 patients from the EVINCI study was selected for the present analysis. Selection criteria included, demonstration of intermediate stenosis severity (30-70%) at quantitative ICA core-lab analysis, availability of invasive FFR measurement and satisfactory-to-excellent image quality of CTCA acquisition as defined by the EVINCI CTCA core-lab based on absence of motion artifact, image noise or extensive coronary calcifications. In addition, 9 randomly selected patients fulfilling the aforementioned requirements were also included from the database of TURKU PET Centre (Figure 26). Ethical approval was provided by each center, and all subjects gave written informed consent.

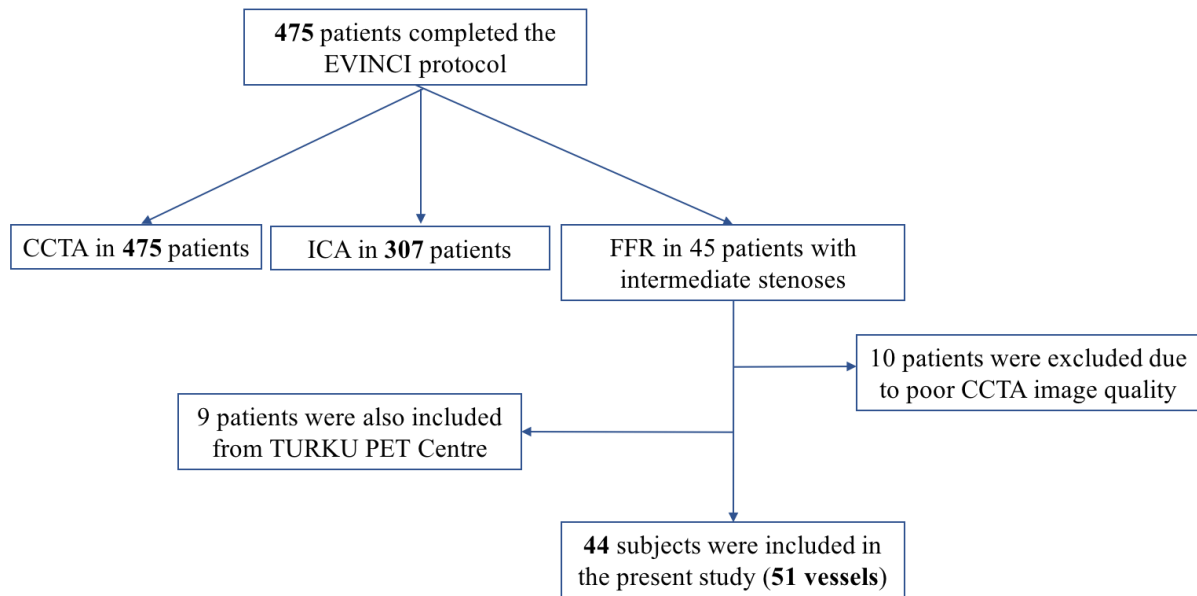


Figure 26: Enrolment and diagnostic procedures.

#### 4.2.1.2 Invasive coronary angiography and FFR measurements

ICA was performed using standard techniques and multiple projections. Quantitative analysis by ICA core-lab was available in all the selected patients. The FFR was invasively measured in vessels with intermediate stenoses using a Combo-Wire (Volcano Therapeutics, Rancho Cordova, California), under the administration of 140  $\mu\text{g/kg/min}$  of intravenous adenosine. Segments with FFR values  $\leq 0.8$  were considered to indicate significant stenoses.

#### 4.2.1.3 CTCA acquisition protocol

Coronary CTCA was performed using  $\geq 64$ -slice CT scanners. The arterial segments of interest were reconstructed in mid to end diastole (70%-80% of the R-R interval) with an average slice thickness of 0.6 mm and an increment of 0.6 mm. To optimize image acquisition and final CTCA quality, beta-blockers and sub-lingual nitrates were used as per study protocol. The presence of coronary calcifications was evaluated in each patient by computation of calcium score (CACS), which was considered extensive when it was higher than 400. Scan quality of the CTCA was categorized by the independent EVINCI Core-Lab into 4 categories (i.e. excellent, good, satisfactory and poor). Scans of poor quality were excluded from the present analysis. The aforementioned acquisition protocol was followed for all 44 subjects, including the randomly selected ones from TURKU PET Centre.



#### 4.2.1.4 CTCA 3D Reconstruction

The 3D reconstruction was performed using our in-house developed software. Briefly, the reconstruction process is carried out in 6 steps:

- 1) The CTCA images are automatically pre-processed in order for potential vessels to be detected and artifacts to be removed. In each image, the following procedure is applied: a) contrast enhancement, b) image thresholding to create images with potential vessel regions and, c) Frangi Vesselness filter to detect structures in the images that correspond to potential vessels.
- 2) The artery borders are roughly detected in order to extract an initial centerline of the vessel.
- 3) Using a minimum cost path approach, the 3D centerline of the vessels is extracted.
- 4) The lumen-outer and wall-plaque parameters are adapted in Hounsfield Units (HU) in order to optimize a 4-component Gaussian Mixture Model (GMM) to the Hounsfield Unit (HU) histogram.
- 5) An extension of active contour models for a) lumen and b) outer wall segmentation are implemented. The main improvement is an additional term forcing the level set to include a prior shape. Regarding the lumen, the prior shape is a tabular mask across centerline with a small radius.
- 6) A level set method is applied regarding plaque segmentation, taking into account calcified objects of significant size.
- 7) Finally, the 3D surfaces for the lumen, outer wall and calcified plaques are created

All arterial segments were reconstructed using the exact same landmarks for each patient. Regarding the RCA, the reconstructed models include segments 1-3 (as dictated from the well-established SYNTAX SCORE chart). Regarding the LAD artery, segments 6-8 were included whereas for the LCx artery segments 11-13 were included in the reconstruction process. Multiple lesions are included in the final 3D model, if present. The reconstruction process as well as the vFAI calculation process are depicted in Figure 27.

#### 4.2.1.5 Virtual Functional Assessment Index (vFAI) calculation

Blood flow simulations were performed on the 3D models of the arteries by generating a mesh of tetrahedral finite elements which then allows the solution of the appropriate Navier-Stokes and continuity equations using ANSYS® CFX 15 (Canonsburg, USA).

For the vFAI calculation, we performed two separate simulations for each case, applying flow rates of 1 and 3 ml/s. These values correspond to the average blood flow during rest and under stress (i.e. after the induction of hyperemia using adenosine), respectively. Finally, we calculated the pressure gradient in each case using the pressure at the inlet ( $P_a$ ) and the outlet ( $P_d$ ). The obtained results were then used to create the case-specific pressure gradient ( $\Delta P$ )-flow relationship for each case (Eq. 51):

$$\Delta P = 0 + f_v Q + f_s Q^2 \quad (51)$$

where  $\Delta P$  is the pressure gradient,  $Q$  is the flow rate,  $f_v$  is the coefficient of pressure loss due to viscous friction and  $f_s$  is the coefficient of pressure loss due to flow separation [113, 114]. Then, the two calculated  $\Delta P$  values are used to solve the fully determined system of the aforementioned equation resulting to the solution of the previously unknown parameters ( $f_v$  and  $f_s$ ). In order to calculate  $P_d/P_a$ , we substituted  $\Delta P$  with  $P_a - P_d$  and inserted the two solved parameters, resulting to (Eq. 52):

$$\frac{P_d}{P_a} = 1 - f_v \frac{Q}{P_a} - f_s \frac{Q^2}{P_a} \quad (52)$$

$P_a$  was set at 100 mmHg (mean aortic pressure) and since the other two coefficients were calculated at the previous step, the area under the  $P_d/P_a$  vs. flow curve is then calculated for a flow range between 0 and 4 ml/s, which corresponds to the mean+2SD increase of the hyperaemic flow rate in a normal human coronary artery, initiating from an average flow rate value of 1 ml/s during rest [115]. Finally, we calculated the vFAI for each case as the ratio of the area under the artery-specific  $P_d/P_a$  vs. flow curve to the reference area, a value that has been shown to correlate well to the invasively measured FFR value. Although vFAI was tested and validated on ICA derived 3D arterial models, the fluid dynamics background of the aforementioned method may be applicable on CCTA derived models as well, since it takes into account only the geometry itself of the model of interest and not other hemodynamic or biological factors.

Image analysis was performed by an independent reader (PS) with experience in analysing CTCA images and in using the 3D reconstruction module optimally. Following appropriate training and for testing interobserver agreement, the same analysis was performed by a second experienced reader in a randomly selected subset of studies. Moreover, the analysis was performed without prior knowledge of the FFR values deriving from the pressure wire in order to remain unbiased towards the overall analysis. The average analysis time required for each of the assessed arteries was 25 minutes ( $\pm$  10 minutes). The required average 3D reconstruction time was around 3 minutes, whereas the rest was needed for the necessary blood flow simulations.

#### **4.2.1.6 Statistical analysis**

The relationship between FFR and vFAI was quantified by calculating the Pearson's correlation coefficient. Bland-Altman plots and the corresponding 95% limits of agreement were used to assess the agreement between the two methods. ROC analysis was performed for identifying the cut-off values of the examined variables. Categorization of FFR and vFAI values was made using the cut-off of 0.8 and the calculated cut-off from ROC curve for the FFR and vFAI, respectively. Sensitivity (SE), specificity (SP), positive predictive value (PPV), negative predictive value (NPV), and diagnostic accuracy (the percentage of patients correctly diagnosed by vFAI) were used to assess the performance of vFAI. P values  $<0.05$  were considered statistically significant.

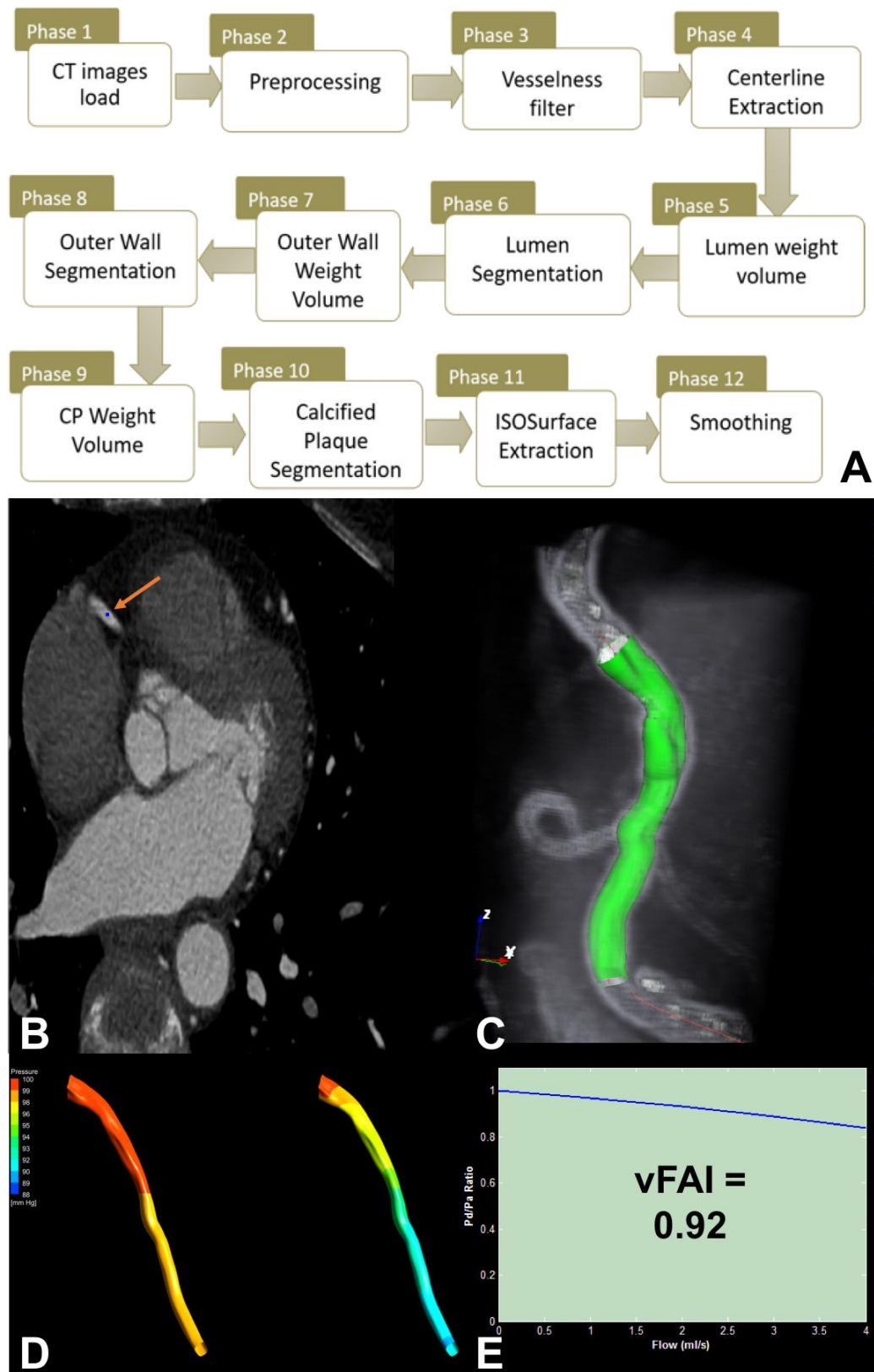


Figure 27: A) Reconstruction process flow chart. B) Reconstruction process. The arrow indicates the point of the RCA that was annotated by the user. C) 3D reconstructed artery, which is derived from the previously annotated point. D) Pressure distribution for flow rates of 1 ml/s and 3 ml/s. E) Invasively measured FFR was 0.92, the same as the respective vFAI.

#### 4.2.1.7 Results

The population of the present study included 44 patients (mean age  $63 \pm 7$  years, 61 % males) with stable symptoms. Hypercholesterolemia, hypertension and CAC score  $> 100$  were present in more than 60% of patients. The mean heart rate during the CTCA scans was  $60 \pm 7$  beats/min. Obstructive CAD ( $\geq 50\%$  stenosis in at least one major coronary vessels) was demonstrated by CTCA in 28 patients (63.6%) and by quantitative ICA in 25 patients (56.8%). Hemodynamically significant disease was documented by an invasive FFR  $\leq 0.8$  in at least one major coronary vessel in 13 patients (29.5%). Patients' characteristics are summarized in Table 9.

Table 9: Baseline Characteristics of the study population (N=44)

<b>Cardiovascular Risk Factors</b>	
Age	63 ( $\pm 6.7$ )
BMI, kg/m <sup>2</sup>	27.5 ( $\pm 4.5$ )
Body Mass, kg	80.3 ( $\pm 15.3$ )
Diabetes (N, %)	9 (20.5%)
Smoker during past year (N, %)	9 (20.5%)
Hypertension (N, %)	29 (65.9%)
Hypercholesterolemia (N, %)	30 (68.2%)
<b>CT Coronary Calcium Score –Agatston (N, %)</b>	
CAC = 0	3 (6.8%)
CAC = 1 – 99	11 (25%)
CAC = 100 – 399	14 (31.8%)
CAC $\geq 400$	13 (29.6%)
CAC Not done	3 (6.8%)
<b>Obstructive CAD (N, %)</b>	
Obstructive CAD at CTCA ( $> 50\%$ stenosis)	28 (54.9%)
Obstructive CAD at ICA ( $> 50\%$ stenosis)	25 (49.1%)
Hemodynamically significant CAD at ICA (FFR $\leq 0.80$ )	13 (25.5%)

#### 4.2.1.8 CTCA derived vFAI measurements and FFR

A total of 51 coronary arteries with intermediate coronary stenoses at quantitative ICA were interrogated by invasive FFR. In particular, 25 vessels (49.1%) had a lesion between 50% and 70% while FFR was  $\leq 0.80$  in 13 (25.5 %). Characteristics of the arterial segments at invasive evaluation are summarized in Table 10.

Table 10: Characteristics of the coronary vessels at invasive evaluation (N=51)

Coronary vessels (N, %)	
Right coronary artery	13 (25.5%)
Left anterior descending	27 (52.9%)
Left Circumflex	11 (21.6%)
Severity of coronary lesions at ICA (N, %)	
Stenosis 30-49%	26 (50.9%)
Stenosis 50-70%	25 (49.1%)
FFR categories (N, %)	
FFR $\leq 0.75$	7 (13.7%)
FFR $> 0.75$ and $\leq 0.8$	6 (11.8%)
FFR $> 0.8$	38 (74.5%)

CTCA scan quality was defined as good-excellent for 45 (88.2%) coronary arteries and satisfactory for 6 (11.8%) vessels. The interobserver agreement for vFAI measurements was tested in 11 randomly selected coronary vessels (4 RCA, 7 LAD) (8 of good-excellent and 3 of satisfactory quality). There was a strong agreement between the two observers with no significant difference in vFAI values (mean difference=0.0046, SD=0.028,  $p=0.29$ ). Both vFAI measurements and FFR were associated with the degree of coronary stenosis at quantitative ICA. Mean vFAI was  $0.90 \pm 0.06$  for stenoses of 30%-49% and  $0.84 \pm 0.1$  for stenoses of 50%-70% ( $p=0.017$ ). Similarly, FFR was  $0.87 \pm 0.07$  for stenoses of 30%-49% and  $0.82 \pm 0.09$  for stenoses of 50%-70%, ( $p=0.034$ ). There was a strong correlation between vFAI and FFR ( $R=0.80$ ) (Figure 28) and a good agreement between the two parameters by the Bland-Altman method of analysis (Figure 29). The mean difference of measurements was 0.037 (SD=0.052,

$p < 0.02$ ), indicating a small systematic overestimation of the FFR by vFAI. The corresponding limits of agreement were from -0.065 to 0.14, with 95% confidence intervals of -0.089 to -0.039 for the lower limit and 0.114 to 0.165 for the upper limit. Agreement was unaffected by calcification level. For heavily calcified vessels (Agatston Score  $> 400$ ,  $n = 17$ ) the mean difference was  $0.046 \pm 0.062$ , whereas for milder calcifications (Agatston Score  $< 400$ ,  $n = 34$ ), the mean difference was  $0.033 \pm 0.046$ , ( $p = 0.40$ ).

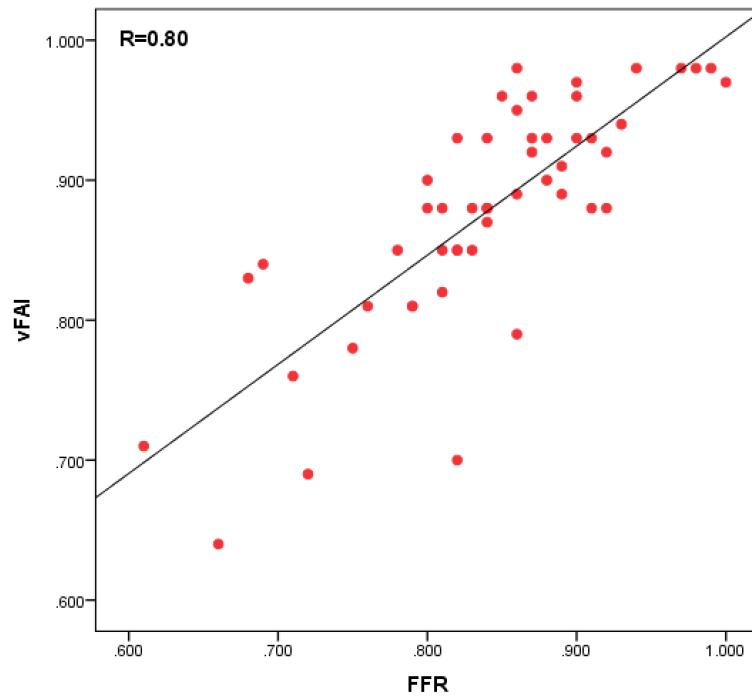


Figure 28: Regression plot comparing the two methods.

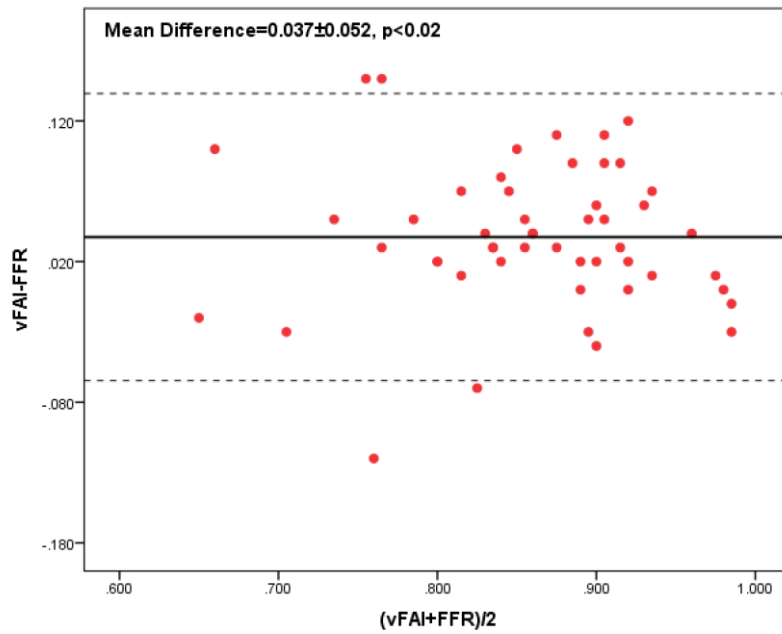


Figure 29: Bland-Altman plot comparing the two methods

#### 4.2.1.9 Diagnostic accuracy of vFAI

Using a receiver-operating characteristic curve analysis, the optimal vFAI cut-off value for identifying an FFR threshold of  $\leq 0.8$  was  $\leq 0.84$  (95% CI: 0.81 to 0.90). Figure 30 shows the ROC curves comparing the diagnostic accuracy of vFAI and traditional CTCA analysis (stenosis  $\geq 50\%$ ) to identify a coronary lesion with  $\text{FFR} \leq 0.8$ . There were 3 vessels with  $\text{FFR}=0.80$ , resulting in 2 false negative vFAI cases. Using a threshold of  $<0.80$ , as the FFR cut-off value for hemodynamically significant lesions, the overall diagnostic performance of vFAI increases, while that of CTCA decreases. The overall diagnostic performance of vFAI and CTCA for both FFR thresholds (i.e.  $\leq 0.80$  and  $<0.80$ ), is presented in Table 11.

Table 11: Per-vessel Diagnostic performance for vFAI and CTCA

<b>FFR<math>\leq 0.80</math></b>									
	Accuracy	Sensitivity	Specificity	PPV	NPV	TP	TN	FP	FN
<b>vFAI <math>\leq 0.84</math></b>	88.2%	76.9%	92.1%	76.9%	92.1%	10	35	3	3
<b>CTCA Stenosis <math>\geq 50\%</math></b>	47.1%	53.8%	44.7%	25%	73.9%	7	17	21	6



### FFR<0.80

	Accuracy	Sensitivity	Specificity	PPV	NPV	TP	TN	FP	FN
<b>vFAI <math>\leq 0.84</math></b>	92.2%	90.9%	92.5%	76.9%	97.4%	10	37	3	1
<b>CTCA Stenosis <math>\geq 50\%</math></b>	43.1%	45.5%	42.5%	17.9%	73.9%	5	17	23	6

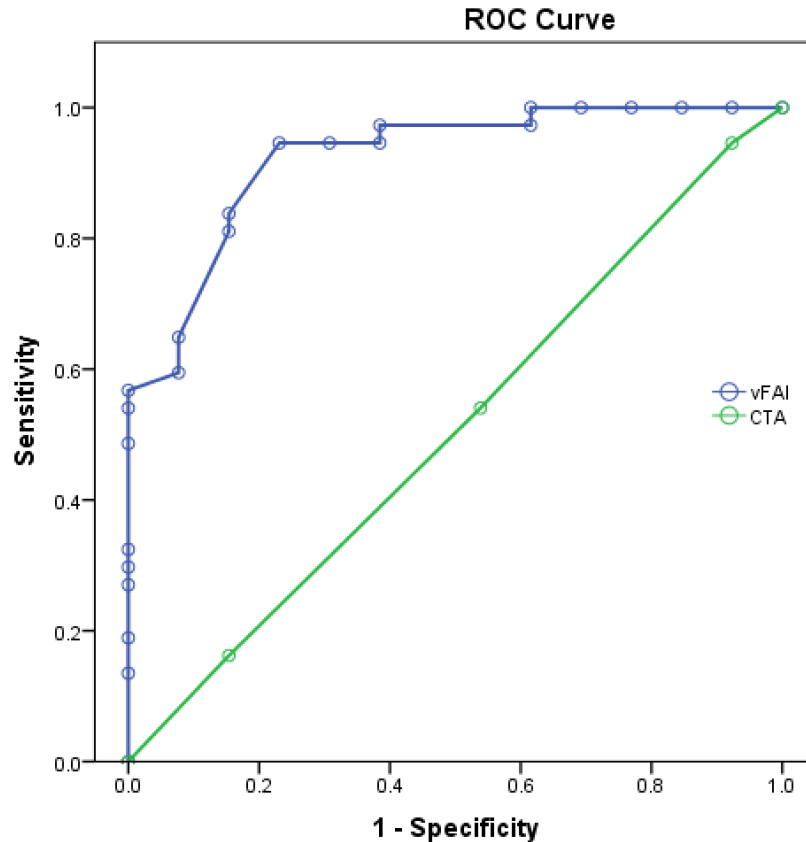


Figure 30: ROC curves comparing vFAI vs. CTCA diagnostic performance to recognize hemodynamically significant coronary lesions (FFR  $\leq 0.80$ ). The area under the curve for the vFAI is 0.90 ( $P < 0.0001$ ), whereas for CTCA is 0.51 ( $P = 0.93$ ).

#### 4.2.1.10 Discussion

We have demonstrated the feasibility of deriving an accurate index of hemodynamically significant coronary lesions through non-invasive quantitation of CTCA-based vFAI. Specifically, in a population of patients with intermediate probability of CAD and stenosis severity ranging from 30% to 70%, vFAI could be readily obtained within a few-minutes computation time, well matching the results of the accepted gold-standard represented by invasive FFR. A cut off vFAI value of  $\leq 0.84$  was associated with a modest sensitivity (76.9%), but high specificity and NPV (88.2% and 92.1%, respectively) for identifying lesions with FFR  $\leq 0.8$ . An FFR cut-off value  $< 0.80$  resulted in even higher sensitivity and NPV [116].

A number of studies have already reported the ability of CTCA derived functional indexes to mimic invasive FFR measurements for the detection of hemodynamically significant CAD [79-81]. In particular, while initial reports had suggested the existence of only a moderate agreement between FFR<sub>CT</sub> and invasive FFR [87], recent refinements of computational techniques and CFD modelization have improved the accuracy of FFR<sub>CT</sub> in unmasking the presence of hemodynamically significant coronary lesions and quantifying their severity [79]. Our results show that vFAI slightly overestimates FFR, but can distinguish functionally significant from non-significant lesions with high specificity and NPV. In our study population, the cut off vFAI value of 0.8, which has been used in prior studies, would have resulted in a low sensitivity (45.5 %). Due to the slight overestimation of FFR by vFAI demonstrated in the present study, the best cut off value for vFAI was 0.84 which increased sensitivity to levels comparable to those of similar studies without affecting significantly the specificity. Even a sensitivity value of 76.5% could seem rather modest for unmasking the presence of a pathological FFR however, since in our study only 13 out of 51 lesions had a FFR  $\leq$  0.8, the diagnostic sensitivity of vFAI might have been spuriously diminished. Furthermore, our results demonstrate that for studies of adequate quality, coronary calcification did not affect significantly the agreement between vFAI and FFR. Intense calcification affects image quality by creating the so-called “blooming effect” leading to an overestimation of the arterial lumen and thus restricting data analysis only to studies without obvious artefactual effects. We are currently working to resolve these issues by developing a dedicated “blooming removal” algorithm and further denoising filters.

Today’s advanced computational methods are based on modeling of the physiological parameters of coronary microcirculation and vascular resistance and their influence in coronary flow during hyperemia [79, 80]. Considering that virtual functional assessment reflects only vessel geometry-related changes without taking into account alterations at the microcirculation level, slight disagreement between ours and other FFR<sub>CT</sub> techniques regarding the optimal threshold for disease detection should be expected. The same holds true for the comparison between vFAI and ICA-FFR. A further difference between our approach and those of prior studies on FFR<sub>CT</sub> is that vFAI is not influenced by the effect of any side branch on the calculated coronary flow, assuming that flow is the same alongside the length of an artery.

Previous studies found that FFR<sub>CT</sub> slightly overestimates the actual FFR values [79-81, 97] (Mean difference between FFR-FFR<sub>CT</sub>: Kruk et al.: +0.01, Koo et al.: +0.022, Min et al.:

+0.058 and Norgaard et al.: +0.03). These studies use a different approach regarding the calculation of  $\text{FFR}_{\text{CT}}$ , where the entire coronary vasculature is reconstructed in 3D and the lumped parameter models of the microcirculation to the outflow boundaries are coupled but at the expense, of increased computational time and need of strong computational power. Using another approach, Taylor et al. [117], computed the vascular resistance and calculated the LV mass for estimating FFR. Despite the small overestimation of FFR compared to the aforementioned studies, our diagnostic accuracy is not inferior to them. In particular, diagnostic accuracy, sensitivity, specificity, PPV, and NPV for a per-vessel analysis for vFAI were 88.2%, 76.9%, 92.1%, 76.9% and 92.1% whereas for  $\text{FFR}_{\text{CT}}$  71%, 82%, 66%, 54%, and 88% for the study by Min et al. [79] (for intermediate stenoses of 30%-70%) and 83%, 66.7%, 88.6%, 66.7% and 88.6% (for lesions from 50%-69%) for the DISCOVER-FLOW study [81], respectively.

In the present study, we have included patients with coronary stenoses ranging from 30% to 70% in whom estimation of hemodynamic significance of coronary disease is more clinically meaningful [118, 119]. Moreover, the agreement between CT derived indexes and invasive FFR is expected to be increased by the presence of highly ( $\geq 70\%$ ) or minimally ( $< 30\%$ ) stenosed lesions. Thus, testing the agreement between vFAI and FFR only in lesions ranging between 30% and 70% was a more severe challenge for the non-invasive index. On the other hand, such lesions are often associated with an FFR value in the range of 0.75-0.80, where even invasively derived measurements may demonstrate low reproducibility [55]. However, our own dataset included only 6 (11.8 %) vessels with FFR values in this range.

### **Clinical Implications**

A preemptive non-invasive evaluation of the presence of hemodynamically relevant CAD is favored by current clinical guidelines for avoiding unnecessary coronary interventions [120]. Whilst different cardiac imaging tests can be used to rule out the presence of functionally significant CAD, a significant proportion of patients currently submitted to ICA still show no hemodynamically significant coronary lesions [121]. Many of these patients have coronary atherosclerosis that can be depicted by CTCA. A combined assessment of coronary anatomy and function is therefore desirable, but it generally requires two separate diagnostic tests resulting in higher immediate costs. Accordingly, although the advantages of a comprehensive anatomic-functional evaluation of patients with suspected ischemic heart disease have been confirmed [122, 123], such an integrated assessment is rarely performed in daily routine.

While CTCA has long represented the reference standard for the non-invasive depiction of coronary anatomy, more recently it is also being used to obtain quantitative measures of CAD functional relevance through the modelization of coronary flow dynamics [81, 124]. The calculation of  $\text{FFR}_{\text{CT}}$ , the most validated of such functional parameters, typically requires the use of proprietary software with long computation times and a dedicated core-laboratory [79, 80]. Our preliminary results suggest that vFAI might represent a valid alternative to the more technically demanding  $\text{FFR}_{\text{CT}}$ , allowing a close estimation of invasive FFR and discriminating hemodynamically significant coronary lesions with good accuracy. The required analysis time was around 25 minutes that is significantly lower when compared to that of the most well-known  $\text{FFR}_{\text{CT}}$  software (1-4 hours) [95] and is directly comparable to that of the study by Kruk et al. (average of 20 minutes per case) [97], or of the study by Ko et al. (average of 27 minutes per case) [98]. Moreover, the proposed method requires minimal user interaction regarding the 3D reconstruction process of the desired arterial segment, resulting in a good interobserver agreement.

### **Study Limitations**

One of the main limitations of our study was the rather modest sample size, which is however comparable to that of some prior studies reporting diagnostic accuracy of  $\text{FFR}_{\text{CT}}$  in patients with lesions of intermediate severity [81]. On the other hand, in contrast to most previous reports, we evaluated only patients with intermediate likelihood of CAD. We have demonstrated good agreement between vFAI and FFR and our results compare well with prior studies on CTCA-based modelization of coronary flow dynamics. This may partially be explained by the fact that the FFRs of 75% of patients fell in the relatively narrow range (i.e. 0.8 to 1.0). A low number of false negatives in general increases both sensitivity and NPV. However, when the diseased samples (i.e.  $\text{FFR} \leq 0.8$ ) are a minority compared with the normal samples, a few false negative results affect more sensitivity than NPV. Accordingly, despite demonstrating the operative validity of vFAI as an accurate measure of CAD functional relevance [88], our results should be confirmed in a larger population of patients with a wider range of FFR values. Moreover, for the time being, our method can only perform a vessel-based reconstruction and not that of the entire arterial tree. Nevertheless, for the purposes of the current study this was not a drawback, since we only assessed specific segments on which the FFR was invasively measured. We are currently improving our algorithm in order to have the ability to perform a full 3D reconstruction of the entire arterial tree and this will be tested in a larger prospective study. Finally, striving for an almost absolute agreement between vFAI and FFR is probably an

elusive task considering the intrinsic nature of vFAI. The latter mainly expresses the "potential" functional impact of anatomy, which differs fundamentally from the invasively calculated FFR that measures directly the effect of anatomy on real pathophysiologic conditions and thus, may be influenced by the vasodilating capability of the whole coronary system.

#### **4.2.2 Characterization of functionally significant coronary artery disease by a novel coronary computed tomography angiography-based index: a comparison with PET perfusion**

Coronary blood flow is probably a better marker of the functional status of the coronary circulation providing an integrated assessment both of the epicardial vessels and the microcirculation and therefore, constitutes a parameter of great interest for diagnostic and management strategies [125, 126]. In the non-invasive setting, quantitative measurement of myocardial blood flow (MBF) at rest and stress and myocardial flow reserve (MFR) using Positron Emission Tomography (PET) provide accurate assessment of functionally significant CAD. In particular, it has been demonstrated that addition of MFR provides incremental risk stratification above that obtained by semi-quantitative analysis of PET images, leading to significant and meaningful risk reclassification (of approximately 35%) of intermediate-risk patients and modifies the effect of revascularization [127].

A number of studies have explored the relationship between FFR and PET derived MBF stress and MFR showing a moderate correlation [128-130]. However, no data exists on the relationship between FFR<sub>CT</sub> or vFAI, and PET derived measures of quantitative perfusion. Similarly, there are no studies to date testing the ability of CCTA derived functional indices to predict perfusion changes by PET in stenotic vessels at CCTA. The purpose of the present study was to test the hypothesis that vFAI is related with regional flow parameters derived by quantitative PET and can be used to predict perfusion abnormalities in vessels with stenosis at least 30% of the vessel diameter at CCTA.

##### **4.2.2.1 Study Population**

In the context of the FP-7 EVINCI (NCT00979199) and Horizon 2020 SMARTool ([www.smartool.eu](http://www.smartool.eu)) projects, individuals who have undergone both CCTA and PET perfusion with quantification were identified (Figure 31). The characteristics of the study population, details on imaging procedures and protocols have already been described elsewhere [111]. Dedicated core-labs were responsible for the harmonization of imaging protocols, quality

assessment of imaging tests and independent imaging analysis. Based on the selection criteria for the SMARTool project, only EVINCI studies with a fair to excellent CCTA image quality were included for analysis. Accordingly, 23 from the 99 EVINCI patients were excluded, as they did not meet the pre-specified standards. For consistency in image analysis and subsequent simulations in all data sets, five additional patients requiring extra smoothing and processing of the images were also excluded. The remaining 73 patients had at least one vessel free of noise, motion artifacts or heavy calcifications and had a maximum increment between slices of 0.625 mm.

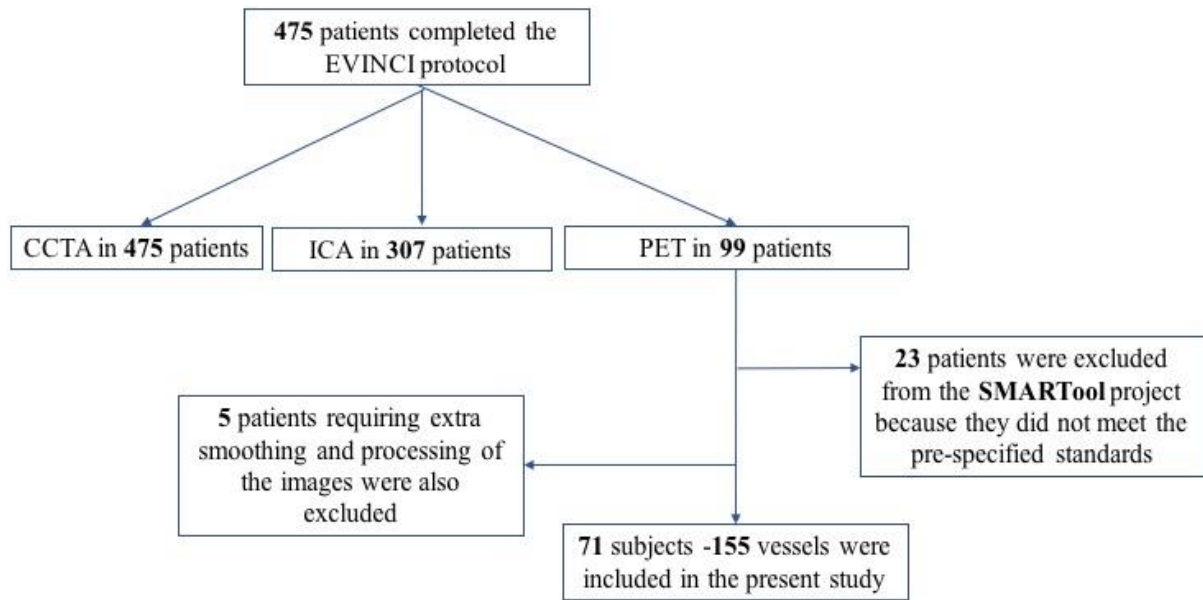


Figure 31: Enrolment and data acquisition scheme.

#### 4.2.2.2 CCTA Imaging

CCTA acquisition protocol has been previously described [111]. Briefly, CTCA was carried out in  $\geq 64$  slice scanners. The arterial segments of interest were reconstructed in mid to end diastole (70%-80% of the R-R interval) with an average slice thickness of 0.6 mm and an increment of 0.6 mm. To optimize image acquisition and final CTCA quality, beta-blockers and sub-lingual nitrates were used as per study protocol. The presence of coronary calcifications was evaluated in each patient by computation of calcium score (CACS), which was considered extensive when it was higher than 400. Scan quality of the CTCA was categorized 4 categories (i.e. excellent, good, fair and poor). Angiographic stenosis severity was classified into four groups (<30%, 30-50%, 50-70% and 70-90%).

#### 4.2.2.3 PET imaging and data analysis

PET scanning with  $^{15}\text{O}$ -water or  $^{13}\text{N}$ -ammonia was performed according to international guidelines [131] as described elsewhere [132]. To assign each of the 17 myocardial segments to the pertinent coronary artery, image fusion of CCTA and PET derived datasets was performed on a dedicated workstation (Advantage Workstation 4.4, GE Healthcare) using the CardIQ Fusion software package (GE Healthcare) as previously described [122, 133]. Based on existing literature, an MFR  $<2$  that has been consistently found to be associated with adverse prognosis, was used as a common cut off for the combined analysis of  $^{15}\text{O}$ -water and  $^{13}\text{N}$ -ammonia studies [126]. For tracer-based sub-analysis, thresholds selection for detection of significant CAD was based on prior studies from the investigators' group. PET studies were considered positive for significant CAD, when more than one contiguous segments showed stress MBF  $\leq 2.3$  ml/g/min for  $^{15}\text{O}$ -water [134] or  $<1.79$  ml/g/min for  $^{13}\text{N}$ -ammonia [132]. The corresponding MFR thresholds were  $\leq 2.5$  and  $\leq 2$  for  $^{15}\text{O}$ -water and  $^{13}\text{N}$ -ammonia respectively.

Finally, for assessing the value of vFAI to predict the presence of inducible perfusion abnormalities, perfusion in  $^{13}\text{N}$ -ammonia studies was classified in each of 17 segments as normal, mildly reduced, moderately reduced, severely reduced, or absence of perfusion, and the segmental scores were summed for the stress and rest images. An inducible perfusion abnormality was defined as a summed segmental difference score (SDS) between stress and rest images  $\geq 2$ , either from a score  $\geq 1$  in  $\geq 2$  contiguous segments, or  $\geq 2$  in  $\geq 1$  segment. The extent of perfusion defects was also computed as % of the left ventricle and significant reversibility was defined as regional perfusion defect involving  $\geq 10\%$  of the left ventricle. Analysis of all PET images was performed by two experienced independent physicians who were unaware of the patients' data.

#### 4.2.2.4 Statistical analysis

Quantitative data are presented as mean values  $\pm$  SD, while qualitative variables as absolute and relative frequencies. Probability values are two-sided from the Student t-test or Mann-Whitney U test for continuous and categorical variables, according to the normal or skewed distribution of the variables. When there were more than 2 categories, ANOVA or Kruskal-Wallis test was used. For between subgroups comparisons, a Bonferroni correction was performed. Non-continuous values were compared by chi-square test. A value of  $p < 0.05$  was considered significant. To assess relationships between CCTA-vFAI values and PET derived parameters,

Pearson's correlation coefficient was used. In agreement with recent recommendations for  $\text{FFR}_{\text{CT}}$  utilization, a threshold  $\geq 30\%$  of the vessel diameter was selected for calculating the predictive value of CCTA-vFAI to detect an attenuated stress MBF or MFR response [135]. Further analysis using the more conventional threshold of  $\geq 50\%$  from combined data of both two tracers was also performed. The optimal threshold of CCTA-vFAI for predicting an attenuated stress MBF or MFR was determined using the Youden index. Finally, the diagnostic accuracy of CCTA-vFAI was compared with stress MBF and MFR for predicting regional perfusion defects, using receiver-operating characteristic [136] area under the curve [137] analysis according to DeLong et al. Statistical analyses were performed using SPSS version 20 (Chicago, Illinois, USA), while MedCalc version 13 (Ostend, Belgium) was used for the comparison of the areas under the ROC curves (DeLong et al Biometrics 1988).

#### 4.2.2.5 Results

vFAI assessment was feasible in 155 vessels (114 with corresponding PET  $^{15}\text{O}$ -water and 41 with PET  $^{13}\text{N}$ -ammonia studies). Seventy-three coronary vessels (52 with corresponding PET  $^{15}\text{O}$ -water and 21 with PET  $^{13}\text{N}$ -ammonia studies) from 65 patients, exhibited a stenosis  $\geq 30\%$ . Most of patients (mean age:  $62.23 \pm 7.96$  years old) were men with dyslipidaemia and had lesions of intermediate (median 30-50%) severity in CTA. Forty-one arteries had a 30-49% stenosis (56.2%), 26 had a 50–70% (35. 6%), and 6 arteries had 70-90% stenosis (8.2%). Baseline demographic, clinical and lesion characteristics of the study population are summarized in Table 12. Nineteen vessels presented multiple lesions (12.9%).

Table 12: Baseline demographic, clinical and lesion characteristics

<b>Patients (n=71)</b>	<b>N (%)</b>
Age	62.2±7.7
Gender (male)	38 (54)
<b>Symptoms</b>	
Typical angina	11 (15)
Atypical angina	42 (60)
Non anginal chest pain	18 (25)
<b>Risk factors</b>	
Arterial Hypertension	37 (52)
Dyslipidaemia	43 (61)
Smoking	14 (20)



Family history of CAD	26 (37)
Diabetes Mellitus	11 (15)
Obesity	13 (18)
BMI	26.9±3.7
<b>Medications</b>	
Oral antidiabetics	8 (11)
Insulin	4 (6)
Statins	42 (59)
ACEI	22 (31)
Diuretics	10 (14)
ARBs	11 (15)
b-blockers	39 (55)
Ca antagonists	9 (13)
ASA	53 (75)
Nitrates	9 (13)
<b>Total vessels analyzed (vFAI)</b>	155
LAD	60 (38.70)
RCA	44 (28.4)
LCx	51 (32.9)
<b>Total vessels with stenosis ≥ 30% (vFAI)</b>	73
<sup>15</sup> O-water	52 (71.2)
<sup>13</sup> N-ammonia	21 (28.8)
<b>LVEF</b>	54.94±7.05

---

#### 4.2.2.6 Impact of stenosis severity on quantitative PET indices

In regions supplied by vessels without significant narrowing (<30%), MFR was 3.1 (CI range 2.12 to 4.08). Compared to the latter, MFR was reduced as stenosis severity increased ( $p<0.001$ ) (Figure 32). Specifically, for stenotic lesions 30-50%, MFR was 2.68 (CI range 1.88 to 3.49), between 50-70%, 2.25 (CI range 1.51 to 2.99) and for coronary stenoses >70%, MFR was 1.64 (CI range 0.93 to 2.35), respectively. MFR was also significantly reduced in regions supplied by vessels with a stenosis >70% compared to those with stenosis 30-50% ( $p<0.001$ ). For measurements obtained from <sup>15</sup>O-water PET studies only, a significant progressive reduction of stress MBF and MFR was observed as stenosis severity increased ( $p<0.001$  for both) (Figure 33). For measurements computed from <sup>13</sup>N-ammonia PET scans only, no significant

differences of stress MBF or MFR were observed in arteries with narrowing  $\geq 30\%$  compared to vessels without significant narrowing (Figure 32).

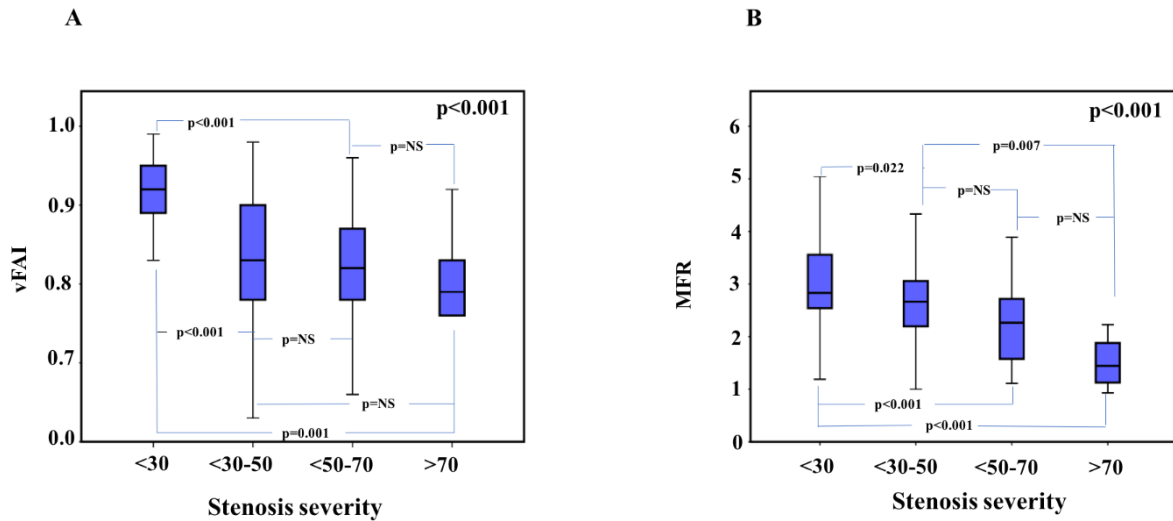


Figure 32: Impact of stenosis severity on vFAI and MFR, respectively.

#### 4.2.2.7 Impact of stenosis severity on vFAI

In the total vessel analysis, vFAI values corresponding to lesions of intermediate severity (30-70%) was lower compared to non-stenotic lesions and it was further reduced in lesions  $>70\%$  of the vessel diameter ( $p<0.001$ ). Regarding PET measurements with  $^{15}\text{O}$ -water, stress MBF progressively declined as stenosis severity increased ( $p<0.001$ ). MFR in coronary lesions of intermediate severity (30-50% and 50-70%) was also significantly lower compared to non-stenotic vessels and it was further reduced for stenoses  $>70\%$  ( $p<0.001$ ). MFR in the latter was also lower compared to lesions with a diameter stenosis 30-50% ( $p=0.02$ ). In  $^{13}\text{N}$ -ammonia studies, stress MBF and MFR were unaffected by stenosis severity. vFAI for arteries with diameter stenosis  $<30\%$  was 0.91 (CI range: 0.90-0.93). Compared to the latter, vFAI declined ( $p<0.001$ ) as stenosis severity increased: 0.82 (CI range 0.74 to 0.91) for stenoses 30-50%, 0.80 (CI range 0.69 to 0.91) for 50-70% and 0.79 (CI range 0.7 to 0.88) for 70% -90% respectively.

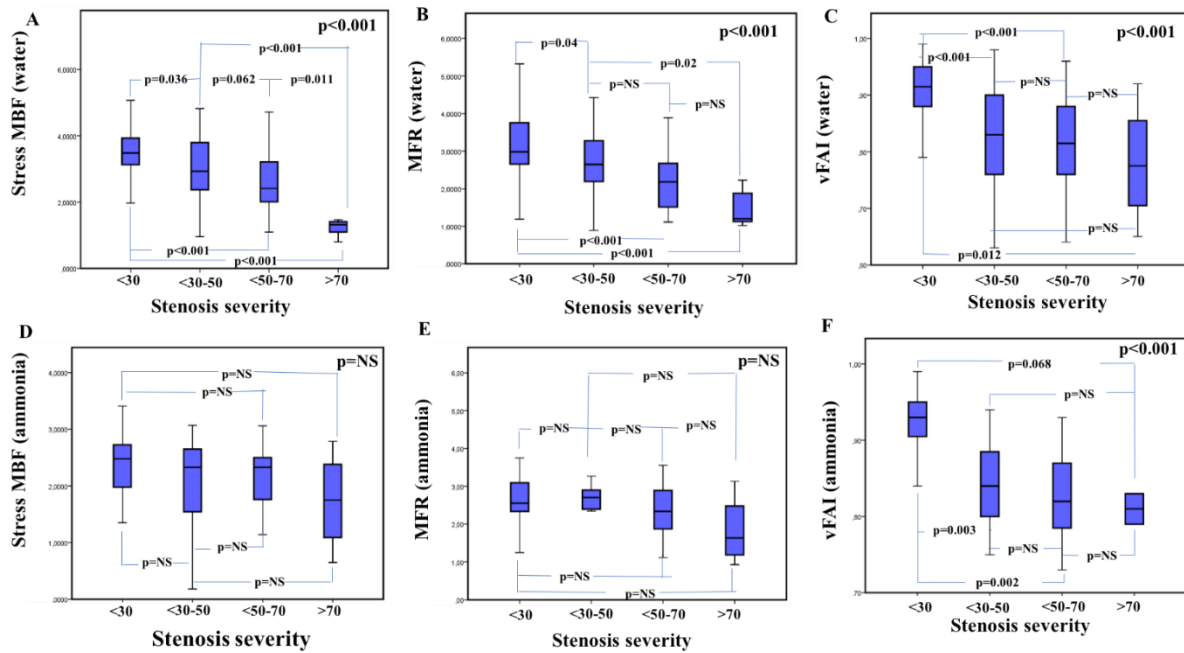


Figure 33: Impact of stenosis severity on several PET indices.

#### 4.2.2.8 Relationship between vFAI and quantitative PET indices

There was a positive modest statistically significant relationship between vFAI and MFR ( $R=0.41$ ,  $p<0.001$ ). (Figure 34). In vessels with narrowing  $\geq 30\%$ , vFAI and MFR were concordantly normal in 54.8% of vessels and concordantly abnormal in 21.9%. Discordance was observed in 27.4% of vessels (17.8% with abnormal vFAI but normal MFR values and 5.5% with abnormal MFR and vFAI  $> 0.8$ ) (Tables 11-13). For  $^{15}\text{O}$ -water PET measurements only, there was a modest but statistically significant association between vFAI and MFR ( $R=0.41$ ,  $p<0.001$ ). vFAI was also positively associated with stress MBF ( $R=0.48$ ,  $p < 0.001$ ). For  $^{13}\text{N}$ -ammonia PET measurements only, the corresponding values were  $R=0.32$ , ( $p=0.04$ ) and  $R=0.5$  ( $P=0.001$ ), respectively). Agreement between vFAI and MFR in these sub groups is shown in Tables 11-13.

Table 13: Agreement between vFAI and MFR for  $^{15}\text{O}$ -water PET measurements (vessels  $>30\%$ ,  $n=73$ )

	vFAI $\geq 0.8$	vFAI $< 0.8$
CFR $\geq 2.0$	40 (54.8%)	13 (17.8%)
CFR $< 2.0$	4 (5.5%)	16 (21.9%)

**Kappa value=0.49,  $p<0.001$**

Table 14: Agreement between vFAI and MFR for  $^{15}\text{O}$ -water PET measurements

	vFAI $\geq$ 0.8	vFAI<0.8
CFR $\geq$ 2.5	74 (64.9%)	5 (4.4%)
CFR<2.5	16 (14%)	19 (16.7%)

**Kappa value=0.53, p<0.001**

Table 15: Agreement between vFAI and MFR for  $^{13}\text{N}$ -ammonia PET measurements

	vFAI $\geq$ 0.8	vFAI<0.8
CFR $\geq$ 2.0	27 (67.5%)	4 (10%)
CFR<2.0	5 (12.5%)	4 (10%)

**Kappa value=0.33, p=0.04**

#### 4.2.2.9 Diagnostic accuracy of vFAI for detecting reduced hyperemic response or MFR

A vFAI threshold of 0.8 (95% CI: 0.6 to 0.82) had a sensitivity, specificity, PPV, NPV and accuracy of 80%, 75.5%, 55% 91% and 76.7% respectively for predicting MFR <2 in regions subtended by vessels with stenosis  $\geq$  30%. (Figure 34). A separate analysis for  $^{15}\text{O}$ -water PET and  $^{13}\text{N}$ -ammonia PET studies respectively was also performed. Regarding the former, the optimal cut-off value of vFAI to identify MFR  $\leq$  2.5 in regions supplied by vessels with stenosis  $\geq$  30% was  $\leq$  0.8 (95% CI: 0.63 to 0.88) with sensitivity, specificity, PPV, NPV and accuracy of 64.3%, 83.3%, 81.8%, 66.77% and 73% respectively. For identifying a stress MBF  $\leq$  2.3, the corresponding values for the same threshold  $\leq$  0.8 (95% CI: 0.69 to 0.91) were 88.9%, 82.4%, 72.7%, 93.3% and 84.6% respectively (Figure 34). For  $^{13}\text{N}$ -ammonia PET analysis, the optimal threshold of vFAI to detect MFR < 2 or stress MBF < 1.79 was  $\leq$  0.79 (95% CI: 0.47 to 0.88, sensitivity, 66.7%; specificity, 80%; PPV=57.1%; NPV=85.7%; accuracy=76.2%) and  $\leq$  0.82 (95% CI: 0.56 to 0.93, sensitivity, 83.3%; specificity, 73.3%; PPV=55.6%; NPV=91.7%; accuracy=76.2%), respectively (Figure 34) .

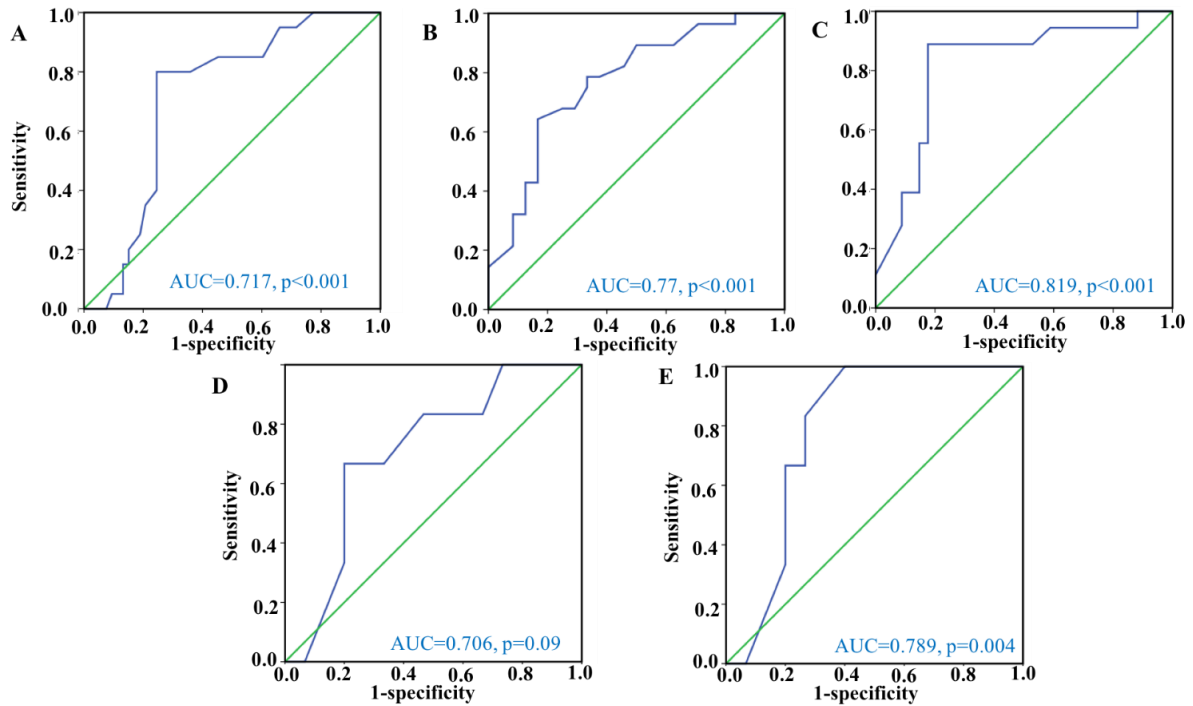


Figure 34: Diagnostic accuracy of vFAI for detecting reduced hyperemic response or MFR.

#### 4.2.2.10 Performance of vFAI and quantitative PET indices for detecting inducible perfusion defects

To further explore the ability of vFAI to detect functionally significant coronary lesions, its diagnostic accuracy was compared to quantitative  $^{13}\text{N}$ -ammonia PET indices for identifying either a regional perfusion defect of any size ( $\text{SDS} \geq 2$ ) or a regional perfusion defect involving  $\geq 10\%$  of the left ventricle downstream a luminal stenosis of  $\geq 30\%$  on CCTA. No statistically significant differences were found between vFAI and MFR or stress MBF, regarding their ability to detect a perfusion defect: pairwise comparisons of ROC curves: vFAI vs. MFR  $p=0.87$ , vFAI vs. stress MBF  $p=0.55$  and MFR vs. stress MBF,  $p=0.62$ . Similar were the results regarding the comparative ability for predicting a regional perfusion defect of  $\geq 10\%$  of the left ventricle: vFAI vs. MFR,  $p=0.87$ ; vFAI vs. stress MBF  $p=0.54$  and MFR vs. stress MBF  $p=0.25$ ) (Figure 35).

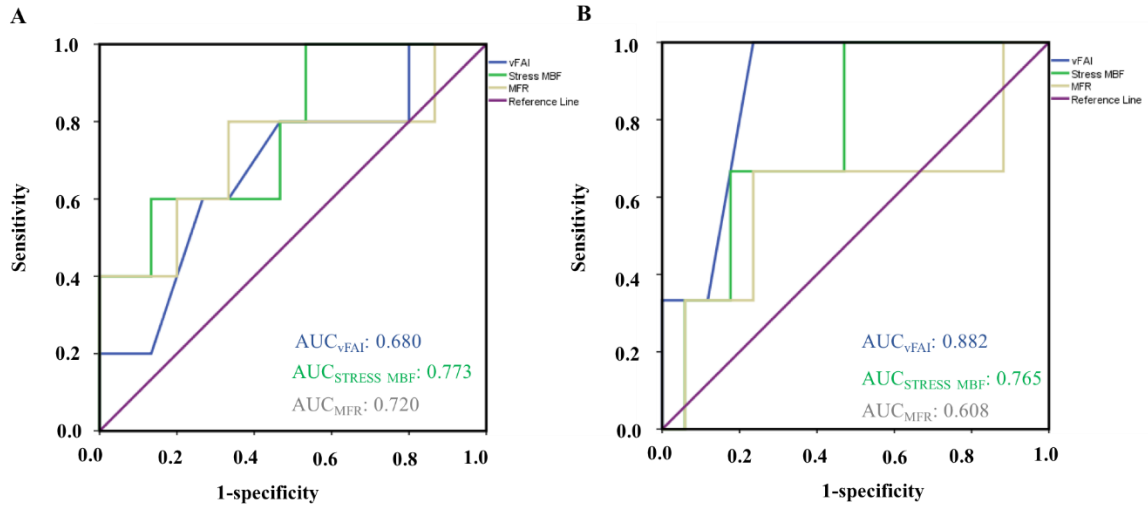


Figure 35: Performance of vFAI and quantitative PET indices for detecting inducible perfusion defects

#### 4.2.2.11 Discussion

Our results show that vFAI can be readily computed in the majority of coronary vessels from standard CCTA datasets, identifying with reasonable accuracy the presence of an attenuated stress MBF or MFR downstream a coronary lesion  $\geq 30\%$  of the vessel diameter at CCTA.

#### Non invasive evaluation of patients with stable symptoms: anatomy versus function

It has been consistently demonstrated that the event-rate of patients with stable symptoms is mainly determined by the functional severity of CAD rather than by anatomic disease burden [138]. Accordingly, current guidelines on the management of stable CAD recommend proceeding to ICA only in the presence of significant myocardial ischemia [2]. However for diagnostic purposes, anatomical imaging in the form of CCTA has been recommend as a first line testing [120], as it is the reference standard for non-invasive evaluation of coronary anatomy, showing excellent accuracy in unmasking the presence of angiographically significant CAD [111].

CCTA can also allow evaluation of CAD hemodynamic relevance, through computation of  $FFR_{CT}$ . No studies so far have assessed the relationship between stenosis severity,  $FFR_{CT}$  measurements and absolute myocardial perfusion parameters. Our study demonstrates that vFAI is lower in vessels with stenotic lesions compared to those without significant stenosis. However, we did not observe a statistically significant stepwise decline of vFAI as stenosis severity increases probably because 91.8 % of all lesions were in the range of 30-70%, confirming the rather unpredictable relationship between hemodynamic significance of

coronary stenoses determined by visual assessment and  $\text{FFR}_{\text{CT}}$  values. Regarding PET measurements with  $^{15}\text{O}$ -water, a significant progressive reduction of stress MBF was observed as stenosis severity increased. MFR was also declined, however, between group comparisons revealed no statistically significant differences for measurements corresponding to coronary stenoses 30-50% vs. those of 50-70% or between the latter and lesions >70%. In contrast,  $^{13}\text{N}$ -ammonia PET measurements were not influenced by coronary stenosis severity. Besides differences between the two tracers in extraction fraction and modeling approaches for perfusion quantification, the lack of statistically significant differences between measurements corresponding to various degrees of disease severity, is more likely due to the fact that more than half of lesions were in the range of 30-50%, for which prior studies have shown no difference in MFR or stress MBF compared to vessels without significant narrowing.

### **Pressure driven measurements versus absolute myocardial perfusion**

Pressure-derived measures of CAD hemodynamic relevance (i.e. FFR and  $\text{FFR}_{\text{CT}}$ ) can only give an indirect assessment of coronary flow capacity, showing a frequent discrepancy with absolute MFR values [22], which becomes more pronounced in patients with coexistent diffuse CAD and/or impaired microvascular function [138]. In keeping with these observations, we have demonstrated a modest statistically significant correlation between vFAI and absolute myocardial perfusion parameters, with discordant values in roughly 20% of the analyzed vessels. A significant determinant of this modest relationship is the methodology used for computation of vFAI that is based on the assumption that minimal coronary resistance does not differ between stenosed and normal coronary arteries [125]. Beyond methodological aspects, in principle, physiological parameters can also contribute to the discordance between MFR and vFAI. The latter can be reduced in cases of epicardial disease as a result of a pressure drop, but MFR can be preserved if there is an intact vasodilator response. Conversely, a normal vFAI with impaired MFR may be the result of an undiseased coronary artery but underlying microvascular disease, or it could be derived by diffuse epicardial disease either on its own or in combination with microvascular pathology, where the low flow through the small vessels does not permit the development of significant pressure gradient across the epicardial stenosis.

In our study, the optimal cut-off value of vFAI to identify significant coronary lesions, defined as stenosis with downstream  $\text{MFR} \leq 2.5$  for  $^{15}\text{O}$ -water studies or  $< 2$  for  $^{13}\text{N}$ -ammonia, was  $\leq 0.8$  and  $\leq 0.79$  respectively, which mirrors previously published studies on the accuracy of  $\text{FFR}_{\text{CT}}$  in unmasking the presence of invasively assessed significant CAD. vFAI thresholds

of  $\leq 0.8$  and 0.82 for  $^{15}\text{O}$ -water studies and  $^{13}\text{N}$ -ammonia respectively were identified for prediction of abnormal stress MBF with accuracy levels comparable to those recorded for MFR, thus providing a comprehensive validation of this novel diagnostic pressure-based measure of coronary vessel behavior.

### **Determinants of inducible myocardial ischemia in patients with intermediate coronary lesions**

A number of studies have demonstrated that coronary revascularization should be limited to patients with high-risk ischemia on MPI (i.e.  $>10\%$  of the LV). Conversely, conservative management is favored for patients with mild or no ischemia on MPI or in the presence of a normal FFR ( $>0.8$ ). However, estimates of CAD hemodynamic relevance on MPI and FFR frequently disagree, questioning the interchangeability of those measures [139]. For instance, the agreement rate between SPECT and FFR has been reported to be in the region of 80% and becomes lower in the acute setting where the two modalities disagree in 30% of patients [139].

Despite extensive validation of FFR<sub>CT</sub> against invasive FFR [140], there is limited data on the relationship between the former and radionuclide MPI-derived parameters. Moreover, no previous study has assessed the relationship between FFR<sub>CT</sub> and high-risk ischemia ( $>10\%$  of the LV) or the ability of the former to predict the latter. The only study so far by Nakanishi R et al. has shown only modest concordance between SPECT MPI and FFR<sub>CT</sub> [141]. Although not directly comparable, our study shows a lack of correlation between vFAI and PET perfusion and in addition, vFAI has only moderate accuracy in unmasking the presence of myocardial ischemia on  $^{13}\text{N}$ -ammonia PET, which increases to 80% when only high-risk ischemia was considered. These findings are expected considering the different physiological concepts underlying MPI and FFR<sub>CT</sub> for identifying the functional significance of epicardial stenoses. These differences appear to be even more pronounced in the absence of absolute quantification, as only a relative assessment of myocardial perfusion heterogeneity is feasible by semi-quantitative image analysis.

### **Clinical implications**

The development of a CCTA based index which could detect reliably the functional significance of a coronary lesion in the range of 30-90% has become of paramount importance as it will allow a complete anatomo-functional characterization of CAD burden by a single investigation, possibly reducing the downstream inappropriate referral to ICA. In this context, vFAI is a



validated pressure-based index of CAD hemodynamic relevance, derived from the application of computational flow dynamics to a standard CTCA datasets, without need for extra radiation exposure, and with a limited computational time [88]. Interestingly, while CT-based coronary functional evaluation has already been shown to mimic the results of invasive FFR [140, 142], a validation of this technique against PET-derived absolute MBF parameters as integrated measures of global coronary fluid dynamics, has never been performed. This latter aspect is of particular relevance, since vFAI/FFR<sub>CT</sub> values, obtained after the three-dimensional modelization of coronary plaque burden, may only simulate the hemodynamic impact of epicardial atherosclerosis, disregarding the possible impact of underlying microvascular dysfunction. Our data show that vFAI correlated moderately with PET-derived absolute stress MBF and MPR values, and were able to predict the presence of impaired myocardial perfusion in the majority of patients. Nevertheless, the disagreement between vFAI and MFR that existed in around 20% of vessels confirms further that no single measure can depict entirely the complexity of coronary physiology, suggesting a potentially complementary role of vFAI for CAD diagnosis and risk stratification.

## **Limitations**

The results of the present study should be interpreted by taking into account its modest sample size. Furthermore, for technical reasons, only a per-vessel evaluation of CCTA and corresponding PET data analysis was feasible. Nevertheless, we have followed a hybrid imaging-based approach of CCTA and PET datasets achieving perfect co-localization of each coronary artery with the pertinent myocardial territory and avoiding any incorrect assignment of vFAI and MBF data. We have excluded from the initial cohort, 28% of patients with CCTA studies because of significant motion or calcification, factors that hamper image quality and vFAI assessment, however, prior studies have also excluded a high rate of CCTA scans. In any case, exclusion of vessels of inadequate quality for calculating vFAI is not an important limitation, since the current study was not designed to assess the diagnostic accuracy of CCTA when vFAI is incorporated in the data analysis. Instead, our aim was only to test the relationship between vFAI and quantitative myocardial perfusion and assess the ability of the former to predict perfusion abnormalities in vessels with stenotic lesions. In our study, the degree of anatomic stenosis was derived from CTCA and not from coronary angiography, which is the gold standard for narrowing assessment. Nonetheless, the excellent accuracy of CCTA in quantifying CAD severity has been already demonstrated, making this technique of particular value in the

evaluation of patients at intermediate pre-test probability of CAD [111]. Finally, ICA-FFR was available only in 13.7% of cases, however, the aim of the current study was not to compare vFAI with FFR. We have already performed such assessment previously, and in agreement with prior studies, we have selected in the present one, functional parameters as the reference standard to test the predictive value of vFAI. We acknowledge that the latter reflects only vessel geometry-related changes without taking into account alterations at the microcirculation level, but is a simple index with limited computational time, which defines with reasonable accuracy the presence of hemodynamically significant coronary lesions on PET imaging.

### **4.3. Computational assessment of coronary stenosis using invasive techniques**

This section describes two of our proposed methods regarding the computational hemodynamic assessment of coronary arteries using data deriving from invasive imaging modalities. In particular, the first method that will be described uses only one imaging modality (IVUS), whereas, the second one utilizes data from two of the most common invasive coronary imaging modalities (IVUS and Angio).

#### **4.3.1 Virtual Functional Assessment of Coronary Stenoses Using Intravascular Ultrasound Imaging**

Functional assessment of intermediate-grade coronary stenoses using fractional flow reserve (FFR) is valuable for the management of stable coronary artery disease [49]. Intravascular ultrasound (IVUS) imaging provides significant anatomic information for guidance of percutaneous coronary intervention but the IVUS-based anatomic measures of lesion severity do not correlate well with FFR [59]. The high cost, additional procedure time and the incremental risk during the intervention are among the main factors which preclude the regular use of both FFR and IVUS in the same patient in the catheterization laboratory. Recently, the use of 3D quantitative coronary angiography (3D-QCA) coupled with computational fluid dynamics (CFD) has been proposed for virtual functional assessment of stenosis [85, 88], but a similar approach using IVUS images has not been previously studied.

In the current work, we aimed to investigate the performance of virtual functional assessment of coronary stenoses using IVUS-based 3D coronary artery reconstruction and computational fluid dynamics against FFR measured using the pressure wire.

#### 4.3.1.1 Dataset

22 patients who underwent VH-IVUS were enrolled in the current study. Our study population presented either an abnormal stress test or stable angina and therefore required an invasive evaluation of the coronary physiology. IVUS imaging was performed by using a motorized pullback device (constant speed of 0.5 mm/sec) with either a phase-array 20 MHz transducer (16 arteries; Volcano Corporation, Rancho Cordova, CA-16 arteries) or a mechanical 40 MHz transducer (6 arteries; Opticross, Boston Scientific Corporation, MA, USA). FFR was measured using a pressure wire (ComboWire XT, Volcano Corporation, CA, USA or PressureWire Aeris, St Jude Medical, MN, USA) according to standard clinical practice.

#### 4.3.1.2 Arterial Segment 3D Reconstruction

In order to avoid any artifacts caused by the relative motion of the heart during a cardiac cycle, the end-diastolic (R-peak) frames were extracted from the respective IVUS sequences. The aforementioned R-peak frames were used to annotate the luminal borders using an in-house developed algorithm, thus creating a border of 85 points per frame (Figure 36). These points were then translated into pixel coordinates regarding the x and y axes. Using a pixel spacing value of  $0.02 \text{ mm/pixel}$  in both axes that was acquired from the respective IVUS dicom tag, we transformed the pixel coordinates into Cartesian coordinates. In order to define the actual pullback length in each case, given the fact that the pullback was motorized, we calculated the total pullback time from the IVUS sequence and used Eq. 53 to calculate the total length:

$$L_{total} = \frac{t}{u_{pullback}}, \quad (53)$$

where  $t$  is the total pullback time (s) and  $u_{pullback}$  is the pullback speed (mm/s).

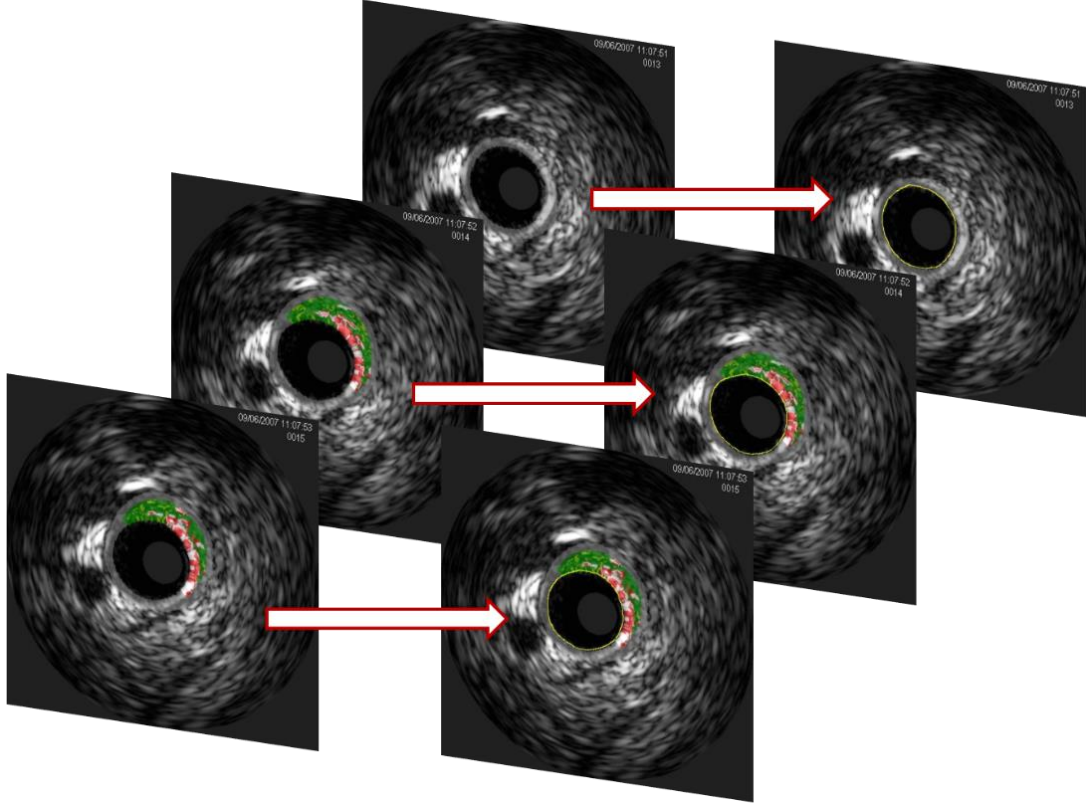


Figure 36: Annotation and segmentation process of the IVUS frames.

Then, for a given number of VH-IVUS frames  $n$ , we have  $n-1$  equidistant spaces between the frames. In order to define the distance between the aforementioned frames in the  $z$  axis, we divide the total length of the examined segment with the total number of spaces that were previously defined (Eq. 54):

$$d = \frac{L_{total}}{n-1} \quad (54)$$

where  $d$  is the distance between two consecutive frames,  $L_{total}$  is the total length of the arterial segment and  $n$  is the number of frames (Figure 37).

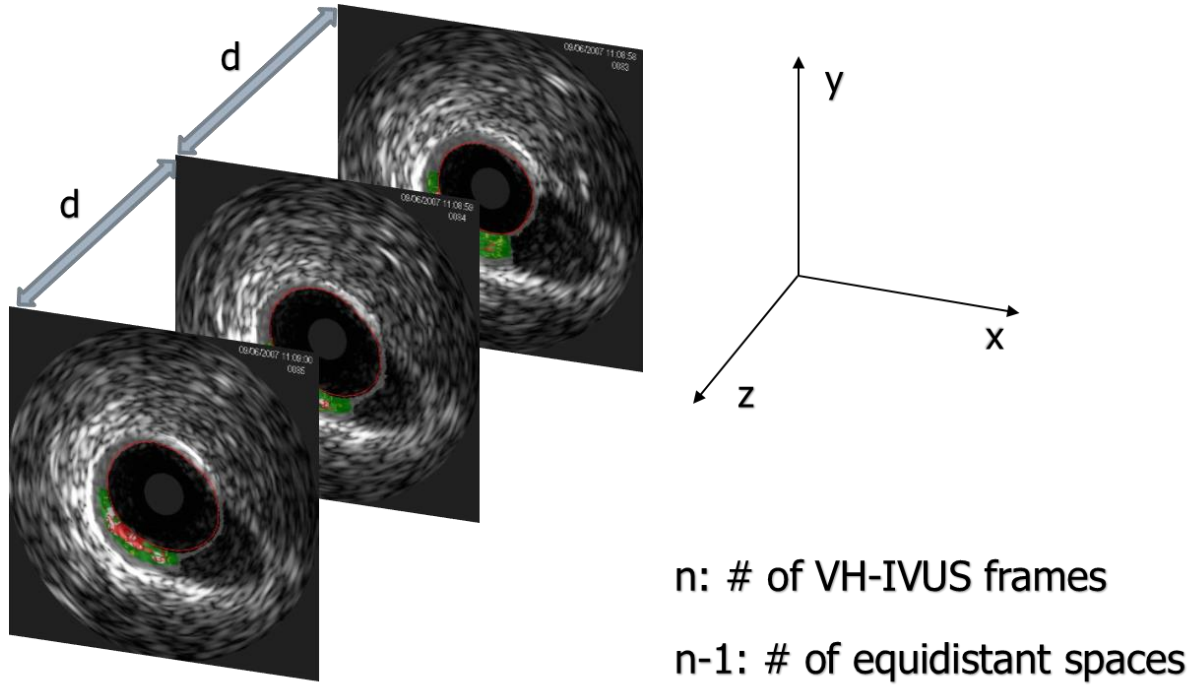


Figure 37: IVUS 3D reconstruction method

Finally, the segmented frames are placed perpendicularly on the z axis at the defined points that are calculated from Eq. 3, thus creating the final point cloud. The point cloud is then transformed into a straight 3D volume (Figure 38).

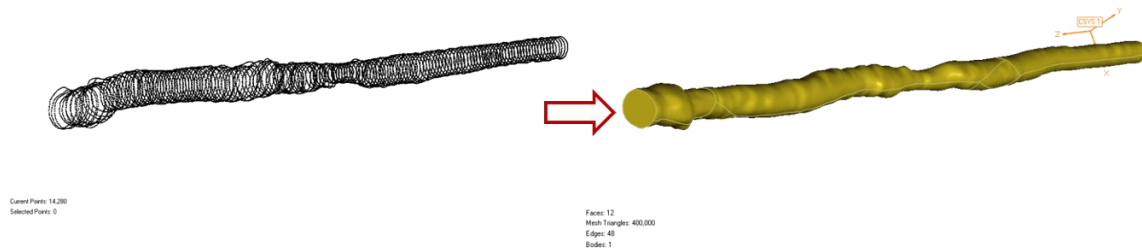


Figure 38: Point cloud to 3D volume transformation process.

#### 4.3.1.3 Results

In the 22 cases studied, the mean FFR was  $0.87 \pm 0.09$ , and 5 cases had  $FFR \leq 0.8$  indicating functionally significant stenoses. There was a close correlation between IVUS-based vFAI and FFR (Spearman correlation coefficient  $[r_s] = 0.88$ ,  $p < 0.0001$ ; Figure 1E). The Bland-Altman plot showed a mean difference of  $0.0196 \pm 0.037$  ( $p = 0.023$  for difference from zero; Figure 1F) indicating that vFAI slightly overestimates on average the FFR. All 5 cases with functionally significant stenoses ( $FFR \leq 0.8$ ) were correctly categorized by the IVUS-based vFAI

(vFAI $\leq$ 0.8). In our very small sample size, the diagnostic accuracy, sensitivity, specificity, positive predictive value and negative predictive value of the IVUS-based vFAI ( $\leq$ 0.80) against FFR ( $\leq$ 0.80) were 95.5, 100, 94.1, 83.3 and 100%, respectively (Figure 39).

#### **4.3.1.4 Discussion**

Our results demonstrate for the first time the feasibility of using routine intravascular imaging for virtual functional assessment of coronary stenoses. Previous studies have shown that anatomic indices (e.g. minimum lumen area) derived from IVUS or optical coherence tomography have a mediocre correlation with FFR and cannot be used in routine practice for identifying functionally significant stenoses with a high diagnostic accuracy [59, 61]. Our approach differs from previous studies, making use of the cross-sectional intravascular images for performing blood flow simulation, thereby providing the pressure distribution across a lesion. Although our method neglects the curved geometry of the coronary arteries on the epicardial surface, our results suggest that the 3D curvature does not have a major impact on the pressure distribution, and thus, this limitation may not be critical for accurate virtual functional assessment of coronary stenoses.

The proposed approach provides both anatomic and physiologic information, thereby enabling complete and comprehensive assessment of coronary lesions pre- and post-intervention using one intravascular imaging catheter without requiring the pressure wire. These observations may have important clinical implications in routine practice, and warrant further investigation in a larger clinical setting in order to appropriately assess the diagnostic performance of the proposed approach.

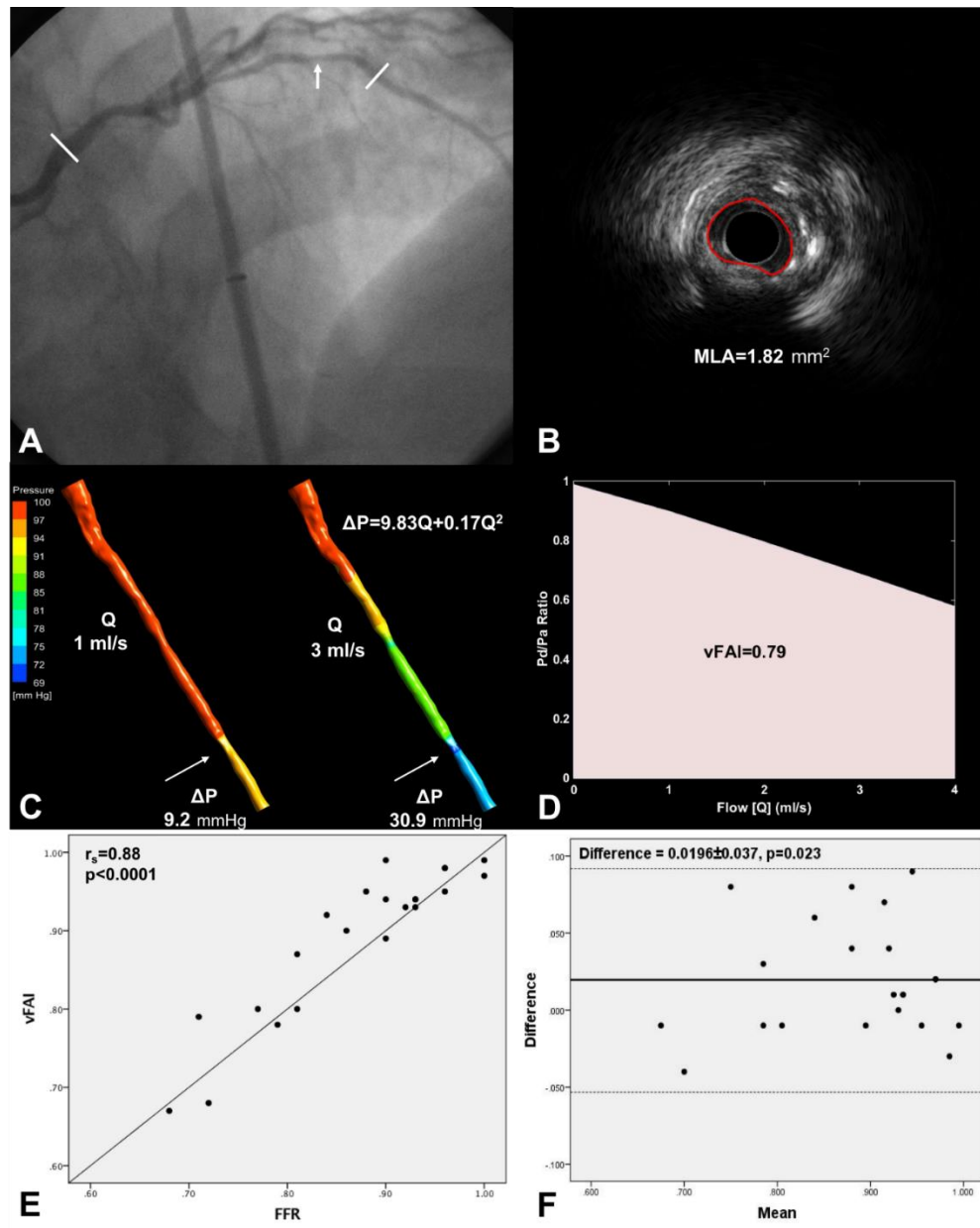


Figure 39: **A.** Angiographic image of a Left Anterior Descending artery with a functionally significant lesion assessed by fractional flow reserve (0.71). The two straight lines indicate the proximal and distal ends of the segment interrogated by intravascular ultrasound (IVUS). The arrow indicates the location of the minimum lumen area. **B.** IVUS image corresponding to the minimum lumen area (1.82 mm<sup>2</sup>) of the lesion. **C.** Three-dimensional coronary lumen reconstruction after linearly stacking the lumen borders of the IVUS images. A color map denotes the pressure distribution for the simulated rest and hyperemic flow rates which are used for the computation of the virtual functional assessment index (vFAI). The arrow denotes the location of the minimum lumen area shown in the IVUS image. **D.** Relationship between the ratio of distal to aortic pressure ( $P_d/P_a$ ) and flow for the studied artery, and calculation of the virtual functional assessment index as the ratio of the area under the curve to the total area. **E.** There was a close correlation between the IVUS-based vFAI and fractional flow reserve (FFR;  $r_s=0.88$ ). **F.** The Bland-Altman plot showed a mean difference of 0.020 (solid line) between vFAI and FFR; the dashed lines represent the values at  $\text{mean} \pm 1.96\text{SD}$ . Of note, 20 plotted values are shown in graphs E and F due to overlapping of cases with identical FFR and vFAI values (i.e. there were two cases with  $\text{FFR}=0.96$  and  $\text{vFAI}=0.98$ , and another two cases with  $\text{FFR}=0.93$  and  $\text{vFAI}=0.94$ ).

### **4.3.2 Computational Assessment of the Fractional Flow Reserve using IVUS and ICA**

In this section, we present a method that allows the calculation of the FFR values in 3D coronary arterial models, reconstructed from IVUS and coronary angiographic images without the induction of hyperemia, and we compare the FFR estimations to the actual FFR values measured invasively using a pressure wire. The key aspect of the proposed method lies on the fact that the use of the pressure wire is not required since routine data from the angiography sequence and aortic pressure during diagnostic catheterization are used for estimating the appropriate boundary conditions for the simulation. Thus, FFR assessment using our method does not require a pressure wire and the induction of hyperemia, and thus it is cost effective. Moreover, it provides the opportunity of retrospective FFR assessment after the completion of the catheterization.

#### **4.3.2.1 Dataset**

In this report, seven coronary arterial segments (4 right coronary arteries [RCA] and 3 left anterior descending arteries [LAD]) were studied in 6 patients that underwent angiography and IVUS examination. Pressure values were obtained at a distal artery location of interest (i.e., distal to a stenosis visible in angiography) using a coronary guide wire with miniaturized transducers at the tip of the wire (Combo wire, Volcano Corp., San Diego, CA). The examined segments were mildly diseased, presenting FFR values ranging between 0.92-0.99. Only one patient presented angina, a fact that constitutes a limitation in our study and will be presented in detail in the last section.

#### **4.3.2.2 3D Reconstruction of the Arterial Segments**

The 3D reconstruction process consists of several steps and has been previously presented and validated by our group. In brief, the catheter path is identified in the biplane end-diastolic angiographic images, and the 3D catheter path is extracted. Then, the end-diastolic frames are identified and extracted from the IVUS sequence. The lumen borders are segmented from the end-diastolic images and placed onto the 3D catheter path. Finally, the IVUS contours are appropriately orientated using efficient 3D geometry algorithms, and the orientation of the first IVUS frame is determined so that the 3D model matches the silhouette of the lumen in the biplane angiographic images.



#### 4.3.2.3 Flow Measurement

A key feature of the presented method is the calculation of the volumetric flow rate (average flow during the cardiac cycle) under resting conditions from the angiographic image sequence. The flow rate is calculated by the angiographic frames required for the radio-opaque contrast material to pass from the inlet to the outlet of the studied segment, the corresponding volume directly computed from the 3D reconstructed coronary segment and the frame rate. A representative case with the flow calculation is presented in Figure 40. The final equation that is used to calculate the flow rate is the following:

$$\text{Flow Rate} = \frac{\text{Frame Rate (frames/sec)} \times \text{3D Volume (ml)}}{\text{Frame Count}} \quad (55)$$

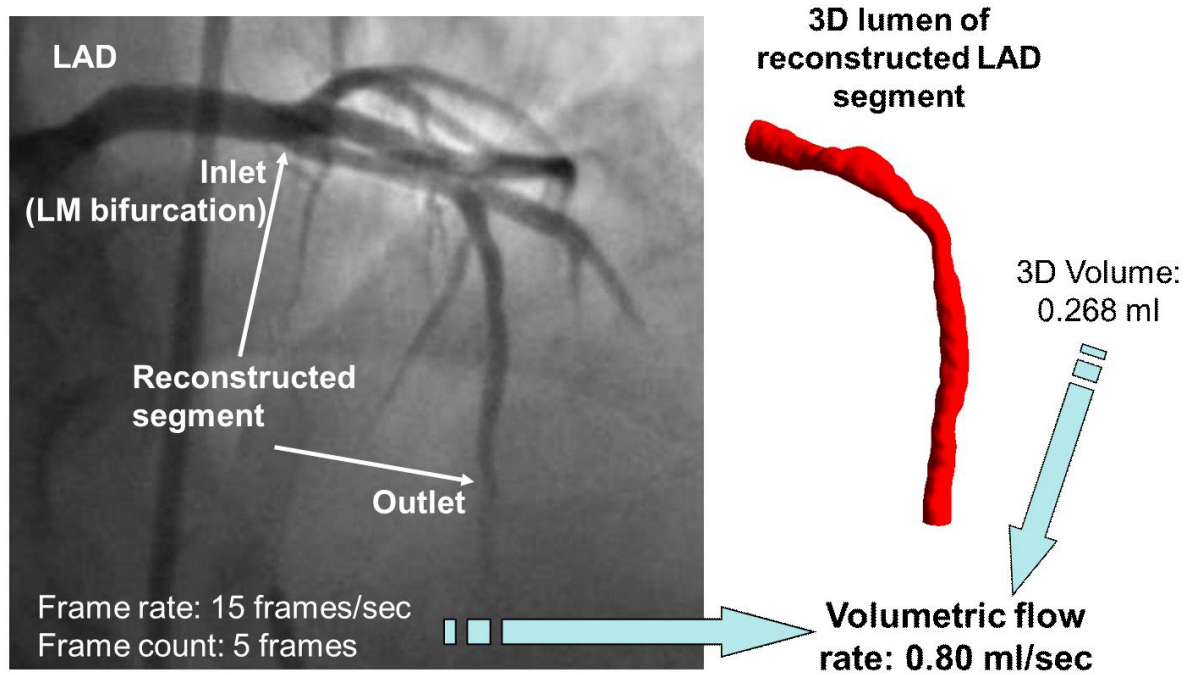


Figure 40: Flow Rate Measurement Process.

#### 4.3.2.4 Boundary Conditions

The average patient-specific aortic pressure under resting conditions was applied at the inlet, while at the outlet the average coronary blood flow under resting conditions in the diastolic wave-free period (derived from the iFR paradigm [54]) of the cardiac cycle was determined and applied. The wave-free period in diastole begins 25% of the way into diastole and ends 5 ms

before the end of diastole. Figure 41 presents the wave-free period in a generic flow waveform. The average coronary blood flow during the diastolic wave-free period was determined using the average patient-specific volumetric flow rate throughout the cardiac cycle (as described above) and a generic coronary flow waveform for all patients. At the wall of the artery, no-slip boundary condition was imposed.

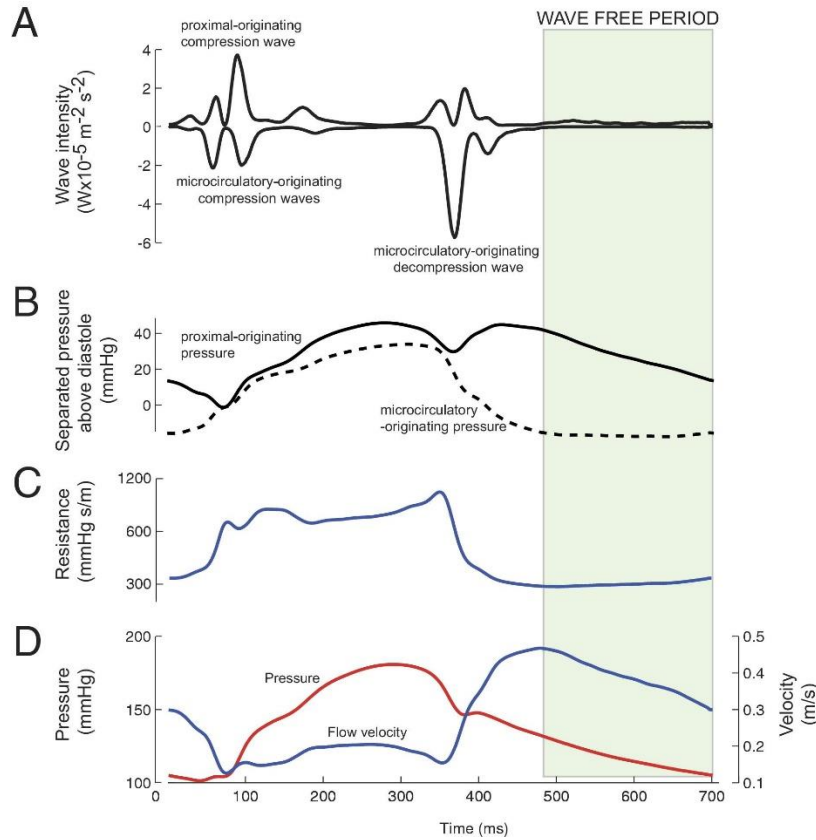


Figure 41: Pressure and flow waveforms during the cardiac cycle; the wave-free period in diastole is denoted [54].

#### 4.3.2.5 Results

The objective of the presented work was to investigate the efficiency of the proposed FFR calculation method in a dataset of 7 patient-specific coronary arterial segments. Linear regression analysis and the Bland-Altman plot were performed to investigate the correlation and agreement between the simulated and the actual FFR values. Figure 42 illustrates a representative example of an LAD segment (corresponding to the angiographic images in Fig. 2) with the simulated FFR (sFFR) assessment along the length of the artery; sFFR at the outlet was 0.92, while the invasively measured FFR value was 0.94. The linear regression analysis showed a good correlation between the sFFR and the actual FFR values with an  $r$  value of 0.85. The regression analysis is shown in detail in Figure 43. The Bland-Altman plot demonstrated

a high similarity between the calculated and the invasively measured FFR values with a mean difference of 0.002 between the sFFR estimations and the invasively measured FFR. The Bland Altman plot is presented in Figure 43.

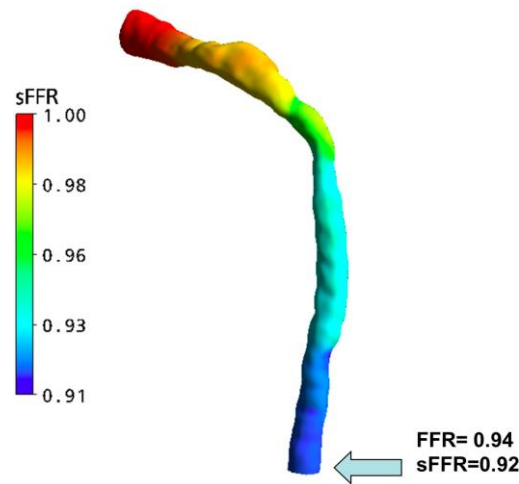


Figure 42: Simulated FFR distribution throughout a LAD segment and comparison to the measured FFR value.

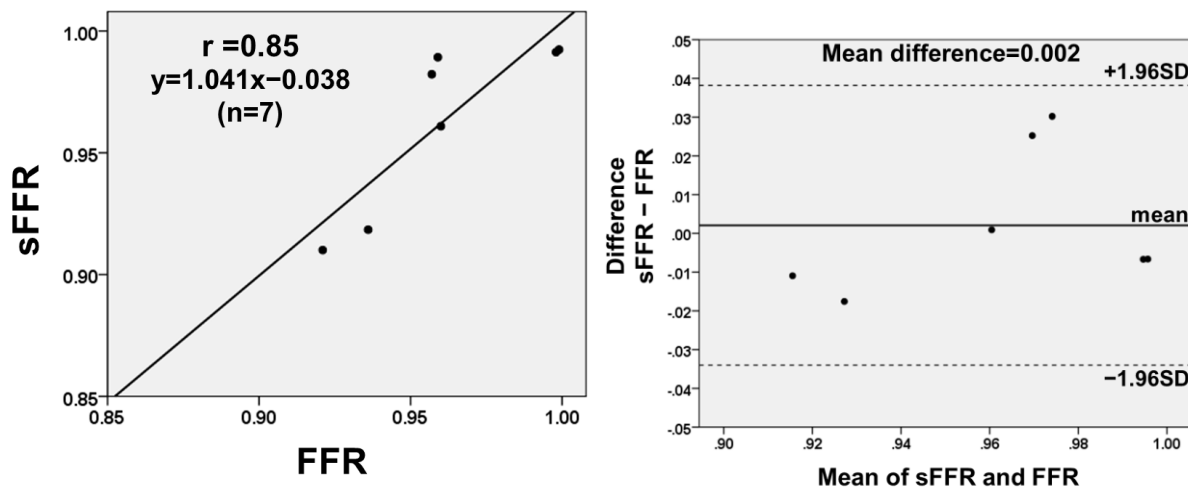


Figure 43: Linear Regression plot and Bland Altman plots for all 7 cases.

#### 4.3.2.6 Discussion

In the current study, we proposed a method which enables FFR assessment in 3D coronary arterial models reconstructed from IVUS and angiographic images without the use of a pressure wire, and we validated our approach by comparing the sFFR values to the FFR values that were measured conventionally using a pressure wire. Arterial segments from 6 patients with mild lesions were included in this pilot study. The results that were obtained with the proposed method correlated very well to the invasively measured FFR values, indicating the efficiency

of our method. Moreover, one main advantage is that the simulated FFR values are obtained without the induction of hyperemia. Another key element of our study is the fact that our method can be considered as semi-invasive whereas the traditional FFR measurement method is fully invasive since it requires the insertion of a wire in the coronary artery. Of note, our approach could provide a cost-effective method for measuring FFR since the use of costly materials/drugs (i.e., pressure wire and adenosine) is not required. Finally, our method also enables FFR assessment using retrospective data after the completion of the catheterization if the appropriate data are available. Future work will be focused on the 3D reconstruction of coronary segments using only biplane angiographic images, which in combination with the current methodology, will constitute a powerful tool for the calculation of the FFR value using only routine angiographic data.

Our study is limited by the small number of cases included. Furthermore, all cases presented only mild lesions with FFR values from 0.92-0.99, values that belong to the upper normal range which is above the 0.75-0.80 cut-off value which indicates the absence/presence of inducible ischemia. Finally, our method does not allow the reconstruction of side branches, and thus, their effect on blood flow is not incorporated.

#### **4.3.3 smartFFR: a novel, fast index for the functional assessment of coronary stenoses**

In the majority of our previously described studies, the functional assessment of coronary stenoses was performed using vFAI, which was initially validated using ICA derived 3D models. We extended the validation of the method by using both CCTA derived models, as well as, IVUS derived 3D models reconstructed in a straight manner. The vFAI rationale is based on building the theoretical case-specific pressure gradient ( $\Delta P$ )-flow relationship by performing two separate blood flow simulations in order to calculate the pressure gradient during rest and under stress. This is done in order to calculate the  $P_d/P_a$  values for a range of flow varying from 0 ml/s to 4 ml/s. However, this is based on only two calculated  $\Delta P$  values which are then used to solve the theoretical case-specific pressure gradient ( $\Delta P$ )-flow relationship. In order to tackle this issue and create a more robust method, we proposed a fully computational approach in order to create the  $P_d/P_a$  curve using actual simulated data.

#### 4.3.3.1 Boundary Conditions

Regarding the inlet, an average pressure of 100 mmHg is used, following the rationale of vFAI. The arterial wall is assumed to be rigid and a no-slip and no-penetration boundary condition is used.

The main point of deviation in comparison to the previously validated method is the approach used regarding the outlet boundary condition. A transient blood flow simulation is performed with 5 timesteps is performed with a timestep duration of 0.25 sec and a total simulation time of 1 second. For each timestep, the flow rate that is applied as a boundary condition is 0, 1, 2, 3 and 4 ml/s, respectively (Figure 44). In each timestep, we calculate the  $P_d/P_a$  values and then, the calculated  $P_d/P_a$  values are plotted and fitted using a smoothing spline of 100 points between two calculated values. The final  $P_d/P_a$  curve is then used to calculate the area under the curve using a trapezoidal numerical integration. The final smartFFR value is calculated by dividing the AUC value to the respective AUC value if we had a healthy arterial segment (i.e. AUC=4).

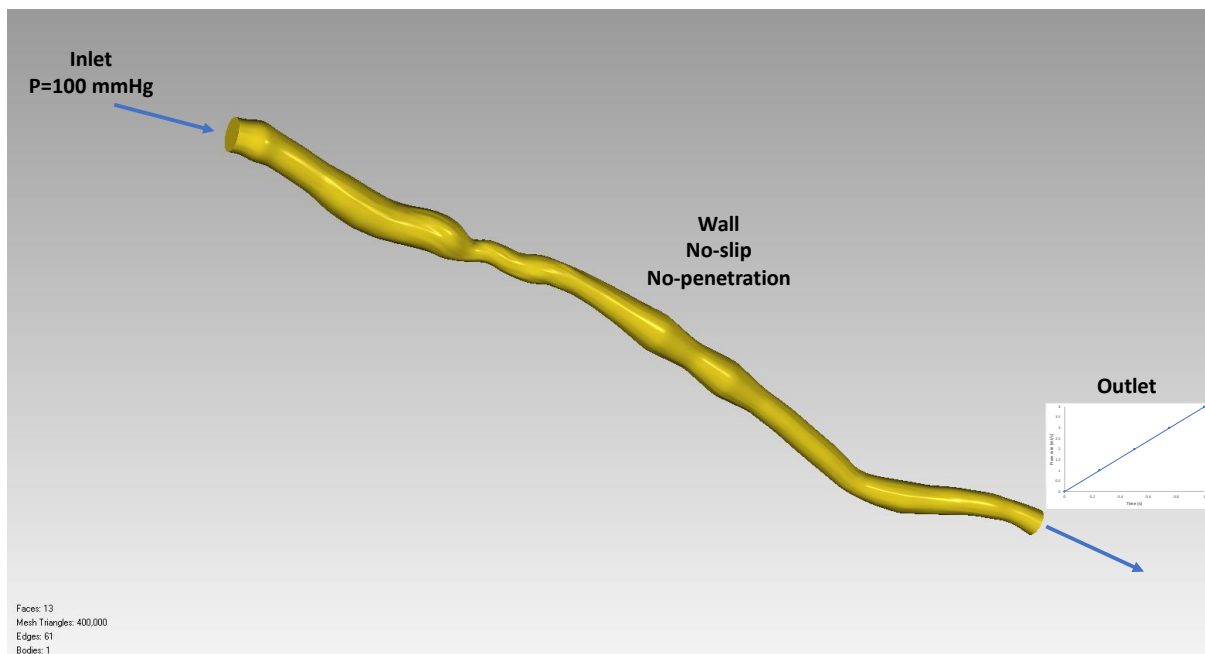


Figure 44: Boundary conditions for the smartFFR calculation.

#### 4.3.3.2 Results

So far, 30 cases have been examined and tested using smartFFR. The dataset consists of 3D models deriving from ICA, CCTA or IVUS-ICA fusion. There is a strong correlation ( $r=0.78$ ,  $P<0.001$ ) and good agreement (Difference= $-0.003\pm0.048$ ,  $P=0.736$ , lower limit= $-0.097$ , 95%

CI -0.1288 to -0.06649, upper limit=0.09165, 95% CI 0.06049 to 0.1228) between smartFFR and the invasively measured FFR as it can be depicted from Figure 45 and Figure 46. Moreover, a ROC analysis was also performed in order to identify the optimal threshold to diagnose ischemia for smartFFR. The optimal threshold to predict ischemia, deriving from the Youden index, was  $\leq 0.78$ . The accuracy, sensitivity, specificity, positive predictive value (PPV) and negative predictive value (NPV) of the proposed method was 85%, 66.9%, 100%, 100% and 70%, respectively (Table 16).

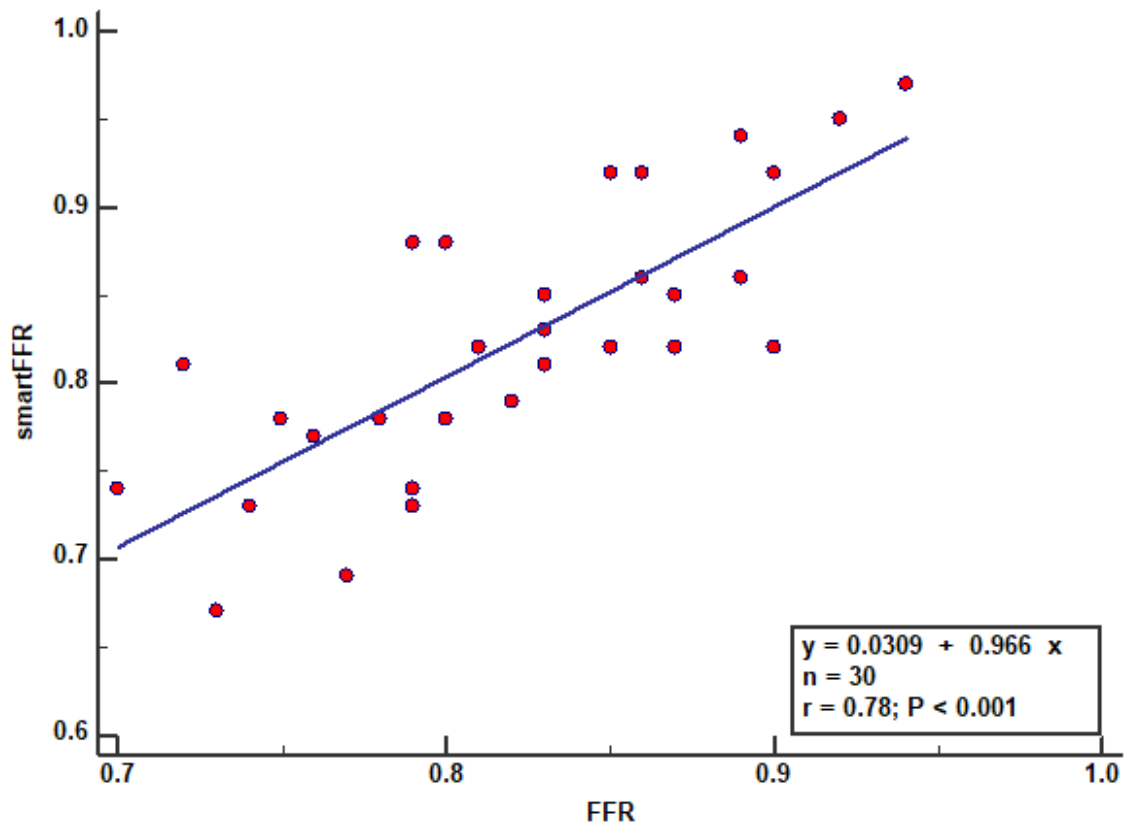


Figure 45: Regression plot between smartFFR and the invasively measured FFR.

Table 16: Per-vessel Diagnostic performance for smartFFR

**FFR $\leq 0.80$**

	Accuracy	Sensitivity	Specificity	PPV	NPV	TP	TN	FP	FN
<b>smartFFR <math>\leq 0.78</math></b>	85%	76.9%	100%	100%	70%	10	17	0	3

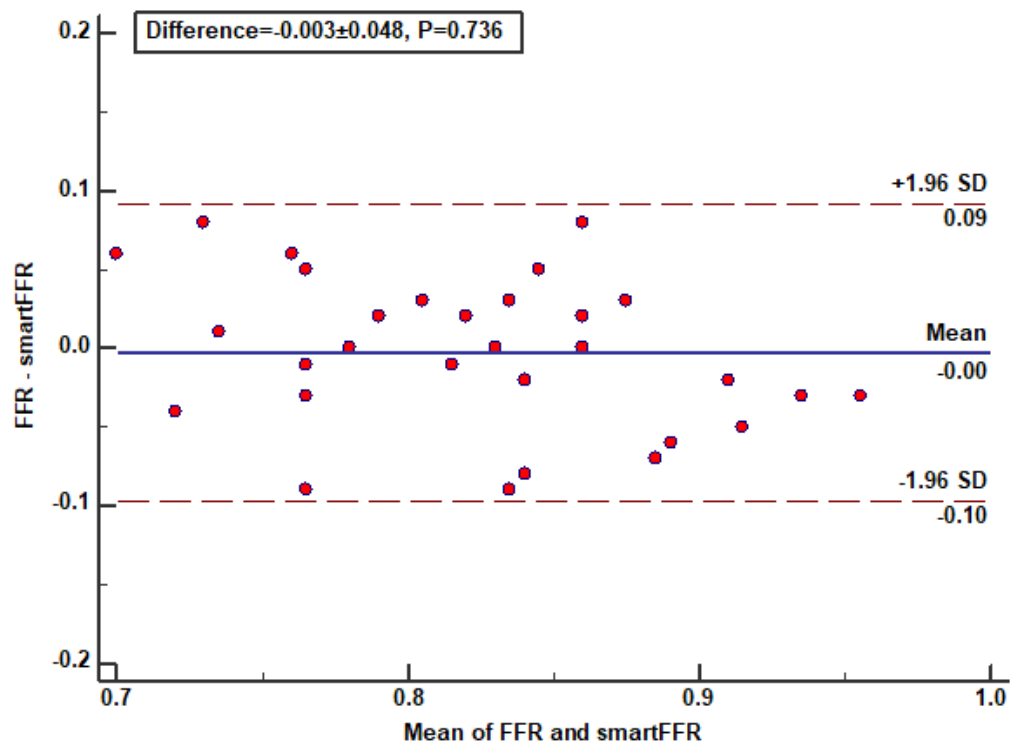


Figure 46: Bland-Altman plot for the two methods.

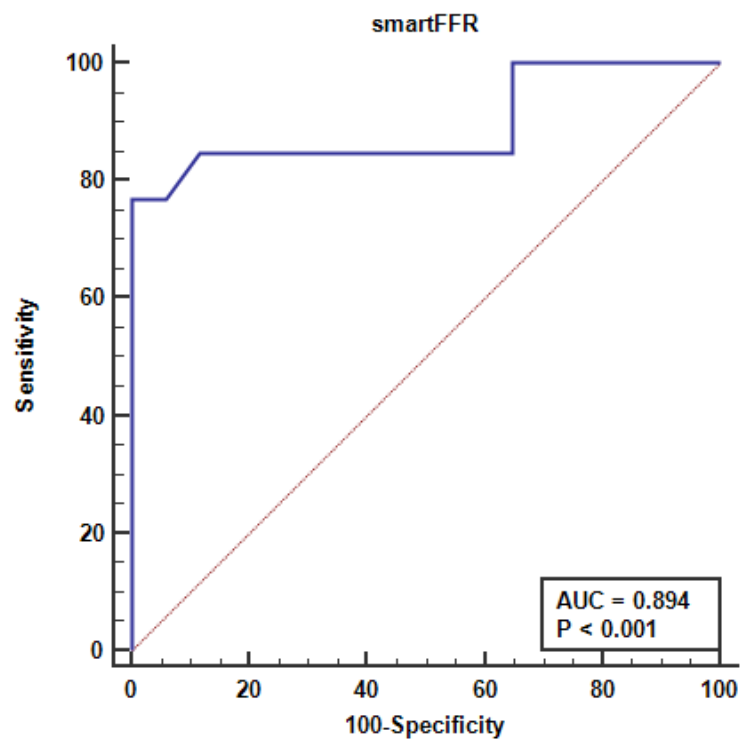


Figure 47: ROC analysis for the smartFFR index.

#### 4.3.3.3 Discussion

We have developed a new, robust index for the computational functional assessment of coronary arteries called smartFFR. The aforementioned index follows the trend of the past 5 years which tends to eliminate the use of a pressure wire for the functional assessment of coronary stenoses. The validation dataset of the method which is currently under constant expansion, consisted of 30 vessels deriving from the most common coronary imaging modalities. Good agreement and strong correlation was found between our method and the invasively measured FFR. When compared to the already validated vFAI, smartFFR differs in the way the  $P_d/P_a$  curve is constructed since it is computationally calculated and does not require the intermediate involvement of the respective theoretical case-specific pressure gradient ( $\Delta P$ )-flow relationship which also requires several assumptions to be made. The total computational time required for the transient blood flow simulation is less than 3 minutes per case, thus constituting the method almost real-time. Moreover, it can be applied to any 3D arterial model deriving from the most well-known coronary imaging modalities. Furthermore, with proper processing of the 3D models, the smartFFR index can be calculated throughout the whole length of the artery and not only at the distal end. This can be easily achieved by creating cross-sectional planes of the artery for every 0.5 mm and calculating smartFFR for each plane.

We also did a sensitivity analysis regarding the timesteps used for each case, as well as the total heart cycles used, in order to see if the produced results were superior to the simpler 5-timestep simulation. However, the produced results did not reveal any noteworthy differences, thus leading us to use the simplest 5-timestep approach. We also did a sensitivity analysis regarding the points used to interpolate the spline fit in the creation of the  $P_d/P_a$  curve, concluding that 100 points is the optimal threshold to achieve accurate results.



## Chapter 5: Integrated Systems for 3D Coronary Reconstruction, Functional Assessment and Multiscale modelling

---

5.1. Introduction

5.2. Multiscale - Patient-Specific Artery and Atherogenesis Models

5.3. Art Care: A Multi-Modality Coronary 3D Reconstruction and Hemodynamic Status Assessment Software

---

### 5.1. Introduction

The continuous increase in the mortality rate due to cardiovascular diseases (CVD) and more particularly due to coronary artery diseases (CAD) has constituted the development of methods that allow the anatomic and functional assessment of coronary vessels of utmost importance. As we described in the previous chapters, several 3D reconstruction methods have been developed throughout the past two decades, utilizing every coronary imaging modality available in everyday clinical practice. Following these reconstruction methods, the constant improvement of CFD techniques has constituted the assessment of the hemodynamic status of the coronary vasculature possible, requiring far less computational time than in the near past. Furthermore, CFD has also been used to create plaque progression models in order to predict the possible evolution over time for diseased coronary segments. Regarding models for mass transport and plaque progression, several studies have been proposed to model the mass transport and endothelial permeability in arteries. The most common used conditions for the endothelial permeability are the Kedem-Katchalsky equations, which describe the permeability in biological membranes. Complex transport models in arteries consider the arterial wall as

multilayer, consisting of more than one layer. These models are more realistic because they represent the arterial wall constituting from the endothelium, the intima, the media and the adventitia.

Over the years, some dedicated 3D-reconstruction and coronary functional assessment commercial packages have also been developed. They can be classified into two categories: a) single modality 3D reconstruction software and, b) 3D reconstruction software packages that fuse two coronary imaging modalities. The first category consists of systems that utilize plain traditional invasive angiography images [81, 143-145] or Coronary Computed Tomography Angiography (CCTA) images [146]. The second category includes systems which fuse IVUS and angiography images [147, 148], as well as, OCT and angiography images [149, 150]. These systems produce accurate 3D coronary models providing the clinician with the ability to analyze the coronary vasculature visually or with some additional information based on the Quantitative Coronary Analysis (QCA) data that are calculated.

In this chapter, we describe two integrated systems for 3D coronary reconstruction, functional assessment and multiscale modelling that were developed during the past 8 years. The first platform called ARTool, integrates technologies of 3D image reconstruction from various image modalities, blood flow and biological models of mass transfer, plaque characterization and plaque growth. The second software suite called Art Care, is an innovative suite of software modules that performs 3D reconstruction of coronary arterial segments using different coronary imaging modalities such as IntraVascular UltraSound (IVUS) and invasive coronary angiography images (ICA), Optical Coherence Tomography (OCT) and ICA images, or plain ICA images and can safely and accurately assess the hemodynamic status of the artery of interest.

## **5.2. Multiscale - Patient-Specific Artery and Atherogenesis Models**

In this section, we present a platform for the development of multiscale patient specific atherogenesis models, called ARTool. The methodology integrates three levels involved in the atherogenesis procedure, that is the anatomical model of the arterial tree, the blood flow model and the molecular/cell model of the arterial wall/blood composition and the biological mechanism involved in the generation and growth of atherosclerotic plaque.

### **5.2.1 3D image reconstruction**

The 3D image reconstruction software that is used within ARTool has been developed based on recent research studies. All algorithms have been previously validated and proven to be effective.

The platform is able to process images from various imaging modalities. More specifically, IVUS and biplane angiography are used for the reconstruction of coronary arterial segments [151]. Two end-diastolic angiographic images are used to predict the catheter path. The artery path is approximated using cubic B – Splines and the catheter path is created by the intersection of two splines. IVUS frames are collected at the peak of the R wave.

MRI is used for the reconstruction of carotid arteries [152]. Active contours with gradient vector flow snakes are used along with edge detection techniques for the estimation of the lumen and outer wall border in Time of Flight (TOF) and T1 Weighted (T1W) MR images, respectively. The frame where the bifurcation appears is detected and an interpolation approach is used for the estimation of the bifurcation.

CT reconstruction is based on [153]. In the proposed approach, the segmentation algorithm traverses the 3D volume twice, which is the minimum number of iterations in order to segment objects in a 3D volume.

### **5.2.2 Blood flow and Biological Process Modelling**

ARTool offers the capability to perform blood flow simulations under the assumption of either rigid or deformable walls regarding the 3D models, using the Finite Element Method (FEM). Fluid Structure Interaction (FSI) models are implemented using the loose coupling method to solve the appropriate equations. The arterial walls are considered to be either elastic or hyperelastic and their distal ends are fixed to prevent motion of those regions.

Wall Shear Stress (WSS) as well as Low Density Lipoprotein (LDL) distribution are calculated in order to reveal areas of high risk of plaque initiation or progression. Fluid shear stress in our model is used for the plaque initiation and position at the wall for higher LDL penetration. Blood flow in the lumen domain, which is considered as a 3D fluid flow, is modelled by the Navier-Stokes equations, together with the continuity equation for incompressible fluid:

$$-\mu \nabla^2 \mathbf{u}_l + \rho (\mathbf{u}_l \cdot \nabla) \mathbf{u}_l + \nabla p_l = 0, \quad (56)$$

$$\nabla \cdot \mathbf{u}_l = 0, \quad (57)$$

where  $\mathbf{u}_l$  is the blood velocity in lumen,  $p_l$  is the pressure,  $\mu$  is the dynamic viscosity of blood, and  $\rho$  is the blood density.

Mass transfer in the lumen is coupled with the blood flow and is modelled by a convection-diffusion equation, in the fluid domain:

$$\nabla \cdot (-D_l \nabla c_l + c_l \mathbf{u}_l) = 0, \quad (58)$$

where  $c_l$  is the solute concentration in the blood and  $D_l$  is the solute diffusivity in the lumen. Mass transfer in the arterial wall is coupled to the transmural flow and modelled by a convection-diffusion-reaction equation as follows:

$$\nabla \cdot (-D_w \nabla c_w + k c_w \mathbf{u}_w) = r_w c_w \quad (59)$$

where  $c_w$  is the solute concentration and  $D_w$  is the solute diffusivity in the arterial wall;  $\mathbf{u}_w$  is the blood velocity in the wall,  $k$  is the solute lag coefficient, and  $r_w$  is the consumption rate constant. The LDL transport in the lumen and in the vessel wall are coupled by the Kedem-Katchalsky equations:

$$J_v = L_p (\Delta p - \sigma_d \Delta \pi), \quad (60)$$

$$J_s = P \Delta c + (1 - \sigma_f) J_v \bar{c}, \quad (61)$$

where  $L_p$  is the hydraulic conductivity of the endothelium;  $\Delta c$  is the solute concentration difference,  $\Delta p$  is the pressure drop and  $\Delta \pi$  is the oncotic pressure difference all across the endothelium;  $\sigma_d$  is the osmotic reflection coefficient,  $\sigma_f$  is the solvent reflection coefficient,  $P$  is the solute endothelial permeability, and  $\bar{c}$  is the mean endothelial concentration. The first term in the Kedem-Katchalsky equations ( $P \Delta c$ ) of the right-hand side (Eq. 61) defines the diffusive flux across the endothelium, while the second term  $(1 - \sigma_f) J_v \bar{c}$  defines the convective flux. Only the oncotic pressure difference  $\Delta \pi$  is neglected in our simulations due to the decoupling of the fluid dynamics from solute dynamics. The above governing equations are transformed into a FE system of incremental-iterative equations and solved over time steps.

The atherosclerotic process starts with the accumulation of LDL in the intima, where part of them are oxidized and become pathological. In order to remove the oxidized particles, circulating immune cells (e.g. monocytes) are recruited. Once in the intima, the monocytes differentiate and become macrophages that phagocytose the oxidized LDL. Fatty macrophages then transform into foam cells. Foam cells are responsible for the growth of a subendothelial plaque which eventually emerges in the artery lumen. The model is a coupled fluid-intima model, since new mass tissue is generated from the foam cells and we have the intima volume increasing, which is fully coupled with the lumen domain. The inflammatory process (transformation of macrophages into foam cells) is modelled using three additional reaction-diffusion partial differential equations.

$$\partial_t Ox = d_1 \Delta Ox - k_1 Ox \cdot M, \quad (62)$$

$$\partial_t M + \text{div}(v_w M) = d_2 \Delta M - k_1 Ox \cdot M + S / (1 - S), \quad (63)$$

$$\partial_t S = d_3 \Delta S - \lambda S + k_1 Ox \cdot M + \gamma(Ox - Ox^{thr}), \quad (64)$$

where  $Ox$  is the oxidized LDL in the wall,  $M$  and  $S$  are concentrations of macrophages and cytokines, respectively, in the intima;  $d_1, d_2, d_3$  are the corresponding diffusion coefficients;  $\lambda$  and  $\gamma$  are the degradation and LDL oxidized detection coefficients; and  $v_w$  is the inflammatory velocity of plaque growth, which satisfies Darcy's law and the incompressibility continuity equation:

$$v_w - \nabla \cdot (p_w) = 0, \quad (65)$$

$$\nabla v_w = 0, \quad (66)$$

where  $p_w$  is the pressure in the arterial wall.

In order to follow the changes of the vessel wall geometry during plaque growth, a 3D mesh moving algorithm, the Arbitrary Lagrangian Eulerian (ALE) is applied. ALE formulation is developed for mesh moving and changing of the structural domain due to intima volume thickness and fluid domain reduction in time. In this way, we included both structural and fluid domain. Macro growth is connected through Eqs. 65-66 and the inflammatory velocity  $v_w$  of the plaque growing from Eqs. 62-64. Two time points were examined, one at the baseline and the other after a period of two months of high fat diet.

### 5.2.3 Plaque Characterization

ARTool includes also an automated plaque characterization application using three image modalities; IVUS, MRI and CT. Concerning the plaque characterization module using IVUS images, a hybrid approach is used, that is based on image filtering and random forests. The classification scheme includes soft plaques (lipid), hard plaques (calcium and fibrotic) and hard calcified (calcium) plaques. The characterization of plaque using MRI was based on an image processing algorithm which uses as input three different contrast weightings of MRI: T1, T2 and Proton Density (PD). The algorithm classifies: fibrous tissue, lipid core, hemorrhages and calcifications. Finally, the method developed to characterize plaque formations using CT images includes the detection and characterization of calcium formations. The image processing technique that was developed is based on the fact that calcium appears brighter than the lumen in the CT.

### 5.2.4 Results

The platform can be used for the visualization, assessment and prediction of the atherosclerotic plaque development. The 3D reconstruction module gives the capability for fast and accurate reconstruction of arterial segments and trees. The algorithms are validated using annotated datasets by expert physicians. The mean error of the lumen and media-adventitia area is  $-0.63 \pm 8.71\%$  and  $-2.09 \pm 8.61\%$ , respectively, in the IVUS and Angiography reconstruction. In the case of the carotid artery reconstruction using MRI the mean error is  $-3.21 \pm 6.39\%$  and  $1.92 \pm 5.88\%$  for the lumen and outer vessel wall, respectively. In the case of CT reconstruction, the MICCAI evaluation framework [153] was employed, by measuring the number of correctly segmented arteries. The accuracy obtained is 84.1%.

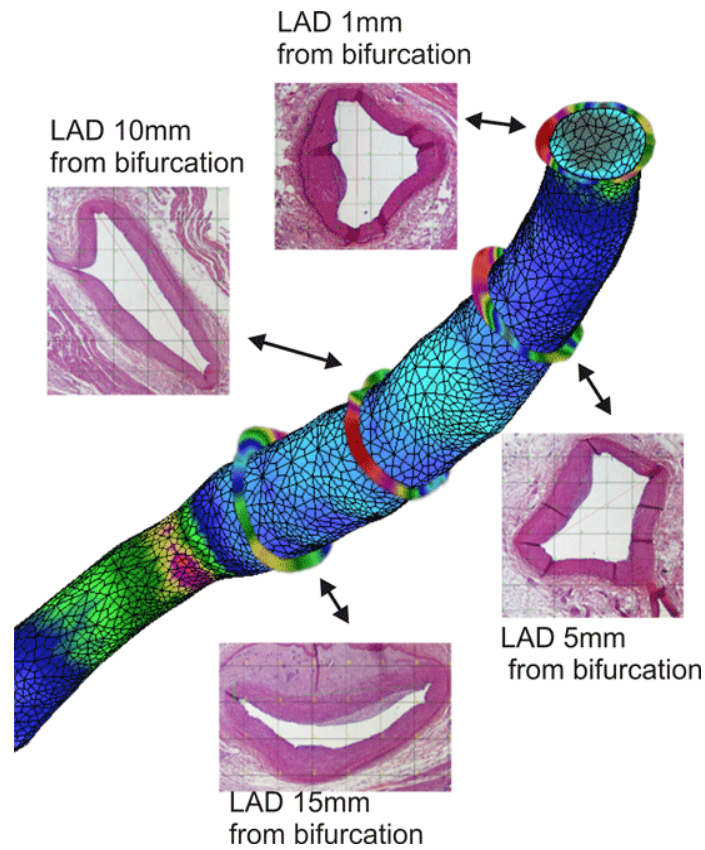


Figure 48: Matching IVUS and histological cross-sectional geometry. Shear stress distribution is shown along the internal arterial wall.

The reconstructed arterial models are used for the simulation of blood flow. FEM is used for calculating blood flow velocities and WSS, which are assessed to have a significant role in plaque development. Validation in blood flow modelling is based on Doppler or MRI data for coronary and carotid arteries, respectively. The mean error is 4%.

Regarding the plaque progression models, we used experimental data from pigs submitted to a high cholesterol diet for two months. The lumen and the outer wall of the arteries were reconstructed and then, matching of histological data and IVUS slices was performed, as it is shown in Figure 48.

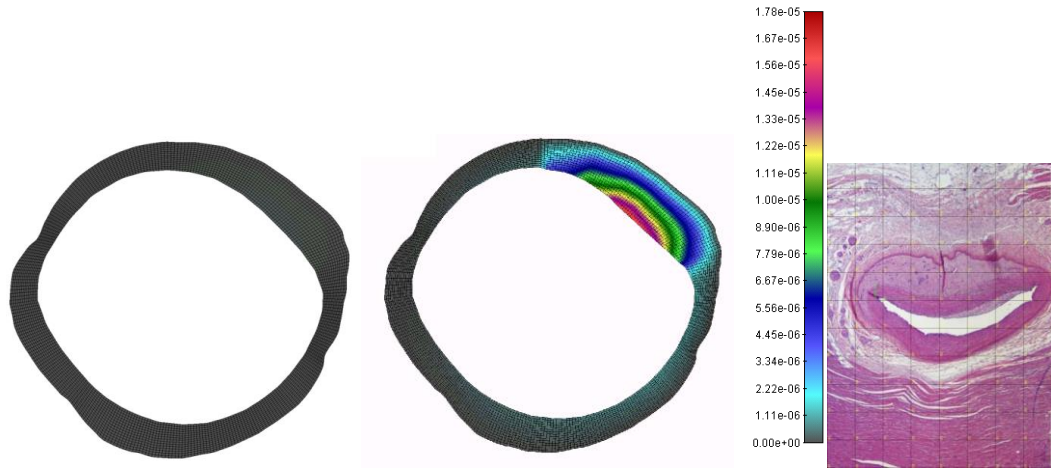


Figure 49: Computer reconstruction of a cross-section of LAD at 15mm after bifurcation (left panel), with computed concentration of macrophages [mg/ml] (middle panel); histological analysis (right panel) after 2 months of the high fat diet.

The Left Anterior Descending (LAD) was selected for this analysis. The process of matching with IVUS images was achieved by 2D modeling of tissue deformation for a number of cross-sections recorded by histological analysis (four cross-sections are shown in Fig. 1); those cross-sections are deformed until the internal lumen circumferential lengths in IVUS images are reached. Macrophages distribution shown in Figure 49 corresponds to the low WSS zone at 15 mm below LAD bifurcation from the left circumflex artery, where the largest plaque formation was found. The volume of plaque was obtained by matching IVUS segmentation cross-section and histological intima thickness at the same radial position. After 3D reconstruction of plaque geometry, the inflammatory velocity  $v_w$  from Eqs. 57-58 was fitted using nonlinear least square analysis for two time points, baseline and after 2 months high fat diet. It was assumed that the intimal thickness corresponds to the geometrical volume change in time. The diffusion coefficients  $d_1, d_2, d_3$  for oxidized LDL, macrophages and cytokines as well as degradation and LDL oxidized detection coefficients  $\lambda$  and  $\gamma$ , coefficient  $k_I$  are fitted using least square analysis. The threshold for oxidized LDL  $ox^{thr}$  and cytokines was assumed to be zero. Other material parameters for the lumen are taken from literature and boundary conditions for flow and pressure are averaged from experimental measurements for a specific pig. The fitted numerical parameters are given in Table 17.

Regarding the results of the plaque characterization, the plaque characterization application using IVUS was tested using 40 annotated IVUS images, and resulted to 87.81% accuracy for hard calcified plaque formations, 84.05% for soft plaque formations and 88.32% accuracy for the hard, non-calcified plaque formations. The designed algorithm for



characterizing the plaque using MR images, was tested using 521 MR images (from three sequences) annotated by experts. Statistical analysis for the lipid component in terms of Cohen's  $k$  and Pearson correlation coefficient  $r$  resulted to  $k=0.68$ ,  $r=0.95$ . Finally, CT plaque characterization method was compared with expert annotation. The algorithm showed high correlation and accuracy. More specifically, plaque formations from ten patients were annotated by experts. Concerning the plaque formations in coronary arteries, statistical analysis resulted to  $k=0.74$ ,  $r=0.97$  while for the carotid arteries the analysis resulted to  $k=0.96$ ,  $r=0.98$ .

Table 17: Values for the animal experiments.

Lumen	Intima	Inflammation
$\rho=1000 \text{ kg/m}^3$		$d_1=10^{-8} \text{ m}^2/\text{s}$
$\mu = 0.035 [P]$		$d_2=10^{-10} \text{ m}^2/\text{s}$
$D_l = 3.2 \times 10^{-11} \text{ m}^2/\text{s}$	$D_w = 1.3 \times 10^{-11} \text{ m}^2/\text{s}$	$d_3=10^{-8} \text{ m}^2/\text{s}$
$U_{\max}=0.4 \text{ m/s}$	$r_w = -2.6 \times 10^{-4}$	$k_1=20^{-6} \text{ m}^3/\text{kg s}$
$P_{\text{out}}=100 \text{ mmHg}$	$P_{\text{med}}=100 \text{ mmHg}$	$\lambda=25 \text{ s}^{-1}$
$C_o=3.0 \times 10^{-12} \text{ kg/m}^3$		$\gamma = 1 \text{ s}^{-1}$

### 5.2.5 Discussion

A multiscale model for the biological process of plaque formation and progression is presented. The model includes the 3D reconstructed arterial model, the blood flow, the WSS distribution, the molecular/cell model of the arterial wall/blood composition and the biological mechanism involved in the generation and growth of atherosclerotic plaque. The governing partial differential equations for plaque formation rely on the mass balance and Darcy's law in the domain of plaque development; the Navier-Stokes equations and diffusion equations are used for the LDL transport within the arterial lumen; the transport-diffusion-reaction equations are employed for the transmural mass transport, including the Kedem-Katchalsky equations to couple the transmural and transport within the lumen. The wall permeability was assumed to be a function of the wall shear stress with lower permeability at low and oscillatory shear stress.

We describe the inflammatory process using Reaction-Diffusion equations. Our model starts with passive penetration of LDL in particular areas of the intima. We assume that once in the intima, LDL is immediately oxidized. When the oxidized LDL exceeds a threshold, there is recruitment of monocytes. The incoming monocytes immediately differentiate into macrophages. Transformation of macrophages into foam cells contribute to the recruitment of new monocytes. This yields the secretion of a pro-inflammatory signal (cytokines), self-support

inflammatory reaction. Newly formed foam cells are responsible for the local volume increase. Under a local incompressibility assumption, when foam cells are created the intima volume is locally increasing. Volume change of the wall affects the fluid lumen domain, which means that fully coupling is achieved. The specific numerical procedures using ALE were developed for this purpose. Our approach is concentrated on the process on plaque initiation and intimal thickening.

Smooth muscle cells proliferation was not taken into account in this model and will be investigated in a future study. Moreover, we have not taken into account deformation and stress inside the arterial wall which is very important for the plaque rupture and smooth muscle proliferation for plaque growing. Another limitation of the platform is that, currently, plaque characterization is performed in 2D images; however, we are in the process of connecting the 2D characterized images in order to create 3D volumes of the plaque. Then, blood flow modeling and the subsequent plaque progression will become much more realistic.

We examined experimental data obtained for the LAD artery of a pig after 2 months high fat diet, in order to determine material parameters of the model. The matching between computed plaque location and progression in time with experimental observations demonstrates a potential benefit for future prediction of this vascular disease.

### **5.3. Art Care: A Multi-Modality Coronary 3D Reconstruction and Hemodynamic Status Assessment Software**

In this section, we describe a software platform which we have created, that provides the clinician with the ability to reconstruct in 3D the desired vessel using three different imaging modality options: fusion of IVUS and biplane angiography, fusion of OCT and biplane angiography or just biplane angiography (3D-QCA). The proposed system offers numerous 3D visualization options and has the ability to use any given IVUS, OCT or angiography formats. The key point, however, is that using a dedicated finite element module, it can calculate the virtual functional assessment index (vFAI) [29] for the reconstructed model, thus offering both anatomic characteristics, as well as functional assessment of the diseased vessel. The system features have been thoroughly validated, presenting promising results regarding the automatic lumen border detection from IVUS images and from OCT images, as well as the 3D reconstruction from the 3D-QCA module. Moreover, the calculated vFAI deriving from the 3D reconstructed models using the proposed method presented high correlation when compared to

the respective calculated vFAI values deriving from the 3D models reconstructed using the CAAS QCA 3D® (PIE Medical) commercial package. The obtained results are presented in detail in the next sections.

### **5.3.1 System Architecture**

The system incorporates three 3D reconstruction subsystems, regarding the desired imaging modalities (IVUS/Angiography, OCT/Angiography, 3D-QCA). The created 3D model is visualized and then it can be subjected to blood flow simulations, resulting to the calculation of the vFAI. Regarding the IVUS-Angiography and the OCT-Angiography use cases, the user can manually select and extract the end-diastolic (R-peak) frames to perform their segmentation. The luminal borders are manually or automatically selected in the IVUS or the OCT frames. The user can also trace the outer borders of the External Elastic Membrane (EEM) manually or automatically, in order to create the respective outer wall 3D model. The centerline extraction module is common for all the reconstruction modules. Regarding the 3D-QCA use case, the system utilizes the luminal borders from the centerline extraction module and creates the respective contours for the final 3D model. All of the system modules are integrated in a user-oriented graphical interface. The system was developed using C++ [30], combined with Microsoft® .NET Framework 3.5. Furthermore, several other 3rd party libraries were used for the system implementation. DCMTK [31] was used to extract images and metadata from DICOM files and OpenCV [32] was used for the processing of 2D images. The 3D visualization module was developed using the OpenGL [33] and the VTK [34] libraries, respectively. The system requires Windows XP® (or better), C++ and .NET Redistributables (2005/2008), an Intel Core Duo processor and 4 GB of RAM.

### **5.3.2 System Overview**

The system consists of three basic functional subsystems (IVUS-Angio, OCT-Angio, 3D-QCA) which, apart from the dedicated modules of each, have a module in common (3D centerline extraction). The system architecture is presented in Figure 50.

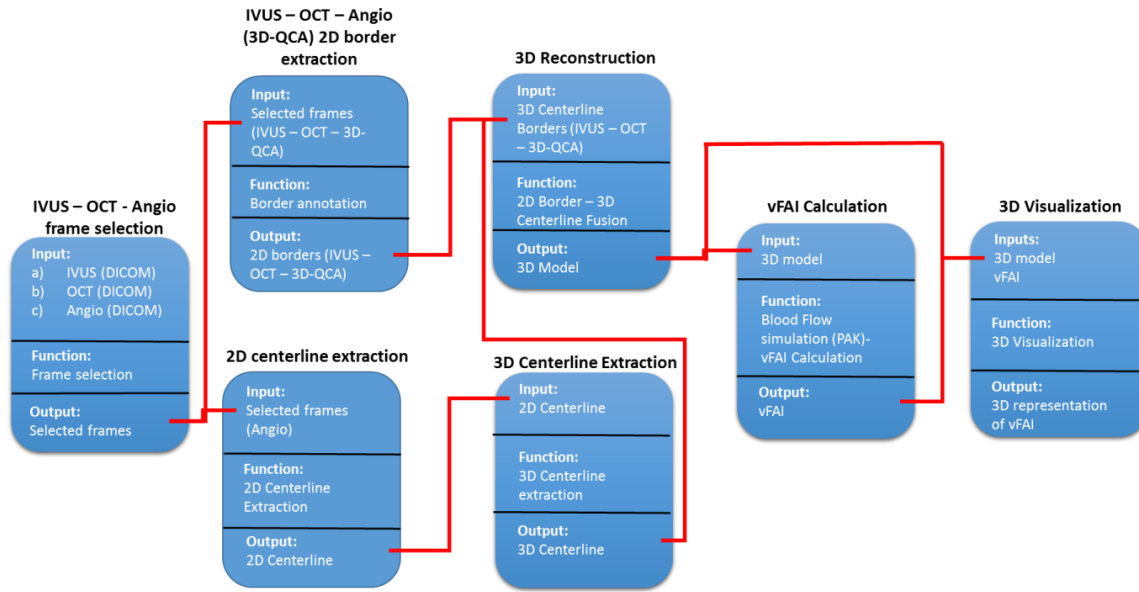


Figure 50: System Architecture Diagram.

### 5.3.3 DICOM Data Acquisition

#### *i) IVUS image and data extraction*

The IVUS sequence of images from the respective DICOM file is loaded into the system. When this process is completed, the user can define the first and last IVUS frames of the region of interest, as well as the respective R-peak frames (Figure 51). There is also an option to set a defined step according to which the R-peak frames will be extracted (i.e. every 50 frames), by selecting the dedicated button (Figure 51).

#### *ii) OCT image and data extraction*

The data loading process as well as the R-peak frame extraction follow the same rationale as the IVUS selection and are depicted in Figure 51.

#### *iii) Angiography image and data extraction*

The user must identify through a series of angiographic views the two most appropriate ones that depict the desired arterial segment more clearly and extract them into two separate DICOM files, using a dedicated DICOM viewer. The two extracted biplane angiographic views in DICOM format are then loaded into the system and the appropriate frame for each projection is chosen in order for the luminal borders for the region of interest to be defined.

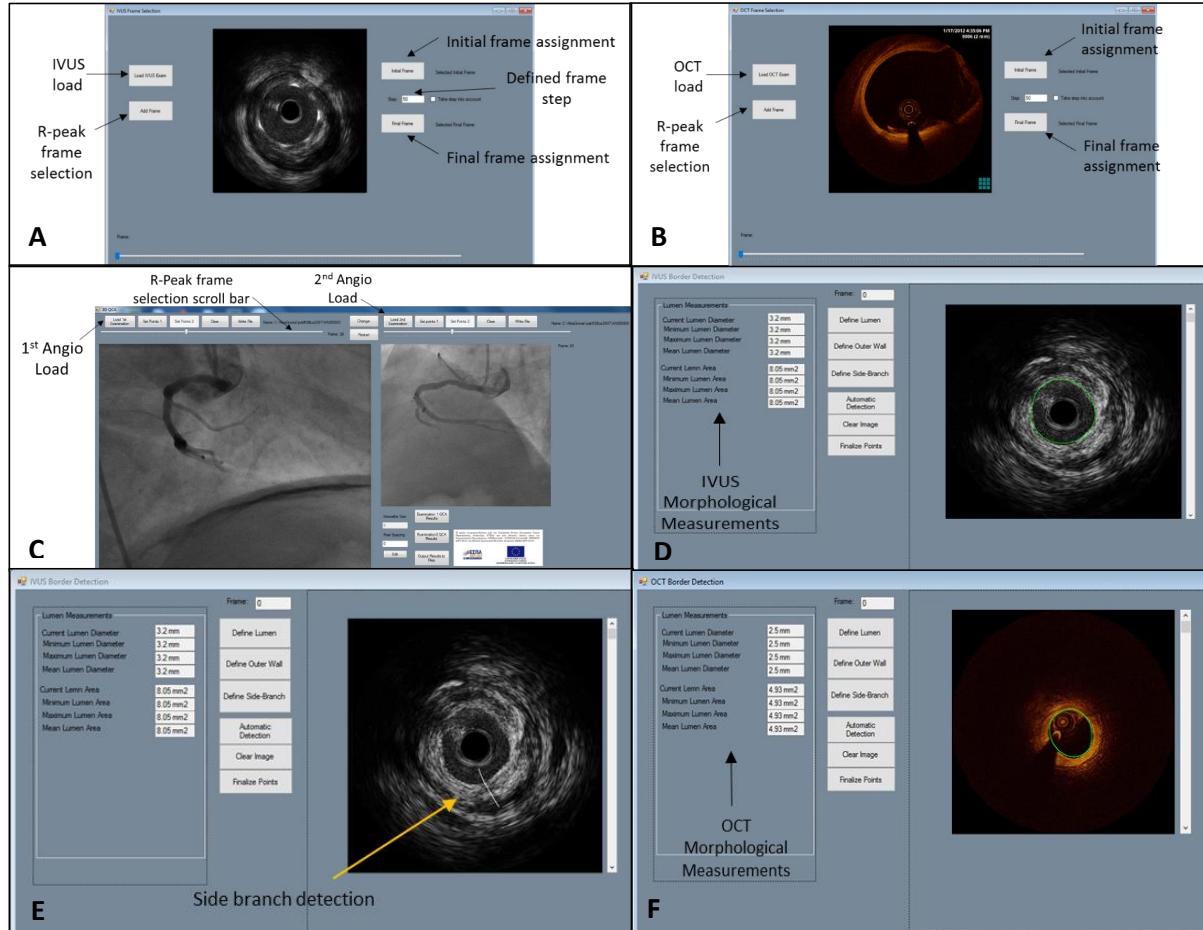


Figure 51: A) IVUS load and R-peak frame selection screen, B) OCT load and R-peak frame selection screen, C) Angiography DICOM file load and R-peak frame selection screen, D) IVUS lumen border detection screen, E) Side branch detection screen and, F) OCT luminal border detection screen.

### 5.3.4 3D Artery Reconstruction

#### i) IVUS Module

The processing of the IVUS frames is performed using an already established segmentation algorithm. In brief, the user can define the luminal and outer wall borders (Figure 51), as well as the arterial side branches. This can be performed in a manual or a fully automated manner [3]. The automatic border detection algorithm is based on deformable models and it uses the detected borders of the ROIs from the previous frame in order to detect the corresponding borders on the subsequent IVUS frame. This detection is performed according to where the energy of the model is minimized, using a fusion of a Hopfield neural network and a simulated annealing schema. When the segmentation of each frame is finalized, the system automatically generates several morphological measurements of interest regarding the examined frame (current lumen diameter, minimum lumen diameter, maximum lumen diameter, mean lumen

diameter, current lumen area, minimum lumen area, maximum lumen area, mean lumen area). The arterial side branch detection option is used to support the clinician for the absolute orientation of the 3D arterial model, which is described in the next section. When a side branch is visible in the IVUS frame, the user creates a straight line that starts from the center of the catheter and ends at the distal end of the side branch. Finally, if the user does not agree with the automatically defined borders, there is the option to correct them manually. Regarding the manual segmentation of the lumen, the user has the ability to erase and redefine any of the previously defined points that he desires to optimize the luminal or the arterial wall borders. There is also the option to move any of the already defined points and recreate the final border. At the end of the segmentation process, the user must finalize the annotated points.

### ***ii) OCT Module***

The segmentation of the OCT images can be done either manually or automatically on the defined frames. The rationale of the automatic lumen border detection is similar to the IVUS based one [35]. The OCT automatic lumen detection is based on 6 main steps: a) a Gaussian filter is applied on the initial image, b) the Otsu's automatic thresholding method is applied in order to reveal binary objects and remove the catheter pixels, c) the artifacts are removed, d) objects with specific characteristics that are near the catheter are removed, e) each column of the image is scanned, the first non-zero pixel of the column is saved and the non-zero pixels are then connected in order to find the lumen contour, and f) the image is finally transformed from polar to Cartesian coordinates [36]. The system also generates the appropriate morphological measurements of each segmented frame (current lumen diameter, minimum lumen diameter, maximum lumen diameter, mean lumen diameter, current lumen area, minimum lumen area, maximum lumen area, mean lumen area) (Figure 51).

### ***iii) 3D-QCA module***

Once the desired frames are selected, the user selects the luminal borders and saves the respective points into a separate file. When the process is completed, the system generates the respective 2D centerline, as well as the respective contours of the arterial segment of interest for the final 3D model. This is performed according to the following steps: a) the two splines of the luminal borders for each angiographic projection are split into the same number of nodes, b) the respective nodes from each luminal spline are connected and the node that expresses their mean distance is found and, c) all of the aforementioned nodes that express the mean distance

of the luminal borders are connected, thus creating the 2D centerline for each projection. The aforementioned contours are created in a circular manner. This is done for both angiographic projections (Figure 52).

#### ***iv) 2D Centerline Extraction from biplane angiography***

This module is common for all reconstruction processes and follows the same rationale as in the 3D-QCA section. The user manually loads the desired angiographic sets, selects the respective end-diastolic frame in each projection and draws the luminal borders in the region of interest. Finally, the algorithm generates and saves the 2D centerlines of the two projections in two separate files along with the points of the luminal borders.

#### ***v) 3D centerline extraction***

The two files that contain the 2D centerlines with the luminal borders are loaded into the system. When the process is completed, the system informs the user about any missing DICOM values (i.e. pixel spacing, primary and secondary angles, distance to detector etc.) and gives him the opportunity to fill them with the appropriate ones, if they are available. Then, when both projections are loaded correctly, the user can bring both of the generated 2D surfaces in a common starting point and create the final 3D centerline. The path length is calculated and reported in a separate box. However, if the length value does not correspond to the actual one, the user can manually change it and recreate the 3D path with the correct length (Figure 52).

#### ***vi) Absolute orientation using side branches***

After the creation of the 3D centerline, the respective 2D contours are placed perpendicularly onto the centerline [3]. However, in order to complete the 3D reconstruction process, the absolute orientation of the 3D model must be calculated. This is performed visually, by loading the 3D model and the two angiographic views, along with the side branches that were created in the previous steps. The side branches that were annotated previously appear as a straight white line in the 3D model, thus allowing for the visual matching of them to the respective angiographic back projection. The 3D model is back-projected on the 2 angiographic views and rotated until the side branches meet the respective bifurcations on the angiography. When the process is completed, the rotation angle is saved and the final 3D model is created (Figure 52).

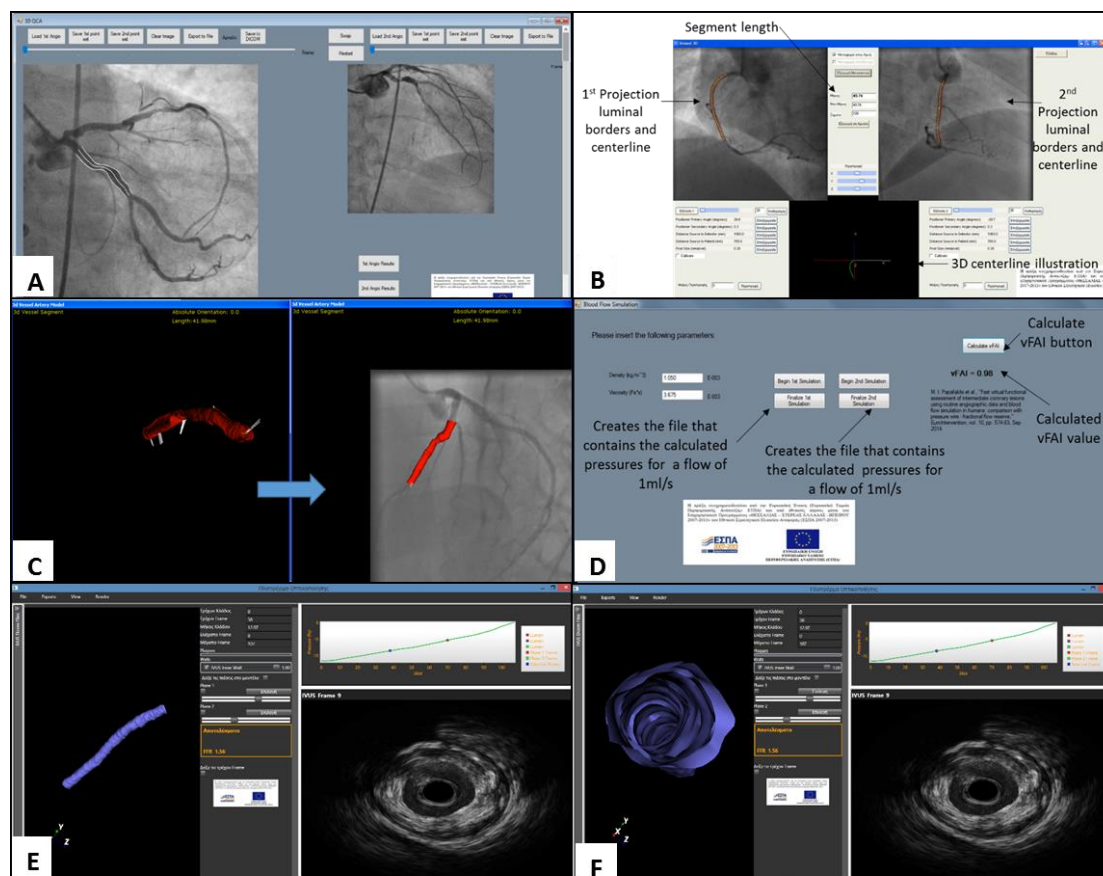


Figure 52: A) 3D-QCA luminal border detection and 2D centerline extraction screen, B) 3D centerline extraction screen, C) 3D model rotation using side branches and final back projection to the respective angiography, D) vFAI calculation screen, E) Final 3D model with the corresponding IVUS frame and the calculated results and, F) Fly-through camera option for the final 3D model.

### 5.3.5 Finite Element Modeling

#### i) 3D Mesh-Blood Flow Modelling

The finite element modeling process is performed by an integrated finite element open-source program (PAK-F, [37]). A penalty formulation is also used in the solver [38]. The software automatically creates a 3D 8-node finite element mesh of around 150000 elements (depending on the length of the arterial segment of interest), after the creation of the final 3D model. The user initially sets the parameters for the material properties blood (i.e. density and viscosity). The predefined values are 1050 kg/m<sup>3</sup> for the density and 0.0035 Pa·s for the dynamic viscosity, respectively. Subsequently, the required blood flow simulations are performed, in order to calculate the virtual Functional Assessment Index (vFAI) [29]. These simulations are carried out under the assumptions that the flow is laminar and incompressible, that blood behaves as a



Newtonian fluid and that the arterial walls are rigid. Two separate simulations need to be executed for this purpose, one for an outlet flow of 1 ml/s and one for 3 ml/s. The user selects the dedicated buttons and executes the two simulations (Figure 52). The software creates two files containing the average pressure of each contour throughout the entire length of the arterial segment.

### ***ii) vFAI Calculation Module***

The process of the vFAI calculation follows the rationale of [29]. Regarding the inlet, a pressure of 100 mmHg is used in both simulations as a boundary condition, a value that corresponds to the average human aortic pressure. At the outlet, two separate flow rates of 1 and 3 ml/s are applied for each model (i.e. during rest and under stress, respectively). The pressure gradient is calculated for each case regarding the inlet ( $P_a$ ) and the outlet ( $P_d$ ) of the segment from the two aforementioned files that contain the average pressure of each contour. When the two pressure files are created, the user can calculate the vFAI by pressing the button entitled “Calculate vFAI” (Figure 52).

### ***iii) 3D Visualization Module***

This functional section is the final 3D representation of the examined model, including the final absolute orientation as well as the vFAI results. The user is able to view the respective 2D IVUS or OCT frames and match them to the actual 3D model. The user can also rotate the model and view inside the luminal area (Figure 52).

## **5.3.6 Validation**

### ***i) Angio (3D-QCA)***

To validate the proposed angiography reconstruction method (3D-QCA), we compared the implemented algorithm to an already validated commercial reconstruction software, which performs 3D reconstruction from a set of biplane angiographies (CAAS QCA 3D®) [20]. The comparison of the two algorithms was made using the following validation metrics:

- a) The volume of the 3D reconstructed models using the respective segments deriving from CAAS QCA 3D® as a gold standard,
- b) The length and the minimum lumen diameter of the examined arterial segments compared to the ones deriving from CAAS QCA 3D® and,

- c) A comparison of the calculated vFAI from both reconstruction methods.

The comparison of the obtained results includes the calculation of a regression analysis of the two methods, as well as the analysis of the respective correlation diagrams and the Bland-Altman plots. For our validation purposes, we used eleven already reconstructed arterial segments deriving from CAAS QCA 3D® software [29] and then, using the exact same angiographic frames and the same path we performed the reconstruction with our in-house developed algorithm, comparing the volume of the generated 3D models, the length, the minimum lumen diameter, as well as the calculated vFAI values from both methods. Our dataset consisted of six Left Anterior Descending (LAD), two Right Coronary Artery (RCA) and three Left Circumflex (LCx) segments. The stenoses severity ranged between 17% and 64%, as calculated by CAAS QCA 3D®.

Strong correlation was found between the two methods for the used validation metrics (Figure 54). In particular, the Pearson's correlation coefficient (R) for the calculated volumes, vFAI, length and minimum lumen diameter was 0.99, 0.99, 0.99 and 0.88, respectively. The respective mean differences of the aforementioned metrics were 3.53 mm<sup>3</sup> (SD=8.07 mm<sup>3</sup>), 0.0146 (SD=0.021 mm), -1.99 mm (SD=2.94 mm) and -0.034 mm (SD=0.163 mm), respectively (Table 18).

Table 18: Validation results of the comparison between CAAS QCA 3D® and Art Care regarding calculated volumes, vFAI, segment length and minimum lumen diameter

	Calculated Volume	Calculated vFAI	Calculated length	Calculated minimum lumen diameter
<b>Pearson's coefficient (R)</b>	0.99	0.99	0.99	0.88
<b>Bland-Altman limits</b>	3.53±1.96*8.07 mm <sup>3</sup>	0.0146±1.96*0.021	-1.99±1.96*2.94 mm	-0.034±1.96*0.163 mm
<b>Mean difference</b>	3.53 mm <sup>3</sup>	0.0146	-1.99 mm	-0.034 mm

Good agreement was also found for the two methods by the Bland-Altman method of analysis (Figure 53). In fact, the corresponding limits of agreement for the calculated volumes, vFAI, length and minimum lumen diameter were from -12.3 to 19.3, from -0.027 to 0.056, from -7.75 to 3.77 and from -0.35 to 0.29, respectively (Table 18).

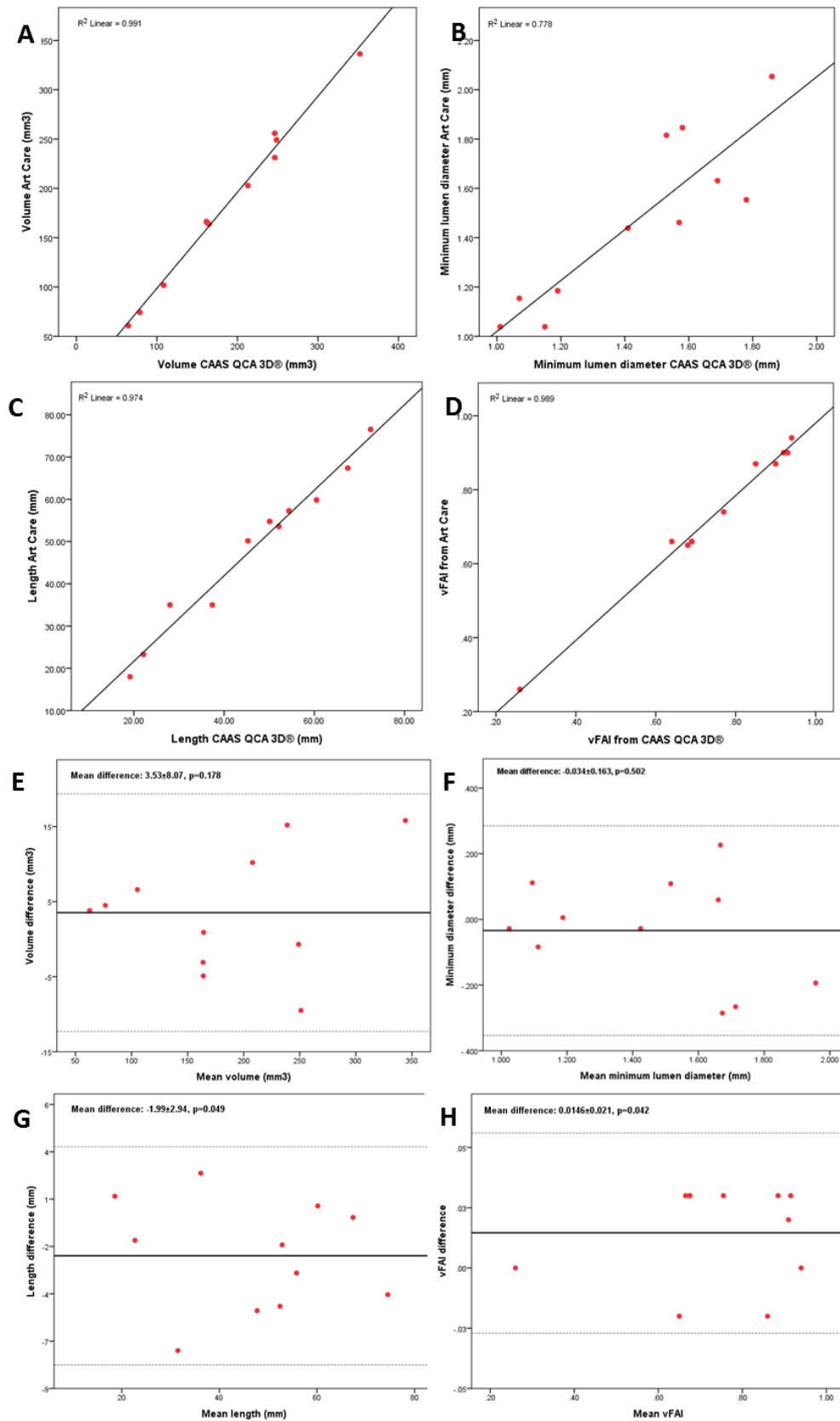


Figure 53: Correlation diagrams and Bland-Altman plots for: A) the calculated volumes, B) minimum lumen diameters, C) segment length, and D) calculated vFAI. Bland-Altman plots for: E) the calculated volumes, F) minimum lumen diameters, G) segment length, and H) calculated vFAI

## ***ii) Border detection (IVUS and OCT)***

### **a. IVUS Dataset**

Five pullbacks acquired from five different patients were used to validate the proposed IVUS border detection step. A medical expert selected 632 images from this dataset and manually annotated the lumen borders. Images having noise artifacts were not included in the validation procedure. To validate the proposed IVUS lumen detection step the annotated images were compared to the lumen detection results of the proposed software.

### **b. OCT Dataset**

Six pullbacks were acquired from six different patients and used to validate the proposed OCT border detection method. A medical expert selected 556 images and manually annotated the lumen borders in these images. Stented images or images having small amount of residual blood artifacts were included in the validation procedure. On the contrary malapposed stented segments and images having residual blood or movement artifacts were not included in the study. To validate the proposed OCT lumen detection step the annotated images were compared to the lumen detection results of the proposed software.

### **c. Validation metrics**

To validate the IVUS and OCT lumen detection algorithms, we computed the Pearson's correlation coefficients between the lumen areas measured by manual lumen detection and by software lumen detection for processing IVUS and OCT images. We performed a Bland-Altman analysis and we computed the positive predictive value:

$$PPV = \frac{TP}{TP + FP} \quad (67)$$

As true positive values (TP) we define the common area between the two measurements, as false positive (FP) values we define the lumen area of the detected area minus the common area and as false negative (FN) the annotated lumen area minus the common area. Finally, the ratio of overlapping/non-overlapping areas was computed. The ratio of overlapping/ non-overlapping areas was defined as:

$$R_{over} = \frac{TP}{TP + FN} \quad (68)$$

$$R_{non-over} = \frac{FN + FP}{TP + FN} \quad (69)$$

The validation results of the IVUS and OCT lumen detection steps are presented in Table 19. Figure 54 presents the Bland-Altman plots for the comparison of manual lumen detection versus software lumen detection of IVUS and OCT, respectively. Figure 54 also presents the correlation plots for the comparison of manual lumen detection versus software lumen detection of IVUS and OCT, respectively.

Table 19: Validation results of the comparison between manual lumen detection and software lumen detection for processing IVUS and OCT images.

Validation metrics	IVUS Lumen	OCT Lumen
<b>Pearson's correlation</b>	0.94	0.99
<b>Bland-Altman limits</b>	$0.01 \pm 1.96 \times 0.14 \text{ mm}^2$	$-0.080 \pm 1.96 \times 0.082 \text{ mm}^2$
<b>Overlapping area</b>	0.98	0.99
<b>Non-overlapping area</b>	0.05	0.02
<b>Positive Predictive Value (PPV)</b>	0.97	0.98

### 5.3.7 Discussion

In this work, we presented a newly developed software that combines the ability to reconstruct in 3D coronary arterial segments using three different sets of imaging modalities and to calculate the vFAI on the segments of interest. All of the system components were extensively validated either comparing to the annotation of clinical experts (IVUS and OCT border detection) or to a valid publically commercial software (3D-QCA module). The system is user-friendly, since it does not require any specialized skills from the user. The novelty of the proposed system is that it can assess the hemodynamic status of a coronary arterial segment in a matter of minutes, utilizing the most well-known coronary imaging modalities, without the use of a dedicated pressure wire. This leads to the reduction of the total cost of the diagnostic examinations and gives the opportunity to the clinician for a quick and valid decision on the

forthcoming type of treatment for the patient. When compared to other publically available software suites, the proposed system offers several advantages since it is the only one that can utilize all three coronary imaging modalities and provides the ability to perform blood flow simulations and assess the hemodynamic status of the vessels of interest (Table 20). The total time that is required to perform a full 3D reconstruction and the subsequent vFAI calculation varies according to the available modality. It ranges from 2 minutes (3D-QCA module), to 10 minutes (IVUS-Angio and OCT-Angio modules).

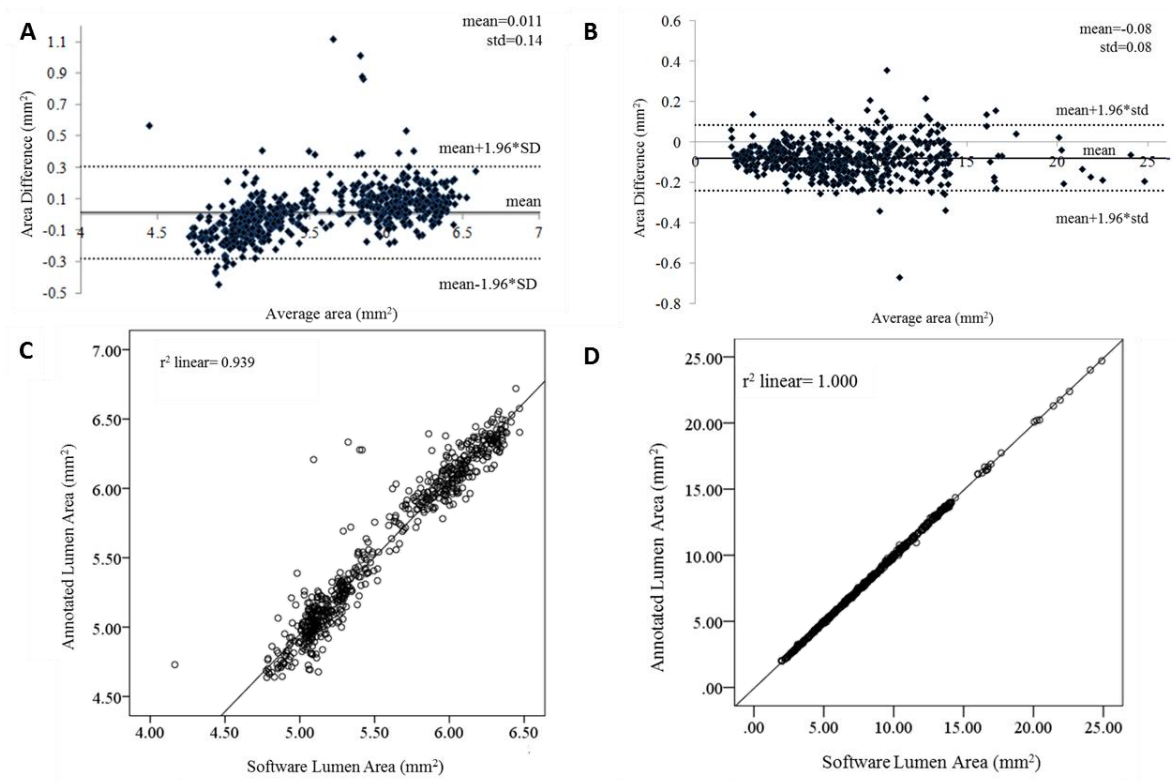


Figure 54: A) Bland-Altman plot for the comparison of manual IVUS lumen detection versus software IVUS lumen detection, B) Bland-Altman plot for the comparison of manual OCT lumen detection versus software OCT lumen detection, C) Correlation plot for the comparison of manual IVUS lumen detection versus software IVUS lumen detection and, D) Correlation plot for the comparison of manual OCT lumen detection versus software OCT lumen detection

Moreover, the automatic border detection regarding the OCT and the IVUS modules decreases the total reconstruction time even more, since their results are very promising. One other aspect worth mentioning is the fact that the IVUS border detection algorithm performs equally using either of the two IVUS catheters (Volcano or Boston Scientific). Regarding the calculation of the vFAI, the system presented a high correlation while compared to the respective 3D models deriving from CAAS QCA 3D® that were previously validated using their actual FFR measurements, thus proving its efficacy.

Table 20: Comparison of similar software suites to the proposed software suite.

Software Suite	Imaging Modalities				Blood Flow Modeling
	IVUS	OCT	Angio	CCTA	Hemodynamic assessment
CAAS QCA 3D® [145]			✓		
QAngio XA (Medis) [149]			✓		
QAngio OCT RE [150]		✓			
IVUSAngio Tool [147]	✓				
HeartFlow® [144]				✓	✓
Art Care	✓	✓	✓		✓

We should however state that the inability of the implemented algorithms to include bifurcations in the final 3D models is the main limitation of the proposed system. Moreover, we are currently developing a new, larger dataset to further validate the 3D-QCA module with a wider variety of cases regarding the severity of the lesions.





## Chapter 6: Conclusions and Future Work

---

6.1 Computational Assessment of the Severity of Coronary Stenoses

6.2 Future Work

---

### 6.1 Computational Assessment of the Severity of Coronary Stenoses

Several studies in current literature have been published, that perform blood flow simulations on coronary arterial segments, calculating mainly hemodynamic factors such as WSS, without however examining the influence of several blood flow simulation parameters such as the use of FSI simulations, time-dependent flow profiles etc. The computational assessment of coronary stenoses is a widely studied field, which has attracted the interest of numerous researchers. Finally, regarding the development of dedicated software for the assessment of coronary stenoses and multiscale modelling, several software suites are commercially available. The current thesis covers three major issues on cardiovascular modelling. At the first stage, an analytical study on blood flow modelling using rigid or deformable walls is presented. At a second stage, several analytical studies on the computational assessment of the severity of coronary stenoses are presented, utilizing every coronary imaging modality that is widely used in current clinical practice. Finally, two integrated systems that perform 3D reconstruction, computational functional assessment of coronary stenoses and multiscale modelling are presented in the last part of the current thesis.

Regarding the first part of the current thesis, we went beyond the state of the art by examining and validating the accuracy of the calculation of intravascular pressures, thus opening the pathway to the assessment of the severity of coronary stenoses. Several parameters were used in this study in order for us to determine the optimal simulation setup for the calculation of intravascular pressures. Our major finding was that the far less demanding blood flow simulations of steady flow and rigid walls exhibited accurate results, directly comparable to the ones that were calculated using transient flow and FSI modeling. The aforementioned finding was therefore used in our subsequent studies, since all of our simulations were carried out using these assumptions.

Regarding the second main part of the current thesis, we went beyond the state of the art in several ways. First, we have proven that vFAI can be safely applied on 3D models that derive from CCTA, thus creating a non-invasive tool for the computational hemodynamic assessment of coronary lesions, which is extremely time-efficient and can be applied almost in real time. The accuracy of the newly proposed method was superior to other studies that were already published. Moreover, we have also proven that vFAI combined with 3D models that derive from CCTA can safely characterize functionally significant stenoses by comparing the calculated vFAI to PET perfusion values. The major finding of this study was that our index could accurately identify the presence of an attenuated stress MBF or MFR downstream a coronary lesion of  $\geq 30\%$ . In another of our studies, we went beyond the state of the art by creating a novel method for the 3D reconstruction of coronary arteries using only routine intravascular imaging and applying vFAI for the virtual functional assessment of coronary stenoses on the aforementioned 3D models. With this study, we go beyond the state of the art by overturning the general trend that anatomic indices have a mediocre correlation with FFR and cannot be used in routine practice for identifying significant stenoses with a high diagnostic accuracy. Our method exhibited promising results, far superior than the already established ones, providing also both anatomic and physiologic information on the hemodynamic status of the examined artery. Furthermore, we also created a method which enabled the FFR assessment using IVUS and ICA derived 3D arterial models and by calculating the flow rate under rest from the respective ICA sequence, thus making the use of a dedicated pressure wire redundant. Finally, we went beyond the state of the art by creating smartFFR, a novel fast index for the computational functional assessment of coronary stenoses. The method relies on the execution of a transient blood flow simulation, therefore enabling the calculation of the desired  $P_d/P_a$

curve. smartFFR has been proven to be faster than vFAI, presenting strong correlation to the invasively measured FFR and superior diagnostic accuracy to the already validated vFAI.

Finally, we also created two integrated software suites for the 3D reconstruction of coronary arteries, the functional assessment of coronary stenoses and the multiscale modeling of atherosclerosis. ARTool is a software suite that integrates a multiscale model regarding the biological process of plaque formation and progression, a point that goes beyond the state of the art. ArtCare on the other hand manages to utilize all the most well-known coronary imaging modalities in order to reconstruct in 3D the coronary vasculature and assess the severity of any existing coronary lesions. Up to date, it is the only software suite that allows the 3D reconstruction from ICA, IVUS-ICA or OCT-ICA and perform the required blood flow simulations to assess the hemodynamic status of the coronary vasculature.

## **6.2 Future Work**

Although the work of the current thesis has produced promising results that have already been published, there are still several things that need to be addressed in the field of the functional assessment of coronary stenoses. smartFFR has already been validated in a cohort of 30 patients, exhibiting high diagnostic accuracy. However, the validation dataset is currently being enhanced using CCTA derived 3D models, as well as, ICA derived models and our goal is to reach a validation cohort of at least 200 vessels in total.

Moreover, as we have discovered, smartFFR can also be used in bifurcations, with some modifications that include the alteration of the boundaries at which the AUC will be calculated, as well as, the application of Murray's law in order to determine the actual flow rate that will pass through each of the examined arterial branches. In order to validate this method, we are planning to use both ICA derived bifurcating models, as well as, CCTA derived bifurcating models.

Finally, we are also planning to evaluate the influence of the presence of atherosclerotic plaque on the calculated smartFFR values, as well as on the calculated WSS values, by performing FSI simulations on 3D models that also contain atherosclerotic plaque segments.



## Bibliography

- [1] I. P.A., *Handbook Of Cardiac Anatomy, Physiology, And Devices*: Humana Press, 2005.
- [2] M. B. Mohr, "A hybrid deformable model of ventricular myocardium," University of Karlsruhe, 2006.
- [3] D. Lindholm, B. C. Bornhauser, and L. Korhonen, "Myliip makes an Idol turn into regulation of LDL receptor," *Cell Mol Life Sci*, vol. 66, pp. 3399-402, Nov 2009.
- [4] S. Vennix, G. D. Musters, I. M. Mulder, H. A. Swank, E. C. Consten, E. H. Belgers, *et al.*, "Laparoscopic peritoneal lavage or sigmoidectomy for perforated diverticulitis with purulent peritonitis: a multicentre, parallel-group, randomised, open-label trial," *Lancet*, vol. 386, pp. 1269-1277, Sep 26 2015.
- [5] V. A. R. O. R. R. Fuster, *Hurst's The Heart*, 10th ed.: McGraw-Hill, 2001.
- [6] E. O. Kung, A. S. Les, C. A. Figueroa, F. Medina, K. Arcaute, R. B. Wicker, *et al.*, "In vitro validation of finite element analysis of blood flow in deformable models," *Ann Biomed Eng*, vol. 39, pp. 1947-60, Jul 2011.
- [7] C. Smuclovsky, *Coronary Artery CTA*: Springer-Verlag New York, 2010.
- [8] G. Millonig, H. Niederegger, and G. Wick, "Analysis of the cellular composition of the arterial intima with modified en face techniques," *Lab Invest*, vol. 81, pp. 639-41, Apr 2001.
- [9] A. Fortier, V. Gullapalli, and R. A. Mirshams, "Review of biomechanical studies of arteries and their effect on stent performance," *IJC Heart & Vessels*, vol. 4, pp. 12-18, 2014/09/01/ 2014.
- [10] J. Eckert, M. Schmidt, A. Magedanz, T. Voigtlander, and A. Schmermund, "Coronary CT angiography in managing atherosclerosis," *Int J Mol Sci*, vol. 16, pp. 3740-56, Feb 09 2015.
- [11] S. a. C. Lorkowski, P. , *Atherosclerosis: Pathogenesis, Clinical Features and Treatment*, 2007.
- [12] P. Libby, P. M. Ridker, and G. K. Hansson, "Progress and challenges in translating the biology of atherosclerosis," *Nature*, vol. 473, pp. 317-25, May 19 2011.
- [13] P. C. Choy, Y. L. Siow, D. Mymin, and K. O, "Lipids and atherosclerosis," *Biochem Cell Biol*, vol. 82, pp. 212-24, Feb 2004.
- [14] M. L. Fitzgerald, Z. Mujawar, and N. Tamehiro, "ABC transporters, atherosclerosis and inflammation," *Atherosclerosis*, vol. 211, pp. 361-70, Aug 2010.
- [15] J. L. Goldstein and M. S. Brown, "The LDL receptor," *Arterioscler Thromb Vasc Biol*, vol. 29, pp. 431-8, Apr 2009.

- [16] A. R. Ithdayhid, A. White, and B. Ko, "Assessment of Serial Coronary Stenoses With Noninvasive Computed Tomography-Derived Fractional Flow Reserve and Treatment Planning Using a Novel Virtual Stenting Application," *JACC Cardiovasc Interv*, vol. 10, pp. e223-e225, Dec 26 2017.
- [17] I. Tabas, "Macrophage death and defective inflammation resolution in atherosclerosis," *Nat Rev Immunol*, vol. 10, pp. 36-46, Jan 2010.
- [18] S. Nicholls and P. Lundman, "The emerging role of lipoproteins in atherogenesis: beyond LDL cholesterol," *Semin Vasc Med*, vol. 4, pp. 187-95, May 2004.
- [19] M. Rafieian-Kopaei, M. Setorki, M. Doudi, A. Baradaran, and H. Nasri, "Atherosclerosis: process, indicators, risk factors and new hopes," *Int J Prev Med*, vol. 5, pp. 927-46, Aug 2014.
- [20] S. Chien, "Molecular and mechanical bases of focal lipid accumulation in arterial wall," *Prog Biophys Mol Biol*, vol. 83, pp. 131-51, Oct 2003.
- [21] Y. Liu, B. P. Chen, M. Lu, Y. Zhu, M. B. Stemerman, S. Chien, *et al.*, "Shear stress activation of SREBP1 in endothelial cells is mediated by integrins," *Arterioscler Thromb Vasc Biol*, vol. 22, pp. 76-81, Jan 2002.
- [22] J. Hwang, M. H. Ing, A. Salazar, B. Lassegue, K. Griendling, M. Navab, *et al.*, "Pulsatile versus oscillatory shear stress regulates NADPH oxidase subunit expression: implication for native LDL oxidation," *Circ Res*, vol. 93, pp. 1225-32, Dec 12 2003.
- [23] D. G. Harrison, J. Widder, I. Grumbach, W. Chen, M. Weber, and C. Searles, "Endothelial mechanotransduction, nitric oxide and vascular inflammation," *J Intern Med*, vol. 259, pp. 351-63, Apr 2006.
- [24] P. Dan, E. Velot, V. Decot, and P. Menu, "The role of mechanical stimuli in the vascular differentiation of mesenchymal stem cells," *J Cell Sci*, vol. 128, pp. 2415-22, Jul 15 2015.
- [25] "WHO publishes definitive atlas on global heart disease and stroke epidemic," *Indian J Med Sci*, vol. 58, pp. 405-6, Sep 2004.
- [26] J. C. Grotta, "Carotid stenosis," *N Engl J Med*, vol. 369, pp. 2360-1, Dec 12 2013.
- [27] R. L. Pande, T. S. Perlstein, J. A. Beckman, and M. A. Creager, "Secondary prevention and mortality in peripheral artery disease: National Health and Nutrition Examination Study, 1999 to 2004," *Circulation*, vol. 124, pp. 17-23, Jul 05 2011.
- [28] R. S. Rosenson, "Statins in atherosclerosis: lipid-lowering agents with antioxidant capabilities," *Atherosclerosis*, vol. 173, pp. 1-12, Mar 2004.

- [29] D. Hackett, G. Davies, and A. Maseri, "Pre-existing coronary stenoses in patients with first myocardial infarction are not necessarily severe," *Eur Heart J*, vol. 9, pp. 1317-23, Dec 1988.
- [30] M. J. Budoff, D. Dowe, J. G. Jollis, M. Gitter, J. Sutherland, E. Halamert, *et al.*, "Diagnostic performance of 64-multidetector row coronary computed tomographic angiography for evaluation of coronary artery stenosis in individuals without known coronary artery disease: results from the prospective multicenter ACCURACY (Assessment by Coronary Computed Tomographic Angiography of Individuals Undergoing Invasive Coronary Angiography) trial," *J Am Coll Cardiol*, vol. 52, pp. 1724-32, Nov 18 2008.
- [31] J. P. Earls, E. L. Berman, B. A. Urban, C. A. Curry, J. L. Lane, R. S. Jennings, *et al.*, "Prospectively gated transverse coronary CT angiography versus retrospectively gated helical technique: improved image quality and reduced radiation dose," *Radiology*, vol. 246, pp. 742-53, Mar 2008.
- [32] L. Husmann, I. Valenta, O. Gaemperli, O. Adda, V. Treyer, C. A. Wyss, *et al.*, "Feasibility of low-dose coronary CT angiography: first experience with prospective ECG-gating," *Eur Heart J*, vol. 29, pp. 191-7, Jan 2008.
- [33] I. Danad, P. G. Raijmakers, R. S. Driessen, J. Leipsic, R. Raju, C. Naoum, *et al.*, "Comparison of Coronary CT Angiography, SPECT, PET, and Hybrid Imaging for Diagnosis of Ischemic Heart Disease Determined by Fractional Flow Reserve," *JAMA Cardiol*, Aug 16 2017.
- [34] G. Mourad, J. Ribstein, A. Argiles, C. Mion, and A. Mimran, "[Hypertension and stenosis of the graft artery: effects of conversion enzyme inhibition]," *Arch Mal Coeur Vaiss*, vol. 79, pp. 892-5, Jun 1986.
- [35] A. Chiribiri, R. M. Botnar, and E. Nagel, "Magnetic resonance coronary angiography: where are we today?," *Curr Cardiol Rep*, vol. 15, p. 328, Feb 2013.
- [36] S. E. Nissen and P. Yock, "Intravascular ultrasound: novel pathophysiological insights and current clinical applications," *Circulation*, vol. 103, pp. 604-16, Jan 30 2001.
- [37] H. M. Garcia-Garcia, B. D. Gogas, P. W. Serruys, and N. Bruining, "IVUS-based imaging modalities for tissue characterization: similarities and differences," *Int J Cardiovasc Imaging*, vol. 27, pp. 215-24, Feb 2011.
- [38] T. Pawlowski, F. Prati, T. Kulawik, E. Ficarra, J. Bil, and R. Gil, "Optical coherence tomography criteria for defining functional severity of intermediate lesions: a comparative study with FFR," *Int J Cardiovasc Imaging*, vol. 29, pp. 1685-91, Dec 2013.

- [39] R. Waksman, H. Kitabata, F. Prati, M. Albertucci, and G. S. Mintz, "Intravascular ultrasound versus optical coherence tomography guidance," *J Am Coll Cardiol*, vol. 62, pp. S32-40, Oct 22 2013.
- [40] S. Brugaletta, H. M. Garcia-Garcia, P. W. Serruys, S. de Boer, J. Ligthart, J. Gomez-Lara, *et al.*, "NIRS and IVUS for characterization of atherosclerosis in patients undergoing coronary angiography," *JACC Cardiovasc Imaging*, vol. 4, pp. 647-55, Jun 2011.
- [41] J. E. Van Velzen, J. D. Schuijf, F. R. De Graaf, J. W. Jukema, A. D. Roos, L. J. Kroft, *et al.*, "Imaging of atherosclerosis: invasive and noninvasive techniques," *Hellenic J Cardiol*, vol. 50, pp. 245-63, Jul-Aug 2009.
- [42] S. D. Fihn, J. M. Gardin, J. Abrams, K. Berra, J. C. Blankenship, A. P. Dallas, *et al.*, "2012 ACCF/AHA/ACP/AATS/PCNA/SCAI/STS Guideline for the diagnosis and management of patients with stable ischemic heart disease: a report of the American College of Cardiology Foundation/American Heart Association Task Force on Practice Guidelines, and the American College of Physicians, American Association for Thoracic Surgery, Preventive Cardiovascular Nurses Association, Society for Cardiovascular Angiography and Interventions, and Society of Thoracic Surgeons," *J Am Coll Cardiol*, vol. 60, pp. e44-e164, Dec 18 2012.
- [43] S. Schneer, G. N. Bachar, E. Atar, R. Koronowski, and D. Dicker, "Evaluation of framingham and systematic coronary risk evaluation scores by coronary computed tomographic angiography in asymptomatic adults," *Am J Cardiol*, vol. 111, pp. 700-4, Mar 01 2013.
- [44] P. A. Tonino, W. F. Fearon, B. De Bruyne, K. G. Oldroyd, M. A. Leesar, P. N. Ver Lee, *et al.*, "Angiographic versus functional severity of coronary artery stenoses in the FAME study fractional flow reserve versus angiography in multivessel evaluation," *J Am Coll Cardiol*, vol. 55, pp. 2816-21, Jun 22 2010.
- [45] R. S. Lima, D. D. Watson, A. R. Goode, M. S. Siadaty, M. Ragosta, G. A. Beller, *et al.*, "Incremental value of combined perfusion and function over perfusion alone by gated SPECT myocardial perfusion imaging for detection of severe three-vessel coronary artery disease," *J Am Coll Cardiol*, vol. 42, pp. 64-70, Jul 02 2003.
- [46] N. H. Pijls, B. De Bruyne, K. Peels, P. H. Van Der Voort, H. J. Bonnier, J. K. J. J. Bartunek, *et al.*, "Measurement of fractional flow reserve to assess the functional severity of coronary-artery stenoses," *N Engl J Med*, vol. 334, pp. 1703-8, Jun 27 1996.
- [47] P. A. Tonino, B. De Bruyne, N. H. Pijls, U. Siebert, F. Ikeno, M. van' t Veer, *et al.*, "Fractional flow reserve versus angiography for guiding percutaneous coronary intervention," *N Engl J Med*, vol. 360, pp. 213-24, Jan 15 2009.



- [48] N. H. Pijls, P. van Schaardenburgh, G. Manoharan, E. Boersma, J. W. Bech, M. van't Veer, *et al.*, "Percutaneous coronary intervention of functionally nonsignificant stenosis: 5-year follow-up of the DEFER Study," *J Am Coll Cardiol*, vol. 49, pp. 2105-11, May 29 2007.
- [49] B. De Bruyne, N. H. Pijls, B. Kalesan, E. Barbato, P. A. Tonino, Z. Piroth, *et al.*, "Fractional flow reserve-guided PCI versus medical therapy in stable coronary disease," *N Engl J Med*, vol. 367, pp. 991-1001, Sep 13 2012.
- [50] G. J. Dehmer, D. Weaver, M. T. Roe, S. Milford-Beland, S. Fitzgerald, A. Hermann, *et al.*, "A contemporary view of diagnostic cardiac catheterization and percutaneous coronary intervention in the United States: a report from the CathPCI Registry of the National Cardiovascular Data Registry, 2010 through June 2011," *J Am Coll Cardiol*, vol. 60, pp. 2017-31, Nov 13 2012.
- [51] W. F. Fearon, B. Bornschein, P. A. Tonino, R. M. Gothe, B. D. Bruyne, N. H. Pijls, *et al.*, "Economic evaluation of fractional flow reserve-guided percutaneous coronary intervention in patients with multivessel disease," *Circulation*, vol. 122, pp. 2545-50, Dec 14 2010.
- [52] I. Kumsars, I. Narbutė, L. Thuesen, M. Niemela, T. K. Steigen, K. Kervinen, *et al.*, "Side branch fractional flow reserve measurements after main vessel stenting: a Nordic-Baltic Bifurcation Study III substudy," *EuroIntervention*, vol. 7, pp. 1155-61, Feb 2012.
- [53] G. Pontone, D. Andreini, A. Baggiano, E. Bertella, S. Mushtaq, E. Conte, *et al.*, "Functional relevance of coronary artery disease by cardiac magnetic resonance and cardiac computed tomography: myocardial perfusion and fractional flow reserve," *Biomed Res Int*, vol. 2015, p. 297696, 2015.
- [54] S. Sen, J. Escaned, I. S. Malik, G. W. Mikhail, R. A. Foale, R. Mila, *et al.*, "Development and validation of a new adenosine-independent index of stenosis severity from coronary wave-intensity analysis: results of the ADVISE (ADenosine Vasodilator Independent Stenosis Evaluation) study," *J Am Coll Cardiol*, vol. 59, pp. 1392-402, Apr 10 2012.
- [55] R. Petraco, J. J. Park, S. Sen, S. S. Nijjer, I. S. Malik, M. Echavarria-Pinto, *et al.*, "Hybrid iFR-FFR decision-making strategy: implications for enhancing universal adoption of physiology-guided coronary revascularisation," *EuroIntervention*, vol. 8, pp. 1157-65, Feb 22 2013.
- [56] M. J. Kern, U. Deligonul, S. Tatineni, H. Serota, F. Aguirre, and T. C. Hilton, "Intravenous adenosine: continuous infusion and low dose bolus administration for determination of coronary vasodilator reserve in patients with and without coronary artery disease," *J Am Coll Cardiol*, vol. 18, pp. 718-29, Sep 1991.

- [57] R. F. Wilson, K. Wyche, B. V. Christensen, S. Zimmer, and D. D. Laxson, "Effects of adenosine on human coronary arterial circulation," *Circulation*, vol. 82, pp. 1595-606, Nov 1990.
- [58] S.-H. investigators, "CT coronary angiography in patients with suspected angina due to coronary heart disease (SCOT-HEART): an open-label, parallel-group, multicentre trial," *Lancet*, vol. 385, pp. 2383-91, Jun 13 2015.
- [59] R. Waksman, J. Legutko, J. Singh, Q. Orlando, S. Marso, T. Schloss, *et al.*, "FIRST: Fractional Flow Reserve and Intravascular Ultrasound Relationship Study," *J Am Coll Cardiol*, vol. 61, pp. 917-23, Mar 05 2013.
- [60] S. J. Kang, J. Y. Lee, J. M. Ahn, G. S. Mintz, W. J. Kim, D. W. Park, *et al.*, "Validation of intravascular ultrasound-derived parameters with fractional flow reserve for assessment of coronary stenosis severity," *Circ Cardiovasc Interv*, vol. 4, pp. 65-71, Feb 01 2011.
- [61] N. Gonzalo, J. Escaned, F. Alfonso, C. Nolte, V. Rodriguez, P. Jimenez-Quevedo, *et al.*, "Morphometric assessment of coronary stenosis relevance with optical coherence tomography: a comparison with fractional flow reserve and intravascular ultrasound," *J Am Coll Cardiol*, vol. 59, pp. 1080-9, Mar 20 2012.
- [62] Y. Shiono, H. Kitabata, T. Kubo, T. Masuno, S. Ohta, Y. Ozaki, *et al.*, "Optical coherence tomography-derived anatomical criteria for functionally significant coronary stenosis assessed by fractional flow reserve," *Circ J*, vol. 76, pp. 2218-25, 2012.
- [63] G. Guagliumi, V. Sirbu, C. Petroff, D. Capodanno, G. Musumeci, H. Yamamoto, *et al.*, "Volumetric assessment of lesion severity with optical coherence tomography: relationship with fractional flow," *EuroIntervention*, vol. 8, pp. 1172-81, Feb 22 2013.
- [64] E. M. Khouri, D. E. Gregg, and H. S. Lowensohn, "Flow in the major branches of the left coronary artery during experimental coronary insufficiency in the unanesthetized dog," *Circ Res*, vol. 23, pp. 99-109, Jul 1968.
- [65] W. M. Fam and M. McGregor, "Pressure-flow relationships in the coronary circulation," *Circ Res*, vol. 25, pp. 293-301, Sep 1969.
- [66] D. N. Ku, D. P. Giddens, C. K. Zarins, and S. Glagov, "Pulsatile flow and atherosclerosis in the human carotid bifurcation. Positive correlation between plaque location and low oscillating shear stress," *Arteriosclerosis*, vol. 5, pp. 293-302, May-Jun 1985.
- [67] C. K. Zarins, D. P. Giddens, B. K. Bharadvaj, V. S. Sottiurai, R. F. Mabon, and S. Glagov, "Carotid bifurcation atherosclerosis. Quantitative correlation of plaque localization with flow velocity profiles and wall shear stress," *Circ Res*, vol. 53, pp. 502-14, Oct 1983.

- [68] C. A. Taylor and D. A. Steinman, "Image-based modeling of blood flow and vessel wall dynamics: applications, methods and future directions: Sixth International Bio-Fluid Mechanics Symposium and Workshop, March 28-30, 2008 Pasadena, California," *Ann Biomed Eng*, vol. 38, pp. 1188-203, Mar 2010.
- [69] A. Santamarina, E. Weydahl, J. M. Siegel, Jr., and J. E. Moore, Jr., "Computational analysis of flow in a curved tube model of the coronary arteries: effects of time-varying curvature," *Ann Biomed Eng*, vol. 26, pp. 944-54, Nov-Dec 1998.
- [70] R. K. Banerjee, L. H. Back, M. R. Back, and Y. I. Cho, "Physiological flow analysis in significant human coronary artery stenoses," *Biorheology*, vol. 40, pp. 451-76, 2003.
- [71] R. K. Banerjee, K. D. Ashtekar, T. A. Helmy, M. A. Effat, L. H. Back, and S. F. Khoury, "Hemodynamic diagnostics of epicardial coronary stenoses: in-vitro experimental and computational study," *Biomed Eng Online*, vol. 7, p. 24, Aug 27 2008.
- [72] A. K. Politis, G. P. Stavropoulos, M. N. Christolis, P. G. Panagopoulos, N. S. Vlachos, and N. C. Markatos, "Numerical modelling of simulated blood flow in idealized composite arterial coronary grafts: transient flow," *J Biomech*, vol. 41, pp. 25-39, 2008.
- [73] A. K. Politis, G. P. Stavropoulos, M. N. Christolis, F. G. Panagopoulos, N. S. Vlachos, and N. C. Markatos, "Numerical modeling of simulated blood flow in idealized composite arterial coronary grafts: steady state simulations," *J Biomech*, vol. 40, pp. 1125-36, 2007.
- [74] P. Vasava, P. Jalali, M. Dabagh, and P. J. Kolari, "Finite element modelling of pulsatile blood flow in idealized model of human aortic arch: study of hypotension and hypertension," *Comput Math Methods Med*, vol. 2012, p. 861837, 2012.
- [75] D. A. Steinman, J. B. Thomas, H. M. Ladak, J. S. Milner, B. K. Rutt, and J. D. Spence, "Reconstruction of carotid bifurcation hemodynamics and wall thickness using computational fluid dynamics and MRI," *Magn Reson Med*, vol. 47, pp. 149-59, Jan 2002.
- [76] J. R. Leach, V. L. Rayz, M. R. Mofrad, and D. Saloner, "An efficient two-stage approach for image-based FSI analysis of atherosclerotic arteries," *Biomech Model Mechanobiol*, vol. 9, pp. 213-23, Apr 2010.
- [77] D. Bluestein, Y. Alemu, I. Avrahami, M. Gharib, K. Dumont, J. J. Ricotta, *et al.*, "Influence of microcalcifications on vulnerable plaque mechanics using FSI modeling," *J Biomech*, vol. 41, pp. 1111-8, 2008.
- [78] S. A. Kock, J. V. Nygaard, N. Eldrup, E. T. Frund, A. Klaerke, W. P. Paaske, *et al.*, "Mechanical stresses in carotid plaques using MRI-based fluid-structure interaction models," *J Biomech*, vol. 41, pp. 1651-8, 2008.

- [79] J. K. Min, J. Leipsic, M. J. Pencina, D. S. Berman, B. K. Koo, C. van Mieghem, *et al.*, "Diagnostic accuracy of fractional flow reserve from anatomic CT angiography," *JAMA*, vol. 308, pp. 1237-45, Sep 26 2012.
- [80] B. L. Norgaard, J. Leipsic, S. Gaur, S. Seneviratne, B. S. Ko, H. Ito, *et al.*, "Diagnostic performance of noninvasive fractional flow reserve derived from coronary computed tomography angiography in suspected coronary artery disease: the NXT trial (Analysis of Coronary Blood Flow Using CT Angiography: Next Steps)," *J Am Coll Cardiol*, vol. 63, pp. 1145-1155, Apr 1 2014.
- [81] B. K. Koo, A. Erglis, J. H. Doh, D. V. Daniels, S. Jegere, H. S. Kim, *et al.*, "Diagnosis of ischemia-causing coronary stenoses by noninvasive fractional flow reserve computed from coronary computed tomographic angiograms. Results from the prospective multicenter DISCOVER-FLOW (Diagnosis of Ischemia-Causing Stenoses Obtained Via Noninvasive Fractional Flow Reserve) study," *J Am Coll Cardiol*, vol. 58, pp. 1989-97, Nov 1 2011.
- [82] P. S. Douglas, G. Pontone, M. A. Hlatky, M. R. Patel, B. L. Norgaard, R. A. Byrne, *et al.*, "Clinical outcomes of fractional flow reserve by computed tomographic angiography-guided diagnostic strategies vs. usual care in patients with suspected coronary artery disease: the prospective longitudinal trial of FFR(CT): outcome and resource impacts study," *Eur Heart J*, vol. 36, pp. 3359-67, Dec 14 2015.
- [83] C. M. Cook, R. Petraco, M. J. Shun-Shin, Y. Ahmad, S. Nijjer, R. Al-Lamee, *et al.*, "Diagnostic Accuracy of Computed Tomography-Derived Fractional Flow Reserve : A Systematic Review," *JAMA Cardiol*, vol. 2, pp. 803-810, Jul 1 2017.
- [84] K. Nieman, "Can CT angiography replace catheter coronary angiography?," *EuroIntervention*, vol. 6 Suppl G, pp. G65-71, May 2010.
- [85] S. Tu, E. Barbato, Z. Koszegi, J. Yang, Z. Sun, N. R. Holm, *et al.*, "Fractional flow reserve calculation from 3-dimensional quantitative coronary angiography and TIMI frame count: a fast computer model to quantify the functional significance of moderately obstructed coronary arteries," *JACC Cardiovasc Interv*, vol. 7, pp. 768-77, Jul 2014.
- [86] S. Tu, J. Westra, J. Yang, C. von Birgelen, A. Ferrara, M. Pellicano, *et al.*, "Diagnostic Accuracy of Fast Computational Approaches to Derive Fractional Flow Reserve From Diagnostic Coronary Angiography: The International Multicenter FAVOR Pilot Study," *JACC Cardiovasc Interv*, vol. 9, pp. 2024-2035, Oct 10 2016.
- [87] P. D. Morris, D. Ryan, A. C. Morton, R. Lycett, P. V. Lawford, D. R. Hose, *et al.*, "Virtual fractional flow reserve from coronary angiography: modeling the significance of

coronary lesions: results from the VIRTU-1 (VIRTUal Fractional Flow Reserve From Coronary Angiography) study," *JACC Cardiovasc Interv*, vol. 6, pp. 149-57, Feb 2013.

[88] M. I. Papafaklis, T. Muramatsu, Y. Ishibashi, L. S. Lakkas, S. Nakatani, C. V. Bourantas, *et al.*, "Fast virtual functional assessment of intermediate coronary lesions using routine angiographic data and blood flow simulation in humans: comparison with pressure wire - fractional flow reserve," *EuroIntervention*, vol. 10, pp. 574-83, Sep 2014.

[89] M. I. Papafaklis, T. Muramatsu, Y. Ishibashi, C. V. Bourantas, D. I. Fotiadis, E. S. Brilakis, *et al.*, "Virtual Resting Pd/Pa From Coronary Angiography and Blood Flow Modelling: Diagnostic Performance Against Fractional Flow Reserve," *Heart Lung Circ*, May 3 2017.

[90] J. E. Davies, S. Sen, and J. Escaned, "Instantaneous Wave-free Ratio versus Fractional Flow Reserve," *N Engl J Med*, vol. 377, pp. 1597-1598, Oct 19 2017.

[91] M. Gotberg, E. H. Christiansen, I. J. Gudmundsdottir, L. Sandhall, M. Danielewicz, L. Jakobsen, *et al.*, "Instantaneous Wave-free Ratio versus Fractional Flow Reserve to Guide PCI," *N Engl J Med*, vol. 376, pp. 1813-1823, May 11 2017.

[92] Y. Ma, H. Liu, Y. Hou, A. Qiao, Y. Hou, Q. Yang, *et al.*, "Instantaneous wave-free ratio derived from coronary computed tomography angiography in evaluation of ischemia-causing coronary stenosis: Feasibility and initial clinical research," *Medicine (Baltimore)*, vol. 96, p. e5979, Jan 2017.

[93] M. I. Papafaklis, M. C. Mavrogiannis, P. K. Siogkas, L. S. Lakkas, C. S. Katsouras, D. I. Fotiadis, *et al.*, "Functional assessment of lesion severity without using the pressure wire: coronary imaging and blood flow simulation," *Expert Rev Cardiovasc Ther*, vol. 15, pp. 863-877, Nov 2017.

[94] K. H. Kim, J. H. Doh, B. K. Koo, J. K. Min, A. Erglis, H. M. Yang, *et al.*, "A novel noninvasive technology for treatment planning using virtual coronary stenting and computed tomography-derived computed fractional flow reserve," *JACC Cardiovasc Interv*, vol. 7, pp. 72-8, Jan 2014.

[95] M. Renker, U. J. Schoepf, R. Wang, F. G. Meinel, J. D. Rier, R. R. Bayer, 2nd, *et al.*, "Comparison of diagnostic value of a novel noninvasive coronary computed tomography angiography method versus standard coronary angiography for assessing fractional flow reserve," *Am J Cardiol*, vol. 114, pp. 1303-8, Nov 1 2014.

[96] A. Coenen, M. M. Lubbers, A. Kurata, A. Kono, A. Dedic, R. G. Chelu, *et al.*, "Fractional flow reserve computed from noninvasive CT angiography data: diagnostic

performance of an on-site clinician-operated computational fluid dynamics algorithm," *Radiology*, vol. 274, pp. 674-83, Mar 2015.

[97] M. Kruk, L. Wardziak, M. Demkow, W. Pleban, J. Pregowski, Z. Dzielinska, *et al.*, "Workstation-Based Calculation of CTA-Based FFR for Intermediate Stenosis," *JACC Cardiovasc Imaging*, vol. 9, pp. 690-9, Jun 2016.

[98] B. S. Ko, J. D. Cameron, R. K. Munnur, D. T. L. Wong, Y. Fujisawa, T. Sakaguchi, *et al.*, "Noninvasive CT-Derived FFR Based on Structural and Fluid Analysis: A Comparison With Invasive FFR for Detection of Functionally Significant Stenosis," *JACC Cardiovasc Imaging*, vol. 10, pp. 663-673, Jun 2017.

[99] M. Trobs, S. Achenbach, J. Rother, T. Redel, M. Scheuering, D. Winneberger, *et al.*, "Comparison of Fractional Flow Reserve Based on Computational Fluid Dynamics Modeling Using Coronary Angiographic Vessel Morphology Versus Invasively Measured Fractional Flow Reserve," *Am J Cardiol*, vol. 117, pp. 29-35, Jan 1 2016.

[100] C. V. Bourantas, M. I. Papafaklis, L. Athanasiou, F. G. Kalatzis, K. K. Naka, P. K. Siogkas, *et al.*, "A new methodology for accurate 3-dimensional coronary artery reconstruction using routine intravascular ultrasound and angiographic data: implications for widespread assessment of endothelial shear stress in humans," *EuroIntervention*, vol. 9, pp. 582-93, Sep 2013.

[101] G. Porenta, H. Schima, A. Pentaris, S. Tsangaris, D. Moertl, P. Probst, *et al.*, "Assessment of coronary stenoses by Doppler wires: a validation study using in vitro modeling and computer simulations," *Ultrasound Med Biol*, vol. 25, pp. 793-801, Jun 1999.

[102] T. D. Mabotuwana, L. K. Cheng, and A. J. Pullan, "A model of blood flow in the mesenteric arterial system," *Biomed Eng Online*, vol. 6, p. 17, May 8 2007.

[103] N. M. Maurits, G. E. Loots, and A. E. Veldman, "The influence of vessel wall elasticity and peripheral resistance on the carotid artery flow wave form: a CFD model compared to in vivo ultrasound measurements," *J Biomech*, vol. 40, pp. 427-36, 2007.

[104] K. Perktold, M. Hofer, G. Rappitsch, M. Loew, B. D. Kuban, and M. H. Friedman, "Validated computation of physiologic flow in a realistic coronary artery branch," *J Biomech*, vol. 31, pp. 217-28, Mar 1998.

[105] S. Z. Zhao, P. Papathanasopoulou, Q. Long, I. Marshall, and X. Y. Xu, "Comparative study of magnetic resonance imaging and image-based computational fluid dynamics for quantification of pulsatile flow in a carotid bifurcation phantom," *Ann Biomed Eng*, vol. 31, pp. 962-71, Sep 2003.

- [106] N. H. Pijls, W. F. Fearon, P. A. Tonino, U. Siebert, F. Ikeno, B. Bornschein, *et al.*, "Fractional flow reserve versus angiography for guiding percutaneous coronary intervention in patients with multivessel coronary artery disease: 2-year follow-up of the FAME (Fractional Flow Reserve Versus Angiography for Multivessel Evaluation) study," *J Am Coll Cardiol*, vol. 56, pp. 177-84, Jul 13 2010.
- [107] W. B. Meijboom, A. C. Weustink, F. Pugliese, C. A. van Mieghem, N. R. Mollet, N. van Pelt, *et al.*, "Comparison of diagnostic accuracy of 64-slice computed tomography coronary angiography in women versus men with angina pectoris," *Am J Cardiol*, vol. 100, pp. 1532-7, Nov 15 2007.
- [108] M. Marzilli, C. N. Merz, W. E. Boden, R. O. Bonow, P. G. Capozza, W. M. Chilian, *et al.*, "Obstructive coronary atherosclerosis and ischemic heart disease: an elusive link!," *J Am Coll Cardiol*, vol. 60, pp. 951-6, Sep 11 2012.
- [109] B. De Bruyne, W. F. Fearon, N. H. Pijls, E. Barbato, P. Tonino, Z. Piroth, *et al.*, "Fractional flow reserve-guided PCI for stable coronary artery disease," *N Engl J Med*, vol. 371, pp. 1208-17, Sep 25 2014.
- [110] L. Athanasiou, G. Rigas, A. I. Sakellarios, T. P. Exarchos, P. K. Siogkas, C. V. Bourantas, *et al.*, "Three-dimensional reconstruction of coronary arteries and plaque morphology using CT angiography--comparison and registration with IVUS," *BMC Med Imaging*, vol. 16, p. 9, Jan 19 2016.
- [111] D. Neglia, D. Rovai, C. Caselli, M. Pietila, A. Teresinska, S. Aguade-Bruix, *et al.*, "Detection of significant coronary artery disease by noninvasive anatomical and functional imaging," *Circ Cardiovasc Imaging*, vol. 8, Mar 2015.
- [112] K. Fox, M. A. Garcia, D. Ardissino, P. Buszman, P. G. Camici, F. Crea, *et al.*, "[Guidelines on the management of stable angina pectoris. Executive summary]," *Rev Esp Cardiol*, vol. 59, pp. 919-70, Sep 2006.
- [113] K. L. Gould, K. O. Kelley, and E. L. Bolson, "Experimental validation of quantitative coronary arteriography for determining pressure-flow characteristics of coronary stenosis," *Circulation*, vol. 66, pp. 930-7, Nov 1982.
- [114] B. G. Brown, E. Bolson, M. Frimer, and H. T. Dodge, "Quantitative coronary arteriography: estimation of dimensions, hemodynamic resistance, and atheroma mass of coronary artery lesions using the arteriogram and digital computation," *Circulation*, vol. 55, pp. 329-37, Feb 1977.

- [115] M. J. Kern, R. G. Bach, C. J. Mechem, E. A. Caracciolo, F. V. Aguirre, L. W. Miller, *et al.*, "Variations in normal coronary vasodilatory reserve stratified by artery, gender, heart transplantation and coronary artery disease," *J Am Coll Cardiol*, vol. 28, pp. 1154-60, Nov 1 1996.
- [116] N. P. Johnson, R. L. Kirkeeide, and K. L. Gould, "Coronary anatomy to predict physiology: fundamental limits," *Circ Cardiovasc Imaging*, vol. 6, pp. 817-32, Sep 2013.
- [117] C. A. Taylor, T. A. Fonte, and J. K. Min, "Computational fluid dynamics applied to cardiac computed tomography for noninvasive quantification of fractional flow reserve: scientific basis," *J Am Coll Cardiol*, vol. 61, pp. 2233-41, Jun 4 2013.
- [118] R. R. Packard, D. Li, M. J. Budoff, and R. P. Karlsberg, "Fractional flow reserve by computerized tomography and subsequent coronary revascularization," *Eur Heart J Cardiovasc Imaging*, vol. 18, pp. 145-152, Feb 2017.
- [119] A. Coenen, A. Rossi, M. M. Lubbers, A. Kurata, A. K. Kono, R. G. Chelu, *et al.*, "Integrating CT Myocardial Perfusion and CT-FFR in the Work-Up of Coronary Artery Disease," *JACC Cardiovasc Imaging*, vol. 10, pp. 760-770, Jul 2017.
- [120] M. Task Force, G. Montalescot, U. Sechtem, S. Achenbach, F. Andreotti, C. Arden, *et al.*, "2013 ESC guidelines on the management of stable coronary artery disease: the Task Force on the management of stable coronary artery disease of the European Society of Cardiology," *Eur Heart J*, vol. 34, pp. 2949-3003, Oct 2013.
- [121] M. R. Patel, E. D. Peterson, D. Dai, J. M. Brennan, R. F. Redberg, H. V. Anderson, *et al.*, "Low diagnostic yield of elective coronary angiography," *N Engl J Med*, vol. 362, pp. 886-95, Mar 11 2010.
- [122] R. Liga, J. Vontobel, D. Rovai, M. Marinelli, C. Caselli, M. Pietila, *et al.*, "Multicentre multi-device hybrid imaging study of coronary artery disease: results from the EVAluation of INtegrated Cardiac Imaging for the Detection and Characterization of Ischaemic Heart Disease (EVINCI) hybrid imaging population," *Eur Heart J Cardiovasc Imaging*, vol. 17, pp. 951-60, Sep 2016.
- [123] S. Kajander, E. Joutsiniemi, M. Saraste, M. Pietila, H. Ukkonen, A. Saraste, *et al.*, "Cardiac positron emission tomography/computed tomography imaging accurately detects anatomically and functionally significant coronary artery disease," *Circulation*, vol. 122, pp. 603-13, Aug 10 2010.



- [124] P. D. Morris, F. N. van de Vosse, P. V. Lawford, D. R. Hose, and J. P. Gunn, ""Virtual" (Computed) Fractional Flow Reserve: Current Challenges and Limitations," *JACC Cardiovasc Interv*, vol. 8, pp. 1009-17, Jul 2015.
- [125] T. P. van de Hoef, M. Siebes, J. A. Spaan, and J. J. Piek, "Fundamentals in clinical coronary physiology: why coronary flow is more important than coronary pressure," *Eur Heart J*, vol. 36, pp. 3312-9a, Dec 14 2015.
- [126] N. P. Johnson, K. L. Gould, M. F. Di Carli, and V. R. Taqueti, "Invasive FFR and Noninvasive CFR in the Evaluation of Ischemia: What Is the Future?," *J Am Coll Cardiol*, vol. 67, pp. 2772-2788, Jun 14 2016.
- [127] V. R. Taqueti and M. F. Di Carli, "Clinical significance of noninvasive coronary flow reserve assessment in patients with ischemic heart disease," *Curr Opin Cardiol*, vol. 31, pp. 662-669, Nov 2016.
- [128] T. P. van de Hoef, M. A. van Lavieren, P. Damman, R. Delewi, M. A. Piek, S. A. Chamuleau, *et al.*, "Physiological basis and long-term clinical outcome of discordance between fractional flow reserve and coronary flow velocity reserve in coronary stenoses of intermediate severity," *Circ Cardiovasc Interv*, vol. 7, pp. 301-11, Jun 2014.
- [129] M. Echavarria-Pinto, J. Escaned, E. Macias, M. Medina, N. Gonzalo, R. Petraco, *et al.*, "Disturbed coronary hemodynamics in vessels with intermediate stenoses evaluated with fractional flow reserve: a combined analysis of epicardial and microcirculatory involvement in ischemic heart disease," *Circulation*, vol. 128, pp. 2557-66, Dec 17 2013.
- [130] I. Danad, J. Szymonifka, J. Schulman-Marcus, and J. K. Min, "Static and dynamic assessment of myocardial perfusion by computed tomography," *Eur Heart J Cardiovasc Imaging*, vol. 17, pp. 836-44, Aug 2016.
- [131] B. Hesse, K. Tagil, A. Cuocolo, C. Anagnostopoulos, M. Bardies, J. Bax, *et al.*, "EANM/ESC procedural guidelines for myocardial perfusion imaging in nuclear cardiology," *Eur J Nucl Med Mol Imaging*, vol. 32, pp. 855-97, Jul 2005.
- [132] V. Berti, R. Sciagra, D. Neglia, M. Pietila, A. J. Scholte, S. Nekolla, *et al.*, "Segmental quantitative myocardial perfusion with PET for the detection of significant coronary artery disease in patients with stable angina," *Eur J Nucl Med Mol Imaging*, vol. 43, pp. 1522-9, Jul 2016.
- [133] O. Gaemperli, T. Schepis, V. Kalff, M. Namdar, I. Valenta, L. Stefani, *et al.*, "Validation of a new cardiac image fusion software for three-dimensional integration of myocardial

perfusion SPECT and stand-alone 64-slice CT angiography," *Eur J Nucl Med Mol Imaging*, vol. 34, pp. 1097-106, Jul 2007.

[134] I. Danad, V. Uusitalo, T. Kero, A. Saraste, P. G. Raijmakers, A. A. Lammertsma, *et al.*, "Quantitative assessment of myocardial perfusion in the detection of significant coronary artery disease: cutoff values and diagnostic accuracy of quantitative [(15)O]H<sub>2</sub>O PET imaging," *J Am Coll Cardiol*, vol. 64, pp. 1464-75, Oct 7 2014.

[135] A. Ahmadi, G. W. Stone, J. Leipsic, L. J. Shaw, T. C. Villines, M. J. Kern, *et al.*, "Prognostic Determinants of Coronary Atherosclerosis in Stable Ischemic Heart Disease: Anatomy, Physiology, or Morphology?," *Circ Res*, vol. 119, pp. 317-29, Jul 8 2016.

[136] C. D. Vizza, C. Letizia, R. Badagliacca, S. Sciomer, R. Poscia, G. Della Rocca, *et al.*, "Plasma adrenomedullin and endothelin-1 concentration during low-dose dobutamine infusion: Relationship between pulmonary uptake and pulmonary vascular pressure/flow characteristics," *Regul Pept*, vol. 136, pp. 85-91, Sep 11 2006.

[137] N. Yamamoto, M. Toyoda, M. Abe, T. Kobayashi, K. Kobayashi, M. Kato, *et al.*, "Lectin-like oxidized LDL receptor-1 (LOX-1) expression in the tubulointerstitial area likely plays an important role in human diabetic nephropathy," *Intern Med*, vol. 48, pp. 189-94, 2009.

[138] K. L. Gould, N. P. Johnson, T. M. Bateman, R. S. Beanlands, F. M. Bengel, R. Bober, *et al.*, "Anatomic versus physiologic assessment of coronary artery disease. Role of coronary flow reserve, fractional flow reserve, and positron emission tomography imaging in revascularization decision-making," *J Am Coll Cardiol*, vol. 62, pp. 1639-1653, Oct 29 2013.

[139] H. Samady, W. Lepper, E. R. Powers, K. Wei, M. Ragosta, G. G. Bishop, *et al.*, "Fractional flow reserve of infarct-related arteries identifies reversible defects on noninvasive myocardial perfusion imaging early after myocardial infarction," *J Am Coll Cardiol*, vol. 47, pp. 2187-93, Jun 6 2006.

[140] J. A. Gonzalez, M. J. Lipinski, L. Flors, P. W. Shaw, C. M. Kramer, and M. Salerno, "Meta-Analysis of Diagnostic Performance of Coronary Computed Tomography Angiography, Computed Tomography Perfusion, and Computed Tomography-Fractional Flow Reserve in Functional Myocardial Ischemia Assessment Versus Invasive Fractional Flow Reserve," *Am J Cardiol*, vol. 116, pp. 1469-78, Nov 1 2015.

[141] R. Nakanishi, K. Osawa, I. Ceponiene, G. Huth, J. Cole, M. Kim, *et al.*, "The diagnostic performance of SPECT-MPI to predict functional significant coronary artery disease by fractional flow reserve derived from CCTA (FFRCT): sub-analysis from ACCURACY and VCT001 studies," *Int J Cardiovasc Imaging*, vol. 33, pp. 2067-2072, Dec 2017.

- [142] R. Nakazato, H. B. Park, D. S. Berman, H. Gransar, B. K. Koo, A. Erglis, *et al.*, "Response to letter regarding article, "Noninvasive fractional flow reserve derived from computed tomography angiography for coronary lesions of intermediate stenosis severity: results from the DeFACTO study"," *Circ Cardiovasc Imaging*, vol. 7, p. 571, May 2014.
- [143] S. Tu, Z. Huang, G. Koning, K. Cui, and J. H. Reiber, "A novel three-dimensional quantitative coronary angiography system: In-vivo comparison with intravascular ultrasound for assessing arterial segment length," *Catheter Cardiovasc Interv*, vol. 76, pp. 291-8, Aug 1 2010.
- [144] S. Gaur, S. Achenbach, J. Leipsic, L. Mauri, H. G. Bezerra, J. M. Jensen, *et al.*, "Rationale and design of the HeartFlowNXT (HeartFlow analysis of coronary blood flow using CT angiography: NeXt sTeps) study," *J Cardiovasc Comput Tomogr*, vol. 7, pp. 279-88, Sep-Oct 2013.
- [145] J. C. Schuurbiers, N. G. Lopez, J. Ligthart, F. J. Gijsen, J. Dijkstra, P. W. Serruys, *et al.*, "In vivo validation of CAAS QCA-3D coronary reconstruction using fusion of angiography and intravascular ultrasound (ANGUS)," *Catheter Cardiovasc Interv*, vol. 73, pp. 620-6, Apr 1 2009.
- [146] M. A. de Graaf, A. Broersen, P. H. Kitslaar, C. J. Roos, J. Dijkstra, B. P. Lelieveldt, *et al.*, "Automatic quantification and characterization of coronary atherosclerosis with computed tomography coronary angiography: cross-correlation with intravascular ultrasound virtual histology," *Int J Cardiovasc Imaging*, vol. 29, pp. 1177-90, Jun 2013.
- [147] C. Doulaverakis, I. Tsampoulatidis, A. P. Antoniadis, Y. S. Chatzizisis, A. Giannopoulos, I. Kompatsiaris, *et al.*, "IVUSAngio tool: a publicly available software for fast and accurate 3D reconstruction of coronary arteries," *Comput Biol Med*, vol. 43, pp. 1793-803, Nov 2013.
- [148] F. Nijhoff, K. G. Van Den Hengel, T. L. Slots, P. R. Stella, and P. Agostoni, "Clinical validation of a novel software for quantitative analysis of coronary intravascular ultrasound," *Cardiovasc Revasc Med*, vol. 15, pp. 393-401, Nov-Dec 2014.
- [149] S. Tu, L. Xu, J. Ligthart, B. Xu, K. Witberg, Z. Sun, *et al.*, "In vivo comparison of arterial lumen dimensions assessed by co-registered three-dimensional (3D) quantitative coronary angiography, intravascular ultrasound and optical coherence tomography," *Int J Cardiovasc Imaging*, vol. 28, pp. 1315-27, Aug 2012.
- [150] S. Tu, N. R. Holm, G. Koning, Z. Huang, and J. H. Reiber, "Fusion of 3D QCA and IVUS/OCT," *Int J Cardiovasc Imaging*, vol. 27, pp. 197-207, Feb 2011.

- [151] C. V. Bourantas, F. G. Kalatzis, M. I. Papafaklis, D. I. Fotiadis, A. C. Tweddel, I. C. Kourtis, *et al.*, "ANGIOCARE: an automated system for fast three-dimensional coronary reconstruction by integrating angiographic and intracoronary ultrasound data," *Catheter Cardiovasc Interv*, vol. 72, pp. 166-75, Aug 1 2008.
- [152] D. C. Barratt, B. B. Ariff, K. N. Humphries, S. A. Thom, and A. D. Hughes, "Reconstruction and quantification of the carotid artery bifurcation from 3-D ultrasound images," *IEEE Trans Med Imaging*, vol. 23, pp. 567-83, May 2004.
- [153] M. Schaap, C. T. Metz, T. van Walsum, A. G. van der Giessen, A. C. Weustink, N. R. Mollet, *et al.*, "Standardized evaluation methodology and reference database for evaluating coronary artery centerline extraction algorithms," *Med Image Anal*, vol. 13, pp. 701-14, Oct 2009.

## Author's Publications

### Journal Publications

1. Siogkas, K., Panagiotis; Sakellarios, I., Antonis; Exarchos, P., Themis; Stefanou, Kostas; Fotiadis, I., Dimitrios; Naka, Katerina; Michalis, Lampros; Filipovic, Nenad; Parodi, Oberdan, "Blood Flow in Arterial Segments: Rigid vs. Deformable Walls Simulations", *Journal of the Serbian Society for Computational Mechanics*, 5 (1), pp. 69-77, 2011.
2. P.Siogkas, A.I.Sakellarios, T.Exarchos, L.Athanasiou, E.Karvounis, K.Stefanou, E.Fotiou, D.I.Fotiadis, K.K.Naka, L.K.Michalis, N.Filipovic, O.Parodi, "Multi-level patient-specific artery and atherogenesis models", *IEEE Transactions on Biomedical Engineering, Special Issue Multi-Scale Modelling and Analysis for Computational Biology and Medicine*, 58 (12 PART 2), 5985488, pp. 3464-3468, 2011.
3. Panagiotis Siogkas, Michail Papafaklis, Antonis Sakellarios, Kostas Stefanou, Christos Bourantas, Lambros Athanasiou, Themis P. Exarchos, Katerina K. Naka, Lampros Michalis, Oberdan Parodi, and Dimitrios I. Fotiadis, "Patient-specific Simulation of Coronary Artery Pressure Measurements: An In Vivo Three-dimensional Validation Study in Humans", *BioMed Research International*, 01/2015; vol. 2015, pp. 1-11, 2015.
4. Panagiotis K. Siogkas, Kostas A. Stefanou, Lambros S. Athanasiou, Michail I. Papafaklis, Lampros K. Michalis, and Dimitrios I. Fotiadis, "Art Care: A Multi-Modality Coronary 3D Reconstruction and Hemodynamic Status Assessment Software", *Technology and Health Care*, doi: 10.3233/THC-170881, [Epub ahead of print] 2017.
5. Panagiotis K. Siogkas, Michail I. Papafaklis, Lampros Lakkas, Themis P. Exarchos, Dimitri Karpaliotis, Ziad A. Ali, Gualtiero Pelosi, Oberdan Parodi, Christos S. Katsouras, Dimitrios I. Fotiadis and Lampros K. Michalis, "Virtual Functional Assessment of Coronary Stenoses Using Intravascular Ultrasound Imaging: A Proof-of-Concept Pilot Study", *Heart Lung and Circulation*, doi: <https://doi.org/10.1016/j.hlc.2018.02.011>, 2018.
6. A.I.Sakellarios, K.Stefanou, P.Siogkas, V.D.Tsakanikas, C.V.Bourantas, L.Athanasiou, T.Exarchis, E.Fotiou, K.Naka, M.I.Papafaklis, A.J.Patterson, V.El.Young, J.H.Gillard, L.K.Michalis, D.I.Fotiadis, "Novel methodology for 3D reconstruction of carotid arteries and plaque characterization based upon magnetic resonance imaging carotid angiography data", *Magnetic Resonance Imaging Journal*, 30 (8), pp. 1068-1082, 2012.

7. T.P. Exarchos, K.Stefanou, P.Siogkas, A.Sakellarios, D.I.Fotiadis, K.Naka, L.Michalis, Lampros, N.Filipovic, O.Parodi, "ARTool: A Platform for the development of multi-level patient-specific artery and atherogenesis models", *Journal of Internet Research, Special Issue on Computational Bioengineering*, 7 (2), pp. 29-32, 2011.
8. Oberdan Parodi, Themis Exarchos, Paolo Marraccini, Federico Vozzi, Zarko Milosevic, Dalibor Nikolic, Antonis Sakellarios, Panagiotis Siogkas, Nenad Filipovic, Dimitris Fotiadis, "Patient-specific prediction of coronary plaque growth from CTA angiography: a multiscale model for plaque formation and progression", *IEEE Transaction on Information Technology in Biomedicine* 16 (5), 6208879, pp. 952-965, 2012.
9. Filipovic, N., Radovic, M., Isailovic, V., Milosevic, Z., Nikolic, D., Saveljic, I., Milosevic, M. Petrovic, D., Obradovic, M, Krsmanovic, D., Themis, E., Sakellarios, A., Siogkas, P., Marraccini, P, Vozzi, F Meunier, N. Teng, Z., Fotiadis, D., Parodi, O, Kojic, M., "Plaque formation and stent deployment with heating thermal effects in arteries", *Journal of the Serbian Society for Computational Mechanics*, 6 (1), pp. 11-28, 2012.
10. Sakellarios, A.I., Papafaklis, M.I., Siogkas, P., Athanasiou, L.S., Exarchos, T.P., Stefanou, K., Bourantas, C.V., Naka, K.K., Michalis, L.K., Parodi, O., Fotiadis, D.I. "Patient-specific computational modeling of subendothelial LDL accumulation in a stenosed right coronary artery: Effect of hemodynamic and biological factors", *American Journal of Physiology - Heart and Circulatory Physiology*, 304 (11), pp. H1455-H1470, 2013.
11. Bourantas, C.V., Papafaklis, M.I., Athanasiou, L., Kalatzis, F.G., Naka, K.K., Siogkas, P.K., Takahashi, S., Saito, S., Fotiadis, D.I., Feldman, C.L., Stone, P.H., Michalis, L.K. "A new methodology for accurate 3-dimensional coronary artery reconstruction using routine intravascular ultrasound and angiographic data: Implications for widespread assessment of endothelial shear stress in humans", *EuroIntervention*, 9 (5), pp. 582-593, 2013.
12. Athanasiou, L.S., Karvelis, P.S., Sakellarios, A.I., Exarchos, T.P., Siogkas, P.K., Tsakanikas, V.D., Naka, K.K., Bourantas, C.V., Papafaklis, M.I., Koutsouri, G., Michalis, L.K., Parodi, O., Fotiadis, D.I. "A hybrid plaque characterization method using intravascular ultrasound images", *Technology and Health Care*, 21 (3), pp. 199-216, 2013.
13. Athanasiou, L.S., Bourantas, C.V., Rigas, G., Sakellarios, A.I., Exarchos, T.P., Siogkas, P.K., Ricciardi, A., Naka, K.K., Papafaklis, M.I., Michalis, L.K., Prati, F., Fotiadis, D.I. "Methodology for fully automated segmentation and plaque characterization in

- intracoronary optical coherence tomography images” *Journal of Biomedical Optics*, 19 (2), 026009, 2014.
14. Athanasiou, L.S., Rigas, G.A., Sakellarios, A.I., Exarchos, T.P., Siogkas, P.K., Naka, K.K., Panetta, D., Pelosi, G., Vozzi, F., Michalis, L.K., Parodi, O., Fotiadis, D.I. “Computerized methodology for micro-CT and histological data inflation using an IVUS based translation map” *Computers in Biology and Medicine*, 65, pp. 168-176, 2015.
  15. Athanasiou, L., Sakellarios, A.I., Bourantas, C.V. , Tsirka, G., Siogkas, P., Exarchos, T.P., Naka, K.K., Michalis, L.K., Fotiadis, D.I. “ Currently available methodologies for the processing of intravascular ultrasound and optical coherence tomography images” *Expert Review of Cardiovascular Therapy*, 12 (7), pp. 885-900, 2014.
  16. Athanasiou, L., Rigas, G., Sakellarios, A.I., Exarchos, T.P., Siogkas, P.K., Bourantas, C.V., Garcia-Garcia, H.M., Lemos, P.A., Falcao, B.A., Michalis, L.K., Parodi, O., Vozzi, F., Fotiadis, D.I. “Three-dimensional reconstruction of coronary arteries and plaque morphology using CT angiography - comparison and registration with IVUS” *BMC Medical Imaging*, 16 (1), 2016.
  17. Michail I. Papafaklis, Michail C. Mavrogiannis, Panagiotis K. Siogkas, Lampros S. Lakkas, Christos S. Katsouras, Dimitrios I. Fotiadis, Lampros K. Michalis. “Functional Assessment of Lesion Severity Without Using the Pressure Wire: Coronary Imaging and Blood Flow Simulation” *Expert Review of Cardiovascular Therapy*, 15 (11), pp. 863-877, 2017.
  18. Vassiliki I. Kigka, George Rigas, Antonis Sakellarios, Siogkas Panagiotis, Ioannis O. Andrikos, Themis P. Exarchos, Dimitra Loggitsi, Constantinos D. Anagnostopoulos, Lampros K. Michalis, Danilo Neglia, Gualtriero Pelosi, Oberdan Parodi, Dimitrios I. Fotiadis. “3D Reconstruction of Coronary Arteries and Atherosclerotic Plaques based on Computed Tomography Angiography Images” *Biomedical Signal Processing & Control*, 40, pp. 286-294, 2018.





## Submitted to Journals

1. Panagiotis K. Siogkas, Constantinos D. Anagnostopoulos, Riccardo Liga, Themis P. Exarchos, Antonis I. Sakellarios, George Rigas, Arthur J.H.A. Scholte, M.I. Papafaklis, Dimitra Loggitsi, Gualtiero Pelosi, Oberdan Parodi, Lampros K. Michalis, Juhani Knuuti, Danilo Neglia, Dimitrios I. Fotiadis, “Computational hemodynamic assessment of coronary lesions from computed tomography angiography: a novel approach”, *International Journal of Cardiology*, 2018.



## Conference Publications

1. Panagiotis K. Siogkas, Antonis I. Sakellarios, Kostas A. Stefanou, Themis P. Exarchos, Lambros Athanasiou, Konstantinos G. Siogas, Lampros K. Michalis, Katerina K. Naka, Christos V. Bourantas, Catrin Bludszuweit-Philipp and Dimitrios I. Fotiadis, “Exploring the Effect of Arterial Geometry in a Realistic 3D Coronary Arterial Model”, *10th International Workshop on Biomedical Engineering*, October 2011, Kos, Greece.
2. P. K. Siogkas, A. I. Sakellarios, K. A. Stefanou, V. D. Tsakanikas, T. P. Exarchos, L. K. Michalis, K. K. Naka, C. Bludszuweit-Philipp and D. I. Fotiadis, “Quantification of the Effect of Percutaneous Coronary Angioplasty on a Stenosed Right Coronary Artery”, *10th IEEE International Conference on Information Technology and Applications in Biomedicine*, November 2010, Corfu, Greece.
3. P. K. Siogkas, A. I. Sakellarios, K. A. Stefanou, T. P. Exarchos, V. D. Tsakanikas, L. K. Michalis, K. K. Naka, M. I. Papafakis, C. V. Bourantas and D. I. Fotiadis, “Blood flow in coronary arteries with deformable walls”, *9th HSTAM International Congress on mechanics*, Limassol, Cyprus, 2010.
4. Antonis I. Sakellarios, Panagiotis K. Siogkas, Vasilis D. Tsakanikas, Kostas A. Stefanou, Lampros K. Michalis, Dimitrios I. Fotiadis, “Simulation of the Effect of Tachycardia on Atherosclerotic Plaque Development Based on the LDL Transport in Coronary Arteries”, *CinC 2010*, Belfast, Ireland, September 2010.
5. Antonis I. Sakellarios, Panagiotis K. Siogkas, Vasilis D. Tsakanikas, Katerina K. Naka, Lampros K. Michalis, Dimitrios I. Fotiadis, “Computational model of atherosclerotic plaque formation in 3D coronary arterial tree of realistic geometry” *ELEMBIO 2010*, Ioannina, 4 - 6 June 2010.
6. A.I.Sakellarios, T.Exarchos, P.Siogkas, K.Stefanou,, C.V.Bourantas, E.Fotiou, K.K.Naka, L.K.Michalis, D.Koutsouris, D.I.Fotiadis, "Influence of arterial geometry and stenosis on LDL accumulation in arteries", *7th GRACM International Congress on Computational Mechanics*, 2011.
7. A. I. Sakellarios, P. Siogkas, T. P. Exarchos, K. Stefanou, C. V. Bourantas, K. K. Naka, D. I. Fotiadis, L. K. Michalis, “Computational Blood Flow Modeling Validation using MRI Carotid Angiography”, *32<sup>ο</sup> Πανελλήνιο Καρδιολογικό Συνέδριο, Θεσσαλονίκη, Ελλάδα, Οκτώβριος 2011.*

8. L. Athanasiou, C. Bourantas, P. Siogkas, A. Sakellarios, T. Exarchos, K. Naka, M. Papafakis, F. Prati, D. Fotiadis, "3D Reconstruction of Coronary Arteries Using Frequency Domain Optical Coherence Tomography Images and Biplane Angiography", *34th Annual International IEEE EMBS Conference, San Diego, California, USA*, August 28 - September 1, 2012.
9. T. Exarchos, A. Sakellarios, P. Siogkas, D. Fotiadis, Z. Milosevic, D. Nikolic, N. Filipovic, P. Maraccini, F. Vozzi, O. Parodi, "Patient Specific Multiscale Modelling for Plaque Formation and Progression, *34th Annual International IEEE EMBS Conference, San Diego, California, USA*, August 28 - September 1, 2012.
10. Athanasiou, L.S., Bourantas, C.V., Siogkas, P.K., Sakellarios, A.I., Exarchos, T.P., Naka, K.K., Papafakis, M.I., Michalis, L.K., Prati, F., Fotiadis, D.I. "3D reconstruction of coronary arteries using Frequency Domain Optical Coherence Tomography images and biplane angiography", *Proceedings of the Annual International Conference of the IEEE Engineering in Medicine and Biology Society, EMBS*, 6346508, pp. 2647-2650, 2012.
11. Exarchos, T.P. , Sakellarios, A. , Siogkas, P.K. , Fotiadis, D.I. , Milosevic, Z. , Nikolic, D. , Filipovic, N. , Marraccini, P., Vozzi, F., Parodi, O., "Patient specific multiscale modelling for plaque formation and progression", *Proceedings of the Annual International Conference of the IEEE Engineering in Medicine and Biology Society, EMBS*, 6346568, pp. 2893-2896, 2012.
12. Athanasiou, L.S. , Bourantas, C.V. , Rigas, G.A. , Exarchos, T.P. , Sakellarios, A.I. , Siogkas, P.K. , Papafakis, M.I. , Naka, K.K. , Michalis, L.K. , Prati, F , Fotiadis, D.I. "Fully automated calcium detection using optical coherence tomography" *Proceedings of the Annual International Conference of the IEEE Engineering in Medicine and Biology Society*, 6609779, pp. 1430-1433, 2013.
13. Siogkas, P.K. , Papafakis, M.I. , Sakellarios, A.I. , Stefanou, K.A. , Bourantas, C.V., Athanasiou, L.M. , Bellos, C.V , Exarchos, T.P. , Naka, K.K. , Michalis, L.K. , Parodi, O., Fotiadis, D.I., "Computational assessment of the fractional flow reserve from intravascular ultrasound and coronary angiography data: A pilot study", *Proceedings of the Annual International Conference of the IEEE Engineering in Medicine and Biology Society*, 6610393, pp. 3885-3888, 2013.
14. Sakellarios, A.I. , Siogkas, P.K , Athanasiou, L.S., Exarchos, T.P., Papafakis, M.I., Bourantas, C.V., Naka, K.K., Michalis, L.K., Filipovic, N., Parodi, O., Fotiadis, D.I., "Three-

- dimensional modeling of oxidized-LDL accumulation and HDL mass transport in a coronary artery: A proof-of-concept study for predicting the region of atherosclerotic plaque development”, *Proceedings of the Annual International Conference of the IEEE Engineering in Medicine and Biology Society*, 6610550, pp. 4513-4516, 2013.
15. Sakellarios, A.I., Siogkas, P.K., Athanasiou, L.S., Exarchos, T.P., Papafaklis, M.I., Bourantas, C.V., Naka, K.K., Iliopoulou, D. Michalis, L.K., Filipovic, N., Parodi, O., Fotiadis, D.I., “Modeling atherosclerotic plaque growth: A case report based on a 3D geometry of left coronary arterial tree from computed tomography”, *13th IEEE International Conference on BioInformatics and BioEngineering, IEEE BIBE 2013*, 6701548, 2013.
  16. Panagiotis Siogkas, Antonis Sakellarios, Michail Papafaklis, Kostas Stefanou, Lambros Athanasiou, Themis P. Exarchos, Katerina Naka, Lampros Michalis, Dimitrios I. Fotiadis, “Assessing the Hemodynamic Influence between Multiple Lesions in a Realistic Right Coronary Artery Segment: a Computational Study”, *Proceedings of the Annual International Conference of the IEEE Engineering in Medicine and Biology Society, EMBS*, 2014.
  17. Lambros Athanasiou, Georgios Rigas, Antonis Sakellarios, Themis P. Exarchos, Panagiotis Siogkas, Lampros Michalis, Oberdan Parodi, Federico Vozzi, Dimitrios I. Fotiadis “Three-Dimensional Reconstruction of Coronary Arteries and Plaque Morphology Using CT Angiography – Comparison and Registration Using IVUS” *Annual International Conference of the IEEE Engineering in Medicine and Biology Society, EMBS*, 2014.
  18. Panagiotis Siogkas, Lambros Athanasiou, Antonis Sakellarios, Kostas A. Stefanou, Themis P. Exarchos, Michail I. Papafaklis, Katerina K. Naka, O. Parodi, Lampros K. Michalis, Dimitrios I. Fotiadis “Validation Study of a 3D-QCA Coronary Reconstruction Method Using a Hybrid IntraVascular UltraSound and Angiography Reconstruction Method and Patient-Specific Fractional Flow Reserve Data” *Proceedings of the Annual International Conference of the IEEE Engineering in Medicine and Biology Society, EMBS*, Vol. 2015, pp. 973-976, 2015.
  19. Panagiotis K. Siogkas, Constantinos D. Anagnostopoulos, Themis P. Exarchos, Riccardo Liga, Juhani Knuuti, Arthur J.H.A. Scholte, Oberdan Parodi, Lampros K. Michalis, Danilo Neglia, Dimitrios I. Fotiadis, “Computational Hemodynamic Assessment of coronary lesions from Computed Tomography Angiography. A novel approach”, *European Society of Cardiology Congress*, 2016.

20. Panagiotis K. Siogkas, Michail I. Papafaklis, Bill D. Gogas, Habib Samady, Lampros K. Michalis and Dimitrios I. Fotiadis, “Computational Estimation of the Severity of Coronary Lesions with IntraVascular UltraSound Images: a pilot study”, *Proceedings of the Annual International Conference of the IEEE Engineering in Medicine and Biology Society, EMBS*, 2016.
21. Panagiotis K. Siogkas, Vassiliki Kigka, George Rigas, Antonis I. Sakellarios, Themis P. Exarchos, Dimitrios I. Fotiadis “Analysis of Coronary Computed Tomography Angiography for 3D reconstruction of arterial trees and plaque detection” *International Conference on Biomedical and Health Informatics*, 2017.
22. Panagiotis K. Siogkas, Antonis I. Sakellarios, George Rigas, Themis P. Exarchos, Michail I. Papafaklis, Gualtiero Pelosi, Oberdan Parodi, Lampros K. Michalis, Dimitrios I. Fotiadis “Computational Estimation of the Hemodynamic Significance of Coronary Stenoses in Arterial Branches deriving from CCTA: a proof-of-concept study” *Proceedings of the Annual International Conference of the IEEE Engineering in Medicine and Biology Society, EMBS*, 2017.
23. Panagiotis K. Siogkas, Danilo Neglia, Antonis I. Sakellarios, Riccardo Liga, Gualtiero Pelosi, M. I. Papafaklis, T. Niittymaki, Arthur J.H.A. Scholte, O. Gaemperli, P.A. Kaufmann, Oberdan Parodi, Lampros K. Michalis, Dimitrios I. Fotiadis, Juhani Knuuti, Constantinos D. Anagnostopoulos “Characterization of functionally significant coronary artery disease by a novel coronary computed tomography angiography based index: a comparison with quantitative PET perfusion” *European Society of Cardiology Congress* 2017.
24. Panagiota I. Tsompou, Panagiotis K. Siogkas, Antonis I. Sakellarios, Pedro A. Lemos, Lampros K. Michalis, Dimitrios I. Fotiadis, “Non-invasive Assessment of Coronary Stenoses and Comparison to Invasive Techniques: A Proof-of-Concept Study” *IEEE 30th International Symposium on Computer-Based Medical Systems (CBMS)*, 2017.
25. Antonis Sakellarios, Nikolaos Tachos, Eleni Georga, George Rigas, Vassiliki Kigka, Panagiotis Siogkas, Savvas Kyriakidis, Georgia Karanasiou, Panagiota Tsobou, Ioannis Andrikos, Silvia Rocchiccioli, Gualtiero Pelosi, Oberdan Parodi, Dimitrios I. Fotiadis, “A novel concept of the management of coronary artery disease patients based on machine learning risk stratification and computational biomechanics: Preliminary results of SMARTool project” *Proceedings of the World Congress of Medical Physics and Biomedical Engineering*, 2018.

26. Panagiotis Siogkas, Antonis Sakellarios, Lampros Michalis, Dimitrios I. Fotiadis, “Non-invasive quantification of coronary artery disease in arterial bifurcations using CCTA and CFD: comparison to fractional flow reserve measurements” *Proceedings of the World Congress of Medical Physics and Biomedical Engineering*, 2018.
27. Ioannis Andrikos, Antonis Sakellarios, Panagiotis Siogkas, Panagiota Tsobou, Vassiliki Kigka, Lampros Michalis, Dimitrios I. Fotiadis, “A novel method for 3D reconstruction of coronary bifurcation using Quantitative Coronary Angiography” *Proceedings of the World Congress of Medical Physics and Biomedical Engineering*, 2018.
28. Π.Κ. Σιόγκας, Α.Ι. Σακελλάριος, Κ.Α. Στεφάνου, Β.Δ. Τσακανίκας, Κ.Κ. Νάκα, Δ.Ι. Φωτιάδης, Λ.Κ. Μιχάλης, “Προσομοίωση της ροής αίματος σε τρισδιάστατο υπολογιστικό μοντέλο αθηρωματικής αρτηρίας με παραμορφώσιμα τοιχώματα”, *31<sup>ο</sup> Πανελλήνιο Καρδιολογικό Συνέδριο, Αθήνα, Ελλάδα, Οκτώβριος 2010*.
29. Π.Κ. Σιόγκας, Α.Ι. Σακελλάριος, Κ.Α. Στεφάνου, Θ.Π. Έξαρχος, Κ.Κ. Νάκα, Δ.Ι. Φωτιάδης, Λ.Κ. Μιχάλης, “Η επίδραση της τοποθέτησης STENT στις παραγόμενες διατμητικές τάσεις και στην τμηματική εφεδρεία ροής σε τρισδιάστατα μοντέλα πραγματικής στενωμένης στεφανιαίας αρτηρίας”, *32<sup>ο</sup> Πανελλήνιο Καρδιολογικό Συνέδριο, Θεσσαλονίκη, Ελλάδα, Οκτώβριος 2011*.
30. A. I. Sakellarios, P. Siogkas, T. P. Exarchos, K. Stefanou, C. V. Bourantas, K. K. Naka, D. I. Fotiadis, L. K. Michalis, “The effects of rheology on the atheromatus plaque development: Presentation of a novel model for the prediction of regions prone to atheromatous plaque formation based on both wall shear stress and LDL transportation to the arterial wall”, *32<sup>ο</sup> Πανελλήνιο Καρδιολογικό Συνέδριο, Θεσσαλονίκη, Ελλάδα, Οκτώβριος 2011*.
31. Antonis I. Sakellarios, Panagiotis K. Siogkas, Vasilis D. Tsakanikas, Kostas A. Stefanou, Katerina K. Naka, Lampros K. Michalis, Dimitrios I. Fotiadis, “Blood Flow Simulation in 3D Patient-Specific MRI Reconstructed Carotid Arteries”, *International VPH Conference, VPH2010, 30th September to 1st October, 2010*.
32. Oberdan Parodi, T. Exarchos, P. Marraccini, F. Vozzi, Z. Milosevic, D. Nikolic, A. Sakellarios, P. Siogkas, N. Filipovic, D. Fotiadis, “Patient-specific prediction of coronary plaque growth from computed tomography angiography: a multiscale model for plaque formation and progression”, *80<sup>th</sup> EAS Congress, Milan, Italy, 2012*.
33. A.I. Sakellarios, Panagiotis Siogkas, T.P. Exarchos, K. Stefanou, L. Athanasiou, M. Papafaklis, C.V. Bourantas, E. Fotiou, K.K. Naka, L.K. Michalis, D.I. Fotiadis, O. Parodi,

“Augmented low density lipoprotein accumulation in coronary regions with endothelial dysfunction and low shear stress: a computational modeling study”, *80<sup>th</sup> EAS Congress, Milan, Italy*, 2012.

34. Georgios Rigas, Lambros Athanasiou, Antonis Sakellarios, Themis P. Exarchos, Panagiotis Siogkas , Katerina Naka, Daniele Panetta, Gualtiero Pelosi, Lampros Michalis, Oberdan Parodi, Dimitrios I. Fotiadis, “Methodology for Micro-CT Data Inflation Using Intravascular Ultrasound Images”, *Proceedings of the Annual International Conference of the IEEE Engineering in Medicine and Biology Society, EMBS*, 2014.
35. Panagiotis Siogkas, Lambros Athanasiou, Antonis Sakellarios, Kostas A. Stefanou, Themis P. Exarchos, Michail I. Papafaklis, Katerina K. Naka, Lampros K. Michalis, Dimitrios I. Fotiadis “Quantitative Coronary Analysis using 3D Coronary Reconstruction Based on Two Biplane Angiographic Images: a Validation Study» *International Conference on Biomedical and Health Informatics, ICBHI*, 2015.



## Scientific Book Chapters

1. P.Siogkas, D.Fotiadis, C.Bourantas, L.Michalis, D.Koutsouris, "Analysis of existing data fusion methodologies for 3D coronary imaging in Intravascular imaging", *Intravascular Imaging: Current Applications and Research Developments*, pp. 278-291 IGI global, 2011.
2. Sakellarios A.I., Karanasiou, G., Siogkas, P., Kigka, V., Exarchos, T., Rigas, G., Michalis, L.K., Fotiadis, D.I., "Available computational techniques to model atherosclerotic plaque progression implementing a multi-level approach», *Computational Biomechanics for Medicine: From Algorithms to Models and Applications*, pp. 39-55, 2017.



## **Short CV**

Panagiotis K. Siogkas was born in Athens in 1982. He received his diploma in Mechanical and Aeronautical Engineering from the University of Patras, Patras, Greece, in 2009. He is currently a Phd candidate in biomedical engineering at the department of Materials Science Engineering at the University of Ioannina, Ioannina, Greece. He has authored or co-authored 19 papers in scientific journals, more than 35 papers in peer-reviewed conference proceedings as well as two chapters in scientific books. His research interests specialize in blood flow modeling in arterial segments and in virtual FFR calculation. He has also worked for five research and development projects funded by the EC and other bodies.